



## UvA-DARE (Digital Academic Repository)

### Accelerated cardiovascular flow MRI

Peper, E.S.

**Publication date**

2020

**Document Version**

Final published version

**License**

Other

[Link to publication](#)

**Citation for published version (APA):**

Peper, E. S. (2020). *Accelerated cardiovascular flow MRI*.

**General rights**

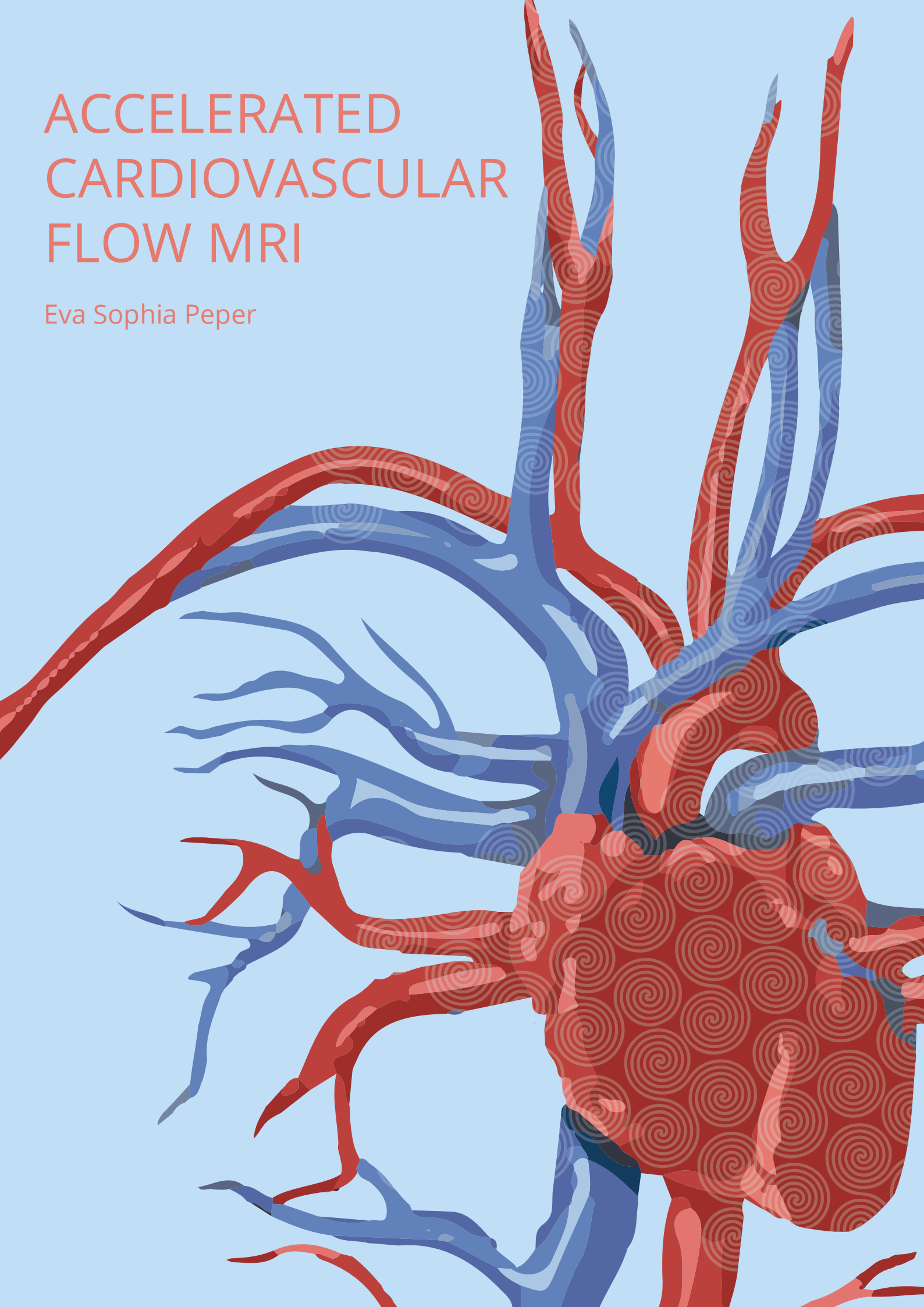
It is not permitted to download or to forward/distribute the text or part of it without the consent of the author(s) and/or copyright holder(s), other than for strictly personal, individual use, unless the work is under an open content license (like Creative Commons).

**Disclaimer/Complaints regulations**

If you believe that digital publication of certain material infringes any of your rights or (privacy) interests, please let the Library know, stating your reasons. In case of a legitimate complaint, the Library will make the material inaccessible and/or remove it from the website. Please Ask the Library: <https://uba.uva.nl/en/contact>, or a letter to: Library of the University of Amsterdam, Secretariat, Singel 425, 1012 WP Amsterdam, The Netherlands. You will be contacted as soon as possible.

# ACCELERATED CARDIOVASCULAR FLOW MRI

Eva Sophia Peper





# **ACCELERATED CARDIOVASCULAR FLOW MRI**

Eva Sophia Peper



Layout & Design Eva Sophia Peper  
Anatomical image lightspring/shutterstock.com  
ISBN 978-94-6332-636-0

Copyright © 2020 Eva Sophia Peper, Amsterdam 2020

The research in this thesis was funded by the Dutch foundation NWO, grant no. 13928.  
All rights reserved. No part of this thesis may be reproduced, stored or transmitted in any form or by any means without the permission in writing of the copyrights owner. Copyright of the published chapters is held by the journals in which the work appears.

# **ACCELERATED CARDIOVASCULAR FLOW MRI**

ACADEMISCH PROEFSCHRIFT

ter verkrijging van de graad van doctor  
aan de Universiteit van Amsterdam  
op gezag van de Rector Magnificus  
prof. dr. ir. K.I.J. Maex  
ten overstaan van een door het College voor Promoties ingestelde commissie,  
in het openbaar te verdedigen  
op vrijdag 19 juni 2020, te 10.00 uur

door Eva Sophia Peper  
geboren te Heidelberg

## Promotiecommissie

Promotores:	prof. dr. ir. A.J. Nederveen	AMC-UvA
	prof. dr. ir. G.J. Strijkers	AMC-UvA
Copromotores:	dr. ir. P. van Ooij	AMC-UvA
	dr. ir. B.F. Coolen	AMC-UvA
Overige leden:	prof. dr. S. Kozerke	ETH Zürich
	dr. M.J.W. Götte	VUmc
	dr. ir. J.J.M. Westenberg	LUMC
	prof. dr. S.A.J. Chamuleau	AMC-UvA
	prof. dr. E.T. van Bavel	AMC-UvA
	prof. mr. dr. B.A.J.M. de Mol	AMC-UvA

Faculteit der Geneeskunde

# CONTENTS

<b>Chapter 1</b>	Introduction and thesis outline	5
<b>Chapter 2</b>	Regional assessment of carotid artery pulse wave velocity using compressed sensing accelerated high temporal resolution 2D CINE phase contrast cardiovascular magnetic resonance	21
<b>Chapter 3</b>	Highly accelerated 4D flow cardiovascular magnetic resonance using a pseudo-spiral Cartesian acquisition and compressed sensing reconstruction for carotid flow and wall shear stress	41
<b>Chapter 4</b>	Pseudo-spiral sampling and compressed sensing reconstruction provides flexibility of temporal resolution in accelerated aortic 4D flow MRI: A comparison with k-t principal component analysis	69
<b>Chapter 5</b>	MRI measurements of carotid pulse wave velocity, wall thickness and wall shear stress in statin treated patients with familial hypercholesterolemia	91
<b>Chapter 6</b>	An isolated beating pig heart platform for a comprehensive evaluation of intracardiac blood flow with 4D flow MRI: a feasibility study	111
<b>Chapter 7</b>	General discussion and summary	133
<b>Appendix</b>	Portfolio and PhD training	147



# CHAPTER 1

Introduction and thesis outline

## 1.1 General introduction

4D flow MRI, or “three-dimensional phase-contrast cine MRI” [1,2], is an MRI technique, which facilitates visualization and quantification of blood flow in the heart and great vessels. It does this by making time-resolved images (or movies) of the blood flow in a three-dimensional volume. 4D flow MRI finds many applications: examples include the assessment of complex flow patterns (intracardiac vortex formation) in the left-ventricular cavity [3] or in the quantification of backflow through the heart valves. As such, 4D flow MRI can improve diagnosis and aid in better understanding of underlying pathological processes.

Many useful hemodynamic parameters can be derived from a 4D-flow measurement. First of all, relevant diagnostic parameters, such as cardiac output (CO), stroke volume (SV), regurgitation fraction and flow rate through the heart valves [4,5] can be measured. Apart from these well-known parameters, other hemodynamic biomarkers can be derived, which are not yet part of clinical practice. Wall shear stress (WSS) for example, can be derived from the blood velocities [6–8]. It is the force that the flowing blood exerts on the vessel wall and it has been shown that low WSS leads to a rearrangement of the endothelial cells of which the wall consist [6–9]. This may in turn lead to an increase in vessel wall thickness [10], a precursor to plaque formation and atherosclerosis. Another useful parameter, which can be investigated with flow MRI is pulse wave velocity (PWV) [11]. PWV relates to vessel stiffness. Stiffening of the artery wall, *e.g.* in the carotid arteries, can be a sign of early plaque formation, even precluding vessel wall thickening [12–14]. An increase of vessel stiffness strongly correlates with age and a decrease can lead to cognitive damage as high blood pressure is directly transmitted to the brain’s microvasculature [6,7]. Generally, atherosclerosis precedes many cardiovascular diseases and can stay asymptomatic for a long time, which is why tools for early stage diagnosis via the measurement of these hemodynamic biomarkers are highly desired.

Traditionally, ultrasound is the method of choice for flow quantification in the heart, aorta, or the Circle of Willis. Accurate ultrasound flow quantification, however, relies on operator skills and experience. For example, when capturing backflow (regurgitations) through the heart valves [15,16], the angle between probe and blood flow as well as the directionality of blood flow need to be carefully considered [17]. In some cases, a transesophageal echocardiography, *i.e.* inserting the echo probe via the esophagus to gain improved access to the heart and aorta, is needed which is very uncomfortable to the patient. 4D flow MRI does not suffer from these drawbacks and is fully non-invasive. Operator and observer variability are strongly reduced, as the MRI operator only needs to define a 3D volume of interest containing the relevant vessels. Flow rates can then be quantified retrospectively in any desired plane or orientation.

Despite its promise, currently the main limitation of 4D flow MRI is the long scan time (10 to 30 min) needed for sufficient spatial coverage and spatiotemporal resolution [18–20]. This practically hampers its use in routine clinics, as lying still for a long time is difficult for patients, leading to movement artifacts and increasing cost and waiting times. Acceleration of 4D flow MRI scans is therefore indispensable to achieve reasonable scan times <10 min.

The scan time depends on the size of the imaging matrix, but also on the number of desired cardiac frames (the framerate of the “4D flow movie”) and respiratory gating efficiency. A simple way to

accelerate the scan is to reduce the number of cardiac frames, which however will lead to loss of temporal information. A better approach is to reduce the number of sampling points in the imaging matrix below the number dictated by the Nyquist sampling criterion. To prevent aliasing artifacts, missing data points can be recovered on the basis of additional information, for example by using parallel imaging with multiple coils (as is done in SENSE) or on the basis of prior information on the nature and complexity of the images (as is done in compressed sensing, CS), or by a combination of both [21,22].

The degree of achievable imaging acceleration depends on the type of the acceleration technique and the performance of the reconstruction algorithms to recover missing data. Generally, the implementation of a new acceleration strategy requires significant changes in the MRI scanner image acquisition and reconstruction software. This is why it takes time for the new imaging acceleration techniques, such as CS, to find their way into vendor products that are approved for routine clinical use. A first important step in this process (as described in this thesis) is the optimization of the data acquisition sampling patterns, the optimization of the image reconstruction pipeline, and proof-of-concept studies in healthy volunteers and patients.

This thesis reports on the implementation and validation of several CS acquisition and reconstruction techniques for highly-accelerated flow MRI. Specifically, the focus was on a fast 4D flow MRI method for the assessment of WSS in the aorta and a high temporal resolution 2D flow MRI technique for carotid artery PWV quantification.

## 1.2 4D flow MRI image acquisition

In 4D flow MRI, motion-sensitive gradients encode the phase of the MRI signal for coherent motion in each principal direction [23]. These bipolar velocity encoding gradients create a net phase accumulation of zero for stationary spins, whereas spins moving along the gradient direction, will accumulate a phase linearly proportional to the velocity of their movement (**Figure 1.1a**).

The phase of a spin after applying a gradient with amplitude  $G$  in direction  $x$  can be written as

$$\phi(t) = \gamma \int_0^t G_x(u) x(u) du \quad (1.1)$$

where  $\phi$  is the accumulated phase,  $t$  is the time, and  $\gamma$  is the gyromagnetic ratio. The time-dependent position  $x(u)$  of the moving spin can be approximated with a Taylor expansion such that it can be written as

$$x(u) = x_0 + uv_0 + \frac{1}{2} u^2 a_0 + \dots + \frac{1}{n!} u^n \left. \frac{dx(u)}{du} \right|_{u=0} \quad (1.2)$$

Where  $x_0$  is,  $v_0$  and  $a_0$  are the position, the velocity and the acceleration at time point  $u=0$ . Equation (1.2) can then be written as

$$\phi(t) = \gamma x_0 \int_0^t G_x(u) du + \gamma v_0 \int_0^t G_x(u) u du + \frac{\gamma}{2} a_0 \int_0^t G_x(u) u^2 du + \dots + \frac{\gamma}{n!} \left. \frac{dx(t)}{dt} \right|_{t=0} \int_0^t G_x(u) u^n du \quad (1.3)$$



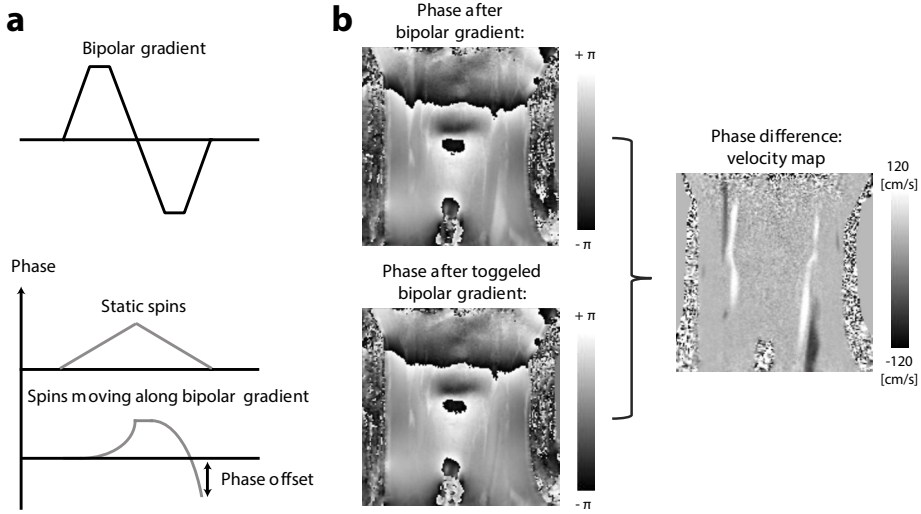


**Figure 1.1** Bipolar gradients and phase encoded images. (a) A unipolar gradient creates a net phase within a pixel for static and moving spins. A bipolar gradient results in compensation of this phase accumulation for static, but not for spins moving along the gradient direction (bottom). (b) 4D flow MRI images of the carotid artery. Image phase after applying a flow encoding gradient (top) and image phase after applying a bipolar gradient with an opposite gradient waveform (bottom). The encoded velocity (right) can be derived from both phase images by complex division. Figures (a-b) are adapted from [23].

By defining the  $n^{\text{th}}$  gradient moment  $m_n = \int_0^t G_x(u) u^n du$ , this simplifies to

$$\phi(t) = \gamma x_0 m_0 + \gamma v_0 m_1 + \frac{\gamma}{2} a_0 m_2 + \dots \quad (1.4)$$

in which  $x$  and  $v$  are displacement and velocity along the gradient direction.

For stationary spins the phase accumulated is described by the  $0^{\text{th}}$  moment and becomes 0 at the end of the bipolar gradient. The phase of moving spins is

$$\phi = \gamma A T v \quad (1.5)$$

with  $A$  the gradient area, which is true for any gradient shape, and  $T$  the gradient duration. The sign of  $m_1$  will be the sign of the second gradient lobe.

Bipolar gradients can be combined with flow compensation gradient waveforms, as gradients required for spatial localization with  $m_1 \neq 0$  can lead to image artefacts and flow-encoding errors. Flow compensation gradients consist of bipolar gradients with  $m_0 = 0$  and  $m_1 = 0$ , such that the phase is independent of both spatial location and velocity [24]. In order to shorten TE, the bipolar flow encoding gradient and the flow compensation gradient are typically combined in a new waveform as can be seen in **Figure 1.2** [23].

### 1.2.1 Velocity maps

The phase of a single voxel is not only a result of the deliberately introduced phase by the flow encoding gradients, but also has a contribution from an unknown background phase by field inhomogeneities.

In order to remove the background phase and to separate the signals of static and moving spins, two measurements (also called points or segments) are acquired with a difference in  $\Delta m_1$ . This is called two-point encoding, see **Figure 1.1a**. The phase difference of both measurements can be derived by division of the complex signals  $S$  after separate reconstruction [25]:

$$\Delta\phi = \arg S_2 - \arg S_1 = \arg \frac{S_2}{S_1} \quad (1.6)$$

from which the true velocity per voxel can be estimated (with  $\Delta m_1$  related to the VENC, see below):

$$v = \frac{\Delta\phi}{\gamma\Delta m_1} \quad (1.7)$$

Encoding in all three principal directions  $v_x$ ,  $v_y$ ,  $v_z$  can be calculated from four separate scans (four-point encoding) consisting of three pairs, one reference scan and three flow encoded scans. The encoding scheme can be asymmetric (**Figure 1.2a**) or symmetric (**Figure 1.2c**), while  $\Delta m_1$  is effectively the same. **Figure 1.2b** shows the same sequence as in **Figure 1.2a**, including flow compensation gradients. Next to these methods balanced flow encoding can be applied, where flow encoding gradients are distributed with a Hadamard encoding scheme (**Figure 1.2c**). This results in a better SNR. However, phase aliasing becomes more difficult to correct [26].

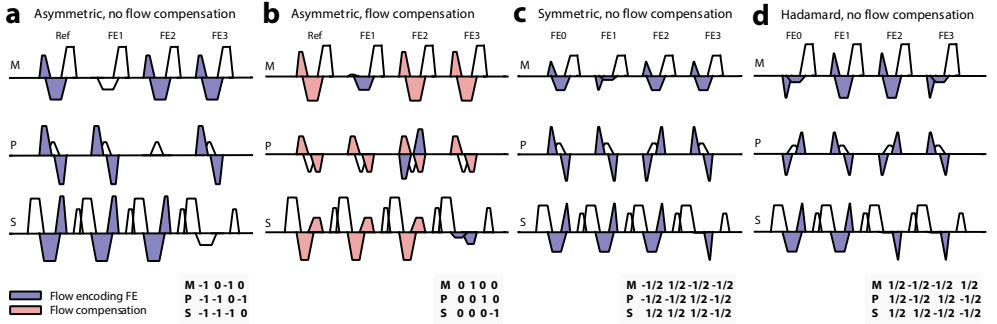


**Figure 1.2** Flow encoding and flow compensation of 4D flow MRI sequences used on a Philips 3T Ingenia scanner. Bipolar gradients in frequency encoding (M) and slice encoding (S) direction are often combined with pre- and re-phasing lobes, which is why their shape varies slightly. (a) Asymmetric flow encoding scheme, with one reference of no flow encoding, and three scans with flow encoding in each M/P/S direction. (b) Asymmetric flow encoding with additional flow compensation gradient. (c) Symmetric flow encoding scheme with flow encoding gradients split equally over all flow encoding directions. (d) Hadamard encoding scheme, leading to shorter TEs. (Remark: Non-flow compensated flow encoding of a Philips 4D flow sequences is shown in (a). As implemented, there are bipolar gradients in all directions except for the FE direction, most likely to still ensure flow compensation.)

### 1.2.2 VENC

An important characteristic of flow encoded MRI is the VENC (velocity **encoding**) in cm/s. The measured phase difference, controlled by the difference of  $m_1$  in the velocity encoding gradients, has a range of  $+\pi$  and  $-\pi$ , corresponding to  $+$  and  $-$  the VENC. In this definition, velocities larger than the VENC will lead to phase values larger than  $\pi$ , resulting in aliasing of the phase image.

$$\text{VENC} = \frac{\pi}{\gamma|\Delta m_1|}$$

The VENC is chosen depending on the expected velocity in the area of interest and is typically set to be slightly higher than the highest expected velocity in a single voxel to prevent aliasing. However, it is difficult to fully prevent aliasing, but if it occurs, it is unwrapped in a post processing step.

### 1.2.3 SNR in velocity maps

The noise introduced in each phase image depends on the complex signals magnitude  $|S|$  with noise  $\sigma$  and is inversely proportional to the SNR of the magnitude image [27].

$$\sigma_\phi^2 = \frac{\sigma^2}{|S|^2} = \frac{1}{\text{SNR}_{\text{mag}}^2} \quad (1.8)$$

The noise in the velocity maps  $\sigma_v$  depends on the noise of the phase and the chosen VENC, which is why the VENC should be as low as possible without causing aliasing [25]:

$$\sigma_v^2 = \frac{2\sigma_\phi^2}{(\gamma\Delta m_1)^2} = \frac{2\sigma_\phi^2 \text{VENC}^2}{\pi^2} \quad (1.9)$$

The dependency of the velocity noise on the magnitude signal leads to random phase in regions without signal such as in the trachea when imaging the carotid arteries. A threshold in the magnitude image can be chosen to mask to the velocity images [25]. However, thresholding does not work when a voxel contains both random phase due to absence of signal as well as flowing spins (partial volume effect), as is sometimes the case in phantom experiments when studying flow through silicon or plastic tubing.

### 1.2.4 Cardiac synchronization

An MRI scan is not fast enough to acquire a 3D k-space with 4 flow encoding gradients in a single heartbeat and, therefore, image acquisition is distributed over multiple cardiac cycles. To assign acquired data to a specific time-point in the cardiac cycle, an ECG signal is acquired alongside the MRI scan (**Figure 1.3a**). In prospective gating, the acquisition time point of each k-line is predefined and the same for each consecutive heartbeat. In contrast, for retrospective triggering, data is continuously sampled simultaneously to the ECG signal. This means that each acquired k-line has an individual time-stamp and can be sorted into a cardiac bin retrospectively (cardiac binning). A complication is that not all heartbeats have the same length due to natural heartbeat variations. This means that for short heart cycles data is missing and for long heart cycles more data than necessary is acquired. This is usually compensated for by averaging data in long cycles or interpolation in short cycles [28]. With increasing number of reconstructed cardiac frames, the acquired k-t space becomes undersampled in a quasi-random fashion due to natural heartbeat variations, which is beneficial for reconstruction algorithms based on CS.

### 1.2.5 Respiratory synchronization

Synchronization with the breathing motion is necessary (**Figure 1.3d**) to avoid motion artefacts. Typically, a breathing navigator (additional RF pulse to acquire diaphragm motion) is acquired, from

which the breathing state can be deduced. However, this disturbs the steady-state of the acquisition which can result in image artifacts. Other approaches, such as self-gating retrieve the breathing information directly from the acquired data, without the need for a navigator by using a principal component or similar analyses of the k-space center.

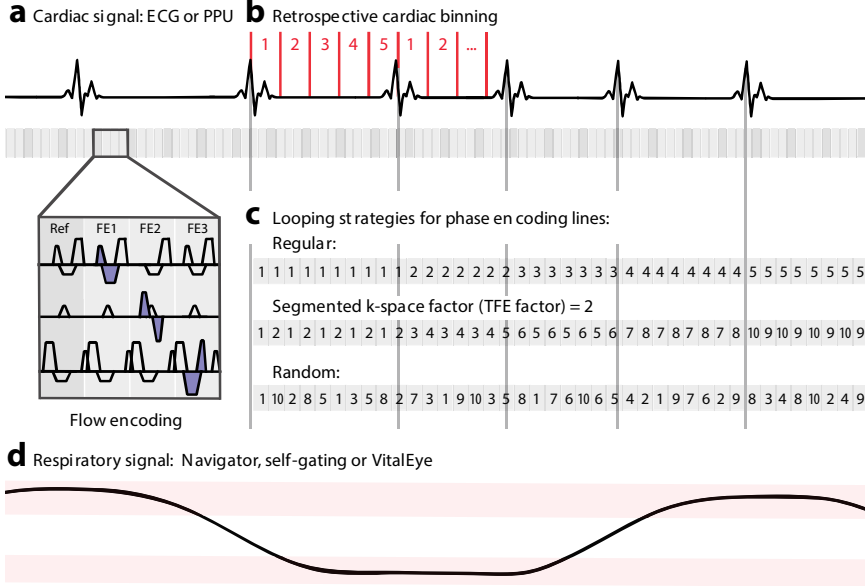


**Figure 1.3** ECG triggering and binning, respiratory signal and phase encoding loops. (a) ECG signal captured independently of the MRI acquisition. Every detected R peak (indicating the start of a new heart cycle) starts a new sequence of phase encoding lines. (b) Retrospective binning defines time steps per heart cycle in which the acquired data will be sorted after the scan is finished. (c) The MRI acquisition loops over all phase encoding steps. In order to accelerate this process, two different k-lines are acquired within one heart beat (segmented imaging factor or TFE factor). This accelerates scan time, but decreases the number of different k-lines that are sampled per heartbeat. Completely random sampling relies on the fact that each k-line will be sampled statistically at each time point of the heartbeat throughout the entire scan. (d) For scans of the aorta or the heart, the respiratory motion signal is traced, such that data only in inspiration or expiration is considered. For some sequences, the respiratory motion can also be derived from the k-space center, without the need of a navigator (right).

### 1.3 Accelerating 4D flow MRI

As 4D flow MRI requires long acquisitions times, it is desirable to decrease scan time by reducing the amount of sampled data. Generally, k-space has to be sampled at a frequency fulfilling the Nyquist criterion and sampling below that rate leads to spatial aliasing image artefacts. Different techniques have been proposed to undersample Cartesian k-space, *i.e.* sample at a sub-Nyquist rate, while avoiding aliasing and recovering images without artifacts. One approach to recover undersampled data is to exploit the (inherent) sparsity of MRI images using an iterative CS reconstruction [29]. 4D flow MRI and other cardiac MRI scans are highly correlated in time, which makes them suitable for undersampling in the time dimension.

### 1.3.1 Compressed Sensing

For a successful CS reconstruction certain criteria need to be fulfilled [29]. First of all, the undersampled dataset should be sparse – the image can be described by a significant number of zero elements. Images can be sparse in the image domain, but also in k-space, the time domain, or an applied transform domain (*e.g.* Wavelet).

4D flow MRI images in particular, are highly correlated in the temporal dimension, as the image information in one cardiac frame is very similar to the previous and following frames. A suitable sparse representation of a 4D flow MRI dataset could therefore be a finite-differences or total variation (TV) transform in time, which is the sum of the absolute variation of the image along the time dimension [21].

Another criterion for CS reconstruction is incoherent undersampling. With incoherent undersampling, aliasing artifacts of undersampling become noise-like. For images sparse under temporal TV it would therefore be desirable to undersample incoherently over time.

The last requirement is a non-linear reconstruction, with the cost function:

$$\text{minimize } \|\psi m\|_1, \text{ s. t. } \|F_u m - y\|_2 < \varepsilon \quad (1.16)$$

For which  $m$  is the to be reconstructed image,  $y$  is the sampled data,  $F_u$  the Fourier operator and  $\varepsilon$  is set to be under the noise level. The first term enforces sparsity, in which the sparsifying transform  $\psi$  (*e.g.* TV) can be chosen.

## 1.4 Validation of accelerated 4D flow MRI

Even with the most advanced image reconstruction algorithms, accelerated images may suffer from, undersampling- or reconstruction-related, artifacts. For estimating the error or the accuracy introduced with the accelerated method, a gold standard measurement in the form of a not-accelerated scan in the same subject would be the best choice. However, for 4D flow MRI, a gold standard – *i.e.* a fully sampled scan with similar spatiotemporal resolution as the accelerated scans – may become impractically long (several hours). In that case, the use of flow-phantoms with realistic geometry and pulsatile flow is a good alternative to test the acceleration method.

### 1.4.1 Phantom experiments

A flow phantom is a simplified but realistic model of a human vessel, which helps in designing and testing novel accelerated flow sequences. As *in vivo* flow depends on physiological parameters, such as blood pressure and heart rate, testing the reproducibility of new sequences and biomarkers *in vivo* is difficult, as heart rate and blood pressure easily change within a few minutes. For validation of accelerated 4D flow MRI scans, phantom experiments have proven essential [30].

A flow phantom consists of a distensible material, simulating arterial stiffness and preferably with T1 and T2 properties similar to the vessel wall, which can be embedded in water or agar (jelly substance created from algae). Ideally a pulsatile flow is applied, with a time-resolved flow profile that mimics artery flow in humans. Important for heart-rate-synchronized flow acquisitions is that flow includes

heart rate variabilities with a given standard deviation. In order simulate the natural surroundings, biological material can be used within a phantom setting. As demonstrated by [31,32], a dissected and resuscitated pig heart, installed in a perfusion cycle and a heart-lung machine, can be used to either passively transport flow blood, or actively pump it.

## 1.5 Blood flow characterization and visualization

From the measured velocity vector field  $\mathbf{v}(\mathbf{r}, t)$  time-resolved flow  $Q(t)$  through a defined area  $A$  can be derived:

$$Q(t) = \int_A \mathbf{v}(\mathbf{r}, t) d^2\mathbf{r} \quad (1.10)$$

With the mean time-resolved velocity  $\bar{v}(t) = Q(t)/A$  within  $A$ . Time-resolved velocity vector fields facilitate visualization of the trace of a single blood element per heartbeat and the formation of vortices with stream- or pathlines. An example is shown for the carotid arteries in **Figure 1.4**.

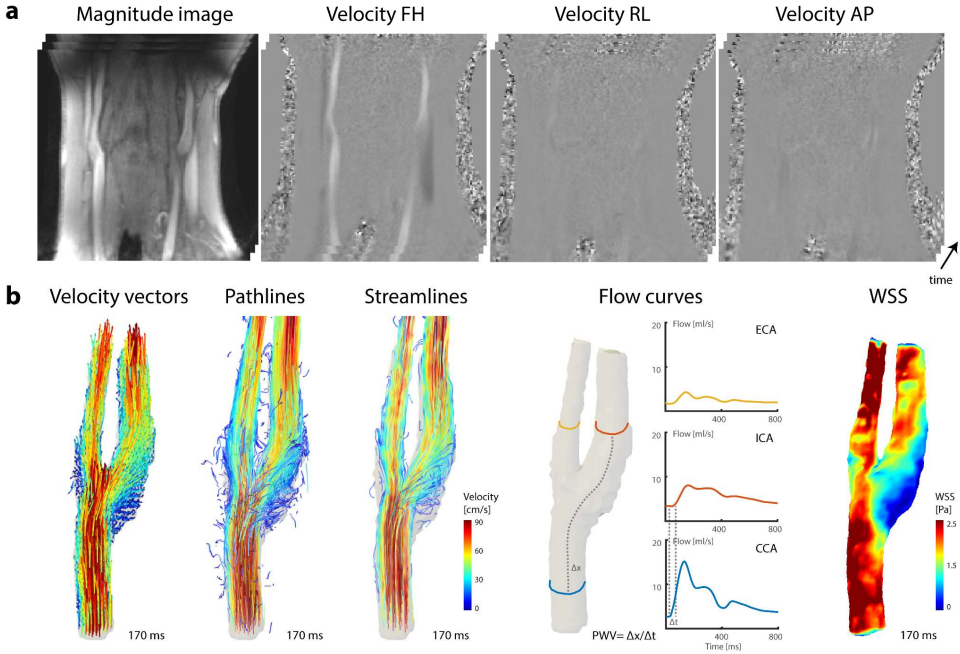


**Figure 1.4** 4D flow MRI scanning of the carotid arteries. (a) Time resolved magnitude and velocity images, for flow encoding directions in foot-head (FH), right-left (RL) and anterior-posterior (AP) direction. (b) From left to right: 3D velocity vectors derived from the velocity maps, time resolved path and streamline visualization (here at a time point of 170 ms), flow curves in common carotid (CCA), internal carotid (ICA) and external carotid (ECA) artery, and WSS at peak systole.

### 1.5.1 Pulse wave velocity

PWV [33] describes the velocity at which the arterial pressure wave travels through the artery. This is related to arterial stiffness through the Moens-Korteweg equation [33]:

$$PWV = \sqrt{\frac{E h}{2 r \rho}} \quad (1.11)$$

with  $E$  the elastic modulus of the artery,  $h$  the vessel wall thickness,  $r$  the inner radius and  $\rho$  the blood density. PWV can be calculated from the time shift (the transit time) between two flow curves measured at different sites  $\Delta t$  divided by the distance  $\Delta x$  that the blood has to travel:

$$PWV = \frac{\Delta x}{\Delta t} \quad (1.12)$$

The transit time (typically 15-30 ms) is calculated by cross-correlation between the flow curves, or the time shift between the 'foot' of the flow curves, both considering that the shape of the flow curve later in the cardiac cycle is influenced by downstream reflections [34].

Doppler flow or arterial tonometry are other modalities that also allow for a (real-time) assessment of flow velocity or pressure in the femoral and carotid arteries, and measure an average PWV of the arterial tree between these sites, called global PWV [34]. However, to better understand the processes of regional plaque development and to more specifically detect early signs of local changes in arterial stiffness [35], it is important to investigate the regional changes of PWV – especially in regions prone to atherosclerotic plaques such as the carotids.

PWV measurement of small segments using MRI techniques are typically more challenging in the carotids than in the aorta [14] because the diameter is about 5 times smaller [12], [13] and PWV is higher [36]. Additionally, small vessel segments lead to a shorter transit time, which requires a very high temporal resolution of the flow MRI scans. Accurate PWV measurements in the carotid artery, thus require high spatial and temporal resolution flow MR images.

### 1.5.2 Wall shear stress

Blood flow exerts a frictional force on the vessel wall called wall shear stress (WSS). WSS can be calculated by multiplying the blood viscosity and the velocity gradient of the velocity field near the vessel wall.

After segmenting the 4D flow MRI data, WSS vectors  $\boldsymbol{\tau}$  can be calculated using the inward normal  $\mathbf{n}$  on the vessel wall and the blood viscosity  $\eta$  (assumed to be  $3.2 \cdot 10^{-3}$  Pa s in this thesis), [37]

$$\boldsymbol{\tau} = 2 \eta \boldsymbol{\varepsilon} \cdot \mathbf{n} \quad (1.13)$$

where  $\boldsymbol{\varepsilon}$  the rate of the deformation tensor

$$\boldsymbol{\varepsilon} = \begin{bmatrix} \frac{\partial v_x}{\partial x} & \frac{1}{2} \left( \frac{\partial v_y}{\partial x} + \frac{\partial v_x}{\partial y} \right) & \frac{1}{2} \left( \frac{\partial v_z}{\partial x} + \frac{\partial v_x}{\partial z} \right) \\ \frac{1}{2} \left( \frac{\partial v_x}{\partial y} + \frac{\partial v_y}{\partial x} \right) & \frac{\partial v_y}{\partial y} & \frac{1}{2} \left( \frac{\partial v_z}{\partial y} + \frac{\partial v_y}{\partial z} \right) \\ \frac{1}{2} \left( \frac{\partial v_x}{\partial z} + \frac{\partial v_z}{\partial x} \right) & \frac{1}{2} \left( \frac{\partial v_y}{\partial z} + \frac{\partial v_z}{\partial y} \right) & \frac{\partial v_z}{\partial z} \end{bmatrix} \quad (1.14)$$

For each point on the vessel wall the coordinate system is rotated such that the  $z'$  axis aligns with the inward normal and  $\mathbf{n} = (0, 0, 1)$ . A simplifying assumption is that  $\mathbf{n} \cdot \mathbf{v} = 0$ , as there is no flow through the wall, and the WSS vector can be written as

$$\boldsymbol{\tau} = \eta \begin{bmatrix} \frac{\partial v_{x'}}{\partial z'} & \frac{\partial v_{y'}}{\partial z'} & 0 \end{bmatrix}. \quad (1.15)$$

The velocity gradient can be defined by fitting splines to the velocities along the inward normal. The WSS vector per time and wall point is then calculated with an inverse transformation. In this work, mostly the absolute value of the WSS vector is considered, typically during peak systole. However, the change of direction over time of the WSS vector, as described by the oscillatory shear index OSI, an indicator for endothelial cell remodeling, was also considered [38,39]:

$$\text{OSI} = 0.5 * \left( 1 - \frac{\left| \int_0^t \boldsymbol{\tau}(t) dt \right|}{\int_0^t |\boldsymbol{\tau}(t)| dt} \right). \quad (1.16)$$

An OSI of 0 represents no directional change of the WSS vector over the cardiac cycle, whereas an OSI of 0.5 represents 180° changes of the vector.

Particular regions, such as the carotid bulb, are regions with a low WSS magnitude, as blood is creating slow moving vortices (**Figure 1.4b**, WSS and vortex formation in the carotid bulb). It has been shown that a high mechanical force on the endothelial cells of the arterial wall can be protective against atherosclerosis and vascular dysfunction. In turn, regions of low WSS magnitude are prone to atherosclerosis and plaque formation by rearrangement of endothelial cells [6–9]. High OSI, represents high temporal variations of the WSS vector and has been associated with regions of low WSS and non-directed flow. Recirculating flow creates a long residence time of fluid particles and macrophages in that region on the one hand, and a lower force of the fluid particles on the vessel wall on the other hand.

### 1.5.3 Wall thickness

Vessel wall thickness (WT), endothelial changes (indicated by WSS) and vessel stiffness (indicated by PWV) are closely related. This is why WT plays an important role when investigating arterial health and the onset of atherosclerosis.

Screening of the WT is typically performed with echocardiography. However, only the intima-media thickness (IMT) is reported, which does not include the outer layer of the vessel wall, the adventitia. As wall thickness varies throughout the vessel diameter ultrasound assessment of the IMT should be performed under multiple view angles as. A high-resolution 3D black blood MRI scan, with suppressed blood signal for a good visualization of the vessel wall, may therefore be a better solution to estimate WT.

## 1.6 Thesis outline

In this thesis the development, testing, and application of CS accelerated flow MRI sequences is described.



**Chapter 2** describes a new clinical protocol for accurate PWV assessment in small arterial segments. This technique is based on high temporal resolution 2D flow MRI, which was achieved by retrospective binning of k-space data combined with a CS reconstruction. Validation of PWV measured with this technique was done in comparison with ultrasound measurements in a phantom tube. *In vivo*, significant age-related differences in regional PWV were measured in two groups of younger and elderly healthy volunteers.

In **chapter 3** a pseudo-spiral Cartesian sampling strategy for 4D flow MRI is described. The technique exploits interleaving of k-space lines in time, to achieve an ideal spatio-temporal undersampling pattern for CS reconstruction using temporal constraints. 4D flow MRI scans at different acceleration factors ( $R=2-30$ ) were evaluated in a flow phantom and in the carotid arteries of 7 healthy volunteers. In particular, velocities, flow curves and WSS values were compared at different accelerations and with a fully sampled 2D flow MRI.

In the research described in **chapter 4** the same acceleration strategy as in chapter 3 was used to accelerate aortic 4D flow MRI measurements  $R=8$  times. We studied how the pseudo-spiral Cartesian acquisition and CS reconstruction technique compares to k-t PCA accelerated 4D flow MRI. For comparison, velocities, flow curves and WSS were estimated from both methods. Additionally, the flexibility of retrospective, temporal re-binning into a higher number of cardiac frames of the CS reconstruction method was investigated and compared to the regular k-t PC acquisition.

**Chapter 5** reports on a clinical research study on early signs of atherosclerosis in the carotid arteries. The study involved assessing PWV from 2D flow MRI scans acquired with the method described in chapter 2, WT from CS accelerated 3D black blood MRI scans, and WSS from k-t PCA accelerated 4D flow MRI scans. In total 43 patients with familial hypercholesterolemia, a genetic disorder leading to accelerated atherosclerosis, were compared to 18 unaffected siblings.

In **chapter 6** the feasibility and reproducibility of 4D flow MRI measurements in an isolated, working pig heart model is described. In five repeated experiments, intra-cardiac flow visualization and quantification was performed after successful resuscitation of the *ex vivo* pig hearts. Additionally, the feasibility of transcatheter aortic valve replacement (TAVR), with subsequent 4D flow MRI scans was tested in two additional pig heart experiments. This may help in investigating the influence of surgical procedures on blood flow patterns in future.

In **chapter 7** the findings of this thesis are summarized and discussed.

## 1.7 Bibliography

1. Markl M, Frydrychowicz A, Kozerke S, Hope M, Wieben O. 4D flow MRI. *J Magn Reson Imaging*. 2012;36:1015–36.
2. Dyverfeldt P, Bissell M, Barker AJ, Bolger AF, Carlhäll CJ, Ebbers T, *et al*. 4D flow cardiovascular magnetic resonance consensus statement. *J Cardiovasc Magn Reson*. 2015;17:1–19.
3. Elbaz MSM, Calkoen EE, Westenberg JJM, Lelieveldt BPF, Roest AAW, Geest RJ Van Der. Vortex flow during early and late left ventricular filling in normal subjects: quantitative characterization using retrospectively-gated 4D flow cardiovascular magnetic resonance and three-dimensional vortex core analysis. *J Cardiovasc Magn Reson*. 2014;1–12.
4. Roes SD, Hammer S, van der Geest RJ, Marsan NA, Bax JJ, Lamb HJ, *et al*. Flow assessment through four heart valves simultaneously using 3-dimensional 3-directional velocity-encoded magnetic resonance imaging with retrospective valve tracking in healthy volunteers and patients with valvular regurgitation. *Invest Radiol*. 2009;44:669–75.
5. Westenberg JJM, Roes SD, Ajmone Marsan N, Binnendijk NMJ, Doornbos J, Bax JJ, *et al*. Mitral valve and tricuspid valve blood flow: accurate quantification with 3D velocity-encoded MR imaging with retrospective valve tracking. *Radiology*. 2008;249:792–800.
6. van Ooij P, Potters W V, Nederveen AJ, Allen BD, Collins J, Carr J, *et al*. A methodology to detect abnormal relative wall shear stress on the full surface of the thoracic aorta using four-dimensional flow MRI. *Magn Reson Med*. 2015;1227:1216–27.
7. Potters W V, van Ooij P, Marquering H, van Bavel E, Nederveen AJ. Volumetric arterial wall shear stress calculation based on cine phase contrast MRI. *J Magn Reson Imaging*. 2015;41:505–16.
8. van Ooij P, Potters W V, Nederveen AJ, Collins JD, Carr JC, Malaisrie S, *et al*. Thoracic aortic wall shear stress atlases in patients with bicuspid aortic valves. *J Cardiovasc Magn Reson*. 2014;16:P161.
9. Chiu J-J, Chien S. Effects of disturbed flow on vascular endothelium: pathophysiological basis and clinical perspectives. *Natl Inst Heal*. 2011;91.
10. van Ooij P, Cibis M, Rowland E, Vernooij M, van der Lugt A, Weinberg P, *et al*. Spatial correlations between MRI-derived wall shear stress and vessel wall thickness in the carotid bifurcation. *Eur Radiol Exp*. 2018;
11. Bogaert J, Dymarkowski S, Taylor A. Clinical cardiac MRI. Beart A, Sartor K, editors. Springer, Medical Radiology, Diagnostic Imaging; 2005.
12. van Popele NM, Grobbee DE, Bots ML, Asmar R, Topouchian J, Reneman RS, *et al*. Association between arterial stiffness and atherosclerosis. *Stroke*. 2001;32:454–61.
13. Lusis AJ. Atherosclerosis. *Nature*. 2000;407:233–41.
14. Markl M, Wallis W, Strecker C, Gladstone BP, Vach W, Harloff A. Analysis of pulse wave velocity in the thoracic aorta by flow-sensitive four-dimensional MRI: Reproducibility and correlation with characteristics in patients with aortic atherosclerosis. *J. Magn. Reson. Imaging*. 2012. p. 1162–8.
15. Smolka G, Wojakowski W. Paravalvular leak - important complication after implantation of prosthetic valve. *E-Journal Cardiol Pract*. 2010;9:1–7.

16. Lázaro C, Hinojar R, Zamorano JL. Cardiac imaging in prosthetic paravalvular leaks. *Cardiovasc Diagn Ther.* 2014;4:307–13.
17. Oglat AA, Matjafri MZ, Suardi N, Oqlat MA, Abdelrahman MA, Oqlat AA. A Review of Medical Doppler Ultrasonography of Blood Flow in General and Especially in Common Carotid Artery. 2018;3–13.
18. Knobloch V, Boesiger P, Kozerke S. Sparsity transform k-t principal component analysis for accelerating cine three-dimensional flow measurements. *Magn Reson Med.* 2013;70:53–63.
19. Giese D, Wong J, Greil GF, Buehrer M, Schaeffter T, Kozerke S. Towards highly accelerated Cartesian time-resolved 3D flow cardiovascular magnetic resonance in the clinical setting. *J Cardiovasc Magn Reson.* 2014;16:42.
20. Pagé G, Bettoni J, Virginie A, Olivier S. Influence of principal component analysis acceleration factor on velocity measurement in 2D and 4D PC-MRI. *Magn Reson Mater Physics, Biol Med.* 2018;469–81.
21. Lustig M, Donoho D, Pauly JM. Sparse MRI: The application of compressed sensing for rapid MR imaging. *Magn Reson Med.* 2007;58:1182–95.
22. Cheng JY, Hanneman K, Zhang T, Alley MT, Lai P, Tamir JI, *et al.* Comprehensive motion-compensated highly accelerated 4D Flow MRI with ferumoxytol enhancement for pediatric congenital heart disease. *J Magn Reson Imaging.* 2015;
23. Bernstein MA, King KF, Zhou XJ. *Handbook of MRI Pulse Sequences.* 2004.
24. Schmitter S, Schnell S. 4D flow MRI. *Quantif Biophys Parameters Med Imaging.* 2018;187–212.
25. Pelc NJ, Bernstein MA, Shimakawa A, Glover GH. Encoding strategies for three-direction phase-contrast MR imaging of flow. *J. Magn. Reson. Imaging.* 1991. p. 405–13.
26. Pelc NJ, Bernstein matt A, Shimakawa A, Glover GH. Encoding strategies for three-direction phase-contrast MR imaging of flow. *J Magn Reson Imaging.* 1991;1:405–13.
27. Haacke EM, Brown RW, Thompson MR, Venkatesan R. Haacke - Magnetic Resonance Imaging - Physical Principles and Sequence Design. *J. Appl. Phys.* 1999. p. 914.
28. Application Guide, Cardiac Imaging. Philips Achieva Panor Release 32 Ser.
29. Lustig, Michael and Donoho, David L and Santos, Juan M and Pauly JM. Compressed sensing MRI. *Signal Process Mag IEEE.* 2008;25:72–82.
30. Montalba C, Urbina J, Sotelo J, Andia ME, Tejos C, Irarrazaval P, *et al.* Variability of 4D Flow Parameters When Subjected to Changes in MRI Acquisition Parameters Using a Realistic Thoracic Aortic Phantom. 2017;00.
31. de Weger A, van Tuijl S, Stijnen M, Steendijk P, de Hart J. Images in cardiovascular medicine direct endoscopic visual assessment of a transcatheter aortic valve implantation and performance in the PhysioHeart, an isolated working heart platform. *Images Cardiovasc Med.* 2010;121:261–3.
32. de Hart J, de Weger A, van Tuijl S, Stijnen JMA, van den Broek CN, Rutter MCM, *et al.* An *ex vivo* platform to simulate cardiac physiology: a new dimension for therapy development and assessment. *Int J Artif Organs.* 2011;34:495–505.
33. Wentland AL, Grist TM, Wieben O. Review of MRI-based measurements of pulse wave velocity: a biomarker of arterial stiffness. *Cardiovasc Diagn Ther.* 2014;4:193–206.

34. Vlachopoulos C, O'Rourke M, Nichols WW. McDonald's Blood Flow in Arteries. Boca Raton, Florida, USA: CRC Press; 2011.
35. Gotschy A, Bauer WR, Winter P, Nordbeck P, Rommel E, Jakob PM, *et al.* Local versus global aortic pulse wave velocity in early atherosclerosis: An animal study in ApoE<sup>-/-</sup> mice using ultrahigh field MRI. *PLoS One*. 2017;12:1–14.
36. Kröner ESJ, Lamb HJ, Siebelink HMJ, Cannegieter SC, van den Boogaard PJ, van der Wall EE, *et al.* Pulse wave velocity and flow in the carotid artery versus the aortic arch: Effects of aging. *J Magn Reson Imaging*. 2014;40:287–93.
37. Potters W V, Marquering HA, VanBavel E, Nederveen AJ. Measuring wall shear stress using velocity-encoded MRI. *Curr Cardiovasc Imaging Rep*. 2014;7:9257.
38. Ku DN, Giddens DP, Zarins CK, Glagov S. Pulsatile flow and atherosclerosis in the human carotid bifurcation. Positive correlation between plaque location and low and oscillating shear stress. *Arteriosclerosis*. 1985;5:293–302.
39. Sotelo J, Urbina J, Valverde I, Tejos C, Irrarrázaval P, Member S, *et al.* 3D Quantification of Wall Shear Stress and Oscillatory Shear Index Using a Finite-Element Method in 3D CINE PC-MRI Data of the Thoracic Aorta. 2016;35:1475–87.
40. Hodges TC, Detmer PR, Dawson DL, Bergelin RO, Beach KW, Hatsukami TS, *et al.* Ultrasound determination of total arterial wall thickness. *J Vasc Surg*. 1994;19:745–53.
41. Harloff A, Zech T, Frydrychowicz A, Schumacher M, Schölhorn J, Hennig J, *et al.* Carotid intima-media thickness and distensibility measured by MRI at 3 T versus high-resolution ultrasound. *Eur Radiol*. 2009;19:1470–9.

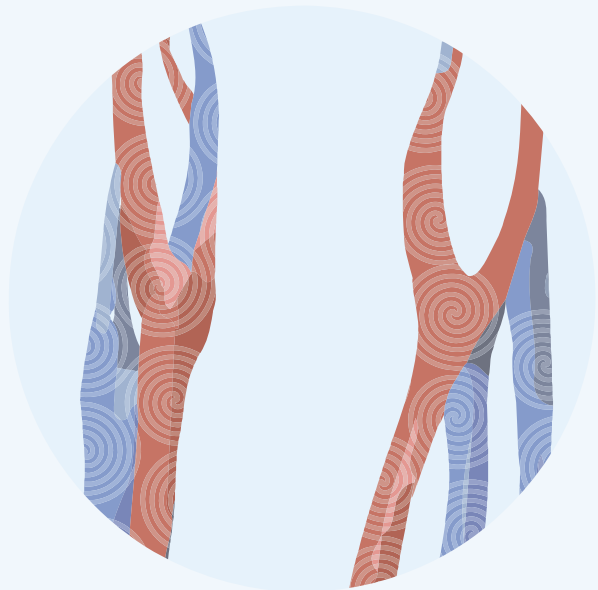


# CHAPTER 2

Regional assessment of  
carotid artery pulse wave velocity using  
compressed sensing accelerated  
high temporal resolution  
2D CINE phase contrast  
cardiovascular magnetic resonance

Eva S. Peper,  
Gustav J. Strijkers,  
Katja Gazzola,  
Wouter V. Potters,  
Abdallah G. Motaal,  
Ilse K. Luirink,  
Barbara A. Hutten,  
Albert Wiegman,  
Pim van Ooij,  
Bert-Jan H. van den Born,  
Aart J. Nederveen  
and Bram F. Coolen

Journal of Cardiovascular  
Magnetic Resonance. 2018



## 2.1 Abstract

**Background:** Cardiovascular magnetic resonance (CMR) allows for non-invasive assessment of arterial stiffness by means of measuring pulse wave velocity (PWV). PWV can be calculated from the time shift between two time-resolved flow curves acquired at two locations within an arterial segment. These flow curves can be derived from two-dimensional CINE phase contrast CMR (2D CINE PC CMR). While CMR-derived PWV measurements have proven to be accurate for the aorta, this is more challenging for smaller arteries such as the carotids due to the need for both high spatial and temporal resolution. In this work, we present a novel method that combines retrospectively gated 2D CINE PC CMR, high temporal binning of data and compressed sensing (CS) reconstruction to accomplish a temporal resolution of 4 ms. This enables accurate flow measurements and assessment of PWV in regional carotid artery segments.

**Methods:** Retrospectively gated 2D CINE PC CMR data acquired in the carotid artery was binned into cardiac frames of 4 ms length, resulting in an incoherently undersampled ky-t-space with a mean undersampling factor of 5. The images were reconstructed by a non-linear CS reconstruction using total variation over time as a sparsifying transform. PWV values were calculated from flow curves by using foot-to-foot and cross-correlation methods. Our method was validated against ultrasound measurements in a flow phantom setup representing the carotid artery. Additionally, PWV values of two groups of 23 young ( $30 \pm 3$  years, 12 [52%] women) and 10 elderly ( $62 \pm 10$  years, 5 [50%] women) healthy subjects were compared using the Wilcoxon rank-sum test.

**Results:** Our proposed method produced very similar flow curves as those measured using ultrasound at 1 ms temporal resolution. Reliable PWV estimation proved possible for transit times down to 7.5 ms. Furthermore, significant differences in PWV values between healthy young and elderly subjects were found ( $4.7 \pm 1.0$  m/s and  $7.9 \pm 2.4$  m/s, respectively;  $p < 0.001$ ) in accordance with literature.

**Conclusions:** Retrospectively gated 2D CINE PC CMR with CS allows for high spatiotemporal resolution flow measurements and accurate regional carotid artery PWV calculations. We foresee this technique will be valuable in protocols investigating early development of carotid atherosclerosis.

## 2.2 Introduction

Cardiovascular magnetic resonance (CMR) has emerged as a powerful tool for non-invasive assessment of biomarkers indicating regional vessel wall diseases [1]. An important and early marker of vessel wall disease is arterial stiffness, which can be characterized by pulse wave velocity (PWV) [2]. PWV is the velocity at which the arterial pressure wave, created by cardiac contraction, travels through the arteries. PWV has been proven to be an independent predictor of cardiovascular events and atherosclerosis [3,4]. Arterial stiffness increases with age, which has been demonstrated by an age-related increase in global PWV and regional aortic PWV [5,6].

Severe atherosclerotic plaques are frequently observed at specific locations [7]. PWV measurements in the carotid arteries are of particular interest, since they are a major atherosclerosis-prone site associated with stroke [7–9]. Increased regional PWV was shown to precede atherosclerotic lesions even before intima-media thickening, another early marker for atherosclerosis [7]. Experimental results also demonstrate that vascular stiffening caused by early atherosclerosis is unequally distributed over the length of large vessels [10]. This implies that assessing heterogeneity of arterial stiffness by multiple local measurements of PWV might be more sensitive than global PWV to identify early atherosclerotic lesions. Therefore, to better understand the processes of regional plaque development and to improve early detection of local changes in arterial stiffness, measurements of regional PWV might prove essential.

In addition, arterial stiffness is not uniform in all vessels and PWV increases distal to the heart and further down the vascular tree. This emphasizes the relevance of regional PWV assessment. For instance, a decreasing aortic to carotid PWV ratio has been implicated in cognitive damage, since it allows the transmission of high blood pressure to the microvasculature of the brain [6,11].

PWV values can be derived using CMR by acquiring time-resolved flow curves from two-dimensional CINE phase contrast CMR (2D CINE PC CMR) measurements at two different sites within the artery of interest. The time shift between the flow curves is the transit time of the arterial pulse wave. PWV is then defined as the distance between the sites divided by the transit time and is related to arterial stiffness through the Moens-Korteweg equation [2]. Compared to PWV measurement in the aorta [12], carotid PWV measurements are more challenging since the smaller lumen diameter (aorta 31-34 mm [12], carotid 4-6 mm [13]) and higher PWV [6] require a significant increase in spatial and temporal resolution. Nevertheless, carotid PWV measurements using cardiac triggered 2D PC CMR have successfully been performed by Kröner *et al.* [6] in arterial segments with a length of 15-20 cm. However, to measure PWV at even shorter distance, a further increase in temporal resolution is required because transit times decrease with the length of the arterial segment. Unfortunately, the spatiotemporal resolution in cardiac triggered PC CMR is limited by available scan time and lowest achievable repetition time (TR).

In previous studies, it was shown that an increased temporal resolution of cardiac gated sequences can be obtained by using retrospective gating and undersampling in combination with a compressed sensing (CS) reconstruction [13]. In short, retrospective gating involves continuous acquisition of data asynchronous to the electrocardiogram (ECG) signal. Due to small variations in the heart rate, phase encoding lines are therefore acquired at incoherent positions throughout the cardiac cycle [13]. This



allows binning of the data into a high number of cardiac frames, although this leads to an undersampled k-space for each cardiac frame. Fortunately, CS reconstruction is highly efficient in exploiting temporal relations between frames and recovering information of undersampled data without significantly sacrificing image quality or the underlying temporal behavior [13,14]. To our knowledge, this approach has never been applied in combination with 2D CINE PC CMR derived PWV measurements.

In this study, we developed a new clinical 3T CMR protocol for high spatiotemporal resolution carotid artery 2D CINE PC CMR. The technique was validated using ultrasound and CMR phantom experiments. The ability of the technique to detect relevant differences in regional PWV was demonstrated in two groups of healthy young and elderly subjects.

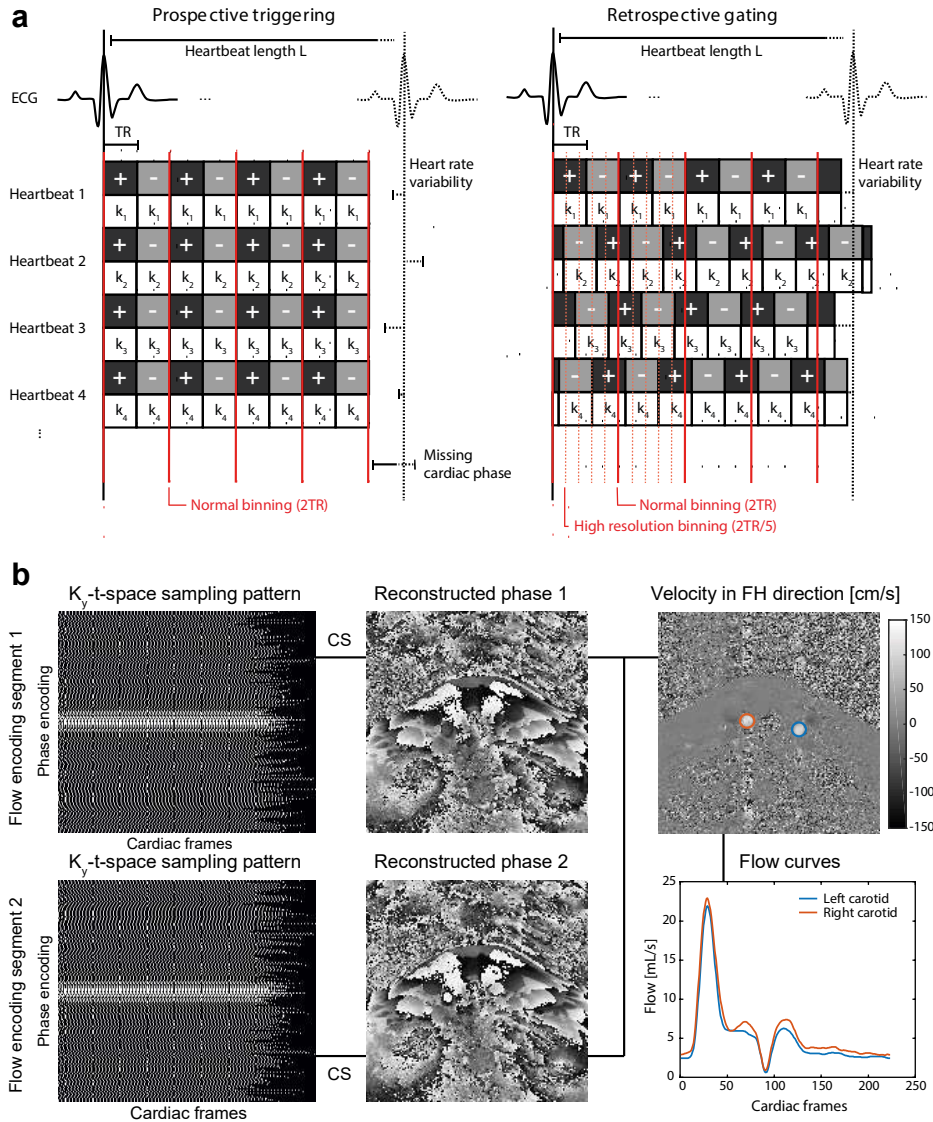


**Figure 2.1** Principle of retrospectively-gated 2D CINE PC CMR. (a) Electrocardiogram (ECG) triggering for a 2D CINE phase contrast (PC) cardiovascular magnetic resonance (CMR) scan using prospective triggering and retrospective gating. In prospective triggering (left) the acquisition is started by the detection of the R-wave peak. This leads to the same time point of acquisition (the trigger time) for each phase encoding step ( $k_1$  to  $k_4$ ) and a uniform binning afterwards. The + and - symbols indicate the 2 encoding segments needed for flow quantification in the foot-head (FH) direction. In retrospective gating (right) every phase encoding step is repetitively sampled during the course of the heart beat asynchronously with the R-peak detection. Due to slight variations in the length of individual heartbeats, the trigger time varies. The data is binned into cardiac frames with a duration shorter than  $2 \times \text{TR}$ , which creates a pseudo-random undersampling pattern. (b) Reconstruction pipeline. After binning the data in 4 ms cardiac frames, each flow encoding segment with a different undersampling pattern is reconstructed separately, after which the two phase images are combined into a velocity-encoded image. Region-of-interests (ROIs) are drawn around the left and right carotid arteries to quantify the flow.

## 2.3 Methods

### 2.3.1 Sequence design and retrospective undersampling

**Figure 2.1** illustrates the principle behind the proposed method. For conventional prospective ECG triggered CINE scans, k-line acquisitions are performed at fixed intervals with respect to the R-peaks, which leads to identical timing of all cardiac frames within each measured cardiac cycle (**Figure 2.1a**, left). Considering two flow encoding directions, the temporal resolution of each cardiac frame is then limited by two times the repetition time (TR). For retrospectively gated CINE scans, acquisitions are performed asynchronously with the ECG. Consequently, due to natural heart rate variations, each acquisition takes place at a random time point within the cardiac cycle. The number of cardiac frames can be chosen retrospectively and, more importantly, can be higher than the number of TRs that fit within one cardiac cycle (**Figure 2.1a**, right). While this results in a significant increase in temporal resolution of the resulting PC data, it also results in an undersampled ky-t-space. To overcome this, reconstruction of the incoherently undersampled data was performed using an iterative CS reconstruction algorithm as shown later. To further facilitate CS reconstruction, ky-lines were sampled more densely towards the k-space center ensuring sufficient filling of the center for all cardiac frames (**Figure 2.1b**, left). For specifically enabling 2D CINE PC CMR scans, each ky-line was repeated using both positive and negative flow encoding gradients. The proposed method was implemented on a whole body 3T CMR scanner (Ingenia, Philips Healthcare, Best, The Netherlands). For PWV measurements, two slices were acquired with a fast field echo (FFE) 2D PC CMR sequence, with unidirectional velocity encoding in the foot-head (FH) direction and the following parameters: VENC = 150 cm/s, TR = 8.0 ms, TE = 3.9 ms, FA = 8°, slice thickness = 3 mm, spatial resolution =  $0.8 \times 0.8 \times 3$  mm<sup>3</sup>, FOV =  $130 \times 130$  mm<sup>2</sup>, acquisition matrix =  $160 \times 160$  and acquisition time (2 slices) = 5 min. Scanning software was adapted in order to acquire custom defined variable density k-space trajectories ensuring that each cardiac frame had sufficient filling of the k-space center.

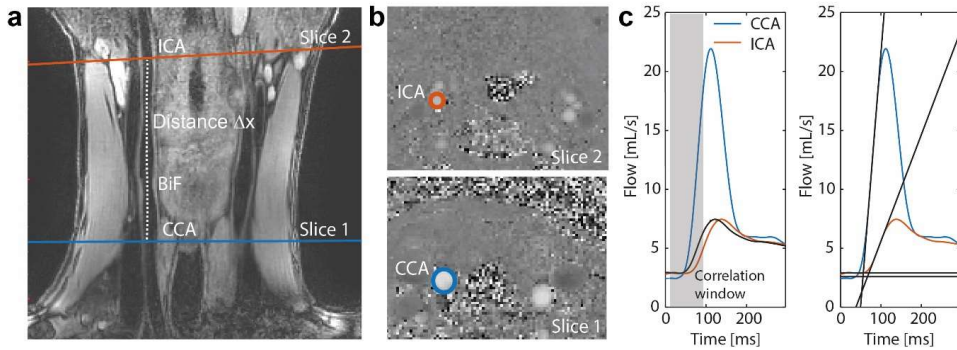


**Figure 2.2** PWV calculation using 2D CINE PC CMR and black-blood CMR. (a) Black-blood image and curved path  $\Delta x$  tracked between the two slices. (b) Velocity images acquired perpendicular to the common carotid artery (slice 1) and the internal carotid artery (slice 2). (c) The transit time was calculated from the two flow curves using the CC (left) and FF (right) method. Details on the CC and FF methods are shown in Supplementary Figure 2.10. CCA=common carotid artery; ICA=internal carotid artery.

### 2.3.2 Retrospective binning and compressed sensing reconstruction

Raw data was processed using MATLAB (MathWorks, Natick, Massachusetts, USA) and MRecon (Gyrotools LLC, Zurich, Switzerland). Retrospective binning of measured  $k_y$ -lines into multiple cardiac frames was based on the R-top delays available from the raw data, which indicated the exact acquisition time point with respect to the detected R-peak. Importantly, we chose an ‘absolute’ binning strategy with a fixed cardiac frame length of 4 ms instead of a ‘relative’ binning strategy with a fixed number of cardiac frames (e.g. 250). This is to ensure that systolic frames of the cardiac cycle overlap between different cardiac cycles, despite possible changes in the R-R interval, which are mostly caused by shortening or lengthening of the diastolic phase [15].

After binning of the data, CS reconstruction of both magnitude and phase images was performed using the BART toolbox [16] (**Figure 2.1b**). This was done independently for each of the two flow encoding segments. Specifically, a general CS reconstruction algorithm was used, described by the minimization function:

$$\arg \min \{ \|F_u m - y\|_2 + \alpha \|Tm\|_1 \} \quad (2.1)$$

with  $m$  and  $y$  being the reconstructed and measured data, respectively and  $F_u$  the undersampled Fourier operator. The  $l_2$  norm enforces data consistency between  $y$  and  $m$ . Although the data is defined in  $x, y$ -space and time, the sparsifying total variation (TV) operator  $T$  is only performed along the time dimension. Furthermore,  $\alpha$  acts as a regularization parameter and was chosen to be 0.001. A non-linear conjugate gradient descending algorithm of 20 iterations was used to solve the minimization problem for all reconstructions. Reconstruction parameters ( $\alpha$  and the number of iterations) were heuristically defined by minimizing the difference between flow curves of the CS reconstruction and flow curves of the fully sampled dataset of 20 ms temporal resolution. For this comparison the CS reconstructions (with a temporal resolution of 4 ms) were down-sampled to 20 ms.

### 2.3.3 PWV calculation

PWV is calculated by dividing the distance between the two measured slices ( $\Delta x$ ) by the transit time ( $\Delta t$ ) between the corresponding flow curves ( $PWV = \Delta x / \Delta t$ ). For the *in vivo* case,  $\Delta x$  was determined from coronal 3D black-blood images (see *in vivo* experiments). The actual path length between the 2D CINE PC slices was determined by tracking the center of the vessel with OsiriX (OsiriX Foundation, Geneva, Switzerland) [17]. To generate the flow curves for each slice, firstly, phase difference images (=velocity images) were calculated from the CS reconstructed phase images from each flow segment. Subsequently, flow per cardiac frame was calculated by averaging all velocity values within a region of interest (ROI) and by multiplying that value with the area of this ROI (**Figure 2.1b**, right).

To determine the transit time between two flow curves, two distinct methods were used: 1) foot-to-foot (FF) method [18], which calculates the shift between the foots of the systolic flow peaks and 2) cross-correlation (CC) method [19], which finds the time shift that results in the best correlation between the flow curves (in the region of the systolic flow peak or the correlation window). For both methods, additionally a normalization of the flow curves and a sigmoidal fit through the systolic flow peak was applied. **Figure 2.2** shows an overview of the PWV methods. A detailed description of the methods

(including normalization and sigmoidal fitting) can be found in the **Supplementary Figure 2.10**. Because no consensus in literature exists on which method performs best, the averaged result of all analyses was used in order to provide a robust performance of PWV calculation [2].

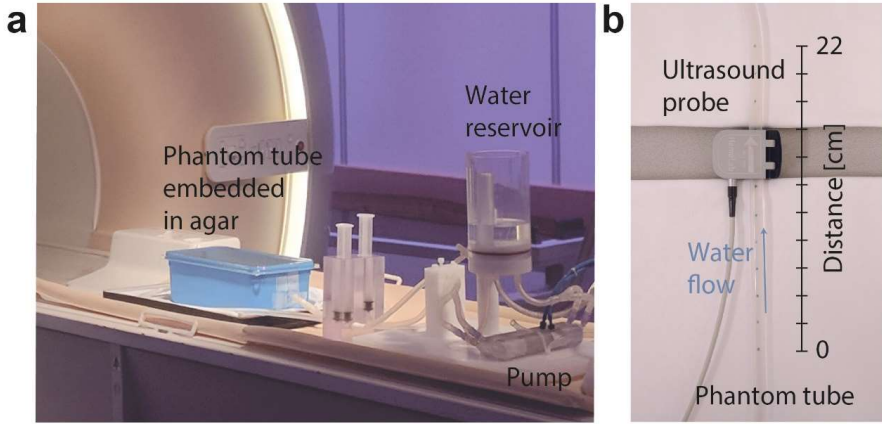


**Figure 2.3** Phantom setup. (a) Flow phantom setup in the CMR scanner and (b) during the ultrasound measurement.

### 2.3.4 Flow phantom experiments

A customized in vitro flow phantom (**Figure 2.3**) was used to validate if our technique provides accurate flow curves at high temporal resolution, as well as accurate PWV values derived from the measured flow data. Results were compared to flow curves obtained from ultrasound probe measurements. The flow phantom (LifeTec Group BV, Eindhoven, The Netherlands), consisted of a silicon tube of 30 cm length, with an inner diameter  $h = 5$  mm and a wall thickness = 2 mm similar to a human common carotid artery. A pulsatile water flow was created at a heart rate of 60 bpm with a simulated heart rate variability of 10% to facilitate incoherent sampling of  $k_y$ - $t$  space. A temporal mean flow of 5 mL/s was established with a peak systolic flow rate of 24 mL/s. Flow was measured with an ultrasound probe (temporal resolution 1 ms) of 2 cm width that was clamped on the tube at 4 cm distance to the connectors and with an inter-slice distance of 2 cm at 12 positions along the tube. Ultrasound data was acquired for at least 30 heart beats per position and retrospectively binned (absolute binning) and averaged according to the signal of the pulse generator of the pump. In this way, ultrasound data consisted an ensemble of heart beats, similar to CMR data. For the CMR experiment, the phantom tube was placed in an agar bath to ensure a stable phase offset correction afterwards. The agar bath was prepared with a relatively high amount of water to ensure sufficient flexibility of the phantom. 2D CINE PC slices were placed at equal positions as compared to those from the ultrasound acquisitions and were acquired perpendicular to the tube. The ECG signal was provided by the pulse generator of the pump. The data was retrospectively binned (absolute binning) in cardiac frames of 4 ms length.

### 2.3.5 *In vivo* experiments

*In vivo* carotid artery PWV scans were performed in the right carotid artery of 23 young ( $30 \pm 3$  years, 12 [52%] women) and 10 elderly ( $62 \pm 10$  years, 5 [50%] women) healthy subjects using a dedicated 8-

channel carotid coil (Shanghai Chenguang Medical Technologies, Shanghai, China). All procedures were approved by the local institutional review board (METC) of the Academic Medical Center in Amsterdam and were carried out according to the declaration of Helsinki. All participant gave written informed consent.

After scout scans, a coronal 3D black-blood iMSDE gradient echo sequence [20] was performed to visualize the carotid arteries (**Figure 2.2a**). Then, retrospectively gated 2D CINE PC acquisitions were performed in two slices (distance  $\Delta x = 7.8 \pm 1.4$  cm) perpendicular to the common and internal carotid artery. After acquisition, datasets from both slices were binned in cardiac frames of 4 ms length. PWV values were calculated as described above.

### 2.3.6 Statistical analysis

Differences in PWV values between the two age groups were tested with a two-sided Wilcoxon rank-sum test. The statistical level of significance was set to 0.05. Statistical analysis was performed in MATLAB (MathWorks, Inc., Natick Massachusetts, USA).

## 2.4 Results

### 2.4.1 General findings of the CS reconstruction

**Figure 2.4a** shows the undersampling pattern in  $k_y$ -t-space of the retrospectively gated CMR sequence obtained from the phantom measurements with either 0% (left) or 10% (middle) heart rate variation, created by the flow phantom setup. Additionally, **Figure 2.4a**, right shows a simulated, ideal incoherent sampling pattern. The respective point spread functions (PSFs = fast Fourier transforms (FFT) in x and y directions of the binary undersampling pattern) as a measure of incoherence are shown in **Figure 2.4b**. For a perfectly regular heart rate ( $60 \pm 0$  bpm), the PSF had high side lobes at a frequency proportional to the undersampling factor (**Figure 2.4b**, left). In contrast, a random heart rate led to incoherent sampling patterns and an improved PSF (**Figure 2.4b**, middle), almost similar to the ideal simulated case (**Figure 2.4b**, right).

The performance of the CS reconstruction was further demonstrated by the *in vivo* example in **Figure 2.5**, where the high temporal resolution CS reconstruction of magnitude and phases images (**Figure 2.5c**) exhibited the same image quality as for a fully sampled low temporal resolution scan (**Figure 2.5a**). The corresponding flow curves of the fully sampled scan and the undersampled scan with a linear reconstruction are shown in **Figure 2.6a-b**. Finally, **Figure 2.6c** shows the difference between a CS reconstruction of the undersampled data as compared to performing a simple smoothing operation on the undersampled data. In case of smoothing, flow values were overestimated and did not compare to those determined from a fully sampled dataset. This demonstrated that temporal smoothing could not replace a CS reconstruction.

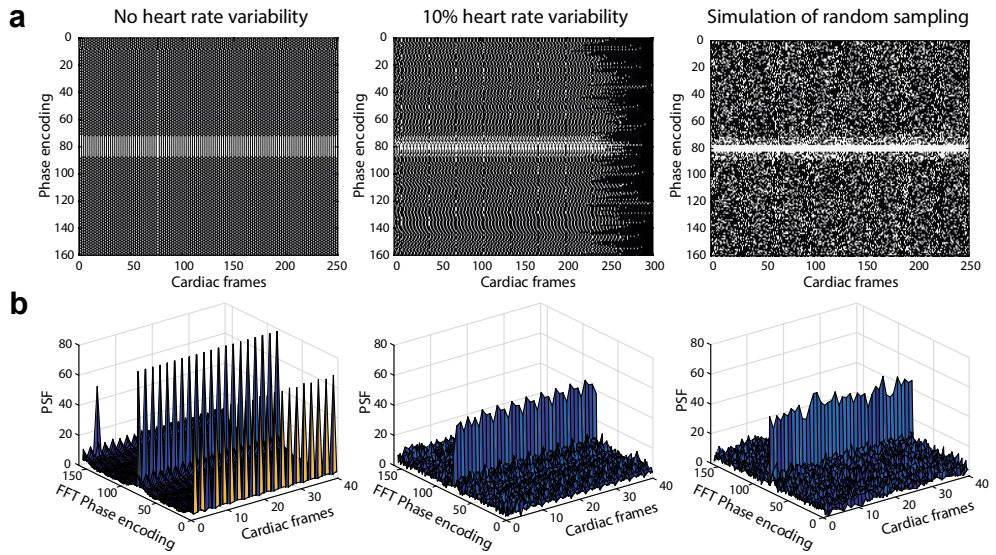


**Figure 2.4** Different undersampling patterns and corresponding point spread function (PSF). **(a)** Binary masks of k-y-t-space of phantom data at 0% heart rate variability (left) and 10% heart rate variability (middle). On the right is an ideal random sampling pattern with the same undersampling factor. **(b)** PSF after inverse fast Fourier transform (FFT) in both spatial dimensions as function of time. The sampling pattern without heart rate variability (left) creates two side peaks, whereas the ideal random undersampling pattern (right) creates incoherent noise next to the main peak. A similar incoherent pattern is found with 10% heart rate variability (middle).

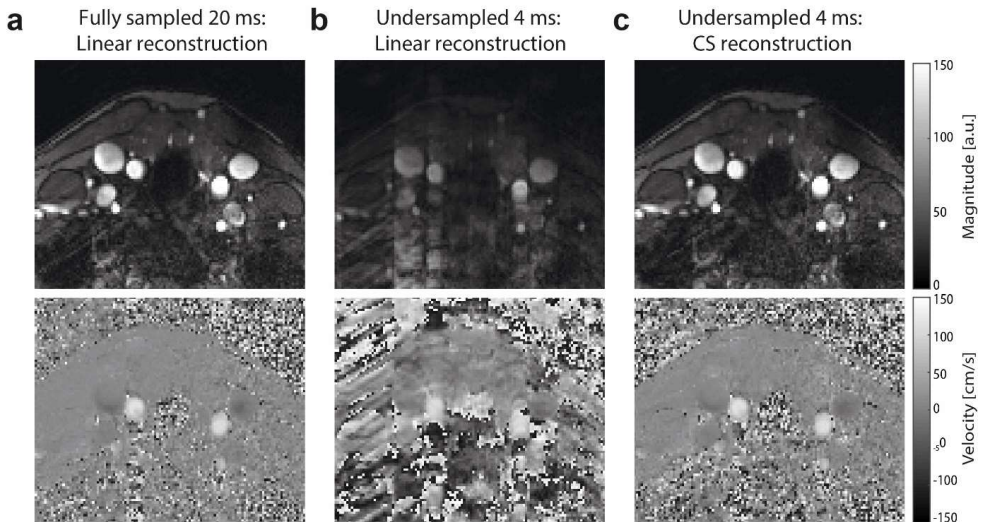


**Figure 2.5** Linear and CS reconstructions of magnitude and velocity images. **(a)** Magnitude and velocity images from a fully sampled *in vivo* dataset of 20 ms temporal resolution. The same dataset reconstructed at a temporal resolution of 4 ms using **(b)** a linear reconstruction and **(c)** a compressed sensing (CS) reconstruction.



With a higher undersampling factor, *i.e.* a higher temporal resolution, undersampling artifacts got more prominent in the images when using a linear reconstruction, which was also visible in the flow curves (**Supplementary Figure 2.11a**, top row). On the other hand, after performing CS reconstruction, all flow curves were recovered (**Supplementary Figure 2.11a**, bottom row), showing the robustness of the method.

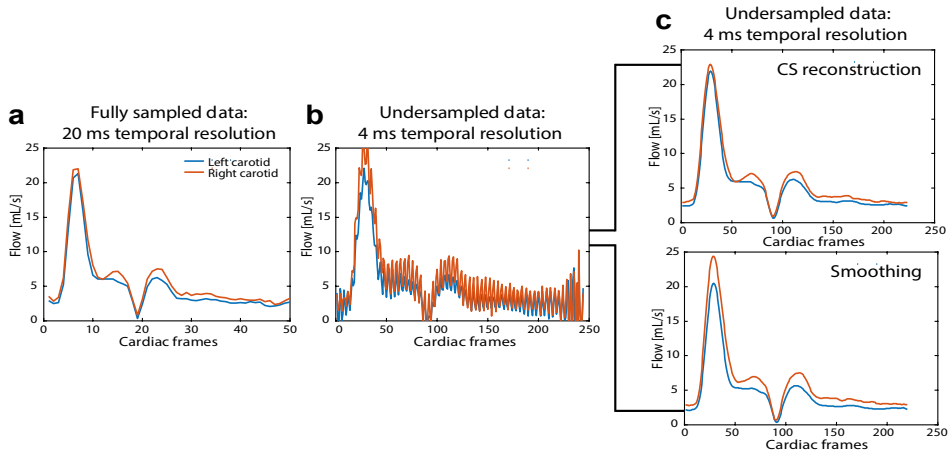


**Figure 2.6** Comparison between smoothing and CS reconstruction. (a) Linear reconstruction of a fully sampled dataset (20 ms temporal resolution). (b) Linear reconstruction of undersampled data with 4 ms temporal resolution. (c) CS reconstruction recovering the undersampled data (top). Smoothing applied to the undersampled data without CS reconstruction (bottom) leads to incorrect reconstruction of the flow profile.

## 2.4.2 Flow phantom experiments

Flow curves measured at 12 positions along the phantom tube showed the expected time shifts along the tube both for ultrasound and MRI measurements (**Figure 2.7**). Also, attenuation and broadening of the systolic flow peak towards the end of the tube was observed. Nevertheless, absolute flow values matched very well between ultrasound and CMR. By assessing the transit time as a function of the position along the tube, PWV could be derived from the slope of the linear relation (**Figure 2.7c**). Error bars indicate the differences for different transit time calculation methods. Resulting PWV values were  $9.8 \pm 1.5$  m/s and  $10.0 \pm 3.5$  m/s for ultrasound and CMR measurements, respectively.



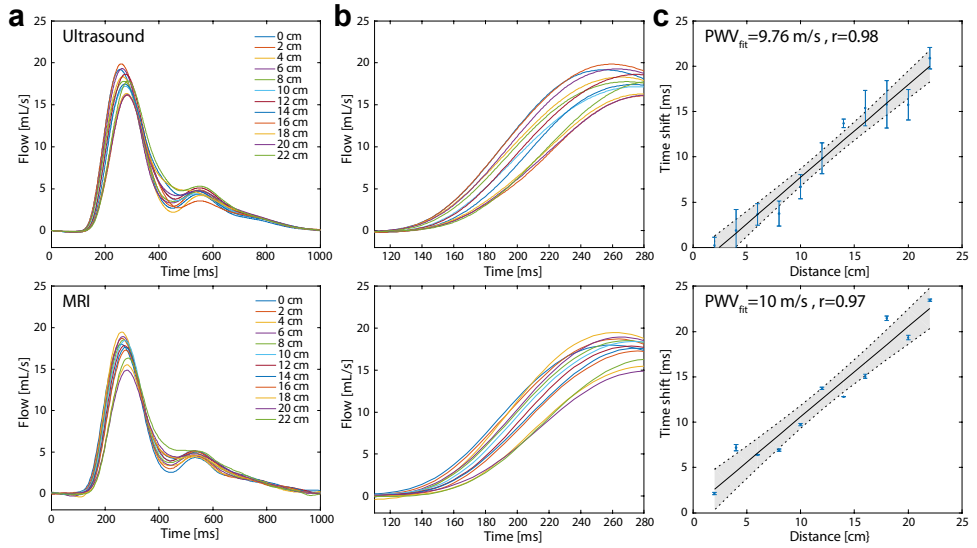


**Figure 2.7** Ultrasound- and CMR-based PWV measurements in the flow phantom. (a) Flow in mL/s measured at 14 positions along the tube (every 2 cm) with the ultrasound probe (top) and with CMR (bottom). (b) Close-up of the region between 120 and 280 ms for better visibility of the time shifts between the curves. (c) Transit time versus the distance between the tubes. A linear fit yields the PWV.

PWV values could additionally be obtained by considering all other combinations of measurement positions. In **Figure 2.8a-b**, PWV values were plotted against the corresponding transit times. PWVs clearly became more inaccurate if the measurement sites were too close and therefore transit times were too short. In **Figure 2.8c-d**, PWVs were grouped according to different transit time lengths, while showing the mean relative error in comparison to the expected PWV of 10 m/s and the standard deviation (SD) of PWV estimation, respectively. Only for the group with the smallest transit time, the mean error was much larger than 10%. SD values dropped below 30% for transit times larger than 7.5 ms. This may for example correspond to accurate PWV estimations up to 10 m/s for an arterial segment as small as 7.5 cm.

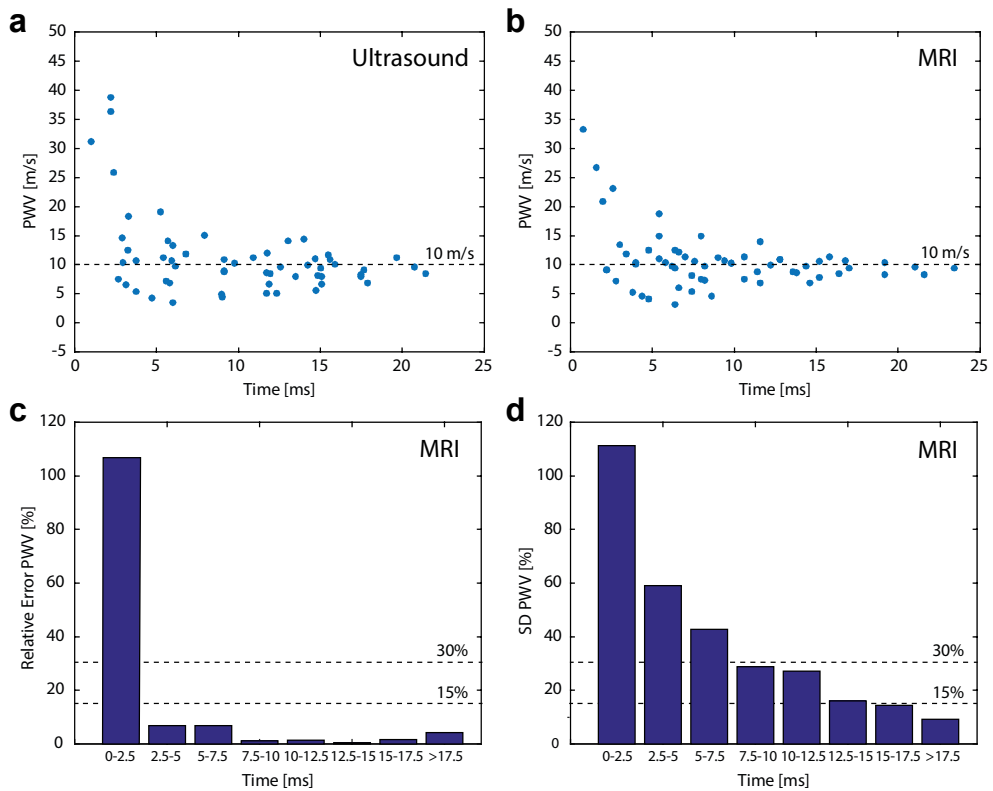


**Figure 2.8** Accuracy and precision of PWVs from CMR. PWV values as function of the transit times in the phantom tube measured with (a) ultrasound and (b) CMR, calculated from all possible distance combinations. At shorter transit times (*i.e.* shorter distances) the PWV values are overestimated and variation is bigger. (c) Relative error of PWV values as function of transit time. For transit times shorter than 2.5 ms the mean PWV values deviate significantly from the expected value of 10 m/s. (d) Standard deviation (SD) of the mean PWV as function of transit time. For transit time above 7.5 ms, the standard deviation decreases below 30%.

### 2.4.3 *In vivo* experiments

The mean carotid artery segment length as measured from the 3D black-blood scans was  $\Delta x = 7.8 \pm 1.4$  cm. The mean transit time was  $\Delta t = 15 \pm 5$  ms, with only 2 healthy subjects having transit times < 7.5 ms. **Figure 2.9a** shows PWV values plotted against age using data from all volunteers. Error bars indicate one standard deviation resulting from calculating PWV with the 5 different methods described previously (**Supplementary Figure 2.10**). Mean PWV for healthy young and elderly subjects were significantly different ( $4.7 \pm 1.0$  m/s and  $7.9 \pm 2.4$  m/s, respectively;  $p < 0.001$ ) as indicated in the boxplot of **Figure 2.9b**.

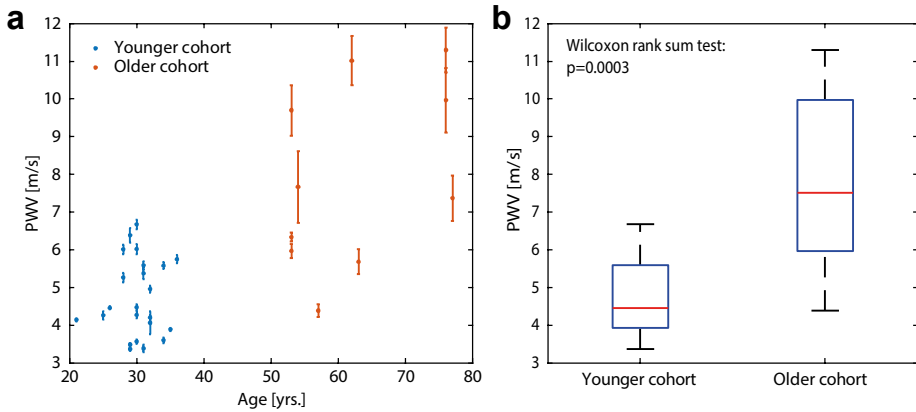


**Figure 2.9** Association between PWV and age *in vivo*. PWV of healthy subjects plotted against age (a). The older cohort (red) has a significant higher PWV than the younger cohort (blue). (b) shows boxplot between the two groups. Error bars indicate one standard deviation resulting from calculating PWV with the 5 different methods.

## 2.5 Discussion

PWV measurements within short carotid artery vessel segments require high spatiotemporal resolution flow data. This study demonstrates the feasibility and accuracy of PWV calculation based on 2D CINE PC CMR with retrospective gating, high temporal resolution binning and CS reconstruction.

Knowledge on regional PWV values in the carotid arteries may help in understanding the causes and consequences of stiffening and plaque development. The development of local vascular stiffening precedes atherosclerotic lesions before intima-media thickening as has been shown in mouse models [7]. However, the relation of PWV and atherosclerosis is still largely unknown in human, which is why further investigations on local PWVs are of high importance. Aortic wall stiffening and the ratio of aortic to carotid stiffness in particular, are implicated in cognitive decline [11]. Reduced PWV differences between aorta and carotid artery are associated with reduced blood flow volume towards the brain at older age [6]. Therefore, regional rather than global PWV measurements are needed to investigate PWV differences between different vessels. In the current form the regional PWV scan can be added to a standard clinical and research CMR protocol, which includes measurements of wall thickness, blood flow, and wall shear stress, to provide a comprehensive picture of vessel function.

Our proposed method was validated against ultrasound measurements showing that accurate PWV estimates can be achieved for transit times above 7.5 ms, with a deviation of mean PWV estimates  $< 5\%$  and a SD of PWV estimates  $< 30\%$ . This includes both deliberately introduced heart rate variations, as well as all variations caused during the measurement and analysis pipeline. Our measurements compete well with others [12,21] reporting intra group SD variations of PWV values of 20% up to 40% for aortic segments which are generally longer and have lower PWV as compared to the carotids. Generally, the sampling frequency of the proposed method of 250 Hz can fully describe the flow curve, rather than a regular (prospectively gated) scan with a sampling frequency of 50 Hz. The frequency content of flow curves is mainly below 40 Hz [22].

Therefore, according to the Nyquist-Shannon rule, a sampling frequency of at least 80 Hz or more suffices to capture the signal information. Besides achieving a sufficient temporal resolution, PWV estimation highly relies on the accuracy of the transit time calculation, which in turn depends on the accuracy the shape of the flow curves. These may be compromised by low SNR, imaging artifacts, or too high VENC values [23]. The relative PWV error decreases as the transit time is longer (either for higher PWVs or for longer vessel segments) as described for one-dimensional MRI technique Bolster *et al.* [21,23]. Based on our current results, we therefore recommend to report a minimal transit time rather than a maximal PWV for this technique. Our data implies accurate PWV estimates of (up to) 10 m/s are possible in regional arterial segments down to 7.5 cm, which is shorter than reported for earlier carotid PWV strategies [7].

Moreover, we show that the systematic bias of our method is low, which is important when studying PWV differences between patient cohorts. Using error propagation one can estimate the PWV value accuracy. Assuming an error in spatial resolution of 0.8 mm and a temporal error of 50% of the temporal resolution, this would lead to a relative PWV error of 30% for 7.5 cm distance and a transit time of 7.5 ms, which agrees with our experimental findings.

The results of *in vivo* PWV measurements are in agreement with other reported values. Luo *et al.* measured PWV with ultrasound in the left carotid artery [24] in 8 male subjects ( $27 \pm 4$  years). PWV was found to be  $4.5 \pm 0.4$  m/s on average. Wang *et al.* [25] measured an average PWV of  $5.3 \pm 0.7$  m/s with ultrasound in 45 healthy subjects (25 male, mean  $\pm$  SD age:  $49 \pm 3$  years). Finally, a significant difference was shown for carotid PWV values between healthy young and elderly subjects, which agrees very well with age-related differences in carotid PWV reported by Kröner *et al.* [6] (PWV young  $5.7 \pm 1.0$  m/s and PWV elderly  $6.9 \pm 1.5$  m/s).

PWV inter-scan variation has been shown to be much larger than the intra-scan variation, not due to technical variability, but most likely caused by physiological variations [12]. The technique developed in this study was therefore validated against ultrasound measurements and by studying PWV differences between age groups.

Currently, Doppler ultrasound measurement of carotid-femoral PWV (global PWV) is considered the non-invasive gold standard for global arterial stiffness assessment [4]. Global PWV is calculated from the time shift between the pulse wave measured in the femoral artery and in the carotid artery divided by the distance between these points. However, global PWV has several limitations as it measures an average elasticity of a vascular system, which is known to be not uniform. Additionally, it is rather difficult to determine the distance between carotid and femoral artery accurately. In contrast, MRI provides flow values as well as detailed anatomical images, making the determination of the actual path length of the arterial segment and PWV calculations more accurate. Nonetheless, regional carotid ultrasound has certain advantages in that it is a fast and cost-efficient method. However, CMR additionally offers a range of imaging protocols to assess other aspects of atherosclerotic disease. Black-blood CMR can be used to accurately determine vessel wall thickness—a surrogate marker of atherosclerosis. With 4D flow CMR blood flow velocity and wall shear stress [26] can be derived. We therefore believe that a CMR-based regional PWV measurement will prove a valuable addition to a comprehensive vascular imaging examination.

In this study, the calculation of the transit time was based on an average value from several analysis methods, an approach which has also been suggested by others [2,27] in order to avoid systematic errors in the transit time calculation. Based on our current results, we cannot conclude that one of the analysis methods is superior to the others, which further warrants this approach. Moreover, differences in PWV values between methods were much smaller than the differences between the two age groups.

Based on the dimension and material properties of the phantom tube, a PWV of 14.1 m/s was expected using the Moens-Korteweg equation [18], which is higher than what we measured experimentally. However, the tube was manually manufactured specifically for this experiment and inaccuracy in the reported elastic modulus ( $\sim 0.5$  GPa) cannot be excluded. Additionally, inflow effects at the inlet of the tube, as well as reflections at the outlet could have had an influence on the measured flow curves. Importantly though, both ultrasound and CMR agreed and measured a PWV of  $\sim 10$  m/s.

A limiting factor to our method is that the 2D slices were acquired sequentially, which means that each slice was acquired during a different ensemble of heart beats. Although we cannot rule out that this may have introduced some variability, the effect is likely minimal because of the use of ‘absolute binning’ and the short acquisition time of only 3 min. An improvement to the current implementation would be a slice-interleaved acquisition or simultaneous multi-slice imaging [28]. Others have suggested the use of 4D flow CRI [29], facilitating flow curves along the entire vessel path. However, at this moment this method would result in clinically unfeasible examination times when combined with the spatiotemporal resolution needed for carotid artery imaging.

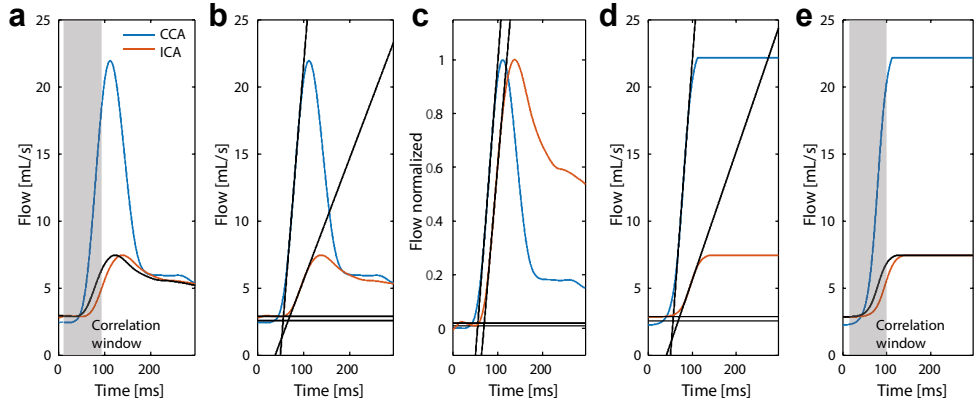
## 2.6 Conclusions

We demonstrate that retrospective gating, undersampling, and a CS reconstruction allow for high temporal resolution 2D CINE PC CMR, enabling accurate and regional carotid PWV quantification. This technique may prove a valuable addition to a comprehensive vascular imaging examination, which addresses various aspects of atherosclerotic disease.

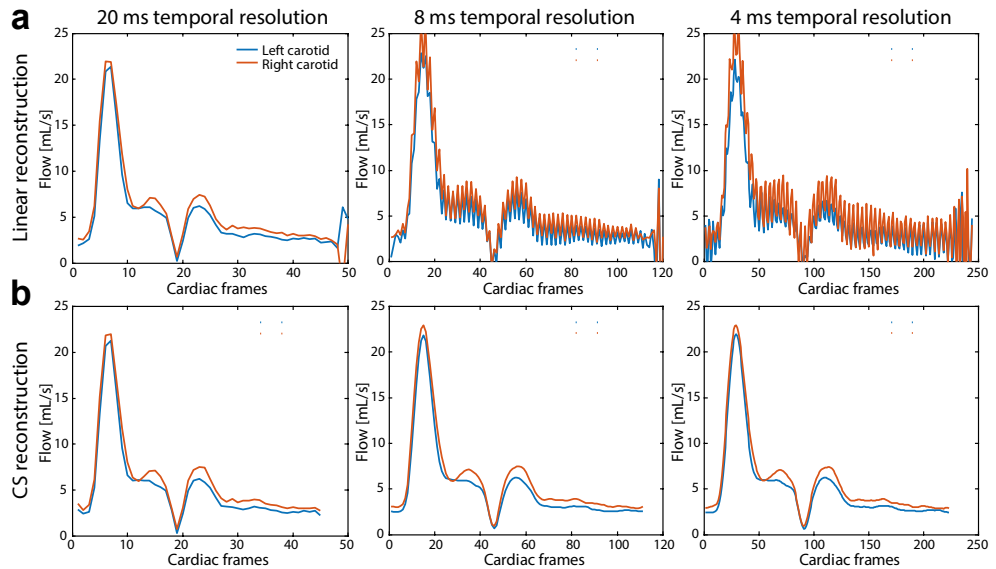
## 2.7 Acknowledgements

We further would like to thank Sandra A. M. van den Berg-Faay, Sanjay Nannan Panday and Marloes Honingh for their efforts in recruiting and scanning volunteers.

## 2.8 Supplementary Material



**Supplementary Figure 2.10** Overview of methods used to calculate transit time between two flow curves. Calculation of the transit time from the two flow curves using (a) the CC method and (b) the FF method. (c) Calculation of transit time using the FF method in combination with a normalization of the flow curves. Calculation of the transit time fitting a sigmoid function through the flow curves for (d) CC and (e) FF method.



**Supplementary Figure 2.11** Flow curves with different temporal resolutions. The same data of one exemplary *in vivo* dataset is binned at a temporal resolution of 10, 8 and 4 ms (from left to right), resulting in 100, 120 and 250 frames across the cardiac cycle. Binning the data at a higher temporal resolution than in 20 ms leads to undersampling. (a) Flow curves derived from a linear image reconstruction with increasing undersampling artifacts at higher undersampling factors. (b) Flow curves after CS reconstruction.

## 2.9 Bibliography

1. Coolen BF, Calcagno C, van Ooij P, Fayad ZA, Strijkers GJ, Nederveen AJ. Vessel wall characterization using quantitative MRI: what's in a number? *Magn Reson Mater Physics, Biol Med.* Springer Berlin Heidelberg; 2017;31:201–22.
2. Wentland AL, Grist TM, Wieben O. Review of MRI-based measurements of pulse wave velocity: a biomarker of arterial stiffness. *Cardiovasc Diagn Ther.* 2014;4:193–206.
3. van Popele NM, Grobbee DE, Bots ML, Asmar R, Topouchian J, Reneman RS, *et al.* Association between arterial stiffness and atherosclerosis. *Stroke.* 2001;32:454–61.
4. Pereira T, Correia C, Cardoso J. Novel Methods for Pulse Wave Velocity Measurement. *J Med Biol Eng.* 2015;35:555–65.
5. Rogers WJ, Hu Y, Coast D, Vido DA, Kramer CM, Pyeritz RE, *et al.* Age-Associated Changes in Regional Aortic Pulse Wave Velocity. *J Am Coll Cardiol.* 2001;38:1123–9.
6. Kröner ESJ, Lamb HJ, Siebelink HMJ, Cannegieter SC, van den Boogaard PJ, van der Wall EE, *et al.* Pulse wave velocity and flow in the carotid artery versus the aortic arch: Effects of aging. *J Magn Reson Imaging.* 2014;40:287–93.
7. Gotschy A, Bauer E, Schrodt C, Lykowsky G, Ye YX, Rommel E, *et al.* Local arterial stiffening assessed by MRI precedes atherosclerotic plaque formation. *Circ Cardiovasc Imaging.* 2013;6:916–23.
8. Bos D, Portegies ML, van der Lugt A, Bos MJ, Koudstaal PJ, Hofman A, *et al.* Intracranial Carotid Artery Atherosclerosis and the Risk of Stroke in Whites The Rotterdam Study. *JAMA Neurol.* 2014;71:405–11.
9. Truijman MTB, Kooi ME, van Dijk AC, de Rotte AAJ, van der Kolk AG, Liem MI, *et al.* Plaque At RISK (PARISK): Prospective multicenter study to improve diagnosis of high-risk carotid plaques. *Int J Stroke.* 2014;9:747–54.
10. Gotschy A, Bauer WR, Winter P, Nordbeck P, Rommel E, Jakob PM, *et al.* Local versus global aortic pulse wave velocity in early atherosclerosis: An animal study in ApoE<sup>-/-</sup> mice using ultrahigh field MRI. *PLoS One.* 2017;12:1–14.
11. de Roos A, van der Grond J, Mitchell G, Westenberg J. Magnetic Resonance Imaging of Cardiovascular Function and the Brain—Is dementia a cardiovascular-driven disease? *Circulation.* 2017;135:2178–95.
12. Markl M, Wallis W, Strecker C, Gladstone BP, Vach W, Harloff A. Analysis of pulse wave velocity in the thoracic aorta by flow-sensitive four-dimensional MRI: Reproducibility and correlation with characteristics in patients with aortic atherosclerosis. *J. Magn. Reson. Imaging.* 2012. p. 1162–8.
13. Coolen BF, Abdurrachim D, Motaal AG, Nicolay K, Prompers JJ, Strijkers GJ. High Frame Rate Retrospectively Triggered Cine MRI for Assessment of Murine Diastolic Function. *Magn Reson Med.* 2013;69:648–56.
14. Lustig M, Donoho D, Pauly JM. Sparse MRI: The application of compressed sensing for rapid MR imaging. *Magn Reson Med.* 2007;58:1182–95.
15. Tran-Gia J, Koestler H, Seiberlich N. Fast Imaging. In: Syed MA, Raman S V, Simonetti OP, editors. *Basic Princ Cardiovasc MRI Phys Imaging Tech.* Basel, Switzerland: Springer; 2015. p. 69–70.

16. Uecker M, Ong F, Tamir JJ, Bahri D, Virtue P, Cheng JY, *et al.* Berkeley Advanced Reconstruction Toolbox. Proc Intl Soc Mag Reson Med. 2015. p. 2486.
17. Rosset A, Spadola L, Ratib O. OsiriX: An Open-Source Software for Navigating in Multidimensional DICOM Images. J Digit Imaging. 2004;17:205–16.
18. Vlachopoulos C, O'Rourke M, Nichols WW. McDonald's Blood Flow in Arteries. Boca Raton, Florida, USA: CRC Press; 2011.
19. Fielden SW, Fornwalt BK, Jerosch-herold M, Eisner RL, Stillman AE, Oshinski JN. A New Method for the Determination of Aortic Pulse Wave Velocity Using Cross-Correlation on 2D PCMR Velocity Data. J Magn Reson Imaging. 2008;27:1382–7.
20. Wang J, Yarnykh VL, Yuan C. Enhanced image quality in black-blood MRI using the improved motion-sensitized driven-equilibrium (iMSDE) sequence. J Magn Reson Imaging. 2010;31:1256–63.
21. Noda C, Ambale Venkatesh B, Ohyama Y, Liu CY, Chamera E, Redheuil A, *et al.* Reproducibility of functional aortic analysis using magnetic resonance imaging: the MESA. Eur Heart J Cardiovasc Imaging. 2016;17:909–17.
22. Muñoz-Tsorrero JFS, Tardio-Fernandez M, Valverde-Valverde JM, Duque-Carrillo F, Vega-Fernandez JM, Joya-Vazquez P, *et al.* Pulse Wave Velocity in Four Extremities for Assessing Cardiovascular Risk Using a New Device. J Clin Hypertens. 2014;16:378–84.
23. Bolster BD, Atalar E, Hardy CJ, McVeigh ER. Accuracy of Arterial Pulse-Wave Velocity Measurement Using MR. J Magn Reson Imaging. 1998;8:878–88.
24. Luo J, Li RX, Konofagou EE. Pulse wave imaging of the human carotid artery: An *in vivo* feasibility study. IEEE Trans Ultrason Ferroelectr Freq Control. 2012;59:174–81.
25. Wang Z, Yang Y, Yuan L, Liu J, Duan Y, Cao T. Noninvasive Method for Measuring Local Pulse Wave Velocity by Dual Pulse Wave Doppler: In Vitro and *In vivo* Studies. PLoS One. 2015;10:e0120482.
26. Potters W V, Marquering HA, VanBavel E, Nederveen AJ. Measuring wall shear stress using velocity-encoded MRI. Curr Cardiovasc Imaging Rep. 2014;7:9257.
27. Dyverfeldt P, Ebberts T, Länne T. Pulse wave velocity with 4D flow MRI: Systematic differences and age-related regional vascular stiffness. Magn Reson Imaging. 2014;32:1266–71.
28. Jin N, Pang J, Giri S, Speier P, Wang D. Simultaneous Multi-Slice Phase Contrast Imaging for Pulse Wave Velocity Measurement in the Vessel. Proc Intl Soc Mag Reson Med. 2017. p. 1265.
29. Markl M, Frydrychowicz A, Kozerke S, Hope M, Wieben O. 4D flow MRI. J Magn Reson Imaging. 2012;36:1015–36.



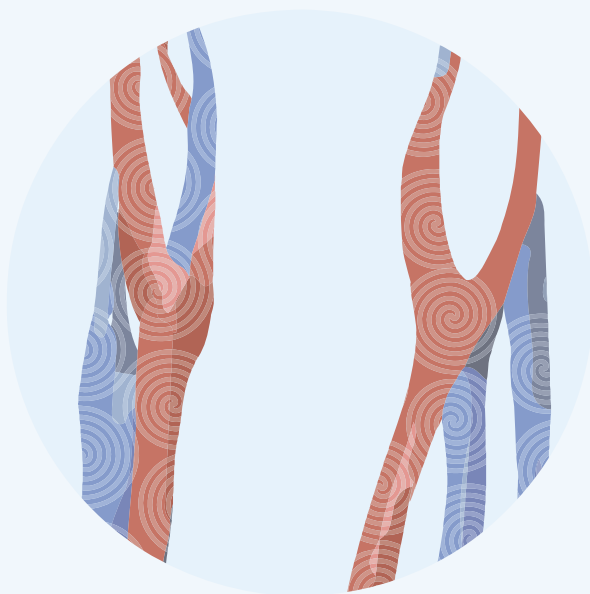


# CHAPTER 3

Highly accelerated 4D flow  
cardiovascular magnetic resonance  
using a pseudo-spiral Cartesian acquisition and  
compressed sensing reconstruction for  
carotid flow and wall shear stress

Eva S. Peper and Lukas M. Gottwald,  
Qinwei Zhang,  
Bram F. Coolen,  
Pim van Ooij,  
Aart J. Nederveen  
and Gustav J. Strijkers

Journal of Cardiovascular  
Magnetic Resonance. 2020



### 3.1 Abstract

**Background:** 4D flow cardiovascular magnetic resonance (CMR) enables visualization of complex blood flow and quantification of biomarkers for vessel wall disease, such as wall shear stress (WSS). Because of the inherently long acquisition times, many efforts have been made to accelerate 4D flow acquisitions, however, no detailed analysis has been made on the effect of Cartesian compressed sensing accelerated 4D flow CMR at different undersampling rates on quantitative flow parameters and WSS.

**Methods:** We implemented a retrospectively triggered 4D flow CMR acquisition with pseudo-spiral Cartesian k-space filling, which results in incoherent undersampling of k-t space. Additionally, this strategy leads to small jumps in k-space thereby minimizing eddy current related artifacts. The pseudo-spirals were rotated in a tiny golden-angle fashion, which provides optimal incoherence and a variable density sampling pattern with a fully sampled center. We evaluated this 4D flow protocol in a carotid flow phantom with accelerations of  $R = 2$ –20, as well as in carotids of 7 healthy subjects ( $27 \pm 2$  years, 4 male) for  $R = 10$ –30. Fully sampled 2D flow CMR served as a flow reference. Arteries were manually segmented and registered to enable voxel-wise comparisons of both velocity and WSS using a Bland-Altman analysis.

**Results:** Magnitude images, velocity images, and pathline reconstructions from phantom and *in vivo* scans were similar for all accelerations. For the phantom data, mean differences at peak systole for the entire vessel volume in comparison to  $R = 2$  ranged from  $-2.3$  to  $-5.3\%$  (WSS) and  $-2.4$  to  $-2.2\%$  (velocity) for acceleration factors  $R = 4$ –20. For the *in vivo* data, mean differences for the entire vessel volume at peak systole in comparison to  $R = 10$  were  $-9.9$ ,  $-13.4$ , and  $-16.9\%$  (WSS) and  $-8.4$ ,  $-10.8$ , and  $-14.0\%$  (velocity), for  $R = 20$ , 25, and 30, respectively. Compared to single slice 2D flow CMR acquisitions, peak systolic flow rates of the phantom showed no differences, whereas peak systolic flow rates in the carotid artery *in vivo* became increasingly underestimated with increasing acceleration.

**Conclusion:** Acquisition of 4D flow CMR of the carotid arteries can be highly accelerated by pseudo-spiral k-space sampling and compressed sensing reconstruction, with consistent data quality facilitating velocity pathline reconstructions, as well as quantitative flow rate and WSS estimations. At an acceleration factor of  $R = 20$  the underestimation of peak velocity and peak WSS was acceptable ( $< 10\%$ ) in comparison to an  $R = 10$  accelerated 4D flow CMR reference scan. Peak flow rates were underestimated in comparison with 2D flow CMR and decreased systematically with higher acceleration factors.

### 3.2 Introduction

3D phase contrast cine cardiovascular magnetic resonance (CMR) (4D flow CMR) [1] may help in risk stratification and follow-up of cardiovascular diseases, which is the leading cause of death worldwide [2]. Atherosclerosis is characterized by the accumulation of fatty deposits in the arterial walls, leading to inflammation, wall thickening, and reduced arterial elasticity [3–5] and is a main cause of cardiovascular disease. In relation to that, low wall shear stress (WSS), the tangential force of the blood flow on the vessel wall [6–8], was found to be an indicator for rearrangement of endothelial cells [9] and increased wall thickness [10]. Since atherosclerosis is a chronic disease that can stay asymptomatic for a long time, a great need exists for diagnostic tools that identify patients at high risk and at an early stage of the disease.

4D flow CMR enables comprehensive visualization and quantification of complex blood flow and the calculation of several relevant hemodynamic biomarkers, including WSS. However, 4D flow CMR acquisitions in general still remain challenging, mostly because of the long acquisition times involved. These can vary between 15 and 40 min [11–13], depending on the desired 3D spatial resolution, number of frames per cardiac cycle, the heart rate, the respiratory gating efficiency and (if applied) the use of acceleration techniques, such as sensitivity encoding (SENSE) or segmented k-space acquisitions. Overall, this seriously complicates its use in routine clinical practice, since apart from practical issues such as long waiting times and costs, it is difficult for patients to remain motionless in the scanner for such a long time. Also, physiological variations and movement during long scans may lead to artifacts and inaccuracies. Therefore, a clear need exists for scan time reduction in 4D flow CMR.

Various methods have been presented to accelerate 4D flow CMR [12,14–17], which are commonly based on undersampling k-space (*e.g.* acquiring a reduced amount of data at a sub-Nyquist rate) and performing reconstructions at full image quality using advanced reconstruction algorithms. 4D flow CMR and other time-resolved cardiac imaging techniques are highly correlated in time. Therefore, these data are very suitable for applying undersampling, particularly in the time dimension. The use of non-Cartesian radial [14], spiral [15] and cone-shaped [16] undersampling techniques has been demonstrated, enabling highly accelerated and motion-robust scans. Nevertheless, non-Cartesian scans can be challenging with respect to implementation, post-processing, and reconstruction time. Cartesian k-t undersampling techniques, such as k-t SENSE [18] or k-t PCA [12] have shown to be successful with acceleration factors up to  $R = 8$ . EPI accelerated 4D flow CMR scans provided acceleration factors of  $R = 5$  [19]. More recently, compressed sensing (CS) accelerated 4D flow techniques have been introduced, which facilitated even higher acceleration factors ( $R = 8$ –27) [17].

However, no comprehensive evaluation has been made on how highly (prospectively) Cartesian undersampling with CS reconstruction in 4D flow CMR affects quantitative flow parameter estimates like WSS *in vivo*. For this study, we therefore aimed to firstly implement a highly accelerated 4D flow acquisition based on a Cartesian pseudo-spiral sampling trajectory. This resulted in incoherent undersampling patterns for each individual cardiac frame, enabling CS reconstructions using temporal constraints. We secondly evaluated the performance of this CS 4D flow CMR technique over a range of acceleration factors ( $R = 2$ –30) for estimating quantitative flow and WSS parameters in a carotid flow phantom, as well as in the carotid arteries of healthy subjects.

### 3.3 Methods

#### 3.3.1 Sampling strategy and implementation

Our specific method of accelerating 4D flow CMR using pseudo-spiral Cartesian sampling is schematically depicted in **Figure 3.1**. 3D k-space consists of two phase encoding directions ( $k_y, k_z$ ) and one fully sampled frequency encoding (readout) direction ( $k_x$ ). In regular Cartesian sampling ( $k_y, k_z$ )-profiles (a combination of  $k_y$  and  $k_z$  coordinates) would be acquired line-by-line (**Figure 3.1a**). Additionally, in traditional cine imaging each ( $k_y, k_z$ )-profile would be sampled multiple times during each heartbeat (regular profile change) to ensure complete filling of k-t-space and a fully sampled time dimension for each ( $k_y, k_z$ )-profile (**Figure 3.1b**). However, highly undersampling k-space in a random order on a Cartesian grid is not preferred since it would involve large steps in k-space. Regular line-by-line undersampling would complicate interleaving k-space sampling of multiple cardiac frames.

We implemented a pseudo-spiral filling strategy which was proposed earlier by Liu and Saloner [20] and also used in a similar fashion in G-CASPR [21], VDRad [17], ROCK-MUSIC [22] and GOCART [23] to create a randomly undersampled k-t-space. The pseudo-spiral trajectory has a couple of advantages. First, it involves only small jumps in k-space thereby minimizing eddy current related artifacts. Secondly, the pseudo-spirals can be rotated in a tiny golden angle fashion, which provides optimal incoherence and a variable density sampling pattern with a fully sampled center (**Figure 3.1c**), which is highly beneficial for CS reconstruction. Finally, despite the pseudo-spiral acquisition, the k-space points are still located on a Cartesian grid (hence the name pseudo-spiral), as shown in **Figure 3.1d**, which improves the reconstruction as no regridding interpolation is required.

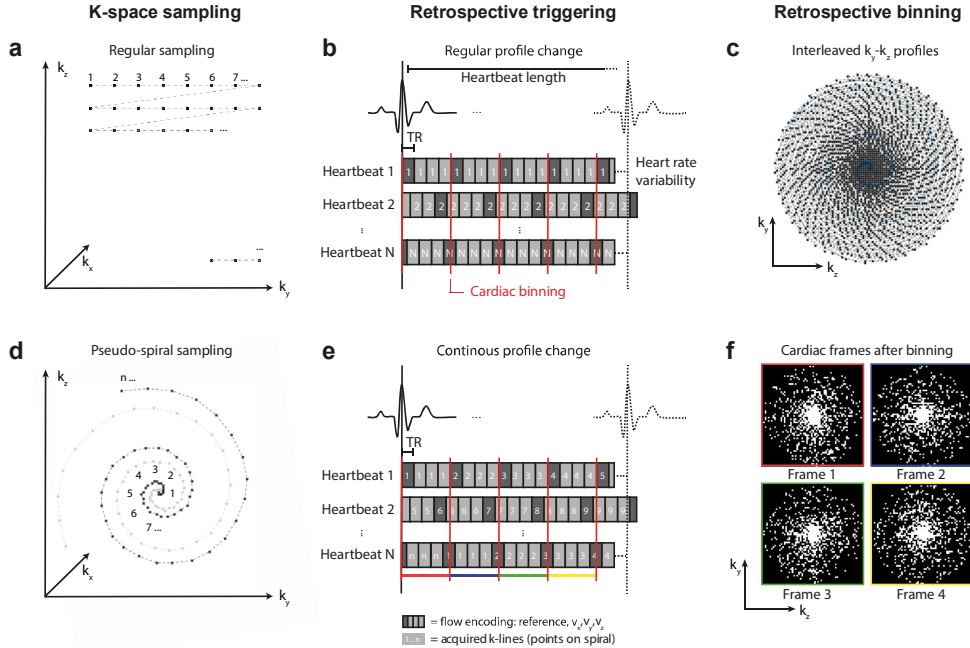


**Figure 3.1** The pseudo-spiral sampling strategy for Cartesian 3D k-space sampling, with two phase encoding directions ( $k_y, k_z$ ) and one fully sampled frequency encoding direction ( $k_x$ ). **(a)** In a regular Cartesian sampling strategy ( $k_y, k_z$ )-profiles are acquired line-by-line. **(b)** Additionally, in regular retrospectively triggered cardiac scans, each ( $k_y, k_z$ )-profile is repeated within each cardiac cycle to ensure complete filling of k-t-space and a fully sampled time dimension for each ( $k_y, k_z$ )-profile. The segments of 4xTR length indicate all 4 flow encoding segments of a 4D flow CMR scan, with the dark segments indicating the reference scan. **(c)** This distribution shows all pseudo-spiral ( $k_y, k_z$ )-coordinates sampled within one scan session. The pseudo-spiral trajectory creates a variable density distribution with an oversampled center. **(d)** In a pseudo-spiral sampling strategy, ( $k_y, k_z$ )-profiles are sampled from the center of k-space to the outside, however still on a Cartesian grid. **(e)** To achieve undersampling in the temporal domain, ( $k_y, k_z$ )-profiles are updated continuously within each cardiac cycle in addition to the pseudo-spiral sampling trajectory. **(f)** After retrospective cardiac binning, this results in a sampling mask of white (sampled) and black (not sampled) ( $k_y, k_z$ )-coordinates, with unique, incoherent sampling patterns per cardiac frames (see color coding in e).

The second important mechanism in our approach is related to the cardiac triggering strategy (**Figure 3.1e-f**). By using retrospective gating and a continuous update of the ( $k_y, k_z$ )-profile throughout the cardiac cycle, each separate cardiac frame will have its unique random k-space filling, but with preservation of the variable density pattern. This maximizes randomness in both the spatial and temporal (*i.e.* cardiac frames) domain. Note that first all four flow-encoding directions are sampled (4xTR) before changing the ( $k_y, k_z$ )-profile number.

The pseudo-spiral sampling trajectory in ( $k_y, k_z$ )-plane can be described in more detail as a spiral with radius  $r$  and linearly increasing angle  $\varphi$  gridded on the scan matrix size:

$$r(\varphi) = \varphi^2 \text{ with } \varphi \in \{\varphi_1 = 0, \dots, \varphi_n = 2\pi l\} \quad (3.1)$$

with  $n$  the number of Cartesian readouts per pseudo-spiral ( $\varphi_0$ - $\varphi_n$ ) and  $l$  the number of turns. In all experiments  $n=100$  and  $l=3$  were used. After one pseudo-spiral arm was sampled a new arm was acquired in a tiny golden-angle increment of 23.63 degrees relative to the previous pseudo-spiral. The

number of pseudo-spirals depends on the desired acceleration factor. For asymmetric matrix size the pseudo-spiral was rescaled according to the ratio  $k_{y,\max}/k_{z,\max}$ .

A text file containing all  $(k_y, k_z)$ -profiles was created in MATLAB (MathWorks Inc., Natick, Massachusetts, USA) and imported in the scanner software (Philips Healthcare, Best, the Netherlands; software release 5.1.8 CDAS). A custom patch was used (PROspective Undersampling in multiple Dimensions (PROUD) patch [24–26]), which allows sampling of predefined trajectories. PROUD also enables continuously updating the  $(k_y, k_z)$ -profiles within each cardiac cycle. Moreover, PROUD controls the acquisition in real time by bitmasking the k-t-space filling and prevents duplicate acquisitions of profiles of the same cardiac frame.

In continuous pseudo-spiral sampling, the acceleration factor  $R$  can be chosen in reference to the number of readouts of a fully sampled scan  $N_{\text{fully}}$  and the number of readouts of an undersampled scan  $N_{\text{undersampled}}$ . Hereby  $N_{\text{fully}}$  depends on the number of phase encoding steps  $N_{k_y}$  and  $N_{k_z}$ , the desired number of cardiac frames  $N_{\text{card}}$  and the number of flow encoding segments  $N_{\text{flow}}$ .

$$R = \frac{N_{\text{fully}}}{N_{\text{undersampled}}} = \frac{N_{k_y} \cdot N_{k_z} \cdot N_{\text{card}} \cdot N_{\text{flow}}}{N_{\text{undersampled}}} \quad (3.2)$$

### 3.3.2 Compressed sensing reconstruction

All image reconstruction steps, including phase-offset corrections, were done offline using MRecon and GTFlow (Gyrotools, Zurich, Switzerland). For each measured k-line, the time distance to the ECG R top was available from the raw data. This allowed binning of the data into a specific number of cardiac frames ( $N_{\text{card}}$ ) using an ‘absolute’ binning approach. The last cardiac frames at end-diastole receive less data due to R-R variabilities and were discarded during flow curve analysis (phantom: last 2 frames see **Figure 3.3b**, *in vivo*: last 3 frames due to larger R-R variability). Data from each flow encoding direction was binned independently. After cardiac binning, the undersampled data was reconstructed with a non-linear CS-PI (compressed sensing and parallel imaging) algorithm available from the Berkeley Advanced Reconstruction Toolbox (BART) [27] according to

$$\hat{\mathbf{m}} = \arg \min_{\mathbf{m}} \{ \|F_U \mathbf{m} - \mathbf{y}\|_2 + \lambda \text{TV} \mathbf{m} \} \quad (3.3)$$

using a sparsifying TV operator performed along the time dimension.  $F_U$  denotes the undersampling Fourier operator,  $\mathbf{y}$  the measured data, and  $\mathbf{m}$  the reconstructed data. While the left term ensures data consistency, the right term enforces sparsity, regularized by parameter  $\lambda$ . Reconstructions were tested for different regularization parameters and number of iterations  $i$ . Heuristically, by reconstructing the data using different settings (ranging from  $0.001 < \lambda < 1$ , and  $2 < i < 100$ )  $\lambda=0.01$  and  $i=10$  were found to lead to the best match in peak flow values in comparison to the 2D flow reference scan, and were thus used for all reconstructions.

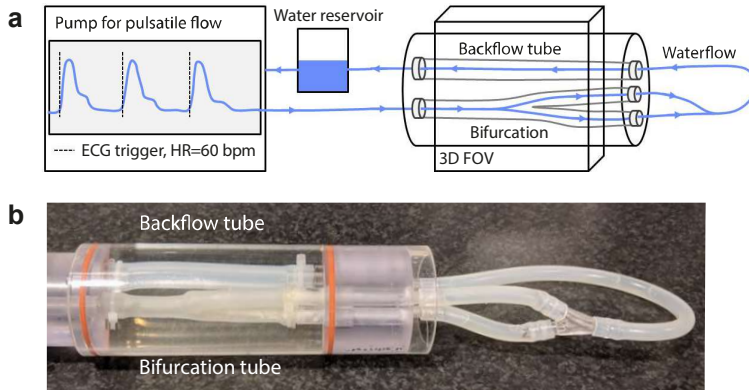


**Figure 3.2 (a)** The phantom setup. A pulsatile water flow enters the phantom in a compliant silicon tube in the shape of a carotid bifurcation and then returns in a straight silicon tube, which leads back to a reservoir. The water flow had a generated heart rate of  $60 \pm 5$  bpm. The silicon tubes were embedded in water. **(b)** Image of the phantom tubes.

### 3.3.3 Flow phantom experiments

A flow phantom was designed (LifeTec, Eindhoven, The Netherlands) (**Figure 3.2**) consisting of a distensible silicon carotid artery embedded in water. A pulsatile water flow was applied at a simulated heart rate of 60 bpm and a random variability with 5% standard deviation. At the inlet of the phantom a peak flow rate of 10 ml/s and a mean flow rate of 3 ml/s was established.

4D flow CMR was performed with a 3 T CMR scanner (Ingenia, Philips Healthcare) using a 32-channel head coil and a referenced four-point flow encoding method (as explained in detail in [28]). Scan parameters were: TR = 8.9 ms, TE = 4.5 ms, FA =  $8^\circ$ , VENC = 150 cm/s (in all three flow encoding directions), matrix size =  $160 \times 160 \times 40$ , FOV =  $128 \times 128 \times 32$  mm<sup>3</sup>, bandwidth = 713 Hz/pixel, spatial resolution =  $0.8 \times 0.8 \times 0.8$  mm<sup>3</sup>, and 19 reconstructed cardiac frames. No segmented k-space was used. As a flow reference, fully sampled 2D flow CMR scans with identical scan settings (except FA =  $20^\circ$  and bandwidth = 217 Hz/pixel) and spatial resolution =  $0.8 \times 0.8 \times 3$  mm<sup>3</sup> were acquired in two planes perpendicular to the tubes. No contrast agent was used. The 4D flow scans were accelerated R = 2, 4, 6, 8, 10, 12, 15, and 20 times, with corresponding scan times decreasing from 45:57, 22:59, 15:18, 11:28, 9:08, 7:32, 5:45, to 4:30 min. The non-accelerated scan time for the given heart rate and number of cardiac frames amounted to 1:32 hours.

### 3.3.4 *In vivo* experiments

The acceleration technique was applied in the carotid arteries of 7 healthy volunteers (average age  $27 \pm 2$  years, 4 male) using an 8-channel neck coil. Using the same settings as for the phantom, the 4D flow scans were accelerated R = 10, 20, 25 and 30 times (scan times: 9:08, 4:16, 3:14 and 2:32 min, respectively). Left and right carotid arteries were analyzed separately. 2D flow CMR reference scans were acquired using the same settings as for the phantom.



### 3.3.5 Flow rate and WSS calculation

To calculate flow rates, regions-of interest (ROIs) in common, internal, and external carotid artery (CCA, ICA and ECA) were drawn using GTFlow in the same slice as the 2D flow reference scans for each artery and each acceleration factor separately. The time resolved flow rate  $Q$  was calculated as:  $Q(t) = \int_{ROI} \mathbf{v}(\mathbf{r}, t) \cdot d^2\mathbf{r}$ , with  $\mathbf{v}(\mathbf{r}, t)$  the absolute velocity at position  $\mathbf{r}$  and cardiac phase  $t$ .

A 3D segmentation of the carotid bifurcation was created per 4D flow scan using Mimics (Materialise, Leuven, The Netherlands) for both phantom and *in vivo* scans. The peak systolic time frame was defined as the time frame with the highest absolute velocity averaged over the segmented volume. WSS vectors  $\boldsymbol{\tau}$  were calculated in MATLAB as described in Potters *et al.* [29]:

$$\boldsymbol{\tau} = 2 \eta \dot{\boldsymbol{\epsilon}} \cdot \mathbf{n} \quad (3.4)$$

With  $\eta$  the blood viscosity of  $3.2 \cdot 10^{-3}$  Pa·s,  $\mathbf{n}$  the inward normal vector on the vessel wall and  $\dot{\boldsymbol{\epsilon}}$  the rate of the deformation tensor

$$\dot{\boldsymbol{\epsilon}} = \begin{bmatrix} \frac{\partial v_x}{\partial x} & \frac{1}{2} \left( \frac{\partial v_y}{\partial x} + \frac{\partial v_x}{\partial y} \right) & \frac{1}{2} \left( \frac{\partial v_z}{\partial x} + \frac{\partial v_x}{\partial z} \right) \\ \frac{1}{2} \left( \frac{\partial v_x}{\partial y} + \frac{\partial v_y}{\partial x} \right) & \frac{\partial v_y}{\partial y} & \frac{1}{2} \left( \frac{\partial v_z}{\partial y} + \frac{\partial v_y}{\partial z} \right) \\ \frac{1}{2} \left( \frac{\partial v_x}{\partial z} + \frac{\partial v_z}{\partial x} \right) & \frac{1}{2} \left( \frac{\partial v_y}{\partial z} + \frac{\partial v_z}{\partial y} \right) & \frac{\partial v_z}{\partial z} \end{bmatrix} \quad (3.5)$$

By selecting a local coordinate system for each point on the vessel wall such that the  $z'$  axis aligns with the inward normal, and by assuming no flow through the vessel wall, *i.e.*  $\mathbf{n} \cdot \mathbf{v} = 0$ , this equation simplifies to

$$\boldsymbol{\tau} = \eta \begin{bmatrix} \frac{\partial v_{x'}}{\partial z'} & \frac{\partial v_{y'}}{\partial z'} & 0 \end{bmatrix}, \quad (3.6)$$

Spatial derivatives of the velocity on the vessel wall were derived from fitted splines. After transforming back to the original coordinate system, the (time resolved) magnitude of the WSS vector is reported throughout the manuscript. The segmented volume of each scan was rigidly registered on the segmented carotid of the scan with the lowest acceleration factor (MATLAB) [30]. For *in vivo* scans this was done per subject. WSS and velocity values at peak systole were interpolated on the reference volume, to facilitate voxel-wise comparisons. Pathlines were visualized using GTFlow.

### 3.3.6 Statistical analysis

Bland-Altman analysis was used to determine the mean difference and the limits of agreement. Orthogonal regression was used to determine the slope, intercept and Pearson correlation coefficient  $\rho$ .

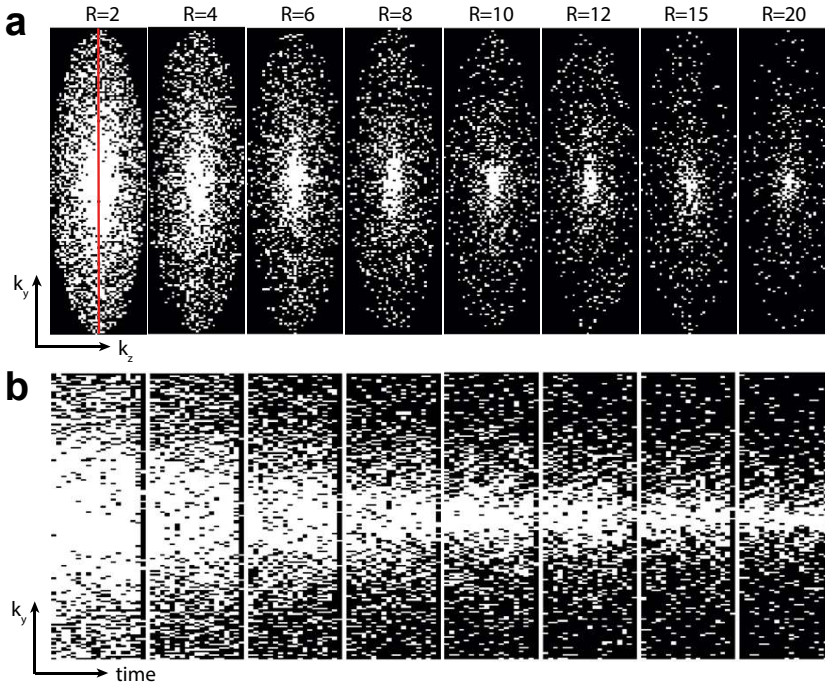


**Figure 3.3** (a) Undersampling patterns in both phase encoding directions ( $k_y, k_z$ ) for acceleration factors  $R = 2 - 20$  as a result of cardiac binning. (b) Undersampling patterns for one phase encoding direction ( $k_y$ ) and 19 cardiac frames (time) for acceleration factors  $R = 2 - 20$ .

### 3.4 Results

#### 3.4.1 Phantom

**Figure 3.3** shows typical k-t-space filling patterns in spatial and temporal direction with from left to right increasing acceleration factors of  $R = 2-20$ . For all the accelerations the resulting k-spaces after cardiac binning had quasi-random filling with a densely sampled center. The undersampling patterns were also incoherent over time (**Figure 3.3b**), which is important for the CS reconstruction with TV constraint.

Reconstructed magnitude and feet-head (FH) velocity images of the phantom visually were very comparable for all acceleration factors (**Figure 3.4a-d**). With increasing acceleration factor some spatial blurring became apparent, particularly for the tube walls. More importantly however, the flow curves for ROIs in CCA, ICA and ECA were comparable for all acceleration factors and in comparison to the fully sampled 2D flow CMR scan (**Figure 3.5a**). More variations in peak flow rate were observed in the smaller vessels (ICA and ECA), than in the CCA.

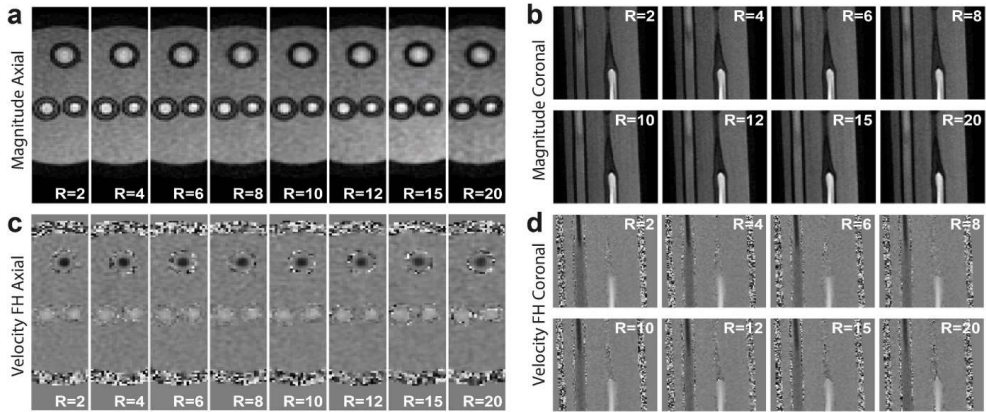


**Figure 3.4** Axial (a) and coronal (b) view of magnitude images of the phantom for  $R = 2-20$ . Axial (c) and coronal (d) view of velocity images for  $R = 2-20$ . Both velocity images show feet-head (FH) flow encoding with a velocity range of  $\sim 150$  to  $150$  cm/s. In axial images the backflow tube is on the top and the bifurcation tube on the bottom. In coronal images, the backflow is on the left and the bifurcation tube on the right.

The largest deviation in flow rate as compared to the 2D reference was observed at peak systole in the CCA, with  $0.5$  ml/s (4.4%) less for the  $R = 12$  times accelerated 4D flow CMR scan (**Supplementary Table 3.1**). The  $R = 20$  times accelerated scan had a deviation in peak systolic flow rate of only  $0.2$  ml/s (1.7%). Pathlines, through plane velocity and WSS of the phantom at peak systole are shown in **Figure 3.5b-c** (pathline movies are available online, see **Supplementary Video 3.1**). Only minor visual differences were observed for WSS values and pathlines at peak systole for scans with varying acceleration factors.

For a quantitative assessment of the influence of high accelerations on the hemodynamic parameters at peak systolic, velocity and WSS values in the phantom and per acceleration factor ( $R = 4-20$ ) were compared voxel-wise within the segmented volume against the values of the lowest acceleration factor ( $R = 2$ ) in a Bland-Altman analysis (**Figure 3.6**).

The mean differences and the limits of agreement (LOA) of the Bland-Altman analysis for all acceleration factors, shown in **Figure 3.6**, are summarized and visualized in **Figure 3.7**. The maximum mean difference for WSS at peak systole was 5.3% for  $R = 20$ . The maximum mean difference for velocity was -2.4% for  $R = 10$ . The LOA increased slightly with increasing acceleration factor. Slope and Pearson correlation coefficients are summarized in **Figure 3.7c-d**. The slope of the correlation for both WSS and velocity at peak systole essentially stayed the same with increasing acceleration, whereas the Pearson correlation coefficients  $\rho$  slightly decreased for higher acceleration factors. **Figure 3.7e-f** depicts the mean WSS and mean velocity of the vessel volume not only at peak systole, but for every time point in the cardiac cycle, demonstrating no variation in other cardiac frames. A summarizing table of the Bland-Altman analyses for peak systolic WSS and velocity values of the phantom experiment is found in **Supplementary Table 3.2**.

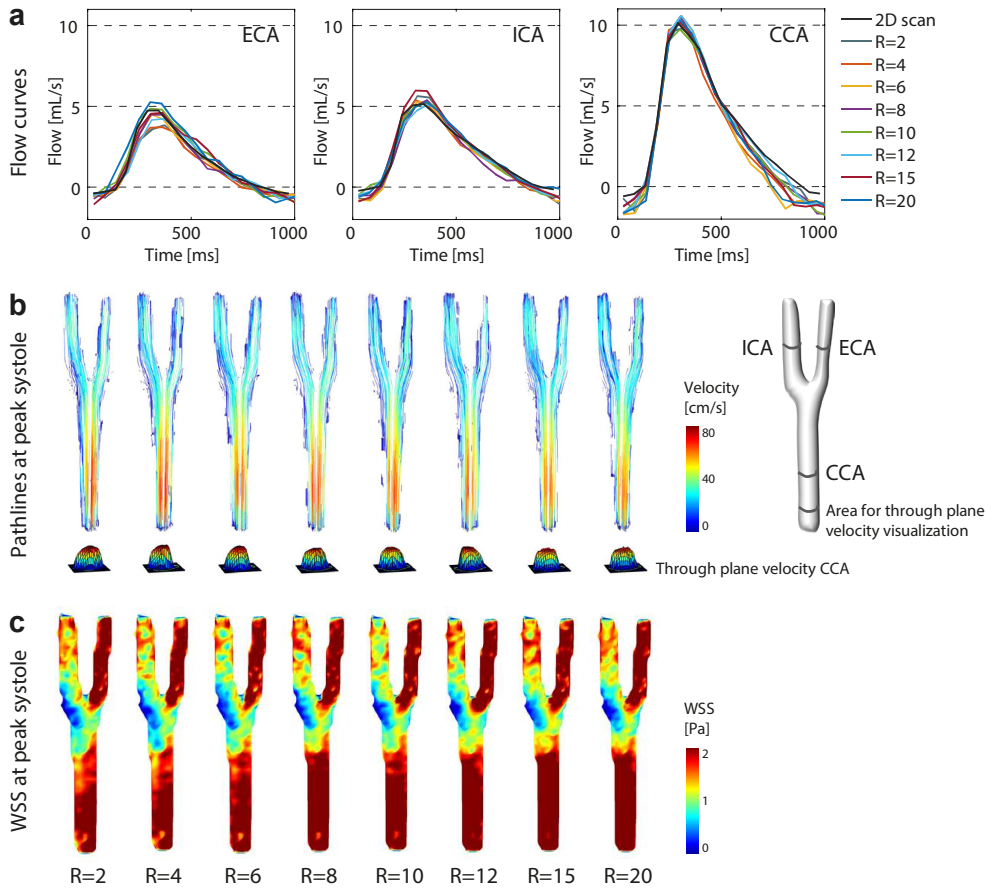


**Figure 3.5** Flow in the carotid phantom at (a) external carotid artery (ECA), internal carotid artery (ICA) and common carotid artery (CCA) for acceleration factors  $R = 2$ –20 and the fully sampled 2D flow CMR scans. (b) Pathlines and wall shear stress (WSS) (c) in the carotid phantom for acceleration factors  $R = 2$ –20 during peak systole

### 3.4.2 *In vivo*

Similar to the phantom scans, the magnitude and velocity images of the *in vivo* scans were visually of good quality up to the highest acceleration factors (**Figure 3.8**). Some blurring occurred with increasing acceleration.

Flow rate was calculated for the accelerated 4D flow CMR scans and compared to the fully sampled 2D flow CMR scan. The flow curves through the cardiac cycle, averaged over all subjects, and left and right carotid, plotted per acceleration factor, are shown in **Figure 3.9a**. The typical carotid flow curves through the cardiac cycle could be appreciated for all the accelerated scans, with consistent flow rate values, albeit with lower flow rate values than for the 2D reference scan. The subject-averaged flow rate at peak systole with respect to the 2D flow reference was lower by  $-5.0 \pm 2.1$  ml/s ( $-24.4 \pm 10.4\%$ ) for  $R = 20$  and  $-6.6 \pm 3.4$  ml/s ( $-32.6 \pm 16.7\%$ ) for  $R = 30$  in the CCA (**Supplementary Table 3.3**). Flow rates in ICA and ECA were lower in accelerated 4D flow scans than in the 2D flow scan.

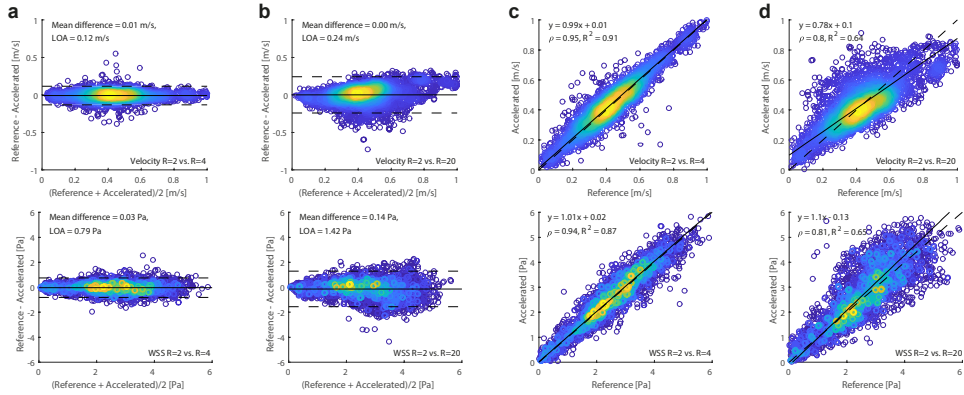


**Figure 3.6** Bland-Altman plots and orthogonal regression for peak systolic velocity (top row) and WSS (bottom row) values of the phantom scan. The scan with the lowest acceleration factor ( $R = 2$ ) is compared to acceleration factor  $R = 4$  (a and c) and to acceleration factor  $R = 20$  (b and d), to visualize the changes occurring at higher undersampling rates.

Calculated pathlines, through plane velocities, and WSS during peak systole of one exemplary *in vivo* scan are shown in **Figure 3.9b-e**. Pathlines movies during the cardiac cycle are also available online in **Supplementary Video 3.2**. Peak systolic WSS at all acceleration factors for all volunteers can be found in **Supplementary Figure 3.14**. Visually, peak systolic WSS spatial patterns, pathline movies, and through plane velocities were similar. However, in contrast to the phantom experiment, the mean WSS during peak systole from voxel-wise BA analysis decreased slightly for higher acceleration factors. WSS values decreased by -9.9%, -13.4% and -16.9% for acceleration factors of  $R = 20$ , 25 and 30, respectively (**Figure 3.10**). Also, the slopes of the correlation plots and the Pearson correlation coefficients  $\rho$  slightly decreased for higher acceleration factors. The velocities within the vessel volume of the carotid arteries showed a similar trend. Velocities decreased by -8.4%, -10.8%, and -14.0% for acceleration factors of  $R = 20$ , 25 and 30, respectively (these results can also be found in **Supplementary Table 3.4**).

### 3.5 Discussion

In this work we demonstrated the feasibility of accelerating 4D flow CMR of the carotids up to 30 times using a pseudo-spiral Cartesian sampling strategy. We recommend an acceleration factor of  $R = 20$  to facilitate fast 4D flow CMR with an acceptable ( $< 10\%$ ) [31] underestimation of *in vivo* peak velocities ( $-8.4 \pm 9.9\%$ ) and WSS ( $-9.9 \pm 10.9\%$ ) in comparison to the  $R = 10$  4D flow CMR reference scan. In comparison to 2D flow CMR,  $R = 20$  times accelerated 4D flow CMR however may result in a peak flow rate underestimation of  $-24.4 \pm 10.4\%$ . We developed and evaluated the protocol using a carotid flow phantom for acceleration factors up to  $R = 20$  and in the carotid arteries of seven healthy subjects for acceleration factors up to  $R = 30$ . For high accelerations, we observed a trend of increased spatiotemporal blurring and decreased image quality *in vivo*. This resulted in a progressive decrease in the hemodynamic velocity and WSS values at systole.

Acceleration of 4D flow CMR has been an important topic since years. Experts in the field have published a consensus paper [32] in which different acceleration strategies for 4D flow CMR are advised. Papers from leading experts in accelerated 4D flow CMR [11,12,17,33], as discussed one by one below, typically use a SENSE  $R = 2$  acceleration (sometimes with a segmented k-space factor of 2–3) as

a reference scan when validating a new acceleration technique. However, there exists no clear consensus on how to validate a 4D flow CMR acceleration techniques and which parameters to report in order to estimate accuracy [32]. Peak velocity or peak flow rate seem important parameters however peak velocity underestimation was not mentioned as an exclusion criterion in the consensus paper, as *e.g.* also k-space segmentation limits the temporal resolution of the scan, leading to peak underestimation. Nevertheless, peak velocity is important and should be considered when using acceleration. Generally, the accuracy of 4D flow CMR is also highly dependent on spatiotemporal resolution and SNR. There might also be a general bias between 4D and 2D flow CMR [32].

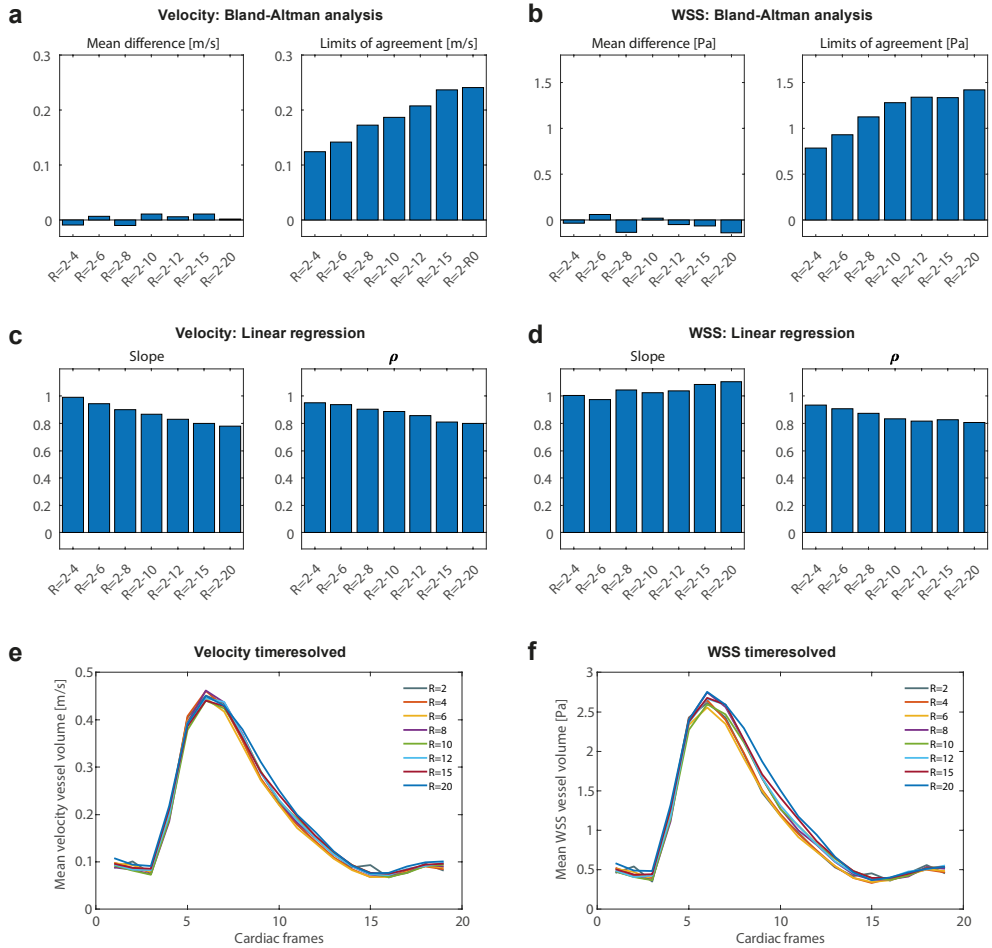


**Figure 3.7** (a) Comparison of peak systolic velocities at  $R = 2$  with all higher acceleration factors  $R = 4-20$  using Bland-Altman analysis (mean differences and limits of agreement (LOA)). (b) The same comparison as in (a) for WSS values at peak systole. (c) Comparison of peak systolic velocities at  $R = 2$  with all higher acceleration factors  $R = 4-20$  using orthogonal regression (slope of the regression line and Pearson correlation coefficient  $\rho$ ). (d) The same comparison as in (c) for WSS values at peak systole. (e-f) Mean velocity and mean WSS (calculated per time point and over the vessel volume), plotted for all cardiac frames.

In **Supplementary Figure 3.12a**, we have repeated our experiments *in vivo* in  $N=1$  subject, including a SENSE ( $R=2$ ) 4D flow CMR acquisition with a k-space segmentation factor of 2. Our CS acceleration performs equally well to this reference method for acceleration factors up to  $R = 20$ . However both CS and SENSE accelerated 4D flow CMR scans underestimate peak flow rate values as compared to 2D flow CMR, which is likely associated with lower SNR (see also magnitude images in **Supplementary Figure 3.12a**, left). In a phantom setting (**Supplementary Figure 3.12b**) both methods perform evenly good up to an acceleration factor of  $R = 30$ . Phantom flow curves up to an acceleration factor of  $R = 100$  are shown. This shows, that  $R = 10$  CS accelerated scans serve as a good reference for scans with higher acceleration factors. It also demonstrates, that very high acceleration factors ( $>50$ ) can be achieved, in which reasonable flow curves can still be recognized.



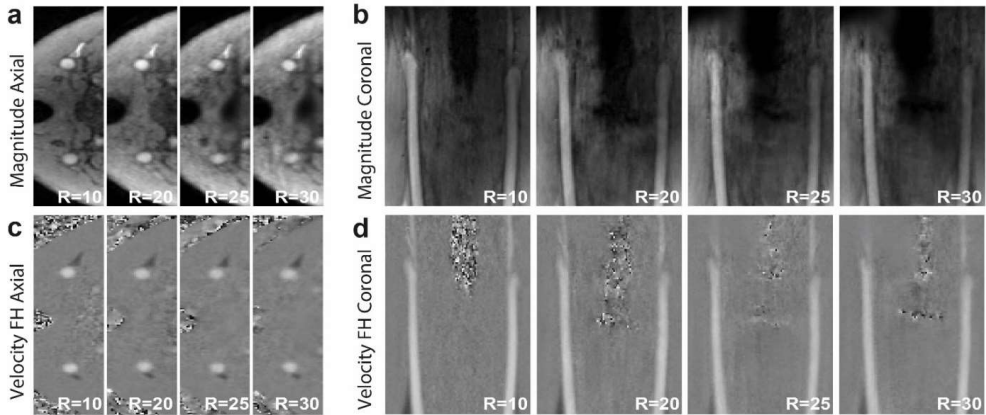


**Figure 3.8** Axial (a) and coronal (b) views of one representative *in vivo* scan at acceleration factors  $R = 10$ – $30$ . For both views velocity images in the range of  $-150$  to  $150$  cm/s are shown (c, d).

A number of 4D flow CMR studies have reported on the accuracy of acceleration techniques. Cheng *et al.* demonstrated 4D flow in pediatric congenital heart disease patients, using a prospective pseudo-spiral sampling strategy with total variation CS reconstruction (VDRad). Effective acceleration factors ranged from  $R = 15$ – $27$ . This resulted in clinically acceptable image quality, as rated by a radiologist. However, no quantitative comparisons with 2D flow were available. 4D flow CMR scans were compared against a CS reconstruction using spatial wavelets after (temporally constant) Poisson disk sampling [17], which had been demonstrated to lead to 12% flow rate underestimation in comparison to 2D flow at  $R = 5$  in a previous study [34]. Valvano *et al.* prospectively accelerated 4D flow CMR in the aorta using a low-rank+sparse reconstruction algorithm. Errors in the aortic peak flow rate were reported in comparison to a standard SENSE = 2 acquisition (segmented k-space factor = 3). The peak flow rate was underestimated at an acceleration factor of  $R = 8$  by  $2.5 \pm 4.6\%$  in the ascending and by  $3.6 \pm 8.4\%$  in the descending aorta [33]. Knobloch *et al.* [11] investigated the effects of k-t PCA acceleration on 4D flow CMR in the carotids (spatial resolution  $1.2 \times 1.2 \times 1.2$  mm<sup>3</sup> vs.  $0.8 \times 0.8 \times 0.8$  mm<sup>3</sup> in our study). Errors in peak flow rate were smaller than  $4.9 \pm 7\%$ . However, the accelerated scans resulted from retrospective undersampling of a 4D flow CMR reference (75% Fourier sampling in  $k_y$  and  $k_z$ , 23 min scan time), which likely will result in a better agreement between accelerated and reference scans than would be obtained for true prospective acceleration [11]. In Giese *et al.*, prospectively k-t PCA accelerated aortic 4D flow CMR was compared to 2D flow [12]. The authors introduced an error metric  $E_{SV}$  for the stroke volume (SV) to compare 4D flow with 2D flow CMR (equation 2 from [12]) and found  $E_{SV} = 2.5 \pm 8.4$  ml ( $5.6 \pm 14.9\%$ ) for  $R = 8$  in the aorta. Applying this metric to our *in vivo* carotid artery measurements, we find  $E_{SV} = 0.2 \pm 0.7$  ml ( $1.8 \pm 10.9\%$ ) for  $R = 10$ ,  $E_{SV} = 0.3 \pm 0.5$  ml ( $4.6 \pm 7.0\%$ ) for  $R = 20$ ,  $E_{SV} = 0.4 \pm 0.4$  ml ( $5.7 \pm 6.7\%$ ) for  $R = 25$  and  $E_{SV} = 0.4 \pm 0.5$  ml ( $5.6 \pm 7.8\%$ ) for  $R = 30$  in comparison to 2D flow. This time-averaged error metric can therefore partially obscure peak velocity differences. Taken together, the above studies show that there is no consensus on how to assess flow errors for accelerated 4D flow CMR protocols. The numbers will depend on whether the scans were retrospectively or prospectively undersampled and the choice of reference scan, being another accelerated 4D flow technique or 2D flow CMR.



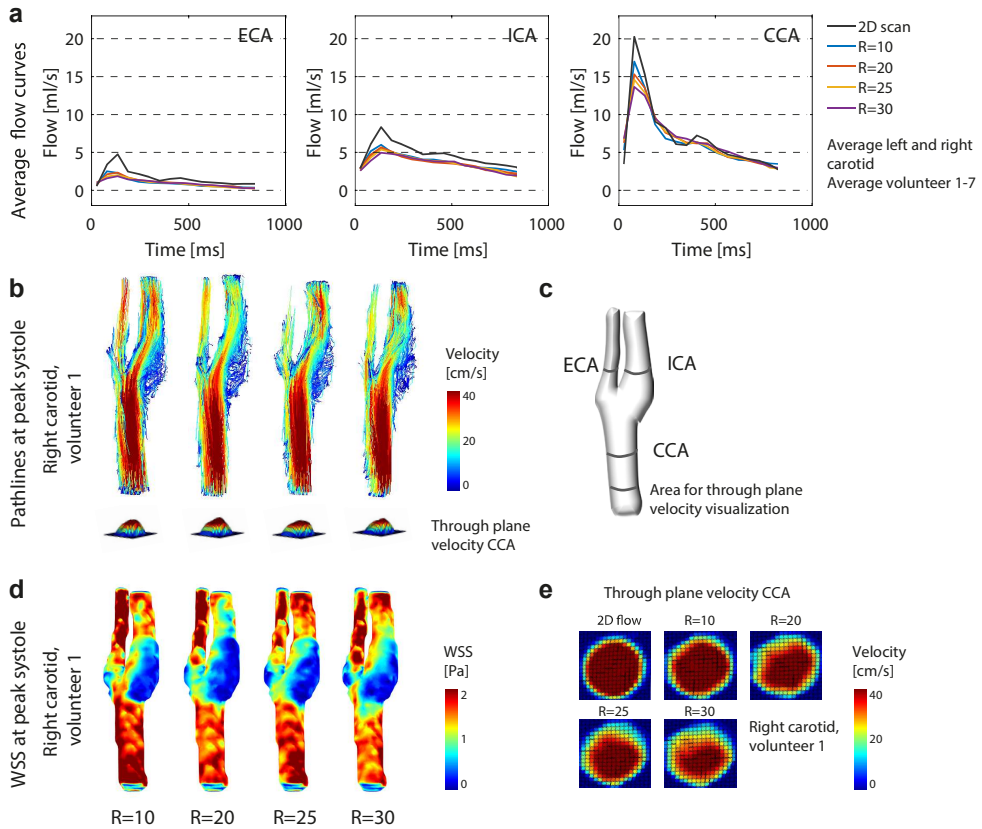


**Figure 3.9** Flow curves in the (a) ECA, ICA and CCA, averaged for left and right carotid, plotted for all acceleration factors. The flow curves are averaged over all 7 subjects and are compared to a fully sampled 2D flow CMR scan at the same position (also averaged over all subjects). (b) Pathlines for all acceleration factors in the right carotid artery of one exemplary subject during peak systole. (c) Regions of interest (ROIs) used in (a). (d) WSS for all acceleration factors in the right carotid of one exemplary subject during peak systole. (e) Through plane velocities in the right CCA of one exemplary subject during peak systole.

In our study we found an underestimation of the *in vivo* carotid peak systolic flow rate for high acceleration factors in the CCA (-24.4% for R = 20 and -32.6% for R = 30) when compared to a 2D phase-contrast reference scan. This underestimation was less in phantoms, in which we found only -1.7% peak flow rate underestimation (R=20) in comparison to the 2D flow scan. The difference between *in vivo* and phantom scans might be explained by smoother flow profiles in the phantom, which might lead to better results when using a total variation operator in the CS reconstruction algorithm. The phantom curves, although very consistent between scans, showed slight variations due to partial volume effects with the tube wall, which had a noisy velocity due to lack of signal (Figure 3.4). Differences between 2D flow and 4D flow CMR might be affected by higher SNR in 2D flow scans. Also, the high contrast of blood vessels in the 2D flow scan, created by inflow enhancement at high flip angles, might result in different partial volume effects and phase offsets than in 4D flow CMR [31,35]. This might also explain deviations in smaller vessels like the ICA and ECA. Within the set of accelerated 4D flow CMR scans, volumetric velocity differences between R = 10 and higher accelerated scans were

much more acceptable (8.4% for  $R = 20$  and 14.0% for  $R = 30$ ) than the results from the flow analysis. For peak systolic WSS, a similar behavior was observed. As the overall trend was to underestimate WSS at very high acceleration factors (similar to velocity), this could conceal small changes in WSS patterns that might be important for disease characterization. Overall we can conclude that, although hemodynamic parameters seem systematically underestimated if we consider the 2D phase contrast scan as a gold standard, the accuracy of WSS and velocity values with decreasing scan time in 4D flow is maintained within acceptable limits for  $R = 20$ . This can also be appreciated in the pathline movies, which remain visually of good quality up to the highest acceleration. Therefore, also clinical 4D flow CMR scans with acceleration factors of up to  $R = 20$  can be used. However, depending on the purpose of the clinical examination, lower (for accurate peak velocity estimation) or higher (for mean flow, stroke volume or streamline visualization) acceleration factors could be considered. Moreover, regional differences in hemodynamic parameters are consistent for all accelerations, as for example shown in **Figure 2.9d** (e.g. low WSS in the carotid bulb vs. high WSS in the rest of the vessel). More advanced pulsatile flow phantoms of the (diseased) carotid artery, with a sharp, systolic peak flow will help to investigate on the effects of 4D flow CMR acceleration in carotid pathology in the future.

Using a repeated scan protocol *in vivo* (repeated 2 times for  $R = 10, 20, 25$  and  $30$ ) and in the phantom (repeated 3 times for  $R = 10, 15, 20, 25$  and  $30$ ) as summarized in **Supplementary Figure 3.13** we could demonstrate, that there was almost no deviation between repeated scans in both cases. The SD of paired differences (scan-rescan) per time frame was *in vivo* SD = 0.6, 0.6, 0.6, 0.6 ml/s and in the phantom SD = 0.4, 0.4, 0.4, 0.5 and 0.6 ml/s, for each acceleration factor respectively.

The comparison between *in vivo* and phantom experiments has some limitations. Although flow rate and mean velocities were similar, maximum velocities of 120 cm/s were achieved in the phantom in comparison to maximum velocities of 80 cm/s *in vivo* (see **Supplementary Figure 3.14b-c**). Because excessively long scan times are an issue *in vivo*, it was not possible to acquire 4D flow CMR data with low or no acceleration and consequently an *in vivo* 4D flow CMR dataset of for example  $R = 2$  was not available. Another limitation to the study is that only a low number of  $N = 7$  participants were included.

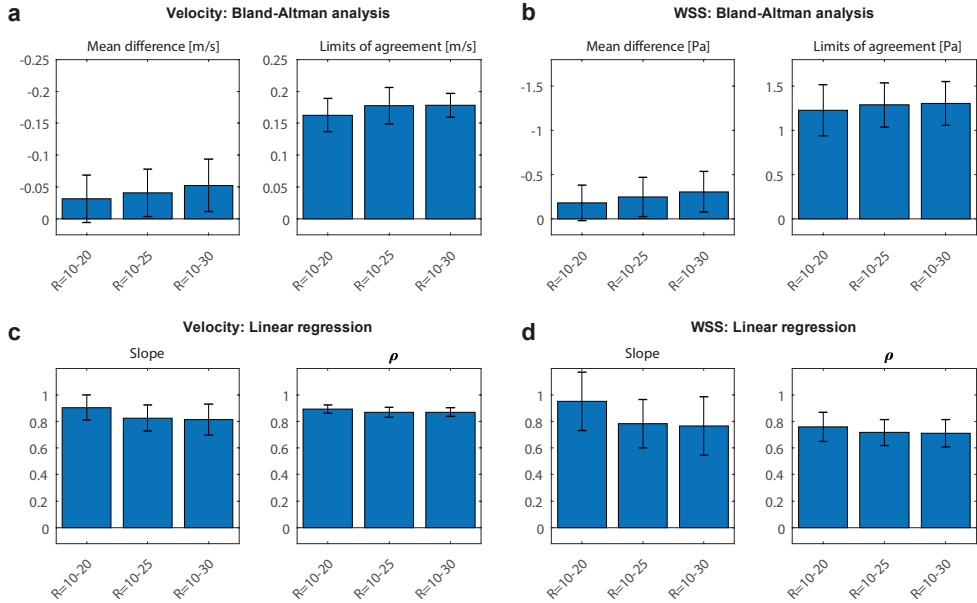


**Figure 3.10** (a) Comparison of peak systolic velocities at R = 10 with acceleration factors R = 20-30 using Bland-Altman analysis (mean differences and limits of agreement (LOA)). The averaged values of all subjects and both carotids are shown. The error bars indicate the standard deviation between the different scans. (b) The same comparison as in (a) for WSS values at peak systole. (c) Comparison of peak systolic velocities at R = 10 with all higher acceleration factors R = 20-30 using orthogonal regression (slope of the regression line and Pearson correlation coefficient  $\rho$ ). (d) The same comparison as in (c) for WSS values at peak systole.

The here reported acceleration factors are calculated before the data acquisition in reference to the scan time of a fully sampled scan acquired with the same acquisition strategy. Effective acceleration factors can be calculated retrospectively to the scan from the ratio of the number of k-lines in a fully sampled k-space versus the actually sampled k-lines, *i.e.*  $N_{\text{undersampled}}$  in equation [2] can vary slightly retrospectively to the scan. For *in vivo* scans  $R_{\text{effective}} (\pm \text{SD})$  was on average  $R = 12.2 \pm 0.8$ ,  $R = 22.6 \pm 0.9$ ,  $R = 27.9 \pm 0.9$ , and  $R = 32.9 \pm 0.9$ , for scans with target acceleration  $R = 10$ ,  $R = 20$ ,  $R = 25$ , and  $R = 30$ , respectively. The effective acceleration factor would also vary slightly with the heart rate of each subject. This behavior is however similar in fully sampled scans, which are only optimal when the number of reconstructed cardiac frames times  $4 \times \text{TR}$  (4 flow encoding steps used) approximately matches the average acquired heart cycle length. If the number of reconstructed cardiac frames is higher, undersampling would be the consequence, which in practice is compensated for by a retrospective interpolation. If the number of reconstructed cardiac frames is lower, oversampling occurs, which results in averaging and higher SNR, but which also leads to a lower temporal resolution. Reporting effective acceleration factors and their variations is similar to variations in regular cardiac triggered scans and therefore not further discussed in this paper.

Potential other applications for the here presented methodology are cine CMR scans and 4D flow CMR scans in other anatomical regions, such as the circle of Willis, the heart, the aorta and for assessing venous flow return. Other, cutting edge algorithms, such as low-rank [33] reconstruction, could be

integrated in the current reconstruction to push the acceleration factors even further or mitigate the spatiotemporal blurring. The pseudo-spiral sampling strategy can be combined with breathing navigators or self-gating, which allows for sorting the data in respiratory bins [21,36].

### **3.6 Conclusion**

We achieved highly accelerated 4D flow CMR of the carotid arteries using pseudo-spiral Cartesian undersampling and a CS reconstruction. At an acceleration factor of  $R = 20$  the underestimation of peak velocity and peak WSS was acceptable ( $< 10\%$ ) in comparison to an  $R = 10$  accelerated 4D flow CMR reference scan. Peak flow rates were underestimated in comparison with 2D flow CMR and decreased systematically with higher acceleration factors. However, even at an acceleration factor of  $R = 30$ , the highly CS accelerated 4D flow CMR scans allowed reconstructions of the 4D velocity field and velocity pathlines, at only 2:30 min scan time.

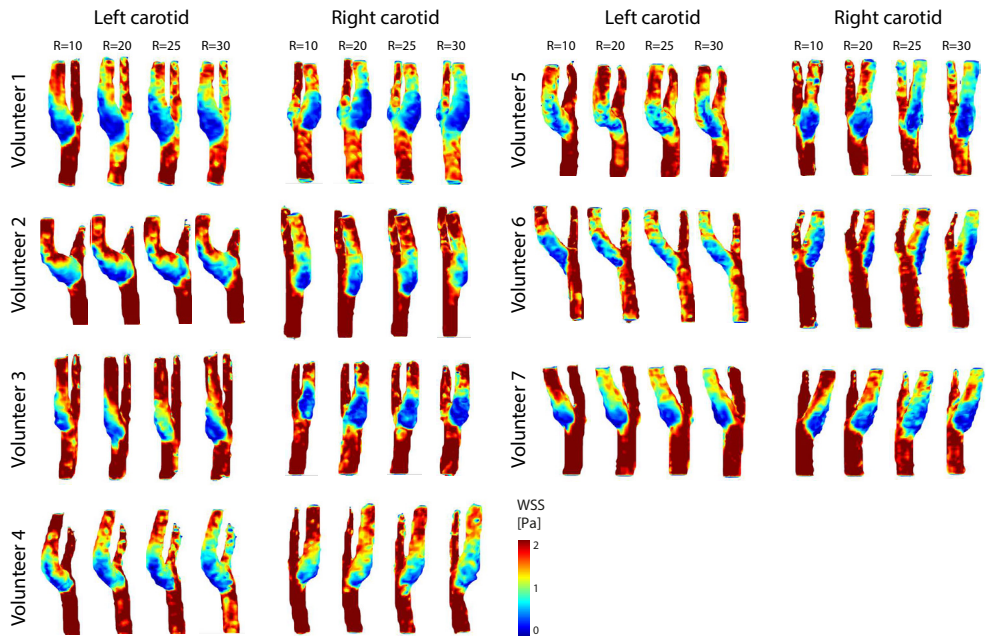
### **3.7 Acknowledgement**

We thank Maarten Versluis (Philips), Gérard Crelier (Gyrotools) and Martin Bührer (Gyrotools) for their support.

### 3.8 Supplementary material

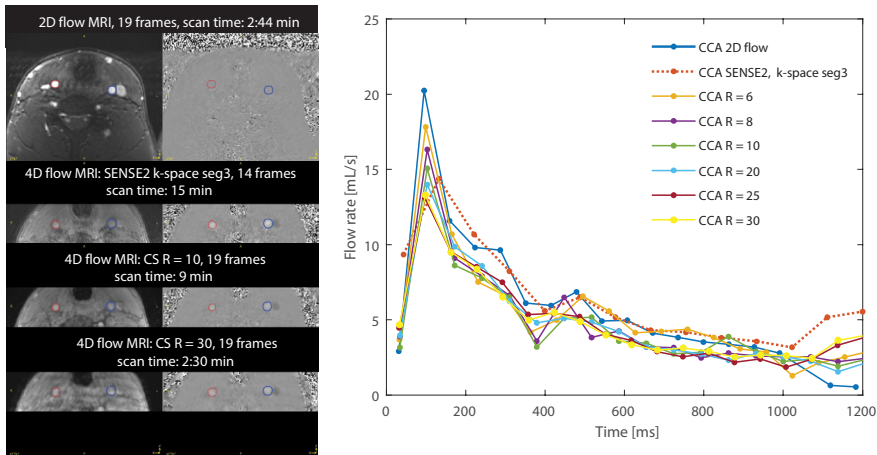
**Supplementary Video 3.1:** Pathline movies of the phantom carotid artery for acceleration factors  $R=2$ -20 can be found under [https://static-content.springer.com/esm/art%3A10.1186%2Fs12968-019-0582-z/MediaObjects/12968\\_2019\\_582\\_MOESM1\\_ESM.gif](https://static-content.springer.com/esm/art%3A10.1186%2Fs12968-019-0582-z/MediaObjects/12968_2019_582_MOESM1_ESM.gif)

**Supplementary Video 3.2:** Pathline movies of the left carotid artery of a healthy volunteer for acceleration factors  $R=10$ ,  $R=20$ ,  $R=25$ , and  $R=30$  can be found under [https://static-content.springer.com/esm/art%3A10.1186%2Fs12968-019-0582-z/MediaObjects/12968\\_2019\\_582\\_MOESM2\\_ESM.gif](https://static-content.springer.com/esm/art%3A10.1186%2Fs12968-019-0582-z/MediaObjects/12968_2019_582_MOESM2_ESM.gif)

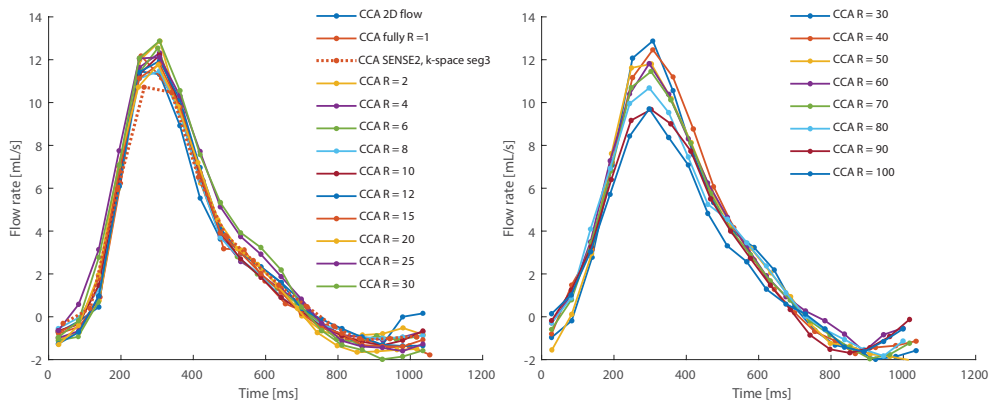


**Supplementary Figure 3.11** WSS in the left and right carotid arteries of all seven *in vivo* experiments. An individual segmentation of the carotid artery was done per volunteer and acceleration factor.

**a** *In vivo* 4D flow MRI for acceleration factors between  $R=6$  and  $R=30$ :  
(longer scan times than 30 min are not feasible)

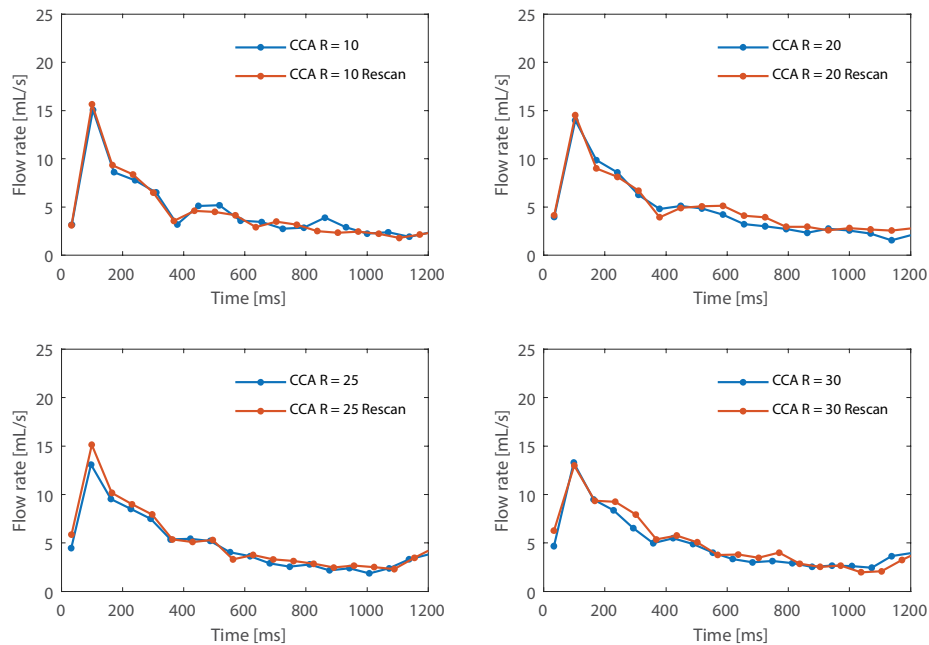


**b** 4D flow MRI in a phantom for acceleration factors between  $R = 0$  and  $R = 100$ :  
(scan times of a fully sampled scan up to 1h 32 min are feasible)

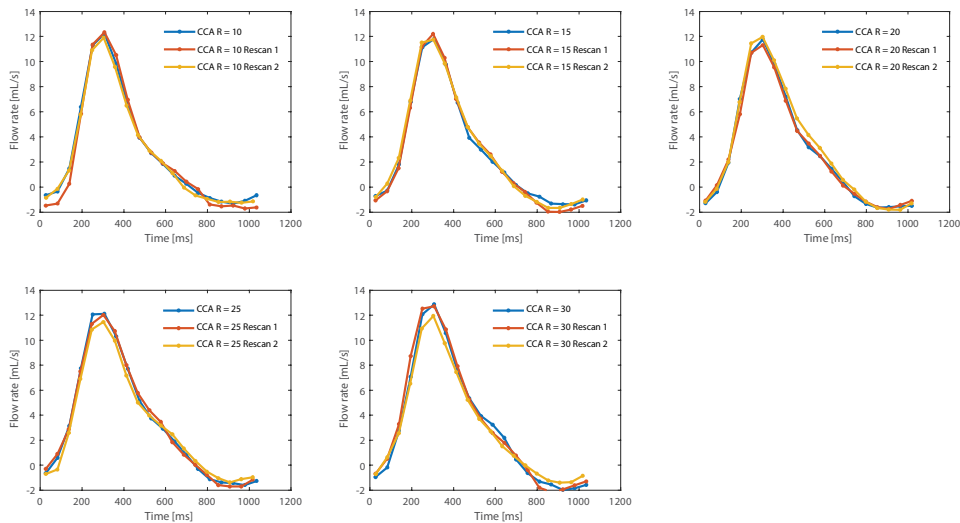


**Supplementary Figure 3.12** (a) Magnitude images and flow curves of an *in vivo* scan of  $N = 1$  volunteer at CS acceleration factors  $R = 6$  to  $R = 30$ , following the same scan protocol as described in the Methods section. Next to the CS acceleration a 2D reference scan and a 4D flow reference scan (SENSE = 2 and segmented k-space factor = 2) are shown. (b) Flow curves of a phantom scan for CS acceleration factors of  $R = 1$  to  $R = 100$ . Next to the CS acceleration a 2D reference scan and a 4D flow reference scan (SENSE = 2 and segmented k-space factor = 2) are shown.

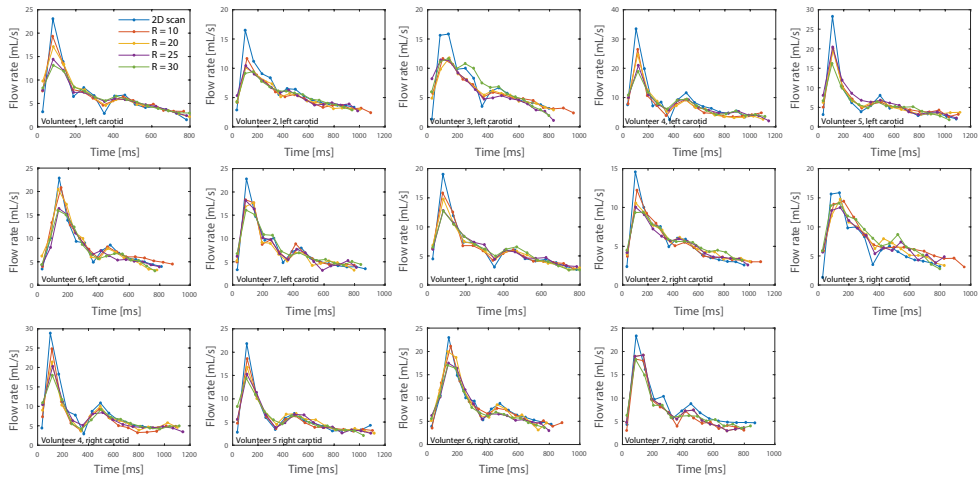
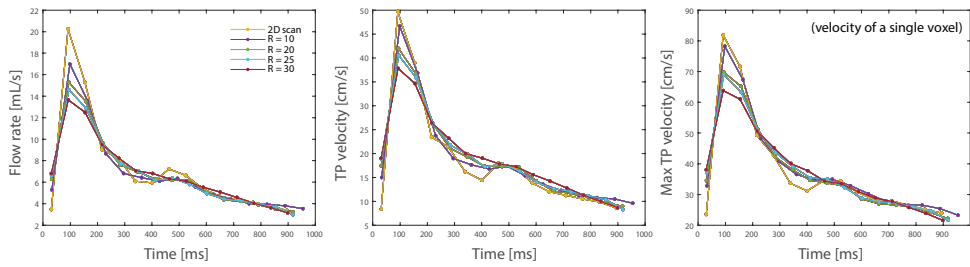
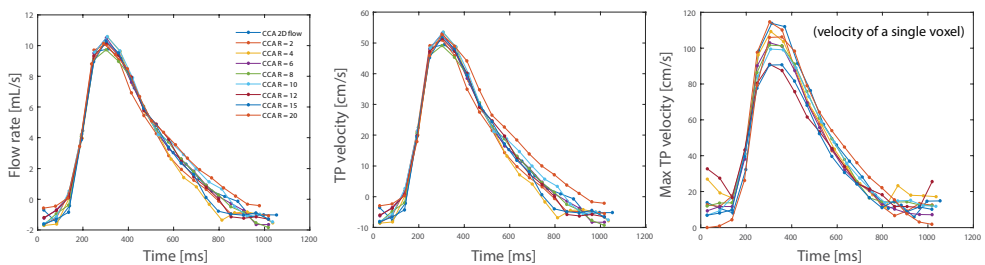
**a** *In vivo* 4D flow MRI Rescans for R = 10, R = 20, R = 25 and R = 30  
(for 2D flow comparison consult Supplemental Figure 2a)



**b** 4D flow MRI Phantom Rescans for R = 10, R = 15, R = 20, R = 25 and R = 30:  
(for 2D flow comparison consult Supplemental Figure 2b)



**Supplementary Figure 3.13 (a)** Flow curves of an *in vivo* scan-rescan setting with 1 rescan for acceleration factors R = 10, 20, 25, 30. **(b)** Flow curves of a phantom scan-rescan setting with 2 rescans for acceleration factors R = 10, 15, 20, 25, 30..

**a** *In vivo* 4D flow MRI: flow curves for all volunteers and both carotids**b** *In vivo* 4D flow MRI: flow rate, through plane (TP) velocity and maximum TP velocity**c** Phantom 4D flow MRI: flow rate, TP velocity and maximum TP velocity

**Supplementary Figure 3.14** (a) Flow curves in the left and right carotid arteries of all seven *in vivo* experiments. (b) *In vivo*: Volunteer-averaged flow rate, through-plane velocity and maximum through-plane velocity for acceleration factors of  $R = 10$ –30. (c) Phantom: Flow rate, through-plane velocity and maximum through-plane velocity for acceleration factors of  $R = 2$ –20.



**Supplemental Table 3.1** Flow rate differences of all accelerated scans in comparison to the 2D reference scan in the phantom experiment.**Phantom: Differences between  
2D flow and R = 2/4/6/8/10/12/15/20**

Peak flow rate CCA	Difference [ml/s] (%*)
2D scan vs. R = 2	-0.4 (-3.4)
2D scan vs. R = 4	-0.1 (-0.6)
2D scan vs. R = 6	0.4 (4.3)
2D scan vs. R = 8	0.4 (3.6)
2D scan vs. R = 10	-0.4 (-4.1)
2D scan vs. R = 12	0.5 (4.4)
2D scan vs. R = 15	0.1 (0.6)
2D scan vs. R = 20	0.2 (1.7)

\* Relative to the 2D scan

**Supplemental Table 3.2** Statistical results from the Bland-Altman analysis and orthogonal regression for WSS and velocity in the phantom experiment.**Phantom: Differences between R = 2 and R = 4/6/8/10/12/15/20**

	Bland-Altman		Orthogonal regression		Correlation
	Mean difference [Pa] (%*)	LOA [Pa]	Slope	Intercept [Pa]	p
<b>WSS</b>					
R = 2 vs. R = 4	0.03 (1.29)	0.79	1.01	0.02	0.94
R = 2 vs. R = 6	-0.06 (-2.29)	0.93	0.97	0.01	0.91
R = 2 vs. R = 8	0.14 (5.15)	1.12	1.04	0.02	0.87
R = 2 vs. R = 10	-0.02 (-0.71)	1.28	1.03	-0.08	0.83
R = 2 vs. R = 12	0.05 (2.03)	1.34	1.04	-0.04	0.82
R = 2 vs. R = 15	0.06 (2.46)	1.33	1.08	-0.16	0.83
R = 2 vs. R = 20	0.14 (5.31)	1.42	1.11	-0.13	0.81
<b>Velocity</b>					
R = 2 vs. R = 4	0.01 (2.00)	0.12	0.99	0.01	0.95
R = 2 vs. R = 6	-0.01 (-1.47)	0.14	0.94	0.02	0.94
R = 2 vs. R = 8	0.01 (2.20)	0.17	0.90	0.06	0.90
R = 2 vs. R = 10	-0.01 (-2.39)	0.19	0.87	0.05	0.89
R = 2 vs. R = 12	-0.01 (-1.31)	0.21	0.83	0.07	0.86
R = 2 vs. R = 15	-0.01 (-2.39)	0.24	0.80	0.08	0.81
R = 2 vs. R = 20	0.00 (-0.29)	0.24	0.78	0.10	0.80

\* Relative to R = 2

**Supplemental Table 3.3** Flow rate and velocity differences of all accelerated scans in comparison to the 2D reference scan as an average of all *in vivo* experiments.

***In vivo*: Peak flow rate and velocity differences between 2D flow and R = 10/20/25/30**  
(averaged left and right carotid, averaged volunteers)

Peak flow rate CCA	Difference $\pm$ SD* [ml/s] (%**)	Difference $\pm$ SD* [m/s] (%**)
2D scan vs. R = 10	-3.3 $\pm$ 2.2 (-16.1 $\pm$ 10.6)	-0.03 $\pm$ 0.07 (-6.2 $\pm$ 18.4)
2D scan vs. R = 20	-5.0 $\pm$ 2.1 (-24.4 $\pm$ 10.4)	-0.08 $\pm$ 0.04 (-15.6 $\pm$ 17.4)
2D scan vs. R = 25	-5.7 $\pm$ 2.4 (-28.0 $\pm$ 12.0)	-0.09 $\pm$ 0.05 (-18.5 $\pm$ 24.3)
2D scan vs. R = 30	-6.6 $\pm$ 3.4 (-32.6 $\pm$ 16.7)	-0.12 $\pm$ 0.06 (-23.9 $\pm$ 29.1)
* Difference for all volunteers $\pm$ SD for volunteer values,		
** Relative to the 2D scan		

**Supplemental Table 3.4** Statistical results from the Bland-Altman analysis and orthogonal regression for WSS and velocity as an average of all *in vivo* experiments.

***In vivo*: Differences between R = 10 and R = 20/25/30**  
(averaged left and right carotid, averaged volunteers)

	Bland-Altman		Orthogonal regression	Correlation
	Mean difference $\pm$ SD* [Pa] (%**)	LOA $\pm$ SD* [Pa]	Slope $\pm$ SD*	P $\pm$ SD*
<b>WSS</b>				
R = 10 vs. R = 20	-0.18 $\pm$ 0.21 (-9.91 $\pm$ 10.93)	1.23 $\pm$ 0.29	0.95 $\pm$ 0.22	0.76 $\pm$ 0.11
R = 10 vs. R = 25	-0.25 $\pm$ 0.22 (-13.44 $\pm$ 11.77)	1.29 $\pm$ 0.25	0.78 $\pm$ 0.18	0.72 $\pm$ 0.10
R = 10 vs. R = 30	-0.31 $\pm$ 0.23 (-16.86 $\pm$ 12.16)	1.30 $\pm$ 0.25	0.77 $\pm$ 0.22	0.71 $\pm$ 0.10
<b>Velocity</b>	[m/s] (%**)	[m/s]		
R = 10 vs. R = 20	-0.03 $\pm$ 0.04 (-8.35 $\pm$ 9.94)	0.16 $\pm$ 0.0	0.90 $\pm$ 0.10	0.89 $\pm$ 0.03
R = 10 vs. R = 25	-0.04 $\pm$ 0.04 (-10.79 $\pm$ 9.64)	0.18 $\pm$ 0.0	0.83 $\pm$ 0.10	0.87 $\pm$ 0.04
R = 10 vs. R = 30	-0.05 $\pm$ 0.04 (-13.97 $\pm$ 10.76)	0.18 $\pm$ 0.0	0.81 $\pm$ 0.12	0.87 $\pm$ 0.03

### 3.9 Bibliography

1. Markl M, Frydrychowicz A, Kozerke S, Hope M, Wieben O. 4D flow MRI. *J Magn Reson Imaging*. 2012;36:1015–36.
2. World Health Organization WHO. Global status report on noncommunicable diseases. 2014.
3. van Popele NM, Grobbee DE, Bots ML, Asmar R, Topouchian J, Reneman RS, *et al*. Association between arterial stiffness and atherosclerosis. *Stroke*. 2001;32:454–61.
4. Lusis AJ. Atherosclerosis. *Nature*. 2000;407:233–41.
5. Markl M, Wallis W, Strecker C, Gladstone BP, Vach W, Harloff A. Analysis of pulse wave velocity in the thoracic aorta by flow-sensitive four-dimensional MRI: Reproducibility and correlation with characteristics in patients with aortic atherosclerosis. *J. Magn. Reson. Imaging*. 2012. p. 1162–8.
6. van Ooij P, Potters W V, Nederveen AJ, Allen BD, Collins J, Carr J, *et al*. A methodology to detect abnormal relative wall shear stress on the full surface of the thoracic aorta using four-dimensional flow MRI. *Magn Reson Med*. 2015;1227:1216–27.
7. Potters W V, van Ooij P, Marquering H, van Bavel E, Nederveen AJ. Volumetric arterial wall shear stress calculation based on cine phase contrast MRI. *J Magn Reson Imaging*. 2015;41:505–16.
8. van Ooij P, Potters W V, Nederveen AJ, Collins JD, Carr JC, Malaisrie S, *et al*. Thoracic aortic wall shear stress atlases in patients with bicuspid aortic valves. *J Cardiovasc Magn Reson*. 2014;16:P161.
9. Chiu J-J, Chien S. Effects of disturbed flow on vascular endothelium: pathophysiological basis and clinical perspectives. *Natl Inst Heal*. 2011;91.
10. van Ooij P, Cibis M, Rowland E, Vernooij M, van der Lugt A, Weinberg P, *et al*. Spatial correlations between MRI-derived wall shear stress and vessel wall thickness in the carotid bifurcation. *Eur Radiol Exp*. 2018;
11. Knobloch V, Boesiger P, Kozerke S. Sparsity transform k-t principal component analysis for accelerating cine three-dimensional flow measurements. *Magn Reson Med*. 2013;70:53–63.
12. Giese D, Wong J, Greil GF, Buehrer M, Schaeffter T, Kozerke S. Towards highly accelerated Cartesian time-resolved 3D flow cardiovascular magnetic resonance in the clinical setting. *J Cardiovasc Magn Reson*. 2014;16:42.
13. Pagé G, Bettoni J, Virginie A, Olivier S. Influence of principal component analysis acceleration factor on velocity measurement in 2D and 4D PC-MRI. *Magn Reson Mater Physics, Biol Med*. 2018;469–81.
14. Gu T, Korosec FR, Block WF, Fain SB, Turk Q, Lum D, *et al*. PC VIPR: A high-speed 3D phase-contrast method for flow quantification and high-resolution angiography. *Am J Neuroradiol*. 2005;26:743–9.
15. Bastkowski R, Weiss K, Maintz D, Giese D. Self-gated golden-angle spiral 4D flow MRI. *Magn Reson Med*. 2018;80:904–13.
16. Zucker EJ, Cheng JY, Haldipur A, Carl M, Vasanawala SS. Free-breathing pediatric chest MRI: Performance of self-navigated golden-angle ordered conical ultrashort echo time acquisition. *J Magn Reson Imaging*. 2018;47:200–9.
17. Cheng JY, Hanneman K, Zhang T, Alley MT, Lai P, Tamir JJ, *et al*. Comprehensive motion-compensated highly accelerated 4D Flow MRI with ferumoxytol enhancement for pediatric congenital heart disease. *J Magn Reson Imaging*. 2015;
18. Tsao J, Boesiger P, Pruessmann KP. k-t BLAST and k-t SENSE: dynamic MRI with high frame rate exploiting spatiotemporal correlations. *Magn Reson Med*. 2003;50:1031–42.
19. Westenberg JJM, Roes SD, Ajmone Marsan N, Binnendijk NMJ, Doornbos J, Bax JJ, *et al*. Mitral valve and tricuspid valve blood flow: accurate quantification with 3D velocity-encoded MR imaging with retrospective valve tracking. *Radiology*. 2008;249:792–800.
20. Liu J, Saloner D. Accelerated MRI with CIRCular Cartesian UnderSampling (CIRCUS): a variable density

- Cartesian sampling strategy for compressed sensing and parallel imaging. *Quant Imaging Med Surg*. 2014;4:57–67.
21. Prieto C, Doneva M, Usman M, Henningsson M, Greil G, Schaeffter T, *et al*. Highly efficient respiratory motion compensated free-breathing coronary MRA using golden-step Cartesian acquisition. *J Magn Reson Imaging*. 2015;41:738–46.
  22. Han F, Zhou Z, Han E, Gao Y, Nguyen KL, Finn JP, *et al*. Self-gated 4D multiphase, steady-state imaging with contrast enhancement (MUSIC) using rotating cartesian K-space (ROCK): Validation in children with congenital heart disease. *Magn Reson Med*. 2017;78:472–83.
  23. Zhu Y, Guo Y, Lingala SG, Leben RM, Law M, Nayak KS. MRI, GOCART: Golden-angle Cartesian randomized time-resolved 3D. *Magn Reson Imaging*. 2019;34:940–50.
  24. Peper E, Gottwald L, Zhang Q, Coolen B, van Ooij P, Strijkers G, *et al*. 30 times accelerated 4D flow MRI in the carotids using a pseudo spiral Cartesian acquisition and a total variation constrained compressed sensing reconstruction. *Proc Intl Soc Mag Reson Med* 26. 2018. p. 0012.
  25. Gottwald L, Peper E, Zhang Q, Coolen B, Strijkers G, Planken R, *et al*. Pseudo spiral compressed sensing for aortic 4D Flow MRI: a comparison with k-t principal component analysis. *Proc Intl Soc Mag Reson Med* 26. 2018. p. 3448.
  26. Peper ES, Strijkers GJ, Gazzola K, Potters W V, Motaal AG, Luirink IK, *et al*. Regional assessment of carotid artery pulse wave velocity using compressed sensing accelerated high temporal resolution 2D CINE phase contrast cardiovascular magnetic resonance. *J Cardiovasc Magn Reson*. 2018;20:1–12.
  27. Uecker M, Ong F, Tamir JI, Bahri D, Virtue P, Cheng JY, *et al*. Berkeley Advanced Reconstruction Toolbox. *Proc Intl Soc Mag Reson Med*. 2015. p. 2486.
  28. Johnson KM, Markl M. Improved SNR in phase contrast velocimetry with 5-Point balanced flow encoding. *Magn Reson Imaging*. 2010;63:349–55.
  29. Potters W V, Marquering HA, VanBavel E, Nederveen AJ. Measuring wall shear stress using velocity-encoded MRI. *Curr Cardiovasc Imaging Rep*. 2014;7:9257.
  30. Ooij P Van, Powell AL, Potters W V, Carr JC, Markl M, Barker AJ. Reproducibility and interobserver variability of systolic blood flow velocity and 3D wall shear stress derived from 4D flow MRI in the healthy aorta. 2015;
  31. Tang C, Blatter DD, Parker DL. Accuracy of phase-contrast flow measurements in the presence of partial-volume effects. *J Magn Reson Imaging*. 1993;3:377–85.
  32. Dyverfeldt P, Bissell M, Barker AJ, Bolger AF, Carlhäll CJ, Ebberts T, *et al*. 4D flow cardiovascular magnetic resonance consensus statement. *J Cardiovasc Magn Reson*. 2015;17:1–19.
  33. Valvano G, Martini N, Huber A, Santelli C, Binter C, Chiappino D, *et al*. Accelerating 4D Flow MRI by exploiting low-rank matrix structure and hadamard sparsity. *Magn Reson Med*. 2017;78:1330–41.
  34. Hsiao A, Lustig M, Alley MT, Murphy M, Chan FP, Herfkens RJ, *et al*. Rapid pediatric cardiac assessment of flow and ventricular volume with compressed sensing parallel imaging volumetric cine phase-contrast MRI. *Am J Roentgenol*. 2012;198:1–20.
  35. Greil G, Geva T, Maier SE, Powell AJ. Effect of acquisition parameters on the accuracy of velocity encoded cine magnetic resonance imaging blood flow measurements. 2002;54:47–54.
  36. Bastkowski R, Weiss K, Maintz D, Giese D. Self-gated golden-angle spiral 4D flow MRI. *Magn Reson Med*. 2018;00:1–10. A

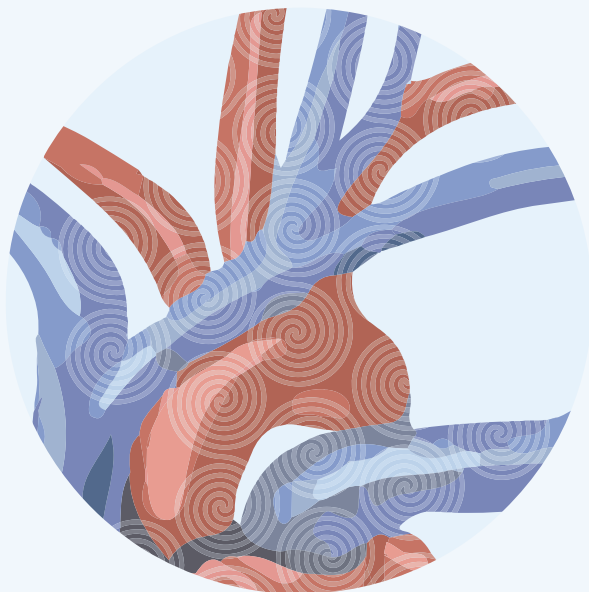


# CHAPTER 4

Pseudo-spiral sampling and  
compressed sensing reconstruction provides  
flexibility of temporal resolution in  
accelerated aortic 4D flow MRI:  
A comparison with  
k-t principal component analysis

Lukas M. Gottwald and Eva S. Peper,  
Qinwei Zhang,  
Bram F. Coolen,  
Gustav J Strijkers,  
Aart J. Nederveen  
and Pim van Ooij

NMR in Biomedicine. 2020



## 4.1 Abstract

**Background:** Time-resolved three-dimensional phase contrast MRI (4D flow) of aortic blood flow requires acceleration to reduce scan time. Two established techniques for highly accelerated 4D flow MRI are k-t principal component analysis (k-t PCA) and compressed sensing (CS), which employ either regular or random k-space undersampling. The goal of this study was to gain insights into the quantitative differences between k-t PCA- and CS-derived aortic blood flow, especially for high temporal resolution CS 4D flow MR.

**Methods:** The scan protocol consisted of both k-t PCA and CS accelerated 4D flow MRI, as well as a 2D flow reference scan through the ascending aorta acquired in 15 subjects. 4D flow scans were accelerated with factor  $R = 8$ . For CS accelerated scans, we used a pseudo-spiral Cartesian sampling scheme, which could additionally be reconstructed at higher temporal resolution, resulting in  $R = 13$ . 4D flow data were compared with the 2D flow scan in terms of flow, peak flow and stroke volume. A 3D peak systolic voxel-wise velocity and wall shear stress (WSS) comparison between k-t PCA and CS 4D flow was also performed.

**Results:** The mean difference in flow/peak flow/stroke volume between the 2D flow scan and the 4D flow CS with  $R = 8$  and  $R = 13$  was 4.2%/9.1%/3.0% and 5.3%/7.1%/1.9%, respectively, whereas for k-t PCA with  $R = 8$  the difference was 9.7%/25.8%/10.4%. In the voxel-by-voxel 4D flow comparison we found 13.6% and 3.5% lower velocity and WSS values of k-t PCA compared with CS with  $R = 8$ , and 15.9% and 5.5% lower velocity and WSS values of k-t PCA compared with CS with  $R = 13$ .

**Conclusion:** Pseudo-spiral accelerated 4D flow acquisitions in combination with CS reconstruction provides a flexible choice of temporal resolution. We showed that our proposed strategy achieves better agreement in flow values with 2D reference scans compared with using k-t PCA accelerated acquisitions.

## 4.2 Introduction

Cardiovascular phase contrast magnetic resonance imaging (PC-MRI) is a well-validated method to quantify pulsatile blood flow in the human aorta [1]. Time-resolved three-dimensional PC MRI scans (4D flow MRI) are used to observe velocity or blood flow patterns and identify possible abnormalities such as flow jets or regurgitation [2]. Moreover, advanced hemodynamic biomarkers can be derived, such as pulse wave velocity and wall-shear stress (WSS). These biomarkers have shown to be valuable tools for risk assessment in aortic aneurysms, aortic plaques and stroke [3,4].

Unfortunately, 4D flow MRI has the inherent problem of requiring a long scan time. Depending on many factors, such as the field of view (FOV), spatial and temporal resolution, and also the breathing pattern and heart rate of the patient, the acquisition time for a 4D flow MRI scan can amount to 25 minutes or more [1,5]. Therefore, acquisition acceleration to reduce scan times to a clinically acceptable duration is imperative.

A commonly known technique to accelerate 4D flow MRI acquisitions is k-t PCA [6], which exploits the time dependency in the 4D flow MRI data for acceleration. K-t PCA allows for an 8-fold acceleration and has shown great potential for clinical application in congenital heart disease [7,8]. In this technique, prospective ECG gating is combined with a highly ordered undersampling scheme in k-t space at a predefined number of cardiac frames, which are reconstructed using principle component analysis (PCA).

Another promising method to speed up 4D flow MRI acquisitions is incoherent undersampling and compressed sensing (CS) reconstruction [9,10]. A flexible approach has been the use of pseudo-radial or pseudo-spiral acquisitions on a Cartesian grid, such as VDRad [11], GOCART [12], MUSIC [13] and ROCK-MUSIC [14], or G-CASPR [15] and CASPR-Tiger [16]. Pseudo-spiral acquisitions in the  $k_y/k_x$ -plane with a golden-angle increment [17] combined with retrospective binning of cardiac frames results in high spatiotemporal incoherency of subsequent cardiac frames, which is optimal for CS reconstruction. Furthermore, this sampling scheme together with retrospective binning provides the option of reconstructing the data in a variable number of cardiac frames.

The above strategies require modification of the scanner software to allow for a predefined undersampling trajectory compatible with cardiac gated sequences. At our institution (Amsterdam University Medical Centers, University of Amsterdam, the Netherlands) we have developed such a software patch, which we refer to as PROUD (PROspective Undersampling in multiple Dimensions). PROUD sampling is most similar to CASPR Tiger [16] and incorporated variable density sampling [11] as well as phase-contrast imaging, but no self-gating.

In the development and integration of 4D flow scans in the clinic, the issue arises as to which acceleration technique will be the most suitable. To address this, comparisons between different methods are needed to evaluate their performances, as well as their advantages and disadvantages.

In this study, we quantified and visualized aortic flow, velocity and WSS data derived from pseudo-spiral CS accelerated 4D flow MRI using PROUD, as well as from k-t PCA accelerated 4D flow MRI. Our purpose was to compare both methods with each other and with 2D flow MRI. Because PROUD CS has



the flexibility of reconstructing at different temporal resolutions, a secondary aim was to investigate flow rate errors with increasing temporal resolution.

### 4.3 Methods

#### 4.3.1 Study design and subject cohort

Fifteen subjects (eight males and seven females) with an average age of  $26.1 \pm 3.5$  years were included in the study. Each subject provided written informed consent prior to the start of the study. The study was waived by the local Medical Ethics Review Committee because the study deals with scan technique comparisons and does not involve patients. Scans were performed on a 3 T Philips Ingenia scanner using a 24-channel torso coil (Philips Healthcare, Best, the Netherlands). After scout scans to locate the aorta, two 4D flow MRI scans covering the thoracic aorta were performed, either using k-t PCA or our proposed pseudo-spiral PROUD CS acceleration. The order of the 4D flow MRI scans was changed randomly per subject to avoid a systematic error due to the scan order. Furthermore, a single-slice 2D flow MRI scan through the ascending aorta (AAo) and descending aorta (DAo) was acquired as a reference. Detailed scan parameters of all scans are given in **Table 4.1** and were chosen according to those described in the consensus statement [5].

#### 4.3.2 Pseudo-spiral PROUD acquisition and CS reconstruction

In this study we used a pseudo-spiral  $k_y/k_x$ -plane acquisition scheme designed for incoherent undersampling. The sampling trajectory list was calculated prior to the scans in MATLAB R2016a (MathWorks, Natick, MA, USA) and was passed to the scanner in the form of a text file. The shape of each outer-in spiral arm can be described in the polar coordinates ( $r$ ,  $\varphi$ ) as

$$r(n) = \varphi_n^2; \varphi_n = n \cdot \frac{2\pi \cdot T}{N} + \emptyset \quad (n \in [0, N]) \quad (4.1)$$

where  $n$  is the index of the sampling location within each spiral arm,  $N$  is the total number of sampling locations (frequency encoding lines), and  $T$  is number of spiral turns. In this study,  $N$  was 75 and  $T$  was 3.  $\emptyset$  is the offset angle. For subsequent spiral arms,  $\emptyset$  increases by a golden-angle of  $\sim 137.51$  degrees or 2.40 radians. Spirals were stretched to match the size of k-space and gridded on Cartesian coordinates by rounding off to the nearest integer. The shapes of three consecutive spirals are illustrated in **Figure 4.1a**. The distance from the sampling locations to the k-space center is changed quadratically along the spiral. Thus, the resulting total sampling has a variable density distribution with a denser sampling of the low-frequency k-space center and sparse sampling of high-frequency peripheral k-space (**Figure 4.1b**).

PROUD CS sampling overruled the scanner sampling on the basis of the desired sampling trajectory and was performed continuously without ECG triggering. The ECG signals were, however, used to store the acquisition time points within each cardiac cycle to allow for retrospective binning of different cardiac frames. Importantly, due to the physiological heart-rate variability, a random filling of k-t space was created with a mean undersampling factor of  $\sim 8$  per cardiac frame (**Figure 4.1b**). Oversampling of the same k-t-space coordinate was avoided in real time by checking whether a k-t

space coordinate had already been scanned and, if this was the case, skipping this acquisition and continuing with the next k-space trajectory coordinate.

The acceleration factor for each PROUD scan,  $R_{\text{proud}}$  was calculated retrospectively based on a theoretical fully sampled scan:

$$R_{\text{proud}} = \frac{N_{\text{full}}}{N_{\text{undersampled}}} = \frac{N_{\text{ky}} * N_{\text{kz}} * N_{\text{card}} * \pi/4}{N_{\text{proud}}} \quad (4.2)$$

where  $N_{\text{ky}}$ ,  $N_{\text{kz}}$  and  $N_{\text{card}}$  are the number of phase encoding steps, number of slices and number of cardiac frames, respectively, for a fully sampled scan; and  $N_{\text{proud}}$  are the total number of PROUD sampling points of all pseudo-spirals. The factor  $\pi/4$  describes the absence of sampling at the outer edges of k-space (elliptical k-space shutter [18]).

The PROUD scans were primarily reconstructed in 24 cardiac frames, resulting in an acceleration factor of 8 (hereafter called PROUD CS 8), and also in 40 cardiac frames, resulting in an acceleration factor of 13 (hereafter called PROUD CS 13). Additional reconstructions were made with 12, 27, 35 and 60 cardiac frames. However, the true acceleration factor,  $R_{\text{true}}$ , which is defined as the number of samples in the full k-space divided by the number of points in the undersampled acquired k-space, is  $\pi/4$  times higher and can vary per cardiac frame as well as per subject. The mean  $R_{\text{true}}$ , over all cardiac frames and all subjects is provided in **Table 4.1**. CS reconstructions were performed on a Linux server in MATLAB using MRecon (Gyrotools, Zurich, Switzerland) in combination with the Berkeley Advanced Reconstruction Toolbox (BART) [19]. the server allowed the use of eight Intel Xeon Gold 6132 CPUs at 2.6 GHz and up to 300 GB RAM. A nonlinear parallel imaging and compressed sensing (PI-CS) reconstruction was performed according to

$$\arg \min_m \{ \|F_U S m - y\|_2 + \lambda \|T m\|_1 \} \quad (4.3)$$

using a sparsifying total variation operator in time  $T$ .  $F_U$  denotes the undersampling Fourier operator,  $S$  the coil sensitivity maps,  $y$  the measured k-space data, and  $m$  the reconstructed image data. While the left term ensures data consistency, the right term enforces sparsity, regularized by parameter  $\lambda$ . The reconstruction was performed with a regularization parameter of  $\lambda = 0.001$  and  $i = 20$  iterations. The applied reconstruction was the result of an L-curve [20] analysis for one slice of one subject in combination with 2D flow comparison. The analysis included the regularization constraints wavelet transformation in space and/or total variation in space and/or time, various regularization parameters  $\lambda$  ranging from 0.0001 to 0.5, and various numbers of iterations  $i$  ranging from 20 to 50.

**Table 4.1** Detailed scan parameters of all scans.

Parameter	4D flow k-t PCA	4D flow PROUD CS	2D flow
FOV (FHxAPxRL) [mm]	315 x 275 x 60	315 x 275 x 60	8 x 350 x 301.4
ACQ voxel size (FHxAPxRL) [mm]	2.5 x 2.5 x 2.5	2.5 x 2.5 x 2.5	8 x 2.5 x 2.5
Recon voxel size (FHxAPxRL) [mm]	2.5 x 2.5 x 2.5	2.5 x 2.5 x 2.5	8 x 1.22 x 1.22
Slices (slice encoding direction)	24 (RL)	24 (RL)	1 (FH)
Cardiac frames	24	24	40
Acceleration factor (technique)	8 (k-t PCA)	8 (CS)	2 (SENSE)
True acceleration factor (full k-space / acquired k-space)	6.92±0.00	10.52±0.22	2
TE / TR [ms]	2.1 / 4.2	2.1 / 3.9	2.5 / 4.1
Flip angle [degrees]	8	8	10
VENC [cm/s]	150	150	150
PC flow directions	FH, AP, RL	FH, AP, RL	FH
ECG-gating	Prospective	Retrospective	Prospective
Respiratory compensation	Navigator	Navigator	breath hold
Respiratory navigator gating window [mm]	7	7	-
Nominal scan time [mm:ss]	05:45	04:25	00:12.7
Estimated scan time (with ~60% gating efficiency) [mm:ss]	09:35	07:22	00:12.7
Offline image reconstruction time [mm]	10 – 15	14 – 18	-

### 4.3.3 k-t PCA acquisition and reconstruction

For k-t PCA, the k-t space was uniformly undersampled on a Cartesian grid [6] using FlowPatch (Gyrotools) with a k-t acceleration factor of  $R = 8$  (hereafter called k-t PCA 8). Prospective ECG-gating was used with an acquisition of 24 cardiac frames. Training data, consisting of 11 center phase-encoding lines for each time point, were collected simultaneously (**Figure 4.1c,d**) resulting in a lower true acceleration factor  $R_{\text{true}}$  (**Table 4.1**). K-t PCA 4D flow data were reconstructed with CRecon (Gyrotools) on a Windows computer with eight Intel Xeon E5–1620 CPUs at 3.5 GHz and up to 16 GB RAM. To avoid temporal blurring, the k-t regularization factor was optimized by 2D peak flow comparison of one exemplary dataset. A value of  $\lambda = 0.2$  resulted in the best image quality and the lowest flow bias, and was thus used for all subsequent k-t PCA reconstructions.

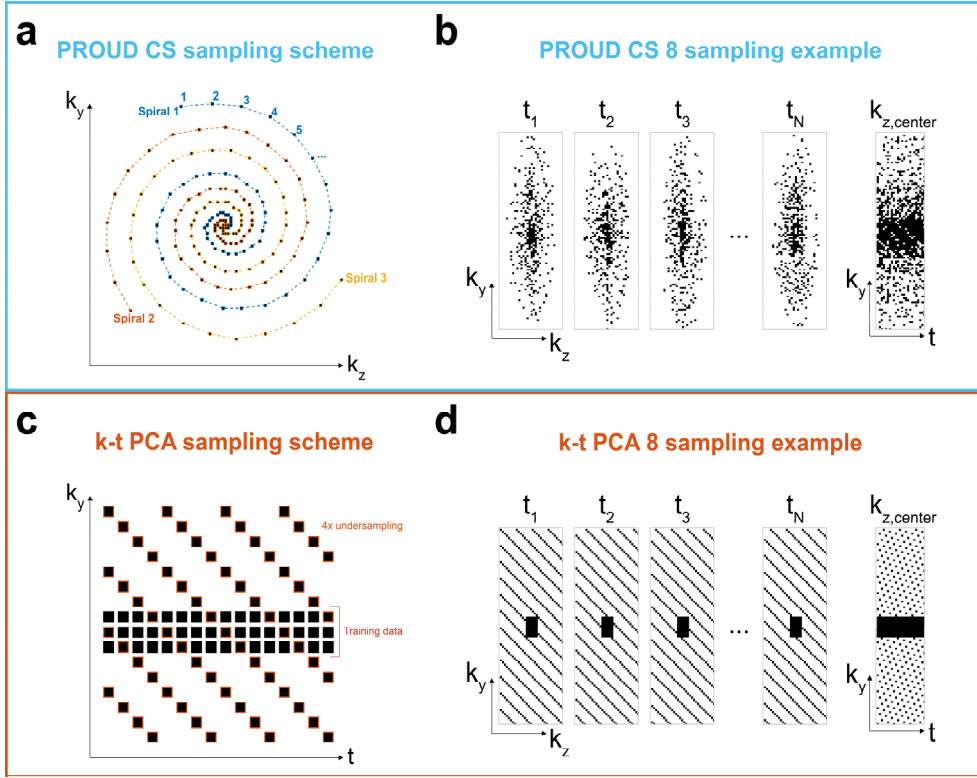


**Figure 4.1** (a) The pseudo-spiral PROUD CS sampling pattern consisted of multiple spirals. Consecutive spirals were turned by a golden angle ( $\sim 137.51^\circ$ ). (b) Resulting sampling distributions for PROUD CS in spatial and time dimensions. (c) The k-t sampling pattern used for k-t PCA was composed of a training set and an undersampled set, which were acquired simultaneously. (d) Sampling distributions for k-t PCA in spatial and time dimensions.

#### 4.3.4 Flow analysis

Following the reconstruction, a phase-contrast MRI angiogram (PC-MRA) was created by voxel-wise multiplication of the phase-contrast magnitude images with the absolute velocity, and subsequently averaged over all cardiac frames [21]. PC-MRA data were used for segmentation of the aorta anatomy in Mimics Research 21.0 (Materialise, Leuven, Belgium) [22]. Segmentations were conducted for all 4D flow MRI sequences separately.

For 2D analysis, 4D flow MRI scans were resliced to the slice position of the 2D flow MRI scan in GTFlow (Gyrotools). ROIs of the AAo and DAo were drawn in the 2D flow MRI scan as well as in the resliced 4D flow MRI images. All ROIs were drawn in the images at the time of peak flow. To match the highest temporal resolution of 40 cardiac frames, all velocity and flow measurements of lower temporal resolution were interpolated by a shape-preserving piecewise cubic interpolation.

For 3D analysis, WSS at the peak velocity time frame was calculated in MATLAB, as previously described [23]. For voxel-wise comparisons of velocity and WSS, datasets were registered by a rigid

transformation followed by nearest neighbour interpolation. Additionally, directional differences in velocity and WSS vectors were assessed by comparing angular difference distribution [22,24].

#### 4.3.5 Statistical analysis

For 2D analysis, the flow of the 4D flow scans were compared with the 2D flow scan as a reference using Bland-Altman (BA) analysis and orthogonal regression plots [25]. Differences in the peak flow and stroke volume—the integral of the measured flow over the cardiac cycle—between each of the 4D flow scans with the 2D scan were reported in ml/s or ml, respectively, or in a percentage difference. Confidence limits are reported as mean and standard error of the mean (SEM). Significance was tested for peak flow and stroke volume by a two-sided t-test with 0.05 used as the cutoff for significance.

For 3D analysis, velocity and WSS values were compared by voxel-by-voxel BA analysis and orthogonal regression. For all analyses, mean differences and limits of agreement (LOA) were reported for the BA analysis and slope, intercept and Pearson's r for the orthogonal regression analysis. Relative difference measures were reported in percentages to the mean of all values.

### 4.4 Results

#### 4.4.1 2D analysis

An example of a 2D flow image with the corresponding images of the three accelerated 4D flow scans is shown in **Figure 4.2a**. Color-coded velocity profiles in the ROIs in the AAo and DAo are shown in **Figure 4.2b** with good agreement of the velocity profiles between the accelerated 4D flow and 2D flow scans as a reference. Flow values of all four scans during the cardiac cycle are shown in **Figure 4.2c** for the AAo and DAo. Here, it can be seen that for both the AAo and the DAo, PROUD CS flow curves were better matched with the 2D flow curve compared with k-t PCA.

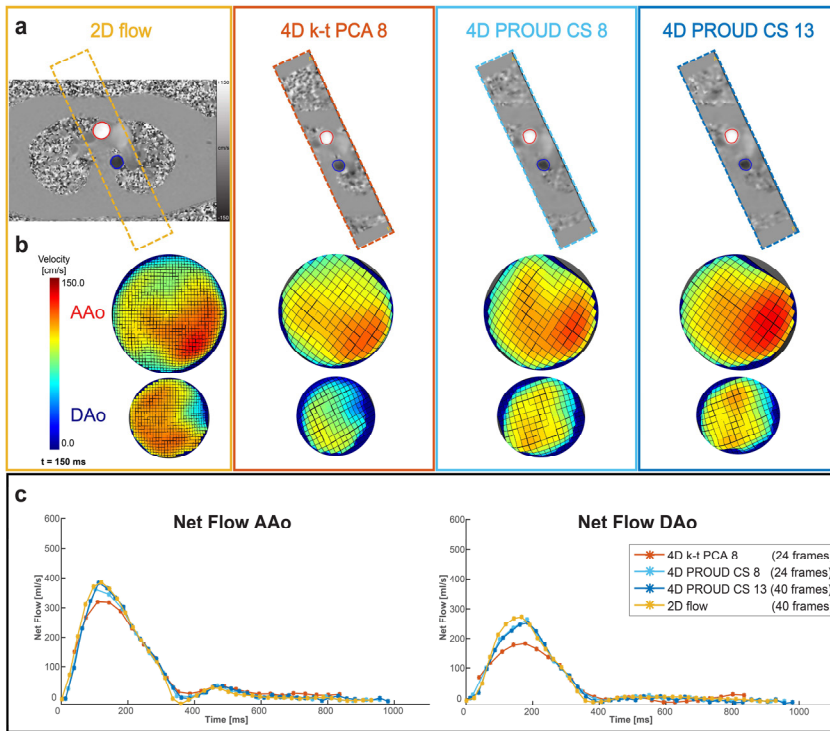


**Figure 4.2** (a), Exemplary through-plane velocity images of the 2D flow MRI as well as accelerated 4D flow MRI scans. ROIs are depicted in the ascending aorta (AAo, red) and descending aorta (DAo, blue). (b), The corresponding velocity scalar maps. (c), The corresponding flow curves for the four flow scans (AAo left and DAo right).

Results for BA and orthogonal regression analyses are given in **Figure 4.3** and **Table 4.2**. Looking at the mean difference as well as difference relative to the mean, it can be seen that all 4D flow scans underestimated flow compared with a 2D flow scan. K-t PCA 8 scans showed a larger underestimation than PROUD CS 8 and PROUD CS 13. Additionally, LoA in the BA plots were smaller for PROUD CS 8 and PROUD CS 13 than for k-t PCA 8. Looking at the orthogonal regression, it can be seen that 4D flow scans underestimated peak systolic flow compared with a 2D flow scan. The slope of the regression equation was smaller for k-t PCA 8 compared with PROUD CS 8 and PROUD CS 13, showing that k-t PCA 8 scans had a larger underestimation. Nevertheless, the Pearson correlation coefficients for k-t PCA 8, PROUD CS 8 and PROUD CS 13 indicated a strong correlation.

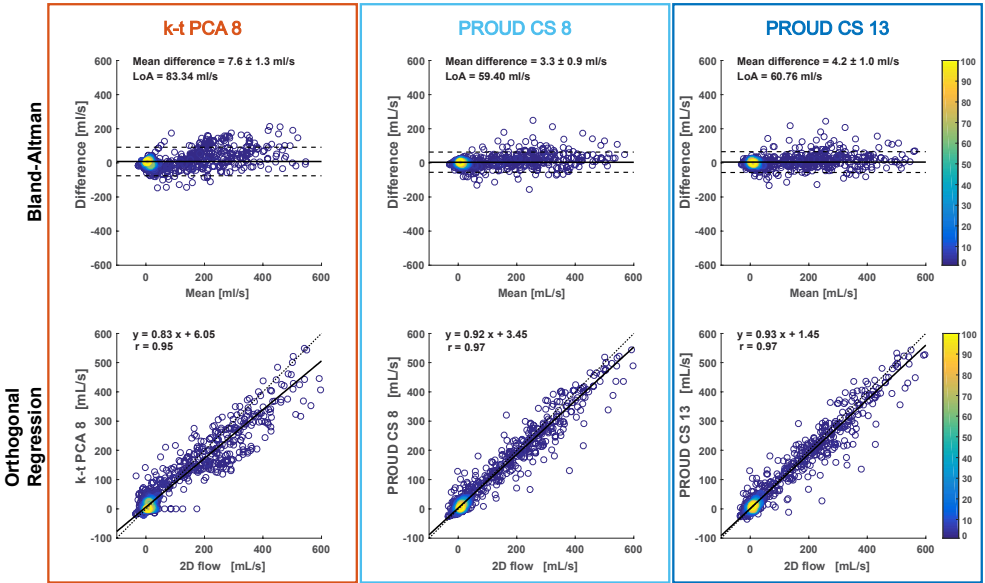
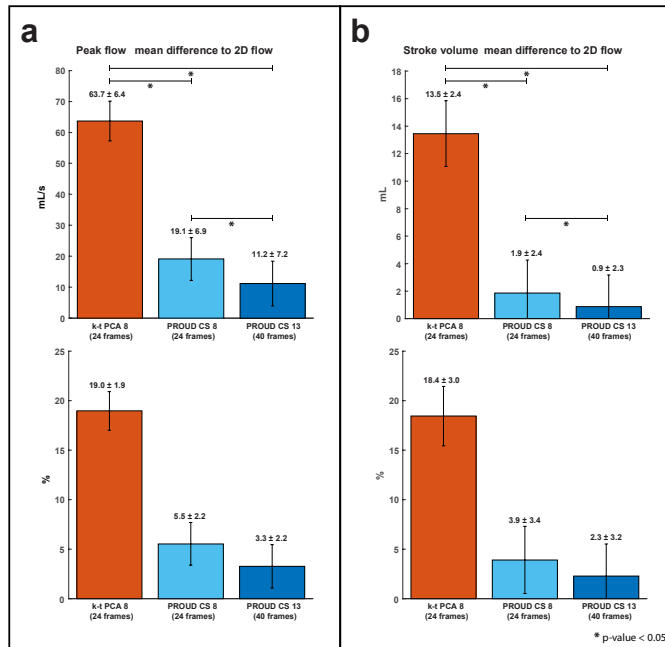


Figure 4.3 Bland-Altman plot (top) and orthogonal regression (bottom) of flow for the accelerated 4D flow MRI scans compared with the 2D flow MRI scan combined for all time frames and subjects. The color bar indicates the number of touching circles.

Table 4.2 2D flow scan compared to corresponding slice of accelerated 4D flow scans.

Accelerated 4D flow MRI vs. 2D flow MRI				Orthogonal regression		Correlation
4D flow scan:	Bland-Altman			Slope	Intercept [ml/s]	r
	Mean difference (±SEM) [ml/s] (%)	Median of the difference relative to the mean [%]	LoA [ml/s]			
k-t PCA 8	-7.6±1.3 (9.7)	-10.3	83.3	0.83	6.06	0.95
PROUD CS 8	-3.3±0.9 (4.2)	-5.0	59.4	0.92	3.45	0.97
PROUD CS 13	-4.2±1.0 (5.3)	-4.1	60.8	0.93	1.45	0.97

Furthermore, the mean difference of the stroke volume and the peak flow per 4D flow MRI scan were compared with the 2D flow scan (Figure 4.4). Higher deviations to 2D flow were found for k-t PCA than for PROUD CS. Stroke volume differences between the 4D flow and 2D flow scans were  $13.5 \pm 2.4$  mL for k-t PCA 8,  $1.9 \pm 2.4$  mL for PROUD CS 8 and  $0.9 \pm 2.3$  mL for PROUD CS 13. Peak flow differences to the 2D flow were  $63.7 \pm 6.4$  mL for k-t PCA 8,  $19.1 \pm 6.9$  mL for PROUD CS 8 and  $11.2 \pm 7.2$  mL for PROUD CS 13. All stroke volume differences as well as all peak flow differences were significantly different to each other. Mean difference of the peak flow and the stroke volume between 2D flow MRI and PROUD CS reconstructed with 12, 24, 27, 30, 35, 40 and 60 cardiac frames are shown in Supplementary Figure 4.7. Stroke volume and peak flow differences to 2D flow decrease with an increasing number of cardiac frames. PROUD CS 13 with 40 cardiac frames proves to be the best option as the stroke volume difference increases again from 40 to 60 cardiac frames. An example magnitude and PC image sequence for the three different 4D flow datasets, k-t PCA 8, PROUD CS 8 and PROUD CS 13, are shown in Supplementary Video 4.1.



**Figure 4.4** Bar charts of the mean difference ( $\pm$ SEM) between accelerated 4D flow MRI and 2D flow MRI for the peak flow (a), and the stroke volume (b). The same charts in percentages are shown at the bottom

#### 4.4.2 3D analysis

Representative 4D flow visualizations in the form of path lines as well as WSS maps are shown in **Figure 4.5**. The path line comparison shows similar flow patterns for all 4D flow scans as well as similar velocity and WSS magnitude values.

Results from voxel-by-voxel BA, orthogonal regression and angle distribution analysis for velocity and WSS are shown in **Figure 4.6** for an example dataset. Orthogonal regression showed an underestimation of velocity and WSS for k-t PCA 8 compared with PROUD CS 8, especially for higher values. The results of velocity and WSS comparisons of all subjects combined are listed in **Table 4.3**. **Table 4.3** shows that mean differences in velocity and WSS values, as well as LoA, Pearson's r and median angle, were similar for k-t PCA versus PROUD 8, and k-t PCA versus PROUD 13. Furthermore, agreement was strongest for PROUD 8 versus PROUD 13. This result indicated that, when using PROUD CS 4D flow, peak systolic cardiac frames can be resolved correctly when reconstructing data into 40 instead of 24 cardiac frames.



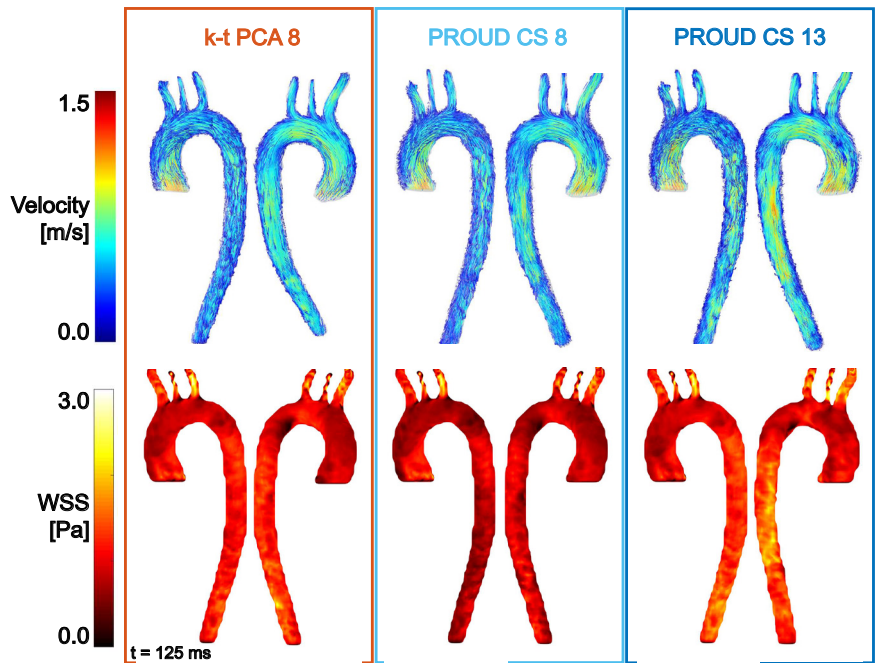


**Figure 4.5** Example visualization of peak systolic flow path lines (top) and wall-shear stress (WSS) (bottom) for the different 4D flow scans of one subject.

**Table 4.3** 3D analysis: Results of Bland-Altman, orthogonal regression and angle distribution analyses for velocity and WSS vectors between the different 4D flow scans.

4D flow comparison						
	Bland-Altman		Orthogonal regression		Correlation	Angle distribution
	Mean difference (±SEM)	LoA	Slope	Intercept	r	Median
<b>Velocity</b>	<b>[cm/s] (%)</b>	<b>[cm/s]</b>		<b>[m/s]</b>		<b>[ ° ]</b>
PROUD CS 8 vs. k-t PCA 8	9.40±0.08 (13.6)	51.8	0.84	0.03	0.51	9.2
PROUD CS 13 vs. PROUD CS 8	1.43±0.04( 1.9)	23.8	0.93	0.04	0.92	4.8
PROUD CS 13 vs. k-t PCA 8	11.10±0.08 (15.9)	54.4	0.73	0.09	0.51	9.6
<b>WSS</b>	<b>[mPa] (%)</b>	<b>[mPa]</b>		<b>[Pa]</b>		<b>[ ° ]</b>
PROUD CS 8 vs. k-t PCA 8	41.0±1.5 ( 3.5)	850	0.92	0.05	0.66	10.1
PROUD CS 13 vs. PROUD CS 8	17.8±0.8 ( 1.5)	444	0.94	0.06	0.92	4.7
PROUD CS 13 vs. k-t PCA 8	65.0±1.6 ( 5.5)	904	0.84	0.14	0.64	10.5

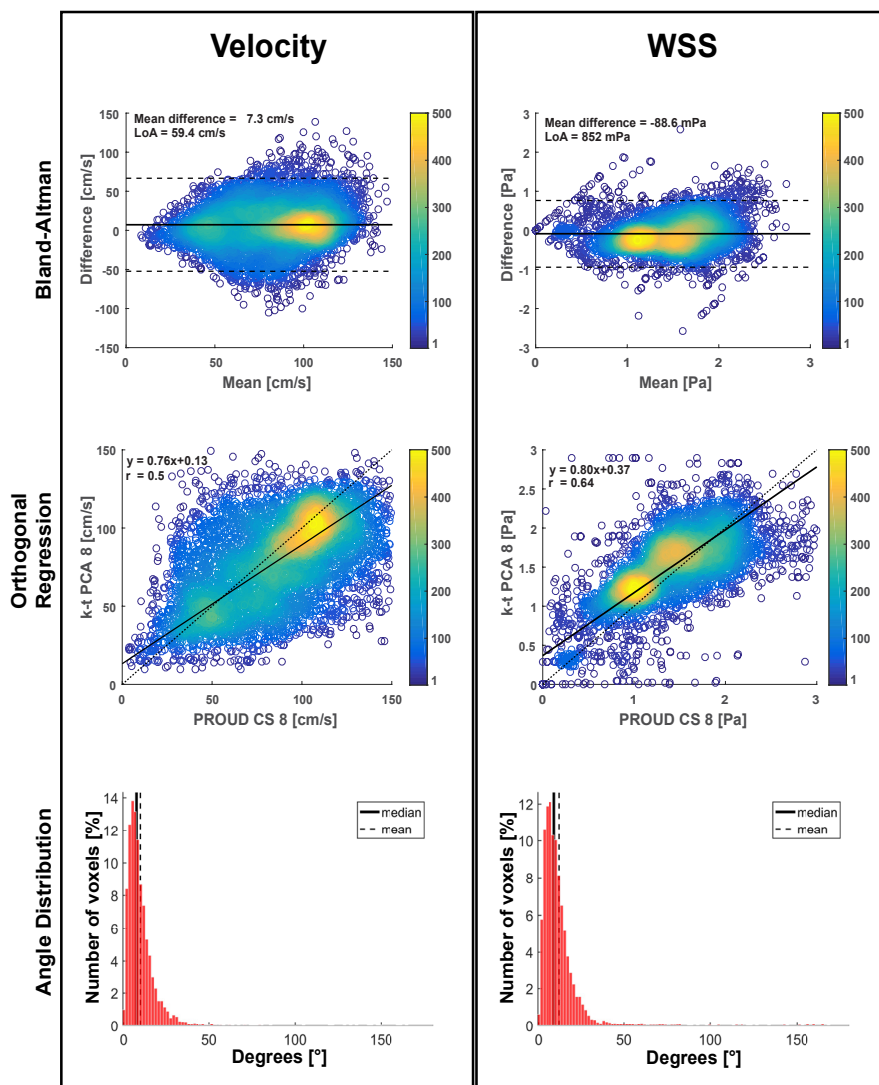


**Figure 4.6** Comparison of peak systolic velocity and wall-shear stress (WSS) for one subject between k-t PCA 8 and PROUD CS 8 scans showing Bland-Altman (top), orthogonal regression (middle) and angle distribution analyses (bottom). The color bar indicates the number of touching circles.

## 4.5 Discussion

In this study, we investigated the performance of pseudo-spiral PROUD CS 4D flow MRI in healthy aorta ( $R = 8$ ). CS reconstruction provided the option of retrospectively increasing the temporal resolution from 24 up to 40 cardiac frames ( $R = 13$ ) without a penalty in flow, velocity and WSS quantification. Results were compared with 2D flow scans and k-t PCA accelerated 4D flow MRI ( $R = 8$ ). k-t PCA and PROUD CS reconstructions resulted in comparable velocity and flow measurements.

Compared with time-resolved 2D flow scan as a reference, a systematic underestimation of flow for all 4D flow scans was found, but PROUD CS scans showed lower differences and variability than k-t PCA. The same observation of a systematic underestimation was found when comparing stroke volume and peak flow between 4D flow and 2D flow scans as reference. Here, peak flow and stroke volume differences to the 2D flow scan showed significantly lower biases for both PROUD CS scans compared with k-t PCA 8, with the smallest difference observed for PROUD CS 13. This demonstrates that a high temporal resolution is favorable for better peak flow measurements (*i.e.*, 40 cardiac frames). This trend is especially highlighted in **Supplementary Figure 4.7**, which showed that reconstructions of the same scan with high temporal resolution, or a high number of cardiac frames, respectively, led to small peak flow and stroke volume differences. Reconstructions with fewer cardiac frames resulted in larger biases.

The larger stroke volume difference for PROUD CS with 60 cardiac frames might be a result of the comparison with a 2D reference scan that contains fewer cardiac frames. Furthermore, a higher temporal resolution requires a higher acceleration factor, which will come at the cost of decreased accuracy in the derived flow parameters. It depends on the type of application how this tradeoff between scan time and accuracy should be weighted.

Voxel-wise comparison of peak systolic 3D velocity and WSS showed good correspondence between k-t PCA and both PROUD CS 4D flow MRI reconstructions and indicated that temporal resolution can be retrospectively increased without a penalty in hemodynamic quantification. However, higher acceleration results in a larger magnitude image penalty, which is visibly more pronounced in the magnitude images for PROUD CS 13 (*i.e.*, **Supplementary Video 4.1**), but we considered this acceptable because the velocity images contain the important information. Small artifacts were seen in the velocity images as well, which may become problematic for slow flow or regurgitant flow. However, for fast forward flow, which most aortic 4D flow MRI studies focus on, this penalty is smaller and tolerable. Both PROUD CS and k-t PCA 4D flow-MRI are able to measure velocity and flow-derived values such as WSS in the aorta. Even although our study showed that in 4D flow of the aorta PROUD CS offers some distinct advantages over k-t PCA—specifically, missing k-space lines could be compensated for in the reconstruction for CS but not for k-t PCA, the temporal resolution could be changed for PROUD CS but not for k-t PCA, and higher temporal resolution led to smaller flow measurement errors in PROUD CS—it is very difficult to generalize these findings to other vascular regions and pathological cases. PROUD CS acceleration benefits from slow temporal variations and spatial sparsity, whereas k-t PCA exploits a limited number of temporal base functions for acceleration, which can also be considered a type of signal sparsity. For different vascular territories, flow patterns

or pathological flow, one or the other type of sparsity might prove more effective to accelerate the acquisition.

The ability to retrospectively change the temporal resolution of the pseudo-spiral PROUD 4D flow scans allows for more flexibility compared with k-t PCA scans, in which the acceleration factor and the temporal resolution must be defined prior to the scan start. Additionally, for k-t PCA, the number of cardiac frames must be a multiple of the acceleration factor [6]. Also, the non-uniform sampling of the PROUD CS scans has no concern with incomplete scans, or aborts in general. That advantage can be seen in the case of a subject in which the PROUD CS scan ended at around only 50% scan percentage, but where data reconstruction was still possible (**Supplementary Figure 4.8**). Moreover, in comparison with the AAO peak flow of the 2D flow scan, the incomplete PROUD CS scans showed lower differences than the complete k-t PCA scan with  $R = 8$ . Therefore, PROUD CS has the important advantage of being able to reconstruct incomplete data that still result in usable 4D flow MRI data. Reconstruction times were in the range of 10 to 15 minutes for PROUD CS and in the range of 14 to 18 minutes for k-t PCA.

Compared with other studies employing k-t or CS acceleration for 4D flow MRI, we found similar results. Recently, Peper *et al.* [26], who also used pseudo-spiral Cartesian imaging with CS reconstruction, found that 4D flow MRI can be accelerated up to  $R=20$  with an acceptable underestimation of less than 10%. Neuhaus *et al.* [27], who used CS accelerated 4D flow MRI with  $R=8$ , reported a peak flow difference of  $4.6 \pm 25.2$  ml/s. Bollache *et al.* [28] found peak flow difference of -4.2% to 3% (k-t acceleration with  $R=5$ ), Knobloch *et al.* [29] found reduced peak velocities of  $4.9 \pm 7\%$  (k-t PCA with  $R=8$ ), and Giese *et al.* [7] found peak flow underestimation of  $5.1 \pm 7.5\%$  (k-t PCA with  $R=8$ ). It was not possible to compare PROUD CS to k-t PCA scans with a higher acceleration factor than 8. For instance, Knobloch *et al.* [29] have defined a k-t PCA factor of 8 as the upper limit and Pedersen *et al.* [6] defined  $R=8$  as a good trade-off considering image quality and acceleration.

Improvements for k-t PCA have been published such as k-t sPCA [29] or k-t PCA [30], where the most promising improvement was the spatial compartment dependent temporal basis function, which showed errors in stroke volume smaller than 5% for 16-fold acceleration. CS reconstructions with subspace constraint based on PCA or equivalently low rank constraint also exist [31], but were not used in this study.

For compressed sensing on the other hand, studies showed acceleration higher than a factor of 8 are feasible [32,33]. Ma *et al.* [32] showed peak flow differences to conventional 4D flow (GRAPPA  $R=2$ ) of -12.6% (AAO) and -3.2% (DAO) for CS accelerated 4D flow MRI by a factor of  $R=12.8$ . Compared to this study, we found a smaller peak flow difference for PROUD CS 13 compared to the reference of 7.1% for both ROIs combined. The smaller peak flow difference might be explained by the higher number of cardiac frames provided for PROUD CS 13 compared to the scan used in Ma *et al.* Interestingly, for intracranial applications Liu *et al.* [33] showed that a higher acceleration factor for CS reconstruction in combination with higher temporal resolution can be used to increase accuracy. In their study, peak velocity differences compared to the reference (GRAPPA  $R=2$ ) could be reduced from -3.83 cm/s for  $R=4$  with 72 ms temporal resolution to -1.72 cm/s for  $R=12$  with 24 ms temporal resolution. This is similar to observations found in this study.

This study had some limitations. One possible explanation for the mentioned k-t PCA flow underestimation is the challenge of the k-t regularization strength selection. On the one hand, a too high value will smooth the flow/velocity over the cardiac cycle and, on the other hand, a too low value will show more image artifacts, such as temporal blurring or flattening of the flow curves. As no optimal regularization strength was available, efforts have been made to choose the best regularization strength. Therefore, like for the CS reconstruction regularization parameter  $\lambda$ , we optimized the k-t regularization strength for one subject reconstruction by comparison to the 2D flow scan, and used these settings for the entire study. Of course, an optimization per subject would possibly lead to better results, but that approach is not feasible, especially for patient care, and therefore not used.

For PROUD CS sampling, we neither explicitly measured the effects of eddy currents nor optimized our sampling scheme with respect to them. However, in this study we used a Cartesian T1-weighted spoiled gradient-echo acquisition, for which eddy currents do not lead to severe image artifacts [34].

Another limitation is that in the 2D analysis, the interpolation of 24 to 40 cardiac phases could have caused additional differences in quantification. Another possibility for discrepancies in quantification is the difference in spatial resolution between 2D flow and 4D flow MRI. Also, the 2D flow MRI scan was acquired in a breath hold, whereas the 4D flow MRI scans were acquired in free breathing with respiratory gating. Therefore, the 2D flow scan can be considered as motion artifact-free. By contrast, motion artifacts are reduced in the 4D flow scans due to the respiratory gating but cannot be eliminated. Moreover, increased intrathoracic pressure during breath hold is associated with flow and stroke volume decrease, which can be another reason for differences between 2D flow and 4D flow MRI [35,36]. Finally, the difference in peak systolic segmentation for the 4D flow scans in contrast to the time-resolved segmentation of the 2D flow scans are another possible error source [37].

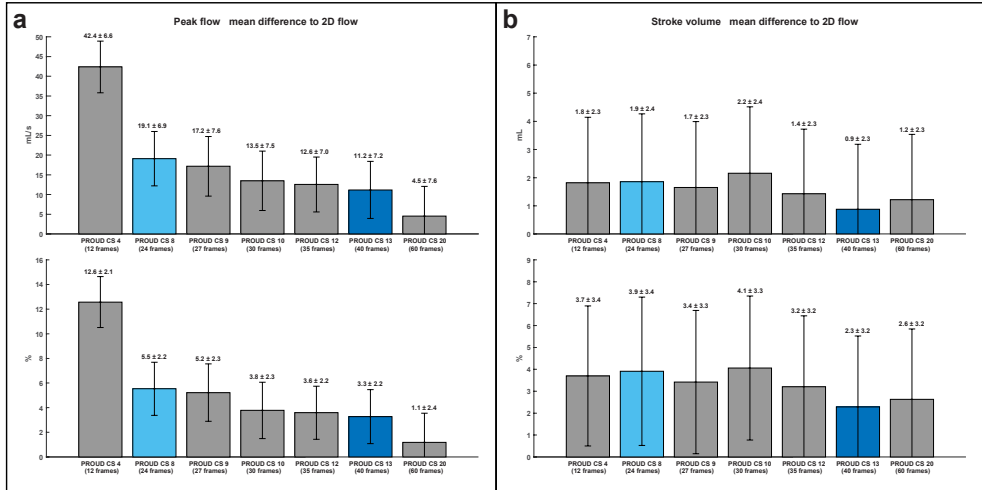
Additional studies can make use of PROUD CS acceleration as a valuable tool in clinical research to speed up 4D flow acquisitions. The scope of PROUD CS includes any type of 4D flow measurements in various patient anatomies. A useful next step would be to compare the proposed PROUD CS method with a self-gating approach such as XD-GRASP [38] or implement self-gating for PROUD CS as it was demonstrated in related Cartesian 5D flow acquisitions [14,39].

## 4.6 Conclusion

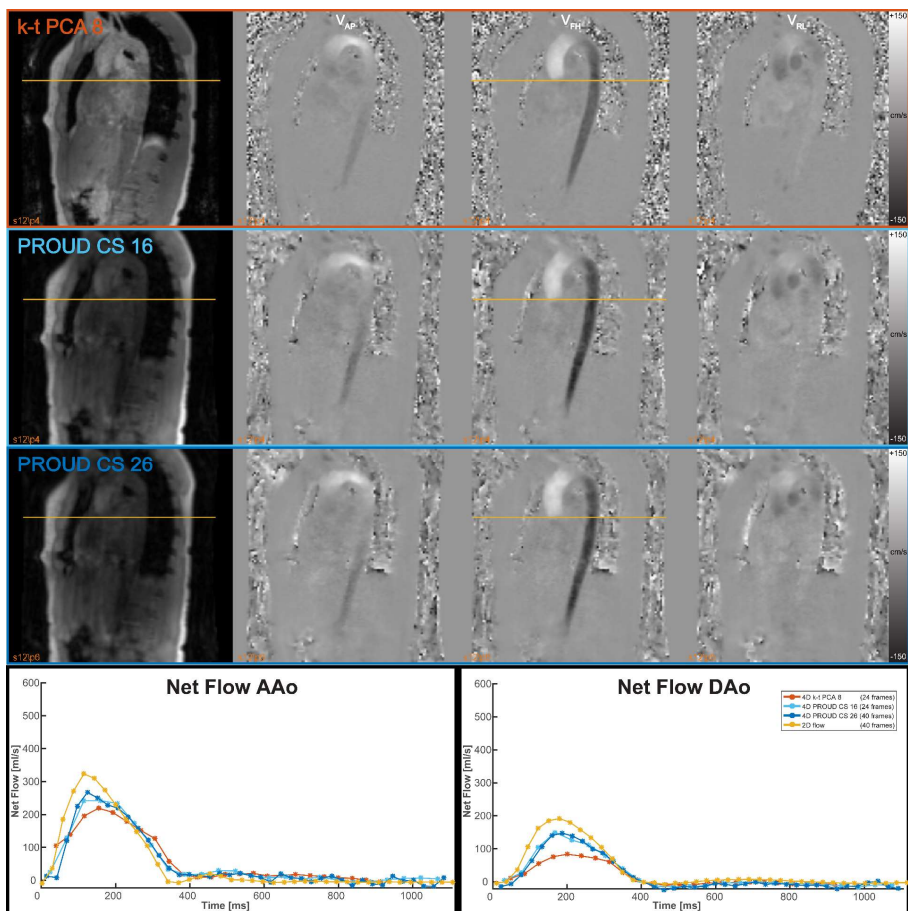
In conclusion, both k-t PCA and pseudo-spiral PROUD CS demonstrated their ability to accelerate 4D flow measurements. We found that in this setting, PROUD CS was slightly superior compared with k-t PCA as, among others, peak flow values were less underestimated in comparison with the 2D flow scan as a reference. Moreover, PROUD CS acquisition has the additional benefit of changing the temporal resolution during reconstruction. We showed that this advantage offers greater reconstruction versatility and led to even higher accuracy in hemodynamic measurements when reconstructing the data at a higher temporal resolution.

## 4.7 Supplementary material

**Supplementary Video 4.1:** Example magnitude and PC image sequence for the three different 4D flow data sets k - t PCA 8, PROUD CS 8, and PROUD CS 13 showing a center slice in sagittal view over time. The video can be found under <https://onlinelibrary.wiley.com/doi/full/10.1002/nbm.4255>



**Supplementary Figure 4.7** Bar charts of the mean difference ( $\pm$ SEM) between accelerated 4D flow MRI and 2D flow MRI for the peak flow (a) and the stroke volume (b). The same charts in percentage are shown at the bottom.



**Supplementary Figure 4.8** Example magnitude and PC images for the three different 4D flow data sets k-t PCA 8, PROUD CS 16, and PROUD CS 26 of the excluded subject for which the PROUD CS scan was incomplete around 50% scan time, resulting in PROUD CS acceleration factors of 16 and 26. The yellow line indicates the slice position of the 2D flow scan. Corresponding flow curves are depicted at the bottom.

## 4.8 Bibliography

1. Markl M, Frydrychowicz A, Kozerke S, Hope M, Wieben O. 4D flow MRI. *J Magn Reson Imaging*. 2012;36:1015–36.
2. Blanken CPS, Farag ES, Boekholdt SM, Leiner T, Kluin J, Nederveen AJ, *et al*. Advanced cardiac MRI techniques for evaluation of left-sided valvular heart disease. *J Magn Reson Imaging*. 2018;48:318–29.
3. van Ooij P, Markl M, Collins JD, Carr JC, Rigsby C, Bonow RO, *et al*. Aortic valve stenosis alters expression of regional aortic wall shear stress: New insights from a 4-dimensional flow magnetic resonance imaging study of 571 subjects. *J Am Heart Assoc*. 2017;6:1–13.
4. Markl M, Kilner PJ, Ebbers T. Comprehensive 4D velocity mapping of the heart and great vessels by cardiovascular magnetic resonance. *J Cardiovasc Magn Reson*. BioMed Central Ltd; 2011;13:7.
5. Dyverfeldt P, Bissell M, Barker AJ, Bolger AF, Carlhäll CJ, Ebbers T, *et al*. 4D flow cardiovascular magnetic resonance consensus statement. *J Cardiovasc Magn Reson*. 2015;17:1–19.
6. Pedersen H, Kozerke S, Ringgaard S, Nehrke K, Won YK. K-t PCA: Temporally constrained k-t BLAST reconstruction using principal component analysis. *Magn Reson Med*. 2009;62:706–16.
7. Giese D, Wong J, Greil GF, Buehrer M, Schaeffter T, Kozerke S. Towards highly accelerated Cartesian time-resolved 3D flow cardiovascular magnetic resonance in the clinical setting. *J Cardiovasc Magn Reson*. 2014;16:42.
8. Farag ES, van Ooij P, Planken RN, Dukker KCP, de Heer F, Bouma BJ, *et al*. Aortic valve stenosis and aortic diameters determine the extent of increased wall shear stress in bicuspid aortic valve disease. *J Magn Reson Imaging*. 2018;
9. Lustig M, Donoho D, Pauly JM. Sparse MRI: The application of compressed sensing for rapid MR imaging. *Magn Reson Med*. 2007;58:1182–95.
10. Cheng JY, Zhang T, Alley MT, Uecker M, Lustig M, Pauly JM, *et al*. Comprehensive Multi-Dimensional MRI for the Simultaneous Assessment of Cardiopulmonary Anatomy and Physiology. *Sci Rep*. 2017;
11. Cheng JY, Hanneman K, Zhang T, Alley MT, Lai P, Tamir JI, *et al*. Comprehensive motion-compensated highly accelerated 4D Flow MRI with ferumoxytol enhancement for pediatric congenital heart disease. *J Magn Reson Imaging*. 2015;
12. Zhu Y, Guo Y, Lingala SG, Marc Lebel R, Law M, Nayak KS, *et al*. GOCART: Golden-angle Cartesian randomized time-resolved 3D MRI. *Magn Reson Imaging*. Elsevier Inc.; 2016;34:940–50.
13. Zhou Z, Han F, Rapacchi S, Nguyen KL, Brunengraber DZ, Kim GHJ, *et al*. Accelerated ferumoxytol-enhanced 4D multiphase, steady-state imaging with contrast enhancement (MUSIC) cardiovascular MRI: validation in pediatric congenital heart disease. *NMR Biomed*. 2017;30:1–11.
14. Han F, Zhou Z, Han E, Gao Y, Nguyen KL, Finn JP, *et al*. Self-gated 4D multiphase, steady-state imaging with contrast enhancement (MUSIC) using rotating cartesian K-space (ROCK): Validation in children with congenital heart disease. *Magn Reson Med*. 2017;78:472–83.
15. Prieto C, Doneva M, Usman M, Henningsson M, Greil G, Schaeffter T, *et al*. Highly efficient respiratory motion compensated free-breathing coronary MRA using golden-step Cartesian acquisition. *J Magn Reson Imaging*. 2015;41:738–46.
16. Usman M, Ruijsink B, Nazir M, Cruz G, Prieto C. Free breathing whole-heart 3D CINE MRI with self-gated Cartesian trajectory. *Magn Reson Imaging*. 2016
17. Winkelmann S, Schaeffter T, Koehler T, Eggers H, Doessel O. An optimal radial profile order based on the golden ratio for time-resolved MRI. *IEEE Trans Med Imaging*. 2007;
18. Kozerke S, Tsao J, Razavi R, Boesiger P. Accelerating cardiac cine 3D imaging using k-t BLAST. *Magn Reson Med*. 2004;
19. Uecker M, Ong F, Tamir JI, Bahri D, Virtue P, Cheng JY, *et al*. Berkeley Advanced Reconstruction Toolbox. *Proc*



Intl Soc Mag Reson Med. 2015. p. 2486.

20. Hansen PC. The L-Curve and its Use in the Numerical Treatment of Inverse Problems. *Comput Inverse Probl Electrocardiology*, ed P Johnston, *Adv Comput Bioeng*. 2000;4:119–42.

21. Bock J, Frydrychowicz A, Stalder AF, Bley TA, Burkhardt H, Hennig J, *et al*. 4D phase contrast MRI at 3 T: Effect of standard and blood-pool contrast agents on SNR, PC-MRA, and blood flow visualization. *Magn Reson Med*. 2010;63:330–8.

22. Ooij P Van, Powell AL, Potters W V, Carr JC, Markl M, Barker AJ. Reproducibility and interobserver variability of systolic blood flow velocity and 3D wall shear stress derived from 4D flow MRI in the healthy aorta. 2015;

23. Potters W V, Marquering HA, VanBavel E, Nederveen AJ. Measuring wall shear stress using velocity-encoded MRI. *Curr Cardiovasc Imaging Rep*. 2014;7:9257.

24. van Ooij P, Guédon A, Poelma C, Schneiders J, Rutten MCM, Marquering HA, *et al*. Complex flow patterns in a real-size intracranial aneurysm phantom: phase contrast MRI compared with particle image velocimetry and computational fluid dynamics. *NMR Biomed*. 2012;25:14–26.

25. Bland JM, Altman DG. Comparing methods of measurement: why plotting difference against standard method is misleading. *Lancet*. 1995;346:1085–7.

26. Peper ES, Gottwald LM, Zhang Q, Coolen BF, van Ooij P, Nederveen AJ, *et al*. Highly accelerated carotid 4D flow MRI using Pseudo-Spiral Cartesian acquisition and a Total Variation constrained Compressed Sensing reconstruction. *J Cardiovasc Magn Reson*. *Journal of Cardiovascular Magnetic Resonance*; 2020;

27. Neuhaus E, Weiss K, Bastkowski R, Koopmann J, Maintz D, Giese D. Accelerated aortic 4D flow cardiovascular magnetic resonance using compressed sensing: Applicability, validation and clinical integration. *J Cardiovasc Magn Reson*. *Journal of Cardiovascular Magnetic Resonance*; 2019;21:1–11.

28. Bollache E, Barker AJ, Dolan RS, Carr JC, van Ooij P, Ahmadian R, *et al*. k-t accelerated aortic 4D flow MRI in under two minutes: Feasibility and impact of resolution, k-space sampling patterns, and respiratory navigator gating on hemodynamic measurements. *Magn Reson Med*. 2018;79:195–207.

29. Knobloch V, Boesiger P, Kozerke S. Sparsity transform k-t principal component analysis for accelerating cine three-dimensional flow measurements. *Magn Reson Med*. 2013;70:53–63.

30. Giese D, Schaeffter T, Kozerke S. Highly undersampled phase-contrast flow measurements using compartment-based k - t principal component analysis. *Magn Reson Med*. 2013;69:434–43.

31. Valvano G, Martini N, Huber A, Santelli C, Binter C, Chiappino D, *et al*. Accelerating 4D Flow MRI by exploiting low-rank matrix structure and hadamard sparsity. *Magn Reson Med*. 2017;78:1330–41.

32. Ma LE, Markl M, Chow K, Huh H, Forman C, Vali A, *et al*. Aortic 4D flow MRI in 2 minutes using compressed sensing, respiratory controlled adaptive k-space reordering, and inline reconstruction. *Magn Reson Med*. 2019;81:3675–90.

33. Liu J, Koskas L, Faraji F, Kao E, Wang Y, Haraldsson H, *et al*. Highly accelerated intracranial 4D flow MRI: evaluation of healthy volunteers and patients with intracranial aneurysms. *Magn Reson Mater Physics, Biol Med*. Springer Berlin Heidelberg; 2018;31:295–307.

34. Brodsky EK, Klaers JL, Samsonov AA, Kijowski R, Block WF. Rapid measurement and correction of phase errors from B0 eddy currents: Impact on image quality for non-cartesian imaging. *Magn Reson Med*. 2013;

35. Sakuma H, Kawada N, Kubo H, Nishide Y, Takano K, Kato N, *et al*. Effect of breath holding on blood flow measurement using fast velocity encoded cine MRI. *Magn Reson Med*. 2001;45:346–8.

36. Kowallick JT, Joseph AA, Unterberg-Buchwald C, Fasshauer M, van Wijk K, Merboldt KD, *et al*. Real-time phase-contrast flow MRI of the ascending aorta and superior vena cava as a function of intrathoracic pressure (Valsalva manoeuvre). *Br J Radiol*. 2014;87:20140401.

37. Bustamante M, Petersson S, Eriksson J, Alehagen U, Dyverfeldt P, Carlhäll C-J, *et al*. Atlas-based analysis of 4D flow CMR: Automated vessel segmentation and flow quantification. *J Cardiovasc Magn Reson*. *Journal of Cardiovascular Magnetic Resonance*; 2015;17:87.

38. Feng L, Axel L, Chandarana H, Block KT, Sodickson DK, Otazo R. XD-GRASP: Golden-angle radial MRI with reconstruction of extra motion-state dimensions using compressed sensing. *Magn Reson Med*. 2016;75.
39. Walheim J, Dillinger H, Kozerke S. Multipoint 5D flow cardiovascular magnetic resonance - accelerated cardiac- and respiratory-motion resolved mapping of mean and turbulent velocities. *J Cardiovasc Magn Reson*. 2019;21:42.

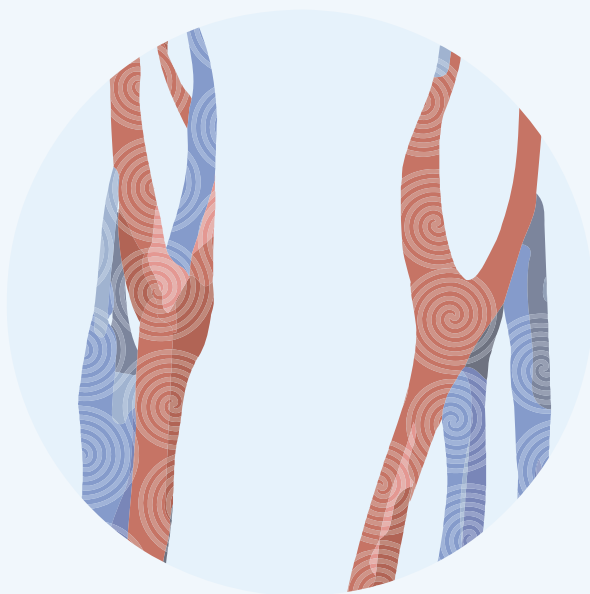


# CHAPTER 5

MRI measurements of  
carotid pulse wave velocity,  
wall thickness and wall shear stress in  
statin treated patients with  
familial hypercholesterolemia

Eva S. Peper,  
Ilse K. Luirink,  
Pim van Ooij,  
Bram F. Coolen,  
Gustav J. Strijkers,  
Vera Čaluković,  
Patrick J.H. de Koning,  
Rob J. van der Geest,  
Albert Wiegman,  
Barbara A. Hutten,  
and Aart J. Nederveen

Manuscript in preparation



## 5.1 Abstract

**Background:** Familial hypercholesterolemia (FH) is characterized by elevated low-density lipoprotein (LDL) cholesterol levels and premature cardiovascular disease. Statins are currently the preferred pharmacological therapy to prevent progression of atherosclerosis and have shown to be effective in a recent study on ultrasound assessed intima-media thickness (IMT). In this study we investigate if we can use MRI to detect differences in pulse wave velocity (PWV), wall thickness (WT), and wall shear stress (WSS) between treated FH patients and unaffected controls. Differences could be indicative for future adverse vessel wall remodeling or atherosclerosis.

**Methods:** MRI scans were performed in a group of 43 early in life treated FH patients (21 males; mean±standard deviation [SD] age: 32.6±2.8 years) and 18 unaffected controls (12 males; mean±SD age: 33.1±3.3 years). Blood samples were drawn to derive the LDL-cholesterol and high-density lipoprotein (HDL) cholesterol levels. The MRI protocol consisted of two 2D flow scans, a 3D black-blood (BB) iMSDE scan and a 4D flow scan of the carotid arteries, which were used for PWV, WT and WSS estimation, respectively. For WT estimation from 3D BB data a machine learning based segmentation was implemented. For statistical analysis, 3D atlases and p-value maps were calculated from 3D WT and WSS maps by registering the data to shared geometries followed by averaging and a Wilcoxon rank sum at every voxel, with significance at  $p < 0.05$ . Voxel-wise linear regression for WT and WSS atlases was done. Additionally, Wilcoxon rank sum tests of PWV, mean WT and mean WSS between FH patients and controls, men and women, and smoking and non-smokers and linear regression with LDL and HDL levels were calculated.

**Results:** The atlas showed that WT in the carotid bulb was higher and WSS was lower. The p-values maps indicated no major differences between FH patients and controls. The voxel-wise correlation between WSS and WT atlas values was found to be stronger for FH ( $R = -0.51$ ), male ( $R = -0.46$ ) and smokers ( $R = -0.48$ ) than for unaffected controls ( $R = -0.32$ ), females ( $R = -0.30$ ) and non-smokers ( $R = -0.42$ ). For smokers a significantly lower PWV of 4.79 m/s (95% CI, 4.34 to 5.23) in comparison to non-smokers with 5.43 m/s (95% CI, 5.08 to 5.78) was found ( $p = 0.043$ ). A significantly higher mean WT ( $p = 0.024$ ) of 1.13 mm (95% CI, 1.10 to 1.16) was observed in males in comparison to females with a mean WT of 1.06 mm (95% CI, 1.02 to 1.10). A significantly lower mean WSS ( $p = 0.011$ ) of 1.37 Pa (95% CI, 1.38 to 1.56) was found in smokers in comparison to non-smokers with 1.59 mm (95% CI, 1.44 to 1.72). No significant differences were found for PWV, mean WT and mean WSS when comparing FH and unaffected controls. Univariate linear regression showed a negative correlation between smoking and PWV ( $p = 0.039$ ), and a positive correlation between mean WT and male gender ( $p = 0.029$ ). Additionally, a negative correlation between mean WSS and smoking ( $p = 0.009$ ), a negative correlation between mean WSS and age ( $p = 0.029$ ), a positive correlation between mean WSS and HDL ( $p = 0.001$ ), and a negative correlation between mean WSS and weight ( $p = 0.014$ ) was found.

**Conclusion:** For individual analysis, no significant differences in PWV, mean WT, and mean WSS for FH patients in comparison to unaffected controls were found. These results indicated that the carotid hemodynamics are not different from unaffected controls, which is in agreement with effective statin treatment.

## 5.2 Introduction

Familial hypercholesterolemia (FH) is a genetic disease characterized by elevated low-density lipoprotein (LDL) cholesterol levels from birth onward, which leads to premature atherosclerotic vessel wall changes [1,2]. Atherosclerosis is an inflammatory disease and highly correlated with cardiovascular events, such as stroke or ischemic heart attack [3]. It is characterized by local fatty deposits (cholesterol, macrophages, etc.), and thickening and stiffening of the vessel wall. However, clinical symptoms, such as angina pectoris or apnea, will only occur at a very late stage of the disease, when arteries are partially or fully occluded and the blood flow is limited. It is therefore of high interest to identify asymptomatic atherosclerotic patients at high risk for a clinical event at an early stage [4]. Atherosclerosis develops over decades [5] and an important indicator of disease progression is the carotid intima-media thickness (IMT) measured *e.g.* with B-mode ultrasound [4]. Other risk factors for vessel wall thickening and cardiovascular disease are age, gender, smoking, cholesterol levels, blood pressure (BP), physical inactivity and any family history of cardiovascular disease.

For patients with FH statins are the preferred pharmacological therapy. In a recent 20-year follow-up study it could be shown that the statin treatment has been effective by measuring ultrasound assessed IMT in the carotid arteries [6]. In studying early markers of cardiovascular disease, MRI has been shown to be a versatile, operator independent technique, which is capable of assessing multiple parameters of interest in a single examination. Even more, MRI can measure parameters indicating atherosclerotic changes, which cannot yet be measured with ultrasound. For wall thickness (WT) assessment for example, a 3D blood suppressed (black blood) MRI image at sub-millimeter resolution can be obtained [7]. Additionally, within the same examination, MRI techniques encoding for blood velocity can be acquired, such as 2D flow MRI (a two-dimensional plane with flow measurement) and 4D flow MRI (a three-dimensional volume with flow measurement). These techniques are time-resolved and provide information over the cardiac cycle. From this data, additional biomarkers such as the shear stress of flowing blood on the vessel wall (WSS) and pulse wave velocity (PWV), a marker for vessel stiffness, can be derived. It is therefore an interesting challenge to investigate if MRI can measure changes in hemodynamic and vessel wall parameters in early in live treated FH patients, or in other risk groups such as smokers or males, even before the onset of atherosclerosis using MRI techniques instead of ultrasound.

In this study we investigate changes in the carotid arteries and the carotid bulb in particular, as these regions are prone to increases in WT and atherosclerotic plaque formation [8]. Also, as the carotid arteries lead to the brain, this is a critical location in case of plaque rupture and thrombus formation, which will eventually occlude arteries downstream [3]. WT can be measured with 2D black blood MRI, *e.g.* in the common carotid artery (CCA), providing a similar measure as ultrasound based IMT [9]. Novel 3D MRI techniques of the entire carotid bifurcation can help in localizing subtle, regional growth of the vessel wall, as may be the case in early stage atherosclerosis. However, high-resolution 3D MRI requires advanced and automated segmentation tools, such as machine learning techniques, to cover the segmentation workload and enable fast, accurate and automated data-processing.

In the carotid arteries, the carotid bulb is subject to regionally low velocities and low WSS. The size of the bulb is large with respect to the CCA and includes the flow divider leading to a skewed velocity

profile, both creating vortical flow in the bulb [10]. It has been shown previously that atherosclerotic changes develop in regions with low WSS [11,12]. Low WSS was shown to lead to remodeling of the endothelial cells of the vessel wall [13,14] and also the directional changes of WSS over time, as can be measured by the oscillatory shear index (OSI), have been related to endothelial remodeling [8]. In addition, low velocities lead to a longer dwell time of the blood, allowing for deposition of macrophages and lipids. WSS and OSI are therefore important biomarkers when investigating the onset of atherosclerosis.

While vessel wall stiffness increases with age, it is also considered as an early marker of regional atherosclerosis [15]. High vessel wall stiffness values have been associated with increases cerebrovascular events [16]. Additionally, it has been shown, that stiffening of the carotid arteries may prevent damping of the pulse wave, which can lead to damage of arterioles in the brain and cognitive damage [17]. With MRI a measure of vessel wall stiffness can be assessed by measuring the PWV. PWV can be determined by measuring the time difference between two flow curves at two different locations of the artery using 2D phase-contrast MRI. With ultrasound PWV is usually measured globally, i.e. between carotid and femoral artery, indicating an overall change of vessel stiffness. When studying regional atherosclerotic changes as in the carotid arteries a regional value of PWV is preferred.

In this study we investigate whether there are differences in PWV, WT, and WSS between patients with FH and unaffected controls, which could be indicative for future adverse vessel wall remodeling or atherosclerosis despite the lipid-lowering treatment.

## 5.3 Methods

### 5.3.1 Study population and study design

MRI scans were performed in a group of 43 FH patients (21 male, mean (SD) age  $32.6 \pm 2.8$  years) and 18 unaffected controls (12 male  $33.1 \pm 3.3$  years). All procedures were approved by the local institutional review board (METC) of the Academic Medical Centre in Amsterdam and were carried out according to the declaration of Helsinki. All participant gave written informed consent. For each participant mean arterial blood pressure (MAP) was measured prior to the examination using an arm cuff in a sitting position. Blood samples were drawn to derive the LDL and HDL protein levels. Additionally, weight, length and smoking status were noted.

### 5.3.2 Acquisition protocol

The MRI protocol consisted of two 2D flow scans, a 3D black-blood (BB) iMSDE scan and a 4D flow scan of the carotid arteries. The scans were used for PWV, WT and WSS estimation, respectively. All scans were performed with a Philips 3T Ingenia scanner using an 8-channel neck coil. Scan parameters were for the 2D flow scans: TR = 8.0 ms, TE = 3.9 ms, flip angle =  $25^\circ$ , VENC = 150 cm/s,  $0.8 \times 0.8 \times 3 \text{ mm}^3$  resolution, 4 ms temporal resolution, for the 3D BB scan: TR = 10 ms, TE = 3.4 ms, flip angle =  $6^\circ$  and  $0.5 \times 0.5 \times 0.5 \text{ mm}^3$  spatial resolution, and for the 4D flow scan: TR = 7.8 ms, TE = 4.6 ms, flip angle =  $8^\circ$ , VENC = 150 cm/s,  $0.8 \times 0.8 \times 0.8 \text{ mm}^3$  spatial and 80 ms temporal resolution. Cardiac synchronization was performed using retrospective ECG triggering. Phase-offset corrections were performed during reconstruction.

**Figure 5.1** illustrates the acquisition and reconstruction pipeline for each sequence. The two 2D flow MRI scans were acquired with a compressed sensing (CS) undersampling and reconstruction technique (**Figure 5.1a**). The CS reconstruction was performed using a total variation regularization over time, a regularization factor of  $r=0.001$ , and  $i=20$  iterations. The mean undersampling factor was  $R=5$ . With this technique, as described in [18], a high temporal

The 3D BB scan was acquired using a CS technique as well for high spatial resolution anatomical imaging of the vessel wall (scan time 3:30 min). K-space was undersampled  $R=5$  times with a Poisson disk pattern (**Figure 5.1b**) and reconstructed using a similar CS algorithm. An l1 regularization was used with  $r=0.01$  and  $i=50$  iterations. For all CS implementations the previously developed PROUD scanner software patch was used [19,20]. Reconstruction was carried out in MATLAB, using MRecon (Gyrotools, Zürich, Switzerland) and the BART reconstruction toolbox [21]. The 4D flow scan was accelerated using a k-t undersampling scheme of factor  $R=8$  and a k-t PCA reconstruction (**Figure 5.1c**), as described in [22]. Reconstruction was performed using CRecon (Gyrotools, Zurich, Switzerland) and a regularization factor of  $r=0.1$ . The acceleration led to a 10 min scan time for 4D flow.



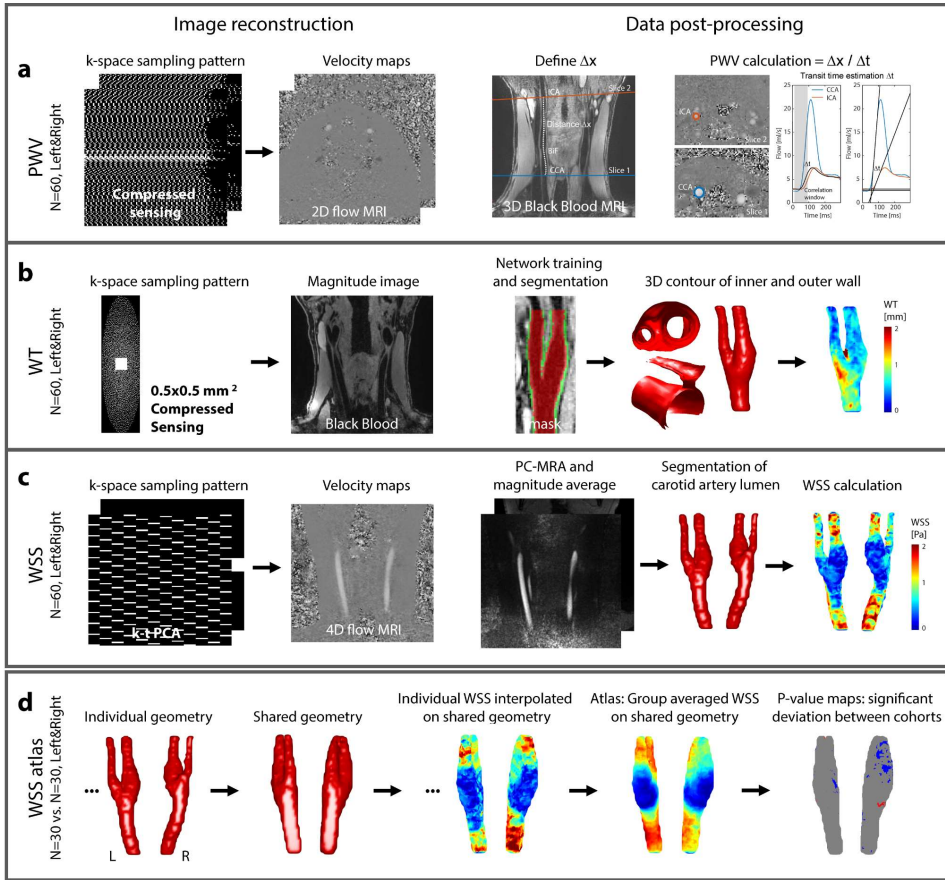


**Figure 5.1** Image reconstruction and post-processing steps for PWV (a), WT (b), WSS (c) and atlas calculation (d). For PWV calculation, a CS based image reconstruction technique enabled high temporal resolution 2D flow MRI scans and flow curves. Similarly, high spatial resolution 3D BB images were acquired with a CS undersampling and reconstruction technique. Vessel wall segmentations were performed using a trained network. A k-t PCA reconstruction recovered 8 times undersampled 4D flow MRI data, from which PC-MRA and averaged magnitude images were calculated for manual segmentation. From individual WSS data, group atlases were calculated.

### 5.3.3 Data post-processing

#### Pulse wave velocity

The two 2D flow scans were planned perpendicular to the CCA and ICA respectively. After CS reconstruction high temporal resolution flow curves could be derived by drawing an ROI in each vessel. Transit times  $\Delta t$  of the blood flow between the scans were then calculated as the time shift between flow curves in CCA and ICA. An average of foot-to-foot and correlation methods was used (Figure 5.1a) [4]. PWV was calculated by  $\text{PWV} = \Delta x / \Delta t$ . Path-lengths  $\Delta x$  were determined from the curved path between the 2D flow slices, as drawn in the 3D BB scan (Osirix [23] using a curved multiplanar reformation).

### Wall thickness

After CS reconstruction the coronal 3D BB scans were axially re-sliced. A manual segmentation of the vessel wall was performed in 80 consecutive slices around the bifurcation in one vessel of 21 subjects (56%FH, 44%female) with VesselMass (Leiden, Netherlands) [9]. Consecutively a neural network, similar to Bai *et al.* [24], was trained for automatic segmentation of the vessel wall. The network was trained to provide two labels, vessel lumen and vessel wall, around the carotid bifurcation. The training was performed slice wise in 2D and convergence was achieved after 50000 iterations. 13 datasets were used for training, 3 for validation and 5 for performance testing prior to application to a larger dataset. For half of the subjects the segmentation was performed on the left carotid, for the other half on the right carotid. In order to increase the amount of input data, for each side the data was horizontally mirrored. A residual neural network (ResNet) was trained with an adaptive learning rate algorithm (Adam) for each carotid side. The accuracy of the model was calculated based on DICE values for the lumen and the vessel wall. The model was then applied to all subjects, for left and right carotid respectively, providing a pixel wise mask for lumen and vessel wall. For WT calculation a smooth surface mesh of the inner and outer vessel wall was calculated based on the segmented masks. The intersection of the outward normal of each point of the inner wall with the outer wall was calculated. This value in mm represented the WT and is visualized as a map on the geometry of the inner wall (**Figure 5.1b**).

### Wall shear stress

After k-t PCA reconstruction, velocity maps, PC-MRAs (absolute value of the velocity vector, weighted by the magnitude image) and time average magnitude images were calculated from the 4D flow MRI data. This was necessary for accurate manual segmentation of the vessel lumen with Mimics (Materialise, Leuven, Belgium) 2 cm above and below the carotid bulb. Peak systolic WSS was then calculated in MATLAB as described in [25] by defining the shear force of the velocity on the segmented vessel wall for each artery.

#### 5.3.4 Statistical analysis

The data vector for each parameter consists of multiple dimensions  $d_{p_{WV}} \in \{\mathbb{R}^{N_{\text{Vessels}} \times N_{\text{Subjects}}}\}$ ,  $d_{WT} \in \{\mathbb{R}^{N_{\text{Vessels}} \times N_{\text{Subjects}} \times N_{3D\text{volume}}}\}$  and  $d_{WSS} \in \{\mathbb{R}^{N_{\text{Vessels}} \times N_{\text{Subjects}} \times N_{3D\text{volume}} \times N_{\text{Timepoints}}}\}$ , with sizes  $N_{\text{Vessels}}=2$ ,  $N_{\text{Subjects}}=61$ ,  $N_{3D\text{volume}} > 3000$ , and  $N_{\text{Timepoints}}=12$ .

For WT and WSS 3D cohort-averaged maps (called atlases) were calculated according to a previously published method [26]. From all lumen segmentations a shared geometry of the left and right carotid artery was created (only the manual segmentations based on 4D flow data were used, however black blood lumen segmentations were in the same range of  $\pm 2$  cm around the bifurcation). Then, individual segmentations were registered per category (*e.g.* females and males) onto the shared geometry [26]. WSS (and WT) values of each individual were interpolated on the surface of the shared geometry (**Figure 5.1d**). Finally, the registered and interpolated WSS (and WT) values were averaged per category to create a 3D atlas [27]. Differences between categories were calculated using a Wilcoxon rank sum test for each voxel. These 3D p-value maps indicated significant differences between two categories.  $P < 0.05$  was considered significant.

For additional comparison, individual WT and WSS values were spatially averaged per subject. Univariate linear regression models with PWV, mean WT and mean WSS as dependent variables were calculated for several patient characteristics (FH status, gender, smoking status, MAP, LDL, HDL, length and weight), separately. Additionally, three multivariate linear regression models were calculated with PWV, mean WT and mean WSS as dependent variables, and all predictors together.

Differences in PWV, mean WT and mean WSS for the categories FH status, gender and smoking status were additionally tested with a Wilcoxon rank sum test.

## 5.4 Results

There was no difference in age between FH patients and unaffected controls ( $p=0.912$ ), as well as there was no age difference for males and females ( $p=0.994$ ) and smokers and non-smokers ( $p=0.828$ ). There was also no difference in smoking status between FH patients and unaffected controls ( $p=0.776$ ), however, there were significantly more smoking males than smoking females ( $p=0.002$ ). FH patients had a significant higher LDL level than unaffected controls ( $p=0.014$ ), and there was no significant difference in HDL level ( $p=0.607$ ). For the male group no difference in LDL level was found ( $p=0.749$ ), but males had a significant lower HDL level than the female group ( $p<0.001$ ). Similarly, smokers did not have a significant different LDL level than non-smokers ( $p=0.254$ ), but smokers had a significant lower HDL level ( $p=0.005$ ). **Table 5.1** summarizes the characteristic per group.

**Table 5.1** Overview of group characteristics. Underlined values indicate significant differences.

	FH	Unaffected	Diff.	Male	Female	Diff.	Smokers	Non-smokers	Diff.
Characteristic	N=43	N=18	p-value	N=34	N=27	p-value	N=22	N=39	p-value
FH no. (%)	-	-	-	21 (62%)	22 (81%)	0.098	15 (68%)	28 (72%)	0.776
Male no. (%)	21 (49%)	13 (72%)	0.098	-	-	-	18 (82%)	16 (41%)	<u>0.002</u>
Smoking no. (%)	15 (35%)	7 (39%)	0.776	18 (53%)	4 (15%)	<u>0.002</u>	-	-	-
Mean age $\pm$ SD [yr]	33.1 $\pm$ 3.4	32.9 $\pm$ 2.9	0.912	32.9 $\pm$ 3.2	33.2 $\pm$ 3.1	0.994	32.7 $\pm$ 3.4	33.2 $\pm$ 3.0	0.828
Mean MAP $\pm$ SD [mm Hg]	88.3 $\pm$ 9.0	89.5 $\pm$ 9.1	0.693	91.5 $\pm$ 8.3	85.0 $\pm$ 8.5	<u>0.003</u>	92.7 $\pm$ 9.8	86.3 $\pm$ 7.6	0.010
Mean LDL $\pm$ SD [mg/dl]	161.8 $\pm$ 73.4	116.0 $\pm$ 50.1	<u>0.014</u>	150.8 $\pm$ 75.6	145.0 $\pm$ 64.0	0.749	157.2 $\pm$ 61.7	143.2 $\pm$ 74.8	0.254
Mean HDL $\pm$ SD [mg/dl]	26.4 $\pm$ 6.7	27.6 $\pm$ 8.6	0.607	23.7 $\pm$ 6.7	30.5 $\pm$ 6.1	<u>&lt;0.001</u>	23.3 $\pm$ 5.8	28.7 $\pm$ 7.3	<u>0.005</u>
Mean length $\pm$ SD [m]	1.73 $\pm$ 0.08	1.79 $\pm$ 0.07	<u>0.009</u>	1.80 $\pm$ 0.05	1.69 $\pm$ 0.07	<u>&lt;0.001</u>	1.78 $\pm$ 0.08	1.74 $\pm$ 0.09	0.105
Mean weight $\pm$ SD [kg]	77.0 $\pm$ 14.2	82.7 $\pm$ 13.5	0.209	83.8 $\pm$ 11.7	72.3 $\pm$ 14.5	<u>0.001</u>	82.5 $\pm$ 14.0	76.6 $\pm$ 14.0	0.081

For 6 datasets PWV could not be calculated due to too short transit times, for 20 (right) and 28 (left) datasets the network failed to segment the vessel wall sufficiently and for 4 datasets image quality of 4D flow MRI was poor. All these datasets were excluded from further analysis.

WSS atlases for all data are shown in **Figure 5.2**. Overall, a similar spatial WSS distribution was observed for all groups, which included low WSS in the carotid bulb and high WSS in the CCA, ICA and external carotid artery (ECA). FH, male and smoking groups revealed slightly lower WSS values in CCA and ICA than the corresponding groups. 13% of the left and 4% of the right vessel surface showed a significant lower WSS for men compared to women. Only 1% of the left carotid surface showed a

significant higher WSS. Similarly, for smoking vs. non-smoking subjects, 24% of the right and 8% of the left carotid surface showed a significant lower WSS for smokers, and no significant higher WSS was observed. For FH vs. unaffected controls 10% of the right and 2% of the left surface showed a significant lower WSS for FH patients, whereas 2% had a significant higher WSS in the left carotid.

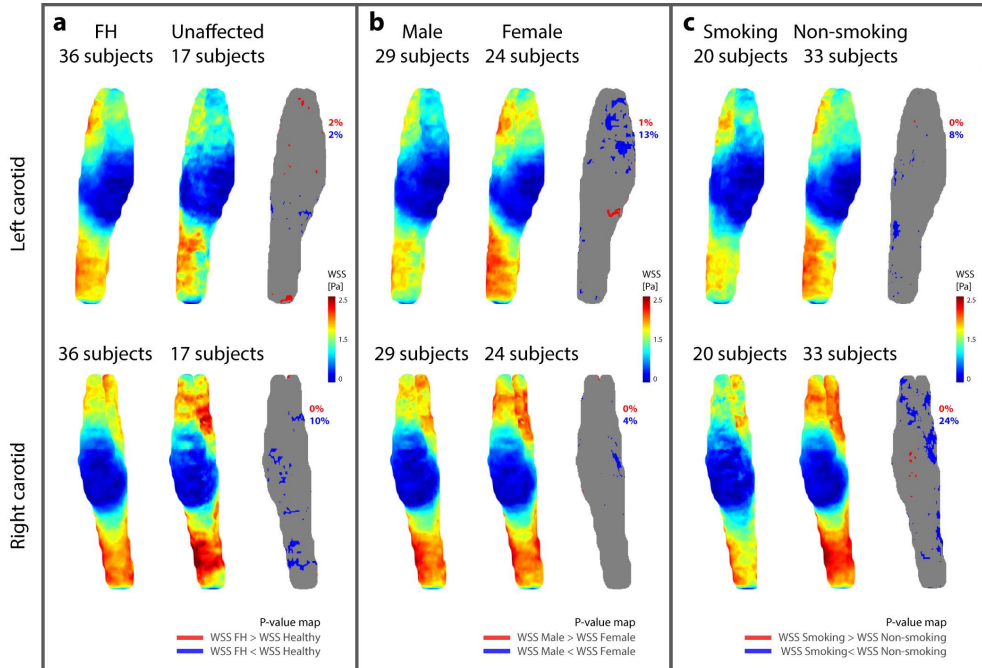


**Figure 5.2** WSS atlases for left and right carotid artery. (a) WSS atlases and p-value maps for FH patients and unaffected controls, (b) WSS atlases and p-value maps for males and females, (c) WSS atlases and p-values maps for smoking and non-smoking subjects. P-value maps indicate regions in which the WSS values of the cohorts are significantly different. Percentages in blue and red are the area of the surface in % which is either significantly lower (blue) or higher (red) than the reference. (Remark: p-value maps do not indicate the absolute difference between the atlases.)

**Figure 5.3** shows the WT atlases. The spatial distribution of WT values showed high WT in the carotid bulb and a low WT in CCA, ICA and ECA in all groups. WT atlases and the p-value maps indicated a higher WT in the male group compared to the female group. For the left 2% and the right 1% of the vessel surface showed a significant higher WT for FH patients compared to unaffected controls. 2% of the surface showed a significant lower WT in the left and right carotid. Similarly, for the male group 6% of the surface showed a significant higher WT of the left and 20% of the right carotid, and 2% a significant lower WT (left). For the smoking group 2% of the left surface showed a higher WT and 7% of the right surface. For the left and right carotid 1% of the smoking group had a lower WT.

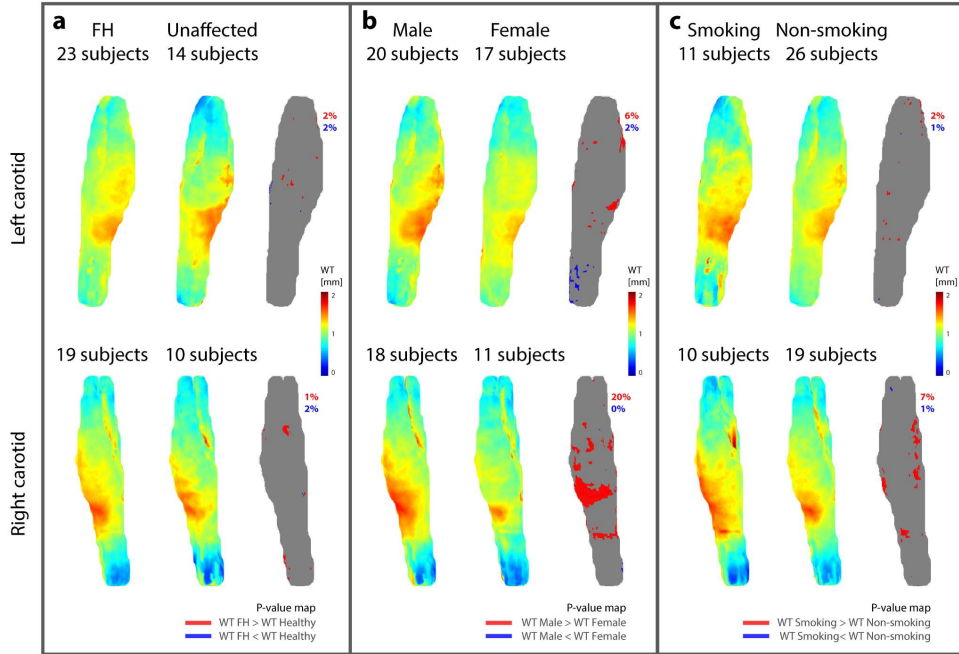


**Figure 5.3** WT atlases for left and right carotid artery. (a) WT atlases and p-value maps for FH patients and unaffected controls, (b) WT atlases and p-value maps for males and females, (c) WT atlases and p-values maps for smoking and non-smoking subjects. P-value maps indicate regions in which the WT values of the cohorts are significantly different. Percentages in blue and red are the area of the surface in % which is either significantly lower (blue) or higher (red) than the reference. (Remark: p-value maps do not indicate the absolute difference between the atlases.)

To better understand differences between atlases, but also between the non-registered non-interpolated individual data, **Figure 5.4** shows normalized histograms of WSS (**Figure 5.4a**) and WT (**Figure 5.4b**) values. In the histogram of atlas values, differences between unaffected/FH, female/male and non-smoking/smoking were found for WSS (differences in medians:  $\Delta_{FH} = -0.03$  Pa,  $\Delta_{male} = -0.18$  Pa,  $\Delta_{smoking} = -0.28$  Pa) and WT (differences in medians:  $\Delta_{FH} = 0.04$  mm,  $\Delta_{male} = 0.12$  mm,  $\Delta_{smoking} = 0.10$  mm). Similar differences were observed in the histograms of the individual non-registered non-interpolated values for WSS (differences in medians:  $\Delta_{FH} = -0.08$  Pa,  $\Delta_{male} = -0.12$  Pa,  $\Delta_{smoking} = -0.22$  Pa) and WT (differences of medians:  $\Delta_{FH} = -0.02$  mm,  $\Delta_{male} = 0.15$  mm,  $\Delta_{smoking} = 0.10$  mm). Overall, in groups in which WSS tended to be lower, WT values tended to be higher.

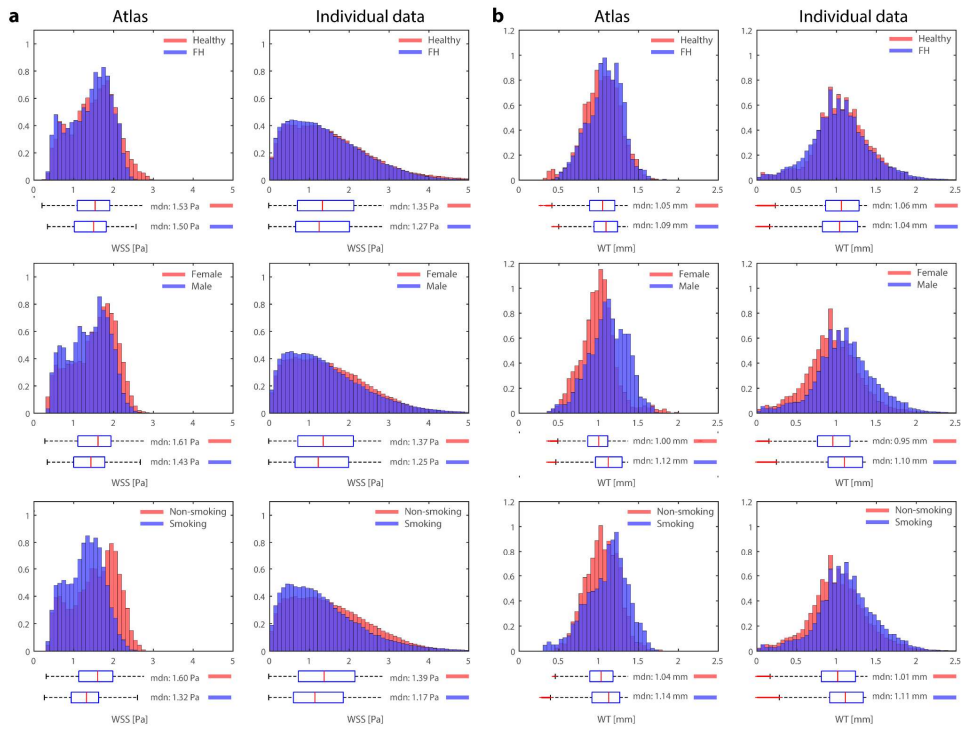


**Figure 5.4** Normalized histograms showing the (a) WSS and (b) WT value distribution per group (FH/unaffected, male/female, smoking/non-smoking). In the left columns of (a) and (b) respectively, the atlas values are plotted per group. In the right columns the individual data (non-registered and non-interpolated) is plotted per group. For each histogram corresponding boxplots are shown below and median values per group are reported.

The results of comparing spatial mean WSS and mean WT for all subjects for each group are summarized in **Table 5.2**. For smokers a significantly lower PWV of 4.79 m/s (95% CI, 4.34 to 5.23) in comparison to non-smokers with 5.43 m/s (95% CI, 5.08 to 5.78) was found ( $p=0.043$ ). A higher mean WT of 1.13 mm (95% CI, 1.10 to 1.16) in smokers than in non-smokers with 1.09 mm (95%, 1.05 to 1.12) was found ( $p=0.169$ ). Additionally, a significantly higher mean WT ( $p=0.024$ ) of 1.13 mm (95% CI, 1.10 to 1.16) was also observed in males in comparison to females with a mean WT of 1.06 mm (95% CI, 1.02 to 1.10). A significantly lower mean WSS ( $p=0.011$ ) of 1.37 Pa (95% CI, 1.38 to 1.56) was found in smokers in comparison to non-smokers with 1.59 mm (95% CI, 1.44 to 1.72). No significant differences were found for PWV, mean WT and mean WSS when comparing FH and unaffected controls.

**Table 5.2** Mean values for all subjects (and left and right carotid) within each group for PWV, mean WT and mean WSS. P-values as calculated with the Wilcoxon rank sum test. Underlined values indicate significant differences.

Groups	PWV [m/s]		Mean WT [mm]		Mean WSS [Pa]	
	Mean (95% CI)	Mean difference (p-value)	Mean (95% CI)	Mean difference (p-value)	Mean (95% CI)	Mean difference (p-value)
FH	5.09 (4.79 to 5.39)	0.25 (0.794)	1.11 (1.08 to 1.14)	-0.02 (0.518)	1.45 (1.38 to 1.56)	0.13 (0.238)
Unaffected	5.34 (4.71 to 5.96)		1.09 (1.05 to 1.13)		1.58 (1.44 to 1.72)	
Males	5.19 (4.82 to 5.56)	-0.07 (0.959)	1.13 (1.10 to 1.16)	-0.07 (0.024)	1.47 (1.37 to 1.56)	0.08 (0.369)
Females	5.12 (4.68 to 5.55)		1.06 (1.02 to 1.10)		1.55 (1.43 to 1.67)	
Smoking	4.79 (4.34 to 5.23)	0.64 (0.043)	1.13 (1.10 to 1.16)	-0.04 (0.169)	1.37 (1.38 to 1.56)	0.22 (0.011)
Non-smoking	5.43 (5.08 to 5.78)		1.09 (1.05 to 1.12)		1.59 (1.44 to 1.72)	

In **Figure 5.5a** a linear regression for PWV, mean WT and mean WSS is shown for all subjects, with the correlation coefficient R not being significant for all three cases (p-values > 0.05). In contrast **Figure 5.5b** shows a linear regression for all voxels of the WSS atlas and WT atlas per group. The correlation was stronger for FH (R=-0.51), male (R=-0.46) and smokers (R=-0.48) than for unaffected controls (R=0.32), females (R=-0.30) and non-smokers (R=-0.42).

**Table 5.3** shows the results of the univariate linear regression with categorical variables FH/unaffected, male/female, smoking/non-smoking. **Table 5.3** shows further the relation of PWV, mean WT and mean WSS with age, MAP, LDL level, HDL level, length and weight of the subject. A negative correlation between smoking and PWV was found. For mean WT the correlation coefficient was significant in one case: a positive correlation between mean WT and male gender. For mean WSS the correlation coefficient was significant for several cases: a negative correlation between mean WSS and smoking, a negative correlation between mean WSS and age, a positive correlation between mean WSS and HDL, and a negative correlation between mean WSS and weight was found.

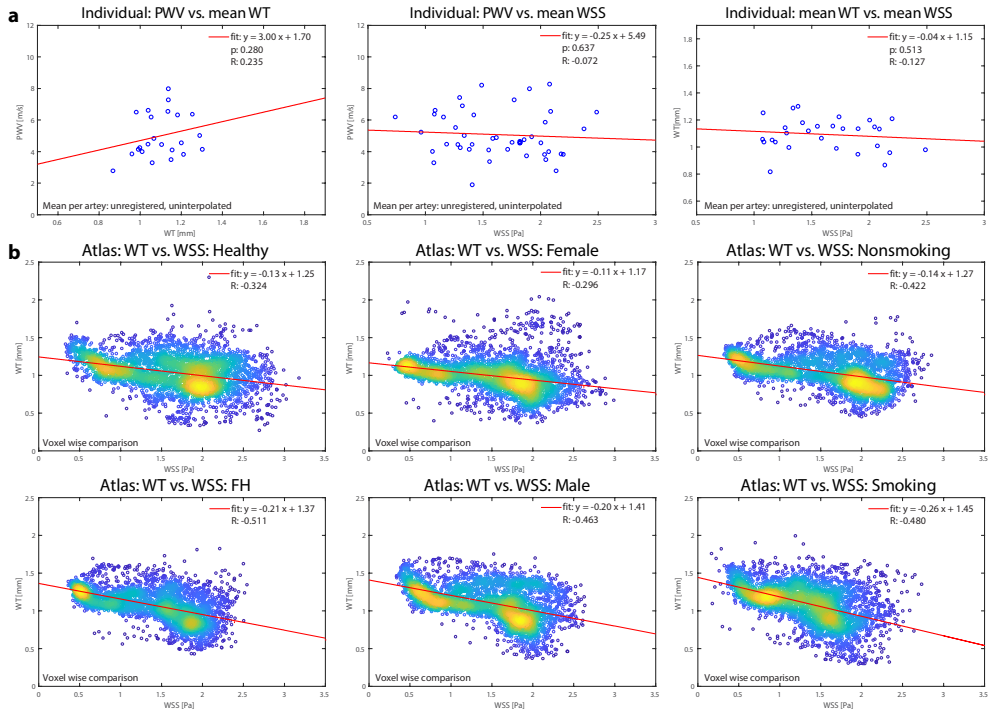


**Figure 5.5** (a) Linear regression of PWV, mean WT and mean WSS values for all subjects. (b) Linear regression of WSS atlas and WT atlas values. Plots represent each voxel on the vessel surface and are done for each group.

**Table 5.4** shows the results of the three multivariate linear regression for PWV, mean WT and mean WSS. It indicated, that smoking and high HDL level might be independent predictors for a lower PWV. No dependencies were found for mean WT, a tendency for male gender being an independent predictor for a higher WT can be seen. The multivariate linear regression also showed, that age is an independent predictor of a lower mean WSS.

**Table 5.3** Univariate linear regression results of PWV, mean WT and mean WSS with separate predictors FH, male and smoking status, as well as age MAP, LDL level, HDL level, body length and weight. Underlined values indicate significant differences.

Risk factor	PWV [m/s]			Mean WT [mm]			Mean WSS [Pa]		
	Slope	R <sup>2</sup>	p	Slope	R <sup>2</sup>	p	Slope	R <sup>2</sup>	p
FH	-0.246	0.005	0.466	0.016	0.004	0.637	-0.108	0.015	0.210
Male	0.072	0.001	0.819	0.072	0.073	<u>0.029</u>	-0.086	0.011	0.283
Smoking	-0.640	0.042	<u>0.039</u>	0.044	0.024	0.215	-0.214	0.064	<u>0.009</u>
Age [years]	-0.002	0.000	0.965	0.002	0.002	0.751	-0.029	0.045	<u>0.029</u>
MAP [mmHg]	0.004	0.001	0.818	0.003	0.030	0.162	-0.008	0.028	0.085
LDL [mg/dl]	0.004	0.026	0.105	0.000	0.002	0.708	0.000	0.011	0.291
HDL [mg/dl]	-0.040	0.036	0.057	-0.003	0.034	0.141	0.018	0.099	<u>0.001</u>
Length [m]	0.022	0.000	0.990	0.184	0.012	0.382	-0.465	0.009	0.339
Weight [kg]	0.005	0.002	0.668	0.002	0.032	0.151	-0.007	0.057	<u>0.014</u>



**Table 5.4** Multivariate linear regression results for PWV, mean WT and mean WSS with predictors FH, male and smoking status, as well as age MAP, LDL level, HDL level, body length and weight. The last column reports  $R^2$  and p-values of the entire model. Underlined values indicate significant differences.

Risk factor	PWV [m/s]		Mean WT [mm]		Mean WSS [Pa]	
	Slope	p	Slope	p	Slope	p
FH	-0.446	0.202	0.068	0.147	-0.112	0.239
Male	-0.178	0.706	0.092	0.078	0.122	0.291
Smoking	-1.095	<u>0.002</u>	0.024	0.543	-0.174	0.051
Age [years]	-0.044	0.379	0.001	0.839	-0.035	<u>0.008</u>
MAP [mmHg]	0.005	0.799	0.000	0.929	0.003	0.578
LDL [mg/dl]	0.005	0.064	0.000	0.551	0.000	0.982
HDL [mg/dl]	-0.071	<u>0.011</u>	0.002	0.651	0.013	0.060
Length [m]	1.516	0.576	-0.089	0.769	-0.432	0.536
Weight [kg]	-0.011	0.425	0.001	0.442	-0.005	0.125
<b>Overall model:</b>	<b><math>R^2 = 0.170</math>, <math>p = 0.037</math></b>		<b><math>R^2 = 0.124</math>, <math>p = 0.546</math></b>		<b><math>R^2 = 0.223</math>, <math>p = 0.003</math></b>	

## 5.5 Discussion

In this study we investigated differences in PWV, 3D WT and 3D WSS between patients with FH on life-long statin treatment and unaffected controls. For individual analysis, no significant differences in PWV, mean WT, and mean WSS for FH patients in comparison to unaffected controls were found. This is in line with previous findings of the same cohort, supporting the effectiveness of the lipid-lowering treatment [6]. An inverse spatial relation between WSS and WT was found at a voxel level, which might indicate a protective character of high WSS [13]. Furthermore, a significantly lower PWV in smokers than in non-smokers was observed, which was not expected. Significantly lower mean WT values in women than in men and lower mean WT values in non-smokers than in smokers however, were as reported in other studies. Mean WSS values were significantly higher in non-smokers than in smokers.

Mean WT values of 1.11 mm (95% CI, 1.08 to 1.14) for FH patients and 1.09 mm (95% CI, 1.05 to 1.13) for unaffected siblings were much larger than mean IMT values of 0.555 mm (95% CI, 0.542 to 0.567) for FH patients and 0.551 mm (95% CI, 0.531 to 0.570) in unaffected siblings as measured in a preceding study measured with ultrasound [6]. Previous studies on the comparison between mean WT measured with 2D black blood MRI and mean IMT measured with ultrasound showed however no differences between the techniques [28]. That study used a high spatial resolution MRI technique with 0.25 mm<sup>2</sup> in-plane resolution, which is why overestimation of the WT in our study could be an effect of partial volume effects and thus highlights the need for higher spatial resolution. Additionally, in our study we reported mean WT values as calculated over the entire vessel surface, which might not compare to WT values of CCA, ICA and bulb which are reported separately. On a relative scale, gender differences in mean WT as reported in our study are similar to gender differences in CCA IMT of around 0.04 mm in a similar aged group [29]. Also, relative difference in mean WT for smoking status were similar in a similar aged group (IMT smokers 0.52±0.034 mm and IMT non-smokers 0.46±0.036 mm [30]).

We did not find correlations between PWV and MAP although it was shown that PWV is blood pressure dependent [31]. This might be explained by physiological changes in the time between MAP measurement and MRI acquisition and from the difference between upright and supine position.

We did not expect to find a significantly lower PWV in smokers in comparison to non-smokers, as smoking is normally associated with vessel stiffening (as *e.g.* measured by Lerant et. al. 7.46±1.1 m/s for smokers and 6.67±0.84 m/s for non-smokers [30]). Smoking, regular or prior to the scan, increases the blood pressure and can therefore effect PWV estimation. It remains difficult to discriminate between adaptive effects of regular smoking, abstinence [32] or smoking before the scan, as we did not control for these factors.

Atherosclerotic changes of the vessel wall are highly correlated with age. Typically, changes become visible in the 30-40s and in men earlier than in women. Lipid-deposition in the vessel wall starts at an age of 20 years old, for FH patients even at an earlier age. Nevertheless, in this study no correlation with age was found for PWV, and mean WT (there was however a correlation for mean WSS). However, the age range of the study cohort was rather small (average age 32.9±3.1 years). Gender and smoking status are amongst the strongest predictors for an enlarged WT as was also found in our study.

Correlations between mean WSS and mean WT are not very strong. Although mean WT values (and also mean values of left and right artery) usually lead to a good prediction of cardiovascular events, it could still be true that the minimum or maximum WSS or WT measurements leads to better predictions [33].

#### **5.5.1 Limitations of this study**

One limitation of the selected group is a significant differences in smoking statues between the male and female group. At the current state this makes an interpretation between male and female, as well as smoking non-smoking groups difficult.

Accurate estimation of absolute WSS on the vessel wall is challenging as the location of the vessel wall can be inaccurate. Yet, regions of low and high WSS in the carotid artery indicate which parts are prone to atherosclerotic changes.

Similarly, automated WT estimation is difficult and prone to errors due to partial volume effects. Also, the step from a voxel wise mask to a smooth vessel surface can lead to errors, which however will be the same for all subjects of this study. Additionally, overestimation of the WT by the trained network cannot be excluded. The neural network can be further optimized and retrained to reduce the number of excluded segmentations.

#### **5.6 Conclusion**

There were no differences found in PWV, WT and WSS in early in life treated FH patients in comparison to unaffected controls. Although the investigated cohort of FH patients is prone to early atherosclerotic changes, the results from this study show that the carotid hemodynamics are not different from unaffected controls, which is in agreement with effective treatment.

## 5.7 Bibliography

1. Braamskamp MJAM, Wiegman A. Familial Hypercholesterolemia: Advances in Understanding the Early Natural History. *Curr Cardiovasc Risk Rep.* 2012;6:562–6.
2. Goldberg AC, Hopkins PN, Toth PP, Ballantyne CM, Rader DJ, Robinson JG, *et al.* Familial Hypercholesterolemia: Screening, diagnosis and management of pediatric and adult patients. *J Clin Lipidol.* 2011;5:S1–8.
3. Bos D, Portegies ML, van der Lugt A, Bos MJ, Koudstaal PJ, Hofman A, *et al.* Intracranial Carotid Artery Atherosclerosis and the Risk of Stroke in Whites The Rotterdam Study. *JAMA Neurol.* 2014;71:405–11.
4. Stein JH, Korcarz CE, Post WS. Use of carotid ultrasound to identify subclinical vascular disease and evaluate cardiovascular disease risk: Summary and discussion of the american society of echocardiography consensus statement. *Prev. Cardiol.* 2009. p. 34–8.
5. Ku DN. Blood flow in arteries. *Edward Arnold Publ.* 1974;£12.-:399–434.
6. Luijckx IK, Wiegman A, Kusters DM, Hof MH, Groothoff JW, de Groot E, *et al.* 20-Year Follow-up of Statins in Children with Familial Hypercholesterolemia. *N Engl J Med.* 2019;381:1547–56.
7. Coolen BF, Calcagno C, van Ooij P, Fayad ZA, Strijkers GJ, Nederveen AJ. Vessel wall characterization using quantitative MRI: what's in a number? *Magn Reson Mater Physics,* 2017;31:201–22.
8. Ku DN, Giddens DP, Zarins CK, Glagov S. Pulsatile flow and atherosclerosis in the human carotid bifurcation. Positive correlation between plaque location and low and oscillating shear stress. *Arteriosclerosis.* 1985;5:293–302.
9. Duivenvoorden R, de Groot E, Afzali H, VanBavel ET, de Boer OJ, Laméris JS, *et al.* Comparison of *In Vivo* Carotid 3.0-T Magnetic Resonance to B-Mode Ultrasound Imaging and Histology in a Porcine Model. *JACC Cardiovasc Imaging.* 2009;2:744–50.
10. Dhawan SS, Nanjundappa RPA. Shear stress and plaque development. *Physiol Behav.* 2017;176:139–48.
11. Markl M, Wegent F, Zech T, Bauer S, Strecker C, Schumacher M, *et al.* *In vivo* wall shear stress distribution in the carotid artery: effect of bifurcation geometry, internal carotid artery stenosis, and recanalization therapy. *Circ Cardiovasc Imaging.* 2010;3:647–55.
12. Gotschy A, Bauer E, Schrodtt C, Lykowsky G, Ye YX, Rommel E, *et al.* Local arterial stiffening assessed by MRI precedes atherosclerotic plaque formation. *Circ Cardiovasc Imaging.* 2013;6:916–23.
13. Malek AM, Alper SL. Hemodynamic Shear Stress and Its Role in Atherosclerosis. *Stress Int J Biol Stress.* 1999;282:2035–42.
14. Lehoux S, Tedgui A. Cellular mechanics and gene expression in blood vessels. *J. Biomech.* 2003. p. 631–43.
15. van Popele NM, Grobbee DE, Bots ML, Asmar R, Topouchian J, Reneman RS, *et al.* Association between arterial stiffness and atherosclerosis. *Stroke.* 2001;32:454–61.
16. Bos D, Portegies MLP, Van Der Lugt A, Bos MJ, Koudstaal PJ, Hofman A, *et al.* Intracranial carotid artery atherosclerosis and the risk of stroke in whites: The Rotterdam study. *JAMA Neurol.* 2014;71:405–11.
17. de Roos A, van der Grond J, Mitchell G, Westenberg J. Magnetic Resonance Imaging of Cardiovascular Function and the Brain—Is dementia a cardiovascular-driven disease? *Circulation.* 2017;135:2178–95.

18. Peper ES, Strijkers GJ, Gazzola K, Potters W V, Motaal AG, Luirink IK, *et al.* Regional assessment of carotid artery pulse wave velocity using compressed sensing accelerated high temporal resolution 2D CINE phase contrast cardiovascular magnetic resonance. *J Cardiovasc Magn Reson.* 2018;20:1–12.
19. Peper ES, Gottwald LM, Zhang Q, Coolen BF, van Ooij P, Nederveen AJ, *et al.* Highly accelerated carotid 4D flow MRI using Pseudo-Spiral Cartesian acquisition and a Total Variation constrained Compressed Sensing reconstruction. *J Cardiovasc Magn Reson. Journal of Cardiovascular Magnetic Resonance;* 2020.
20. Gottwald L, Peper E, Zhang Q, Coolen B, Strijkers G, Planken R, *et al.* Pseudo spiral compressed sensing for aortic 4D Flow MRI: a comparison with k-t principal component analysis. *Proc Intl Soc Mag Reson Med* 26. 2018. p. 3448.
21. Uecker M, Ong F, Tamir JI, Bahri D, Virtue P, Cheng JY, *et al.* Berkeley Advanced Reconstruction Toolbox. *Proc Intl Soc Mag Reson Med.* 2015. p. 2486.
22. Pedersen H, Kozerke S, Ringgaard S, Nehrke K, Won YK. K-t PCA: Temporally constrained k-t BLAST reconstruction using principal component analysis. *Magn Reson Med.* 2009;62:706–16.
23. Rosset A, Spadola L, Ratib O. OsiriX: An Open-Source Software for Navigating in Multidimensional DICOM Images. *J Digit Imaging.* 2004;17:205–16.
24. Bai W, Sinclair M, Tarroni G, Oktay O, Rajchl M, Vaillant G, *et al.* Automated cardiovascular magnetic resonance image analysis with fully convolutional networks. *J Cardiovasc Magn Reson.* 2018;20:1–17.
25. Potters W V., Marquering HA, VanBavel E, Nederveen AJ. Measuring wall shear stress using velocity-encoded MRI. *Curr Cardiovasc Imaging Rep.* 2014;7:1–12.
26. van Ooij P, Cibis M, Rowland E, Vernooij M, van der Lugt A, Weinberg P, *et al.* Spatial correlations between MRI-derived wall shear stress and vessel wall thickness in the carotid bifurcation. *Eur Radiol Exp.* 2018;
27. van Ooij P, Potters W V., Nederveen AJ, Allen BD, Collins J, Carr J, *et al.* A methodology to detect abnormal relative wall shear stress on the full surface of the thoracic aorta using four-dimensional flow MRI. *Magn Reson Med.* 2015;73:1216–27.
28. Duivenvoorden R, De Groot E, Elsen BM, Lamefís JS, Van Der Geest RJ, Stroes ES, *et al.* In vivo quantification of carotid artery wall dimensions 3.0-tesla MRI versus b-mode ultrasound imaging. *Circ Cardiovasc Imaging.* 2009;2:235–42.
29. Tan TY, Lu CH, Lin TK, Liou CW, Chuang YC, Schminke U. Factors associated with gender difference in the intima-media thickness of the common carotid artery. *Clin Radiol. The Royal College of Radiologists;* 2009;64:1097–103.
30. Léránt B, Straesser C, Kovács RK, Oláh L, Kardos L, Csiba L. Morphological, hemodynamic and stiffness changes in arteries of young smokers. *Perspect Med. Elsevier GmbH;* 2012;1–12:152–5.
31. Ma Y, Choi J, Hourlier-Fargette A, Xue Y, Chung HU, Lee JY, *et al.* Relation between blood pressure and pulse wave velocity for human arteries. *Proc Natl Acad Sci USA.* 2018;115:11144–9.
32. Vafaee MS, Gjedde A, Imamirad N, Vang K, Chakravarty MM, Lerch JP, *et al.* Smoking normalizes cerebral blood flow and oxygen consumption after 12-hour abstention. *J Cereb Blood Flow Metab.* 2015;35:699–705.

33. Polak JF, Pencina MJ, Meisner A, Pencina KM, Brown LS, Wolf PA, *et al.* Associations of carotid artery intima-media thickness (IMT) with risk factors and prevalent cardiovascular disease: Comparison of mean common carotid artery IMT with maximum internal carotid artery IMT. *J Ultrasound Med.* 2010;29:1759–68.

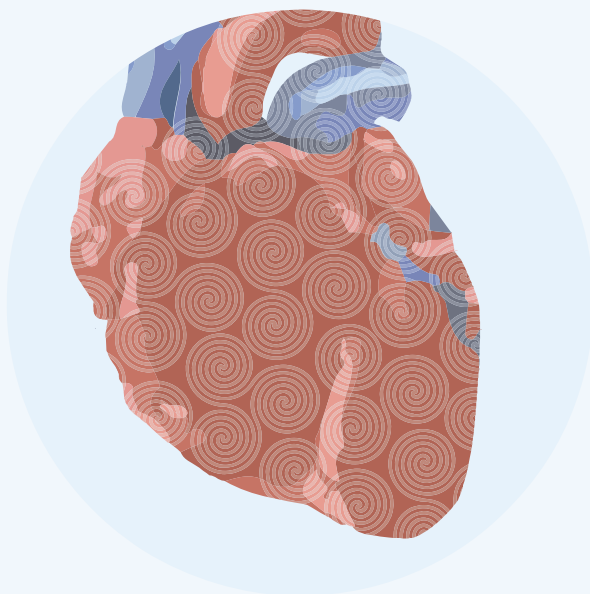


# CHAPTER 6

An isolated beating pig heart platform for a comprehensive evaluation of intracardiac blood flow with 4D flow MRI: a feasibility study

Eva S. Peper,  
Alberto M. Leopaldi,  
Sjoerd van Tuijl,  
Bram F. Coolen,  
Gustav J. Strijkers,  
Jan Baan,  
R. Nils Planken,  
Arend de Weger,  
Aart J. Nederveen,  
Henk A. Marquering  
and Pim van Ooij

European Radiology  
Experimental. 2019





## 6.1 Abstract

**Background:** Cardiac magnetic resonance imaging (MRI) in large animals is cumbersome for various reasons, including ethical considerations, costs of housing and maintenance, and need for anaesthesia. Our primary purpose was to show the feasibility of an isolated beating pig heart model for four-dimensional (4D) flow MRI for investigating intracardiac blood flow patterns and flow parameters using slaughterhouse side products. In addition, the feasibility of evaluating transcatheter aortic valve replacement (TAVR) in the model was investigated.

**Methods:** Seven slaughterhouse pig hearts were installed in the MRI-compatible isolated beating pig heart platform. First Langendorff perfusion mode was established; then, the system switched to working mode, in which blood was actively pumped by the left ventricle. A pacemaker ensured a stable HR during 3-T MRI scanning. All hearts were submitted to human physiological conditions of cardiac output and stayed vital for several hours. Aortic flow was measured from which stroke volume, cardiac output, and regurgitation fraction were calculated

**Results:** 4D flow MRI acquisitions were successfully conducted in all hearts. Stroke volume was  $31 \pm 6$  mL (mean  $\pm$  standard deviation), cardiac output  $3.3 \pm 0.9$  L/min, and regurgitation fraction  $16\% \pm 9\%$ . With 4D flow, intracardiac and coronary flow patterns could be visualized in all hearts. In addition, we could study valve function and regurgitation in two hearts after TAVR.

**Conclusions:** The feasibility of 4D flow MRI in an isolated beating pig heart loaded to physiological conditions was demonstrated. The platform is promising for preclinical assessment of cardiac blood flow and function.

## 6.2 Introduction

Large animal models, in particular sheep and pigs, have provided indispensable and valuable insights in cardiac anatomy and physiology during health and disease, as they are easy to manipulate and to reproduce [1]. Additionally, working animal models have demonstrated to be realistic training models for cardiologic intervention [2]. However, laboratory animal husbandry of sheep or pigs is expensive and medical experiments with large animals are subject to increased ethical objections in many countries. The use of isolated pig hearts harvested from pigs slaughtered for human consumption might be an acceptable alternative, as it leads to a reduction in the use of live animals. Additionally, isolated hearts have the advantage of controlled physiological conditions (*e.g.*, controlled blood pressure) and experimental settings (*e.g.*, surgical intervention or drug administration) [3].

A promising non-invasive imaging modality to measure three-dimensional (3D) blood flow is time-resolved three-dimensional phase contrast magnetic resonance imaging (MRI), *i.e.* four-dimensional (4D) flow MRI [4,5]. This technique facilitates accurate 3D visualization and quantification of blood flow, in conjunction with the quantification of cardiac parameters such as cardiac output (CO), stroke volume (SV), and regurgitation fraction [6]. Studies showed that 4D flow MRI is valuable for intracardiac blood flow visualization [7] and vortex detection [8], flow assessment through all four heart valves [9,10], as well as for detecting flow alterations after TAVR and other surgical procedures in the aorta [11–14]. Traditionally, transthoracic or transesophageal echocardiography are used to follow-up after surgical interventions like transcatheter aortic valve replacement (TAVR) [15]. However, it remains challenging to measure the extent and type of regurgitation or deviations in flow patterns with echocardiography [15,16].

Using 4D flow MRI in animal models, *in vivo* experiments of juvenile pigs have demonstrated that intraventricular flow patterns change under drug-induced stress [17]. This technique has also revealed disturbed left ventricle (LV) flow patterns after mitral annuloplasty in sheep, correlated with the size of the annuloplasty ring [18].

In this study, we introduce an MRI-compatible platform for 4D flow measurements in isolated beating pig hearts, with real blood actively pumped by the LV at physiological pressures. This provides *in vivo* blood flow behavior, resulting in physiological coronary flow and myocardial perfusion with good-to-excellent MRI contrast [3,19]. In a previous study, Schuster *et al.* [3] presented an MRI-compatible isolated beating pig heart model to investigate cardiac perfusion. Its design was based on the Langendorff model [20], which allows for coronary perfusion and LV contraction, but not for LV filling and output. The working heart model presented in this study is similar to that described by Vaillant *et al.* [21]. It actively pumps blood in both ventricles, which, in contrast to Langendorff perfusion, causes natural coronary filling, mimicking physiological heart function and providing real control on the relevant physiological parameters.

We investigate feasibility and reproducibility of 4D flow MRI in an *ex vivo* beating pig heart platform by measuring flow parameters and performing flow visualization in five repeated pig heart experiments with native valves. In two additional experiments we test the feasibility of the working platform for evaluating transcatheter aortic valve replacement (TAVR) procedures. We hypothesized that this platform may help investigating the influence of different surgical procedures on intracardiac

flow and the performance of MRI sequences in different pathophysiological settings, without needing a live animal experiment.

## 6.3 Methods

### 6.3.1 Preparation

In this study seven hearts were retrieved from pigs slaughtered for human consumption (Dutch Landrace hybrids, approximately 110 kg live weight). The protocols at the slaughterhouse and during the experiment were in agreement with European Community regulations 1069/2009 and 142/2011 regarding the use of slaughterhouse byproducts for research, and were approved by the associated legal authorities of animal welfare. 4D flow MRI was applied in five pig hearts with native valves. In two additional experiments described in the supplemental material, the native valves of two other hearts were replaced in the preparation phase of the experiment with TAVR valves by a specialist (AdW) with 12 years of experience. All experimental and post-processing steps were the same as for hearts with native valves. The prosthetic valves available were the CoreValve (29 mm, Medtronic Inc., Minneapolis, Minnesota, USA) and Edwards SAPIENS XT (26 mm, Edwards Lifesciences LLC, Irvine, California, USA). The prosthetic valve sizes were not selected according to the pigs annulus size, which is why the Edwards SAPIENS XT valve was additionally stabilized by a purse string suture.

Each slaughterhouse pig heart was harvested and arrested with crystalloid cardioplegic solution after a very short warm ischaemic time. Approximately 10 L of blood was collected from the same animal and heparinized. The heart was transported in an iced cardioplegic solution and connected to the MRI compatible isolated beating pig heart platform [19] (PhysioHeart™ platform, LifeTec Group BV, Eindhoven, The Netherlands) on average 4 hours after death. During preparation, the pericardial sac was discarded and the right pulmonary veins, vena cava inferior, vena cava superior and the left azygos vein were tied off. A 27-mm cannula was inserted into the opened left pulmonary vein and secured with a purse string suture. The connecting tubes were compliant for blood flow and connected to a preload simulating pulmonary resistances. A cannula with an internal diameter of 24 mm was inserted into the ascending aorta and fixed downstream to the aortic valve.

The aortic tube drained in an afterload simulating body resistance (systolic/diastolic pressure approximately 120/80 mmHg). A CO of approximately 4.5 L/min was maintained during the experiments to match human conditions. The CO was real-time controlled via a flow sensor and regulated by adapting the preload and afterload resistances. A 17-mm cannula was inserted in the pulmonary artery, which was connected directly to a reservoir. The balanced blood was warmed and oxygenated by a heart lung machine outside the MRI room. The blood returned as a nutrient-rich, warm, oxygenated solution of 5% CO<sub>2</sub> and 25% O<sub>2</sub> and with a temperature of 38 °C. A schematic overview of the connections of pre- and afterload is shown in **Figure 6.1a**.

### 6.3.2 Reperfusion

To resuscitate the heart a Langendorff perfusion mode [20] was created by cross clamping preload and afterload systems (**Figure 6.1b**). Via a side port in the aortic cannula blood was pumped retrograde in the aorta at approximately 80 mmHg closing off the aortic valve forcing flow into the coronary system.

After perfusion of the myocardium, the deoxygenated blood drained in the coronary sinus, the right atrium, and the right ventricle. Through the pulmonary artery blood was pumped back to the reservoir. The heart was left in Langendorff perfusion to recover for about 30 min until a steady state (in terms of a physiological color and temperature, stable sinus rhythm, a constant coronary flow and constant pressures) was obtained (**Supplementary Video 6.1**).

Hereafter, the platform was switched to working mode (**Figure 6.1c**): Langendorff perfusion was stopped and the aorta and left pulmonary vein (preload) were opened, resulting in blood actively pumped by the LV with sufficient preload leading to a physiological CO. Coronary filling was created by LV function and aortic pressure only. To ensure a stable heart rate (HR) during MRI scanning, a pacemaker was attached to the heart. The paced HR was approximately 5–10 beats per min (bpm) over the irregular HR of the resuscitated heart. As soon as the heart was beating with a stable rhythm (approximately 20 min after switching from Langendorff mode to working mode), the setup was inserted into the MRI scanner (**Figure 6.1e**) and the acquisitions were started.

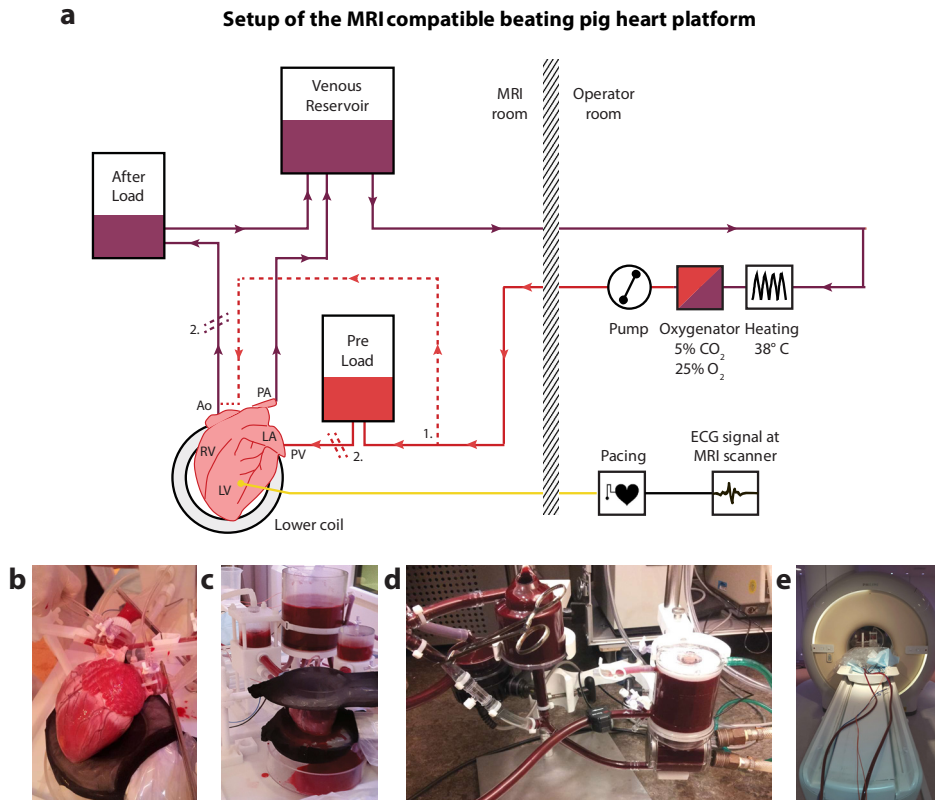


**Figure 6.1** Experimental setup of the MRI-compatible beating pig heart platform: **(a)** Experimental setup of the MRI compatible PhysioHeart™ platform (LifeTec, Eindhoven, The Netherlands). The heart was connected to a preload and afterload system. The venous blood (purple) was heated and oxygenated outside the MRI room and pumped back to the experiment afterwards (red). The dotted lines indicate 1. coronary perfusion during Langendorff mode and 2. the cross clamping of the aorta and the pulmonary vein. Ao: Aorta, LA: Left atrium, LV: Left ventricle, PA: Pulmonary artery, PV: Pulmonary vein, RV: Right ventricle. **(b)** The resuscitated, beating pig heart installed in the platform between the two coils on the patient bed before scanning. **(c)** The heart during preparation, cooled on ice and attached to the aortic cannula and the pulmonary vein cannula. **(d)** Heating device and oxygenator outside the MRI room. **(e)** Setup during the scan, with two tubes leading to the MRI operator room.

### 6.3.3 4D flow MRI

All acquisitions were performed with a 3T scanner (Ingenua, Philips Healthcare, Best, The Netherlands) using retrospectively triggered 4D flow MRI. Two medium flex coils (diameter 10 cm) were connected to the isolated beating pig heart platform below and above the heart (**Figure 6.1c**). Electrocardiography sensors were attached via copper wires on the hearts surface and were used as a cardiac trigger signal. Twenty-four cardiac frames at a temporal resolution of 21 ms were acquired covering the cardiac cycle.

The 4D flow MRI scan had a field of view of  $150 \times 150 \times 150 \text{ mm}^3$  and a non-interpolated spatial resolution of  $2.3 \times 2.3 \times 2.3 \text{ mm}^3$ . Echo time, repetition time, and flip angle were 2.2 ms, 5.2 ms, and  $8^\circ$ , respectively. To reduce the typically long acquisition times of 4D flow MRI, the scan was accelerated 3 times using k-t principal component analysis (Gyrottools, Zürich, Switzerland) resulting in a scan time

of 12 min [22]. K-t principal component analysis acquisitions undersamples k-space regularly over time, together with an interleaved training scan of the k-t space center. The images are recovered during reconstruction by exploiting the relevant signal correlations available in the training data, which are represented as temporal basis functions and can be derived using a principal component analysis. The data was reconstructed using CRecon (Gyrotools, Zürich, Switzerland) with a k-t regularization parameter of  $\lambda=1$ . The velocity encoding was 100 cm/s.

### 6.3.4 Flow measurements

Visualization of 4D flow MRI data and quantification of velocity and flow was done with GTFlow (Gyrotools, Zurich, Switzerland). For flow calculation a region of interest (ROI) was chosen in the ascending aorta close to the sinotubular junction and downstream to the aortic valve. Net flow, forward flow, and backward flow were determined. The net flow was defined as the spatially averaged flow through the defined ROI:

$$Q(t) = \int_{\text{ROI}} v(\mathbf{r}, t) d^2\mathbf{r} \quad (6.1)$$

with  $v(\mathbf{r}, t)$  being the velocity (pointing either in forward or backward direction) at position  $\mathbf{r}$  and cardiac phase  $t$ .

Likewise, forward was defined as:

$$Q(t)_{\text{forward}} = \int_{\text{ROI}} v(\mathbf{r}, t)_{v>0} d^2\mathbf{r} \quad (6.2)$$

and backward flow was defined as:

$$Q(t)_{\text{backward}} = \int_{\text{ROI}} v(\mathbf{r}, t)_{v<0} d^2\mathbf{r}. \quad (6.3)$$

For the per cent quantification of the regurgitation fraction in, for one cardiac cycle  $T$ , forward flow volume were calculated as:

$$V_{\text{forward}} = \int_0^T Q(t)_{\text{forward}} dt \quad (6.4)$$

and backward flow volume was calculated as:

$$V_{\text{backward}} = \int_0^T Q(t)_{\text{backward}} dt. \quad (6.5)$$

The per cent regurgitation fraction was based on the ratio  $RF = V_{\text{backward}}/|V_{\text{forward}}| \cdot 100$ . The stroke volume in mL was defined as  $SV_{\text{flow}} = V_{\text{forward}} - |V_{\text{backward}}|$ . The  $CO_{\text{flow}}$  in L/min was calculated by the product of the mean HR during the acquisition and  $SV_{\text{flow}}$ .

In one heart the 4D flow MRI scan was repeated three times within the same scan session at time points 0 min, 12 min and 1 h 5 min.

### 6.3.5 Volume measurements

The LV volume was quantified for each heart using a 4D segmentation tool of velocity data from Medis (Medis medical imaging systems, Leiden, The Netherlands). Stroke volume was calculated as the difference between end-diastolic volume (EDV) and end-systolic volume (ESV). The per cent ejection fraction (EF) was defined as  $EF = SV_{\text{volume}} * 100 / EDV$ . The size (long axis, short axis and area) of the aortic annulus was measured during systole at the height of the aortic valve. Cardiac output was similarly calculated as the product of mean HR and  $SV_{\text{volume}}$ .

### 6.3.6 Statistical analysis

A statistical comparison between the flow and volumetric measurements was done using a Bland-Altman analysis and linear regression. Normal distribution of the data was tested using a Shapiro-Wilk test. The significance level was set to  $p < 0.05$ .

### Vector plots and flow curves of the *ex vivo* beating pig heart

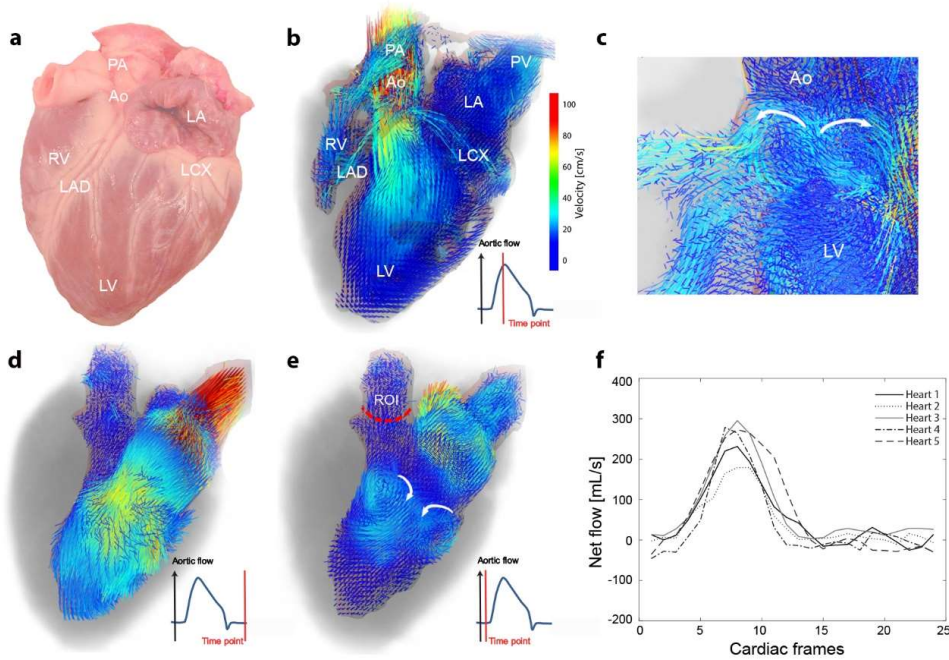


**Figure 6.2** Velocity vector plots of one representative heart and aortic flow curves for all five hearts: (a) Anatomical reference of the heart before the experiment. (b) Vector plots of intracardiac flow in the ejection phase. (c) Vortex formation and coronary filling in the aortic root of the heart during diastole. For better visualization of intracardiac flow, (d) shows the vector plots of the segmented LV at end-systole and at end-diastole (e), where vortex formation can be observed. (f) Net flow downstream to the aortic valve for all five experiments, measured in an ROI indicated in (e). Ao: Aorta, LA: Left atrium, LAD: Left anterior descending artery, LCX: Left circumflex artery, LV: Left ventricle, PA: Pulmonary artery, PV: Pulmonary vein, RV: Right ventricle.

## 6.4 Results

For all seven hearts the installation in the *ex vivo* beating pig heart platform and resuscitation was feasible. 4D flow MRI acquisitions were successful and flow visualization was feasible in all hearts. In **Figure 6.2** snapshot examples from one heart are shown. The **Figure 6.2a** is a photograph of the heart before the MRI scan for anatomical reference. **Figure 6.2b** depicts reconstructed 4D flow MRI velocity vectors at peak systole. Velocity vectors of blood flow in the LV and the left atrium as well as coronary flow in the left anterior descending artery, the left circumflex artery, and the filling and ejection of the right ventricle were visualized. In the aortic root, late systolic vortex formation and filling of the coronary arteries was observed in all hearts as exemplified in **Figure 6.2c**. **Figure 6.2d** and **Figure 6.2e** display velocity vectors of the LV at diastole and end-diastole in detail. In the left atrium and LV, filling and vortex formation after closing of the mitral valve were observed. Quantification of net flow  $Q(t)$  could be performed in ROIs downstream to the aortic valve (indicated in **Figure 6.2e**), resulting in similar flow curves for all hearts as shown in **Figure 6.2f**.



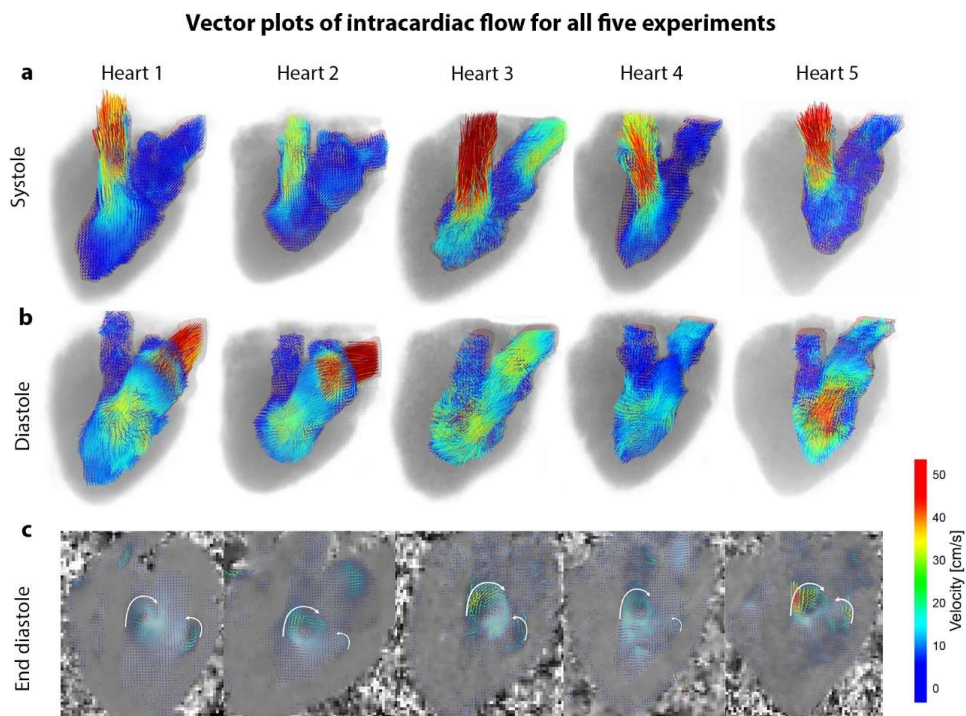


**Figure 6.3** Velocity vector plots of all five experiments at three time points in the cardiac cycle: Vector plots for the segmented left ventricle (LV) of all five experiments during (a) systole and (b) diastole. During end-diastole (c) vortex formation could be observed in all five hearts.

Velocity vectors in the LV of all five hearts are presented in **Figure 6.3**, showing filling and ejection of blood in the LV. In all hearts late diastolic vortex formation was found as shown in the vector plots in **Figure 6.3c**. A video of the vector plots over the cardiac cycle can be found in **Supplementary Video 6.2**. In **Table 6.1**, HR, SV, CO and regurgitation fraction for these hearts are given. The cardiac functional parameters, averaged for all five valves were:  $HR = 105 \pm 12$  bpm,  $SV_{\text{flow}} = 31 \pm 6$  mL,  $CO_{\text{flow}} = 3.3 \pm 0.9$  L/min, and regurgitation fraction =  $16 \pm 9\%$ . Aortic annulus sizes were on average  $31 \pm 1$  mm (mean  $\pm$  standard deviation) for the long axis,  $24 \pm 2$  mm for the short axis and  $600 \pm 31$  mm<sup>2</sup> for the area.

**Figure 6.4** shows Bland-Altman plots for CO and SV calculated from flow data and LV volume segmentations. The  $SV_{\text{volume}}$  calculated from LV volume was on average 11 mL higher than the  $SV_{\text{flow}}$  calculated from flow data.  $CO_{\text{volume}}$  was thus on average 1.2 L/min higher than  $CO_{\text{flow}}$ .

The results of the flow curves, HR,  $CO_{\text{flow}}$  and  $SV_{\text{flow}}$  for the one heart where the 4D flow MRI scan was repeated three times within the same scan session at 0 min, 12 min and 1 h 5 min are summarized in **Supplementary Figure 6.7**. These parameters were similar for all three scans.

**Table 6.1** Heart rate, stroke volume, and cardiac output were calculated from the aortic flow and from left ventricular volume segmentations. Regurgitation fraction was calculated from the aortic flow, ejection fraction from the volumetric measurements. Aortic annulus diameters were measured during peak systole.

Cardiac parameters for the five hearts							
Parameter		Heart 1	Heart 2	Heart 3	Heart 4	Heart 5	Mean ± standard deviation
Heart rate	[bpm]	104	98	109	93	123	105 ± 12
Stroke volume <small>flow</small>	[mL]	31	27	41	25	32	31 ± 6
Cardiac output <small>flow</small>	[L/min]	3.2	2.6	4.5	2.3	3.9	3.3 ± 0.9
Regurgitation fraction	[%]	11	19	5	30	16	16 ± 9
End-systolic volume	[mL]	101	122	59	31	71	77 ± 36
End-diastolic volume	[mL]	143	158	113	72	110	119 ± 33
Ejection fraction	[%]	29	22	48	57	36	38 ± 14
Stroke volume <small>volume</small>	[mL]	42	35	54	41	39	42 ± 7
Cardiac output <small>volume</small>	[L/min]	4.4	3.5	5.9	3.8	4.9	4.5 ± 1.0
Annulus size (long axis, short axis)	[mm]	31, 24	32, 23	31, 27	29, 22	31, 22	31 ± 1, 24 ± 2

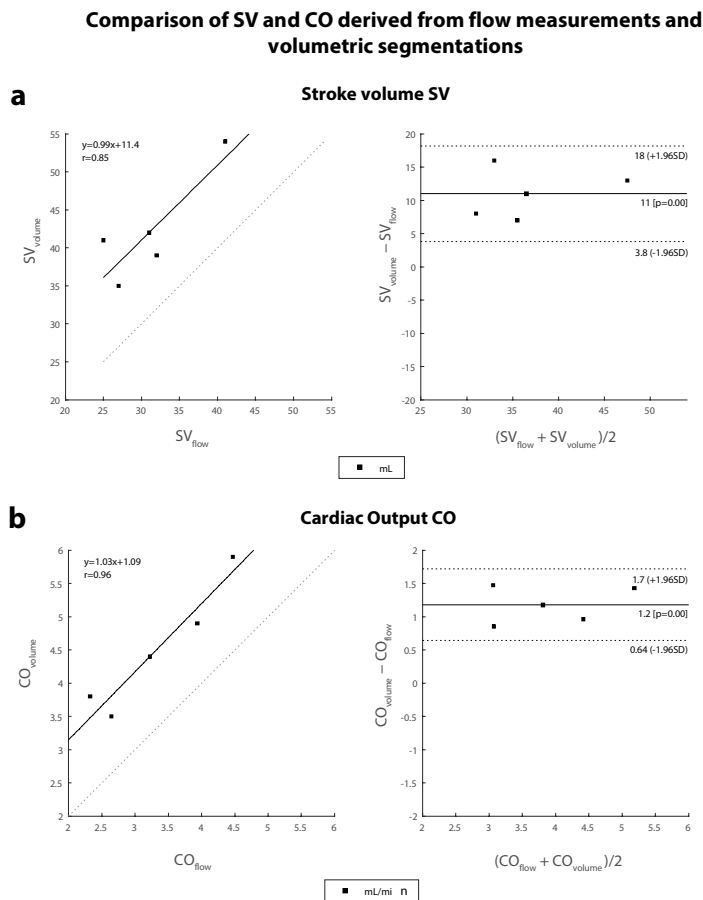


**Figure 6.4** Linear regression and Bland-Altman plots for stroke volume and cardiac output calculated from flow and from volumetric measurements: Comparison of the two techniques used for cardiac output (CO) and stroke volume (SV) estimation using Bland-Altman analysis. **(a)** Linear regression and Bland-Altman plots for SV calculated from aortic flow data ( $SV_{flow}$ ) and from left ventricle (LV) volume ( $SV_{volume}$ ). **(b)** Linear regression and Bland-Altman plots for CO calculated from aortic flow data ( $CO_{flow}$ ) and from LV volume ( $CO_{volume}$ ).

The results of the two hearts in which a TAVR procedure was performed are summarized in the supplemental material.

**6.5 Discussion**

In this study, 4D flow MRI was successfully applied in five pig hearts independently beating after installation and resuscitation in an MRI-compatible *ex vivo* beating pig heart platform. The platform provided detailed, comprehensive visualizations of time-resolved 3D, *i.e.* 4D, intracardiac blood flow and quantification of cardiac functional parameters. In literature, only two other setups have demonstrated *ex vivo* beating pig hearts in an MRI-compatible setup [3,21], none of them using 4D flow MRI, as these scans can be very time consuming. In fact, advanced acceleration and reconstruction techniques are necessary to perform these scans in a feasible acquisition time. Additionally, the use of

slaughterhouse byproducts as shown in this study, is beneficial to reduce the number of *in vivo* animal experiments in view of ethical considerations as well as animal housing labour and costs.

The feasibility of the *ex vivo* beating pig heart platform for cardiac intervention was demonstrated in two additional experiments in which a TAVR procedure was conducted. In these TAVR experiments 4D flow MRI was able to quantify and visualize the type and extend of aortic regurgitations, a typical complication after valve replacement procedure that is difficult to measure with echocardiography [15,16].

Literature values for the SV of a healthy 60-kg pig's LV are typically 65-81 mL [23] (in humans, 95 mL [24]). Literature values for the porcine HR are typically 85-114 bpm [23] (in humans, 60-100 bpm). This results in an porcine CO of 5-10 L/min [25] in comparison to a 4-8 L/min in humans. However, in our *ex vivo* beating pig heart platform, CO was artificially regulated via the preload, independently of the actual heart size. Therefore, at an experimental HR of 100-130 bpm, the porcine SV of the experiments shown in this study was expected to be lower and around 38-50 mL. Additionally, the SV calculated from flow measurements were slightly lower than those from volumetric measurements, since coronary flow could not be considered. In spite of the feasibility of visualizing coronary flow, quantification was hampered by heart motion and spatial resolution.

In *in vivo* 4D flow MRI experiments of 12 juvenile pigs, Cesarovic *et al.* [17] found a stress HR of  $124 \pm 3$  bpm which matched our experimental HR, similar also to the experimental HR reported by Vaillant *et al.* [21]. In their experiments they found EDV =  $55 \pm 8$  mL, ESV =  $19 \pm 6$  mL, SV =  $35 \pm 4$  mL, and an EF =  $65\% \pm 7\%$ . However, the difference between the *in vivo* experiment and the *ex vivo* beating pig heart experiment from this study is that pigs slaughtered for human consumption were used for the *ex vivo* model. The pigs reached a final live weight of approximately 110 kg, which is much more than a juvenile pig (30 kg). That weight difference was expressed in the large ESV and EDV measured in this experiment.

In general, complex flow patterns (such as vortices) are more difficult to capture with echocardiography as with 4D flow MRI. In our study two late diastolic vortices were observed in the LV of all hearts (**Figure 6.2e** and **Figure 6.3c**). These vortices were also described by Elbaz *et al.* [8], who reported on vortex flow analysis during LV filling using 4D flow MRI in normal humans and by Witschey *et al.* [18], who studied LV flow dynamics using 4D flow MRI in sheep.

This study has some limitations. The main idea was to use slaughterhouse waste material to allow an easy and cost efficient setup. However, the use of pig hearts from large pigs raised for human consumptions, limits the similarity between pig and human hearts. Additionally, an artificial human-like CO could limit the viability of the heart, which is why it might be an option to regulated the CO to another value. The hearts stayed vital for approximately 5 hours, however would not survive several resuscitations, which limits its use for pre-procedure versus post-procedure measurements in the case of TAVR or any other intervention. As described by Driessen *et al.* [26], other cardiac MRI techniques such as black-blood, bright blood balanced steady-state free precession, perfusion, angiography and T1-mapping sequences are important to describe the full extent of cardiac function. As real blood is used, the *ex vivo* beating pig heart platform can be used for many of these MRI techniques, as well as for contrast-enhanced imaging, *e.g.* late gadolinium enhancement, as contrast agent could simply be

added to the preload. A limitation for MRI techniques in general however, could be the missing surrounding tissue, improving static phase offset corrections or shimming and which could also cause susceptibility artefacts. Also the attachment of pacemaker lead cables on the hearts surface can create some distortions. In general, the setup is also compatible with standard echocardiography instruments as well as pressure sensors and optical flow sensors. Another limitation is the use of five pig hearts in this feasibility study. The limited number of samples exaggerate the variation shown in the Bland-Altman plots. Including more hearts could reduce this variability.

An advantage of the isolated beating pig heart setup for MRI is that receiver radiofrequency coils can be placed close to the hearts surface, which results in high signal to noise and a high-flow contrast, even in very small anatomical structures such as the coronary arteries. The relatively small differences in velocity fields between the five hearts indicate good reproducibility of the experiments.

As shown in the supplemental material, this platform has a potential for experiments on the performance of prosthetic valves or surgical strategies. Furthermore, with the isolated beating pig heart platform, aortic, pulmonary, and mitral regurgitation can be simulated. Complex settings of multiple regurgitations can be tested and investigated using 4D flow MRI. This is important since for example mitral regurgitation is common in patients with severe aortic regurgitation and aortic stenosis [27].

## 6.6 Conclusion

In conclusion, this study demonstrated the feasibility of 4D flow MRI data in a physiological working pig heart model pumping real blood and simulating physiological conditions. The isolated beating pig heart platform can allow for investigating new MRI sequences, pathophysiologic hemodynamics in relation with implanted artificial heart valves or also drug administration.

## 6.7 Acknowledgement

This research was supported by the Dutch Technology Foundation STW (Stichting voor Technische Wetenschappen) under grant number #11630 and by the STW Grant HTSM2014 (grant number #13928).

## 6.8 Supplementary material

Transcatheter aortic valve replacement (TAVR) is a valve replacement procedure in which a biological prosthetic valve is delivered by a catheter and implanted in the failing native aortic valve. For high-risk patients with symptomatic aortic stenosis (AS), TAVR is the therapy of choice leading to better survival rates when compared to open heart surgery [28,29]. Although generally beneficial, valve replacements are not without complications. Paravalvular leakage (PVL) or less frequent regurgitations of blood through the center of the valve may occur (prosthetic valve regurgitation) [16].

In addition to the five hearts with native valves, we investigated the feasibility of TAVR in the isolated beating pig heart platform. For this purpose, we replaced the native valves in two additional experiments by TAVR valves. Although TAVR procedure is strenuous for the organ, both hearts could be resuscitated after being installed in the isolated beating pig heart platform and 4D flow MRI could be performed successfully.

Cardiac parameters for CoreValve and Edwards valve were  $SV_{\text{CoreValve}} = 27 \text{ mL}$ ,  $CO_{\text{CoreValve}} = 3.5 \text{ L/min}$ ,  $RF_{\text{CoreValve}} = 37\%$  and  $SV_{\text{Edwards}} = 4 \text{ mL}$ ,  $CO_{\text{Edwards}} = 0.5 \text{ L/min}$ ,  $RF_{\text{Edwards}} = 86\%$ , respectively. Aortic regurgitation (AR) grading [28,30] indicated a moderate AR ( $30\% < RF_{\text{CoreValve}} = 37\% < 60\%$ ) for the CoreValve and a severe AR for the Edwards valve ( $RF_{\text{Edwards}} = 86\% > 60\%$ ). Similar to the native hearts, velocity vectors could be visualized in both hearts with prosthetic valves. Due to susceptibility mismatch and shielding, there was signal loss at the site of the prosthetic valves. In **Supplementary Figure 6.5a** and **Supplementary Figure 6.5b**, velocity vectors at peak systole and end diastole are shown for an exemplary native heart and the hearts with both prosthetic valves. Velocity vector plots (**Supplementary Figure 6.5b**, right) indicated a small regurgitation jet for the CoreValve and a large regurgitation jet for the Edwards valve during diastole with local velocities up to  $180 \text{ cm/s}$ . **Supplementary Figure 6.5c** summarizes net-, forward-, and backward flow through the valves during the cardiac cycle (measured in ROIs indicated in **Supplementary Figure 6.5b**), showing high backflow for the Edwards valve. Video files containing vector plots of the cardiac cycle for the CoreValve and the Edwards valve can be found in the **Supplementary Videos 1-2**.

Both TAVR valves did not show regurgitation due to transvalvular regurgitation, but due to PVL, which is characterized by regurgitating blood between cardiac tissue and the prosthetic valve. PVL was visible as (multiple) regurgitation jets at the border between valve and cardiac tissue, *e.g.* as shown for the Edwards valve in **Supplementary Figure 6.6**. Furthermore, mitral regurgitation (MR) was found in the heart with the Edwards valve.

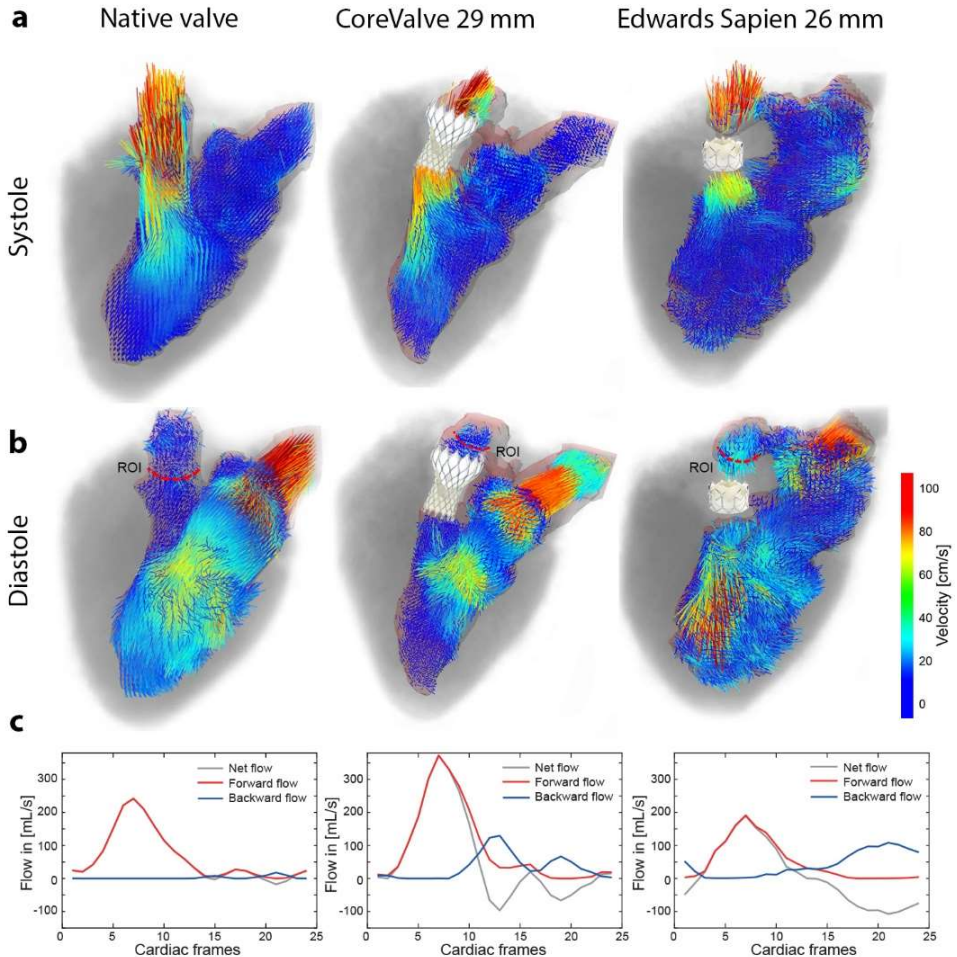
In the two additional TAVR experiments, for both implanted TAVR valves PVL was observed, likely created by insufficient sealing in the absence of aortic valve calcification [31] or due to small prosthetic valve sizes (29 mm and 26 mm) and migration of the valve [16]. In general, the diameter of the aortic annulus of pig and human hearts are comparable (25-30 mm) [32,33], which allows for the use of human TAVR implants in pig hearts. The clinical indication for TAVR procedure is a calcified AS to achieve a stable position inside the native valve, since an excessive radial force is needed to create sufficient sealing [31]. The prosthetic valves available were not larger than the aortic annulus as in common clinical practice in order to create sufficient sealing. PVL was further exacerbated by the absence of a calcified annulus or valve [31,34]. Additionally, regurgitations observed over the mitral

valve were most likely created by the altered loading conditions of the LV with a higher volume and pressure load. Even with insufficient sealing of the TAVR valves still the feasibility of TAVR in the isolated beating pig heart model could be shown. Moreover, the advantages of 4D flow MRI in typical complications after TAVR procedure could be demonstrated, by providing quantitative and visual descriptions of the regurgitation jets.

**Supplementary Video 6.1:** Velocity vectors in the heart with CoreValve throughout the cardiac cycle. Velocity vectors for one average cardiac cycle of the CoreValve. The segmentation includes the LV and velocities range from 0-100 cm/s. In the region of the valve no velocity vectors can be seen due to susceptibility artifacts. The video can be found under <https://eurradioexp.springeropen.com/articles/10.1186/s41747-019-0114-5>

**Supplementary Video 6.2:** Velocity vectors in the heart with Edwards valve throughout the cardiac cycle. Velocity vectors for one average cardiac cycle of the Edwards valve. The segmentation includes the LV and velocities range from 0-100 cm/s. In the region of the valve no velocity vectors can be seen due to susceptibility artifacts, however paravalvular leakage is visible as a regurgitation jet during diastole. The video can be found under <https://eurradioexp.springeropen.com/articles/10.1186/s41747-019-0114-5>

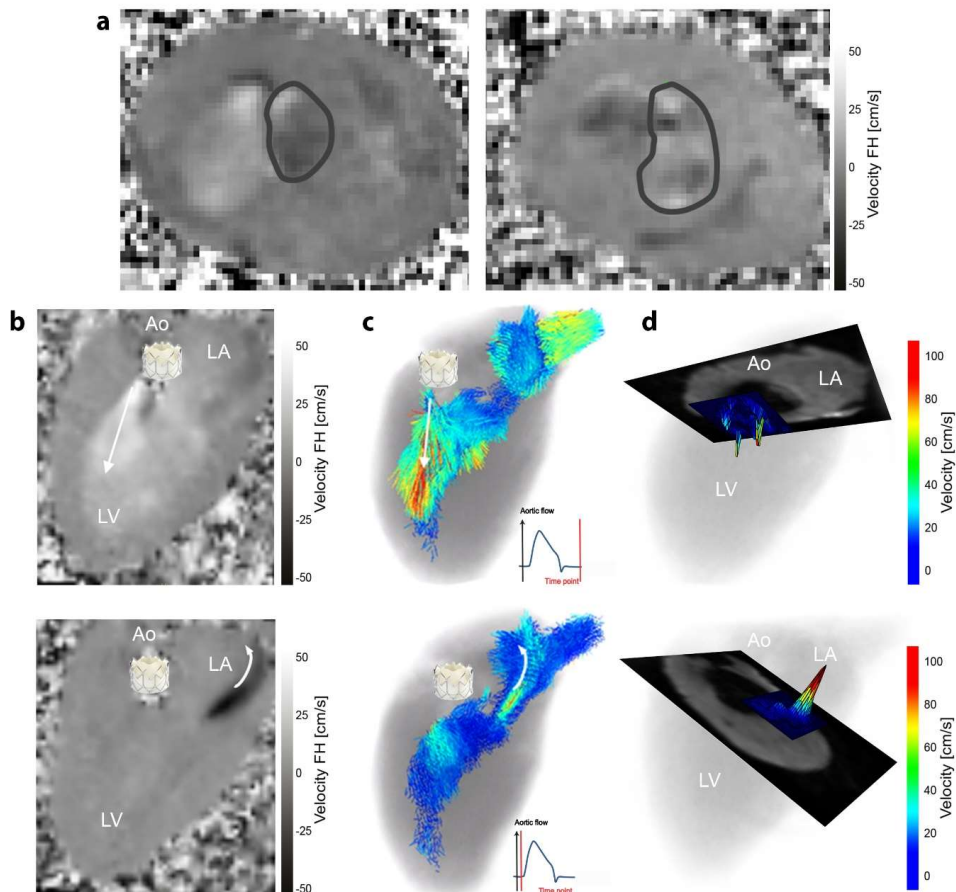
## Vector plots and flow curves of TAVR valves



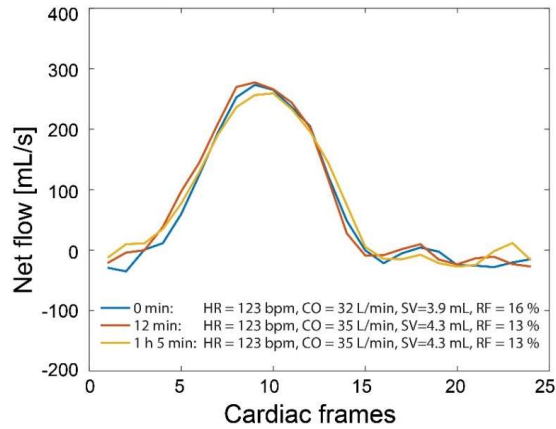
**Supplementary Figure 6.5** Comparison of vector plots and flow curves in hearts with native and TAVR valves during systole and diastole: This figure shows velocity vectors visualized using GTFlow (Gyrotools, Zurich, Switzerland), comparing a heart with native and the hearts with implanted TAVR valves. For better understanding photographs of the valves were placed at the areas of signal loss. Flow curves were calculated per heart from mean velocities in an ROI drawn in the aorta, close to the aortic valve, showing a large backward flow for the Edwards valve. Vector plots of a heart with a native valve (left), the CoreValve (middle) and the Edwards valve (right) at (a) peak systole and (b) diastole. A high velocity aortic regurgitation jet downstream to the Edwards valve as a consequence of paravalvular leakage can be seen during diastole. (c) Aortic (blue) net flow, (red) forward flow and (gray) backward flow, showing no regurgitation for the native valve (left), moderate regurgitation for the CoreValve (middle), and severe regurgitation for the Edwards valve (right).



### Visualization of regurgitation jets



**Supplementary Figure 6.6** Visualization of paravalvular leakage in the Edwards valve: Visualization of aortic and mitral regurgitation jets in the heart with the Edwards valve using phase contrast data (feet-head encoding), vector plots and through-flow planes. **(a)** Short axis view of the heart with the CoreValve (left) and the Edwards valve (right) during diastole at the height of the left ventricular outflow tract. In phase contrast images PVL can be seen as high velocities (brighter areas) flowing back in the LV. **(b)** Edwards valve: Phase contrast data (two chamber view with feet-head flow encoding) and vector plots **(c)** for aortic regurgitation during diastole (top) and mitral regurgitation (bottom) during systole. **(d)** Edwards valve: multiple eccentric regurgitation jets at the position of the prosthetic aortic valve and one central regurgitation jet in the mitral valve.



**Supplementary Figure 6.7** Repeated 4D flow MRI measurements of the same heart with a native valve: The heart was scanned three times, at time points 0 min, 12 min and 1 h 5 min. The flow curves in the aorta are similar for all three scans, as well as HR,  $CO_{flow}$  and  $SV_{flow}$ .

## 6.9 Bibliography

1. Camacho P, Fan H, Liu Z, He J-Q. Large Mammalian Animal Models of Heart Disease. *J Cardiovasc Dev Dis.* 2016;3:30. A
2. Granegger M, Aigner P, Kitzmüller E, Stoiber M, Moscato F, Michel-Behnke I, *et al.* A passive beating heart setup for interventional cardiology training. *Curr Dir Biomed Eng.* 2016;2:735–9.
3. Schuster A, Gruenwald I, Chiribiri A, Southworth R, Ishida M, Hay G, *et al.* An isolated perfused pig heart model for the development, validation and translation of novel cardiovascular magnetic resonance techniques. *J Cardiovasc Magn Reson.* 2010;12:1–9.
4. Markl M, Frydrychowicz A, Kozerke S, Hope M, Wieben O. 4D flow MRI. *J Magn Reson Imaging.* 2012;36:1015–36.
5. Dyverfeldt P, Bissell M, Barker AJ, Bolger AF, Carlhäll CJ, Ebbers T, *et al.* 4D flow cardiovascular magnetic resonance consensus statement. *J Cardiovasc Magn Reson.* 2015
6. Bogaert J, Dymarkowski S, Taylor A. Clinical cardiac MRI. Beart A, Sartor K, editors. Springer, Medical Radiology, Diagnostic Imaging; 2005.
7. Svalbring E, Fredriksson A, Eriksson J, Dyverfeldt P. Altered Diastolic Flow Patterns and Kinetic Energy in Subtle Left Ventricular Remodeling and Dysfunction Detected by 4D Flow MRI. 2016;c:1–12.
8. Elbaz MSM, Calkoen EE, Westenberg JJM, Lelieveldt BPF, Roest AAW, Geest RJ Van Der. Vortex flow during early and late left ventricular filling in normal subjects: quantitative characterization using retrospectively-gated 4D flow cardiovascular magnetic resonance and three-dimensional vortex core analysis. *J Cardiovasc Magn Reson.* 2014;1–12.
9. Roes SD, Hammer S, van der Geest RJ, Marsan NA, Bax JJ, Lamb HJ, *et al.* Flow assessment through four heart valves simultaneously using 3-dimensional 3-directional velocity-encoded magnetic resonance imaging with retrospective valve tracking in healthy volunteers and patients with valvular regurgitation. *Invest Radiol.* 2009;44:669–75.
10. Westenberg JJM, Roes SD, Ajmone Marsan N, Binnendijk NMJ, Doornbos J, Bax JJ, *et al.* Mitral valve and tricuspid valve blood flow: accurate quantification with 3D velocity-encoded MR imaging with retrospective valve tracking. *Radiology.* 2008;249:792–800.
11. Markl M, Mikati I, Carr J, McCarthy P, Malaisrie SC. Three-Dimensional Blood Flow Alterations After Transcatheter Aortic Valve Implantation. *Circulation.* 2012;573–6.
12. van Wijk WHS, Breur JMPJ, Westenberg JJM, Driessen MMP, Meijboom FJ, Driesen B, *et al.* Validation of aortic valve 4D flow analysis and myocardial deformation by cardiovascular magnetic resonance in patients after the arterial switch operation. *J Cardiovasc Magn Reson. Journal of Cardiovascular Magnetic Resonance;* 2019;21:20.
13. Farag ES, Vendrik J, van Ooij P, Poortvliet QL, van Kesteren F, Wollersheim LW, *et al.* Transcatheter aortic valve replacement alters ascending aortic blood flow and wall shear stress patterns: A 4D flow MRI comparison with age-matched, elderly controls. *Eur Radiol.* 2019;29:1444–51.
14. von Knobelsdorff-Brenkenhoff F, Trauzeddel RF, Barker AJ, Gruettner H, Markl M, Schulz-Menger J. Blood flow characteristics in the ascending aorta after aortic valve replacement - a pilot study using 4D-flow MRI. *Int J Cardiol.* 2016;170:426–33.
15. Lázaro C, Hinojar R, Zamorano JL. Cardiac imaging in prosthetic paravalvular leaks. *Cardiovasc Diagn Ther.* 2014;4:307–13.
16. Smolka G, Wojakowski W. Paravalvular leak - important complication after implantation of prosthetic valve. *E-Journal Cardiol Pract.* 2010;9:1–7.
17. Cesarovic N, Busch J, Lipiski M, Fuetterer M, Fleischmann T, Born S, *et al.* Left ventricular blood flow patterns at rest and under dobutamine stress in healthy pigs. *NMR Biomed.* 2018;32.
18. Witschey WR, Zhang D, Contijoch F, McGarvey JR, Madonna L, Takebayashi S, *et al.* The influence of mitral

annuloplasty on left ventricular flow dynamics. *Ann Thorac Surg.* 2015;116:114–21.

19. de Hart J, de Weger A, van Tuijl S, Stijnen JMA, van den Broek CN, Rutter MCM, *et al.* An *ex vivo* platform to simulate cardiac physiology: a new dimension for therapy development and assessment. *Int J Artif Organs.* 2011;34:495–505.

20. Langendorff O. Untersuchungen am Überlebenden Säugethierherzen. *Pflügers Arch Eur J Physiol.* 61st ed. 1895;61:291–332.

21. Vaillant F, Magat J, Bour P, Naulin J, Benoist D, Loyer V, *et al.* Magnetic resonance-compatible model of isolated working heart from large animal for multimodal assessment of cardiac function, electrophysiology, and metabolism. *Am J Physiol Circ Physiol.* 2016;310:H1371–80.

22. Pedersen H, Kozerke S, Ringgaard S, Nehrke K, Won YK. K-t PCA: Temporally constrained k-t BLAST reconstruction using principal component analysis. *Magn Reson Med.* 2009;62:706–16.

23. Reiter U, Reiter G, Manninger M, Adelsmayr G, Schipke J, Alogna A, *et al.* Early-stage heart failure with preserved ejection fraction in the pig: a cardiovascular magnetic resonance study. *J Cardiovasc Magn Reson. Journal of Cardiovascular Magnetic Resonance;* 2016;1–15.

24. Maceira AM, Prasad SK, Khan M, Pennell DJ. Reference right ventricular systolic and diastolic function normalized to age, gender and body surface area from steady-state free precession cardiovascular magnetic resonance. *Eur Heart J.* 2006;28:79–88.

25. Jivegard L, Frid I, Haljamae H, Holm J, Holm S, Wickstrom I. Cardiac output determinations in the pig - thoracic electrical bioimpedance versus thermodilution. *Crit Care Med.* 1990;18:995–8.

26. Driessen MMP, Breur JMPJ, Budde RPJ, van Oorschot JWM, van Kimmenade RRJ, Sieswerda GT, *et al.* Advances in cardiac magnetic resonance imaging of congenital heart disease. *Pediatr Radiol.* 2015;45:5–19.

27. Pai RG, Varadarajan P. Prognostic implications of mitral regurgitation in patients. *Circulation.* 2010;122:43–7.

28. Nishimura RA, Otto CM, Bonow RO, Ruiz CE, Carabello BA, Skubas NJ, *et al.* 2014 AHA/ACC guideline for the management of patients with valvular heart disease: executive summary: a report of the american college of cardiology/american heart association task force on practice guidelines. *Circulation.* 2014;129.

29. Rahimtoola SH. Choice of prosthetic heart valve in adults. *J Am Coll Cardiol.* 2010;55.

30. Maurer G. Aortic regurgitation. *Heart.* 2006;92:994–1000.

31. Haensig M, Rastan AJ. Aortic valve calcium load before TAVI: is it important? *Ann Cardiothorac Surg.* 2012;1:160–4.

32. Sands MP, Rittenhouse EA, Mohri H, Merendino KA. An anatomical comparison of human, pig, calf, and sheep aortic valves. *Ann Thorac Surg.* 1969;8.

33. Iaizzo PA. *Handbook of Cardiac Anatomy, Physiology, and Devices.* Springer;

34. de Weger A, van Tuijl S, Stijnen M, Steendijk P, de Hart J. Images in cardiovascular medicine direct endoscopic visual assessment of a transcatheter aortic valve implantation and performance in the PhysioHeart, an isolated working heart platform. *Images Cardiovasc Med.* 2010;121:261–3.



# CHAPTER 7

General discussion and summary

## 7.1 General discussion

### 7.1.1 Accuracy of accelerated 4D flow MRI

Since there is a clear clinical need for accurate flow information, 4D flow MRI is a very active research field. As with most MRI techniques, the acquisition parameter space is large and therefore consensus is needed on the best 4D flow imaging strategy. This was the purpose of the 4D flow consensus statement [1]. Yet, the verdict on the best strategy for the newer accelerated 4D flow MRI techniques is still open.

In the before-mentioned consensus statement *in vivo* 4D flow MRI scan acceleration is recommended using SENSE=2 or EPI [1]. Additionally, multiple k-lines can be sampled within one heart beat (segmented k-space sampling [2,3]), which shortens the scan time of *e.g.* a factor of 2, at the expense of loss of the temporal resolution. Most papers on 4D flow MRI acceleration therefore refer to one of these acceleration techniques as the ground truth, since there is some consensus on the applicability of these approaches. However, since the ground truth is not perfect and already (moderately) accelerated, a fair comparison with other acceleration strategies may be flawed. For example in **chapter 3**, when comparing a CS acceleration with “ground-truth” SENSE=2 and in **chapter 4**, when comparing to k-t PCA, our CS accelerated scans turned out to be more in line with 2D flow MRI scans than the (consensus paper) SENSE ground-truth was.

2D flow scans may serve as a ground truth, as they can be acquired without the need of acceleration and with a high temporal resolution. However, 2D flow MRI scans as a reference are not ideal either, as they tend to have different phase offset characteristics (which may lead to systematic flow offsets), the SNR is higher, and the resolution is non-isotropic, leading to different partial-volume characteristics. This makes a comparison against accelerated 4D flow MRI difficult as has been described previously in the consensus statement and by others [4].

Determining the reproducibility of the flow measurement derived hemodynamic parameter is difficult. In **chapter 2** inter-scan variation of PWV was shown to be much larger than the intra-scan variation, not due to technical issues, but due to physiological changes [5]. Therefore, we chose not to focus on inter-scan variability, but rather to validate our approach against ultrasound measurements and by reproducing literature reported values on PWV differences between age groups.

In **chapter 2** and **chapter 3** phantom measurements were performed, allowing for ground-truth scans with long scan times and fully sampled scans under controlled conditions. Yet, it remained challenging to reproduce the sharp flow peaks and flow curves *in vitro* which are found *in vivo* in humans. In **Figure 7.1a** the carotid artery flow phantom (LifeTec Group BV, Eindhoven, The Netherlands) used in **chapter 3** is shown and next to it an elastic phantom of the aortic arch, which can be connected to a small reservoir mimicking the left ventricle, contracting with air pressure. WSS, calculated from 4D flow measurements in the aorta phantom are shown in **Figure 7.1b**. Additionally, as shown in the PWV phantom in **Figure 7.1a**, the embedding of the phantom either in water or agar is important for sufficient signal generation and phase offset corrections. Water is generally easier to use than agar but can create B1 inhomogeneities and (flow) artifacts. For the PWV phantom in particular, an elastic tube was chosen, with an elastic modulus as found in the human carotid artery. Ideally a longer tube should

be used, to establish a parabolic flow profile through the area of interest. For velocity images and small phantoms in particular, phantom tubes with MRI signal, in contrast to tubes without signal such as silicon tubes, have been shown to be advantageous (**Figure 7.1c**). The reason is, that low magnitude signal translates into noise in the velocity maps (according to equation 1.8 and 1.9). This in turn leads to noisy flow curves within an ROI due to partial volume effects of tube wall and lumen.

In **Figure 7.1c** a phantom tube created from silicon and polyvinylalcohol (PVA) in comparison to a regular silicon tube is shown. With changing PVA concentrations of the material, different T1 and T2 characteristics could be created as shown in **Figure 7.1d**. Choosing material properties similar to *e.g.* vessel wall T1 and T2 values (at a 20% PVA concentration), helped in creating realistic models of the carotid artery. In velocity maps of 4D flow MRI scans this had the advantage of a background phase of zero. Similarly, PVA phantoms will support sequence testing of vessel wall imaging and black blood techniques, in which a realistic delineation between suppressed water flow and phantom wall is needed.

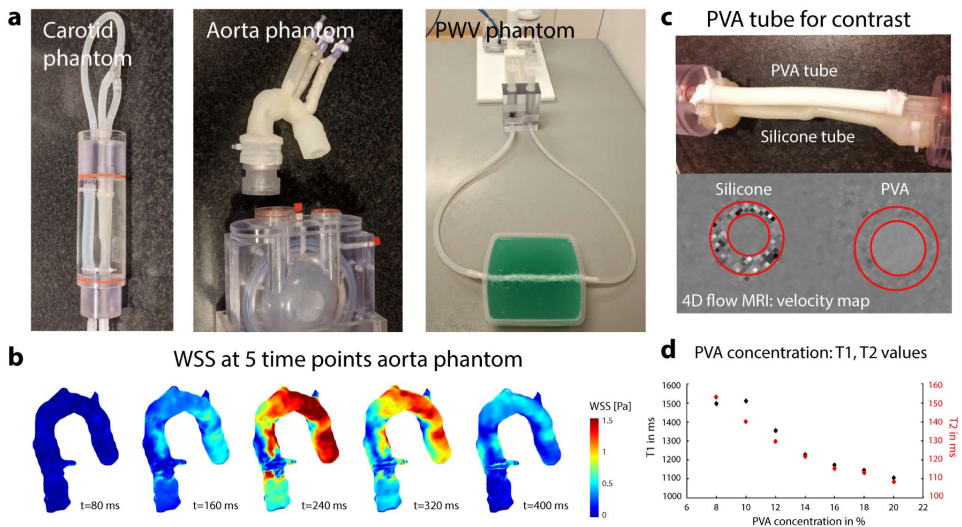


**Figure 7.1** Flow phantom setups used for 4D flow MRI experiments created by LifeTec (Eindhoven, The Netherlands). (a) carotid bifurcation phantom within a water filled cylinder (left), aortic phantom with an air pressure driven left ventricle (middle) and a PWV phantom (right) embedded in an agar bath, consisting of a long, elastic tube. (b) WSS measured with 4D flow MRI in the aortic phantom at different time points of the simulated cardiac cycle. (c) Comparison of the material properties of silicon and PVA (20%), leading to improvement of noise close to the region of interest in 4D flow MRI velocity maps for PVA. (d) T1 and T2 properties of tubes with different PVA concentration, as measured in the same scan. With decreasing PVA concentration, also T1 and T2 values decrease. A concentration of 20% PVA was chosen, as it matches T1 and T2 properties of the vessel wall. Tubes with higher PVA concentration were difficult to produce, as the material became too unstable.

### 7.1.2 Temporal resolution

In **chapter 2** it was shown that high temporal resolution 2D flow MRI is possible. Binning the same data retrospectively into a lower temporal resolution, as shown in **Figure 7.2a-b**, will lead to a decrease in peak flow, which demonstrates again how important a high temporal resolution is for flow MRI. Independently of that, the temporal resolution needed is also determined by the complexity of each



flow curve, such that the highest frequency modulating the flow curve (around 40 Hz [6]) requires a sampling rate of at least 80 Hz, which equals a 12.5 ms temporal resolution.

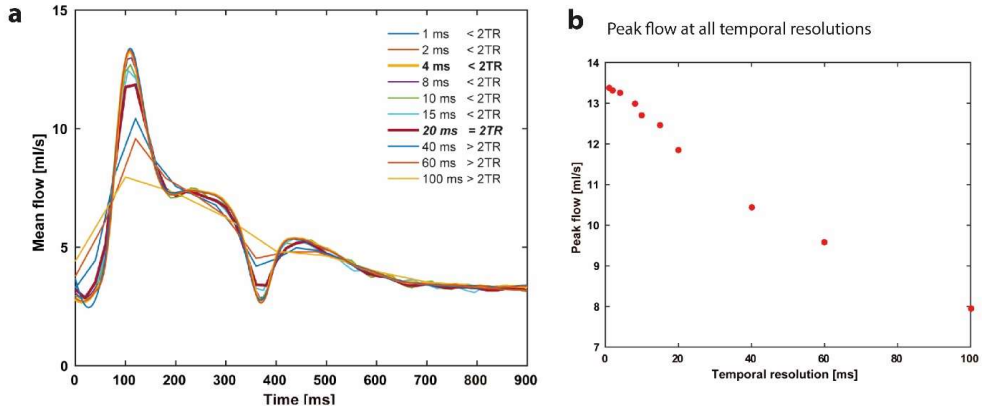


**Figure 7.2** Underestimation of peak flow derived from a 2D flow MRI scan with a TR of 10 ms at decreasing temporal resolution. The flow curves are derived from the same dataset and reconstructed with different temporal resolutions as described in chapter 2. (a) Flow curves in the common carotid artery at different temporal resolutions. With decreasing temporal resolution, the flow curves become shallower. (b) Peak systolic flow plotted against temporal resolution.

The technique described in **chapter 2** led to a temporal resolution of 4 ms of the 2D flow MRI scan, which was higher than the TR at which the scan was acquired. The reason that this technique still worked well, is probably that the bipolar gradient (creating phase accumulation of moving spins according to equation 1.3) had a length of 3.9 ms, which is in the range of the temporal resolution recovered after resorting and CS reconstruction. Re-binning into cardiac bins with even higher temporal resolution (below 4 ms) is probably similar to a view sharing approach between two cardiac bins.

### 7.1.3 Self-gating

For 4D flow MRI scans of the aorta usually a respiratory gating strategy is used to compensate for motion artefacts created through breathing. To track the breathing motion, typically a liver navigator is acquired. With self-gating however the respiratory and/or cardiac gating signals are obtained from the acquired MRI data itself, without the need for a separate navigator, breathing belt, or ECG leads [7].

The self-gating signal is typically derived from the k-space center. When one wants to use self-gating for respiratory binning, it is therefore important to control the number of readouts in such a way that a sufficient sampling frequency of k-space center is obtained to capture the full breathing motion. The human breathing frequency is typically 0.3-0.5 Hz, which means the sampling frequency should be around 1 Hz to fulfill the Nyquist sampling criterion.

To demonstrate the possibility of combining pseudo-spiral sampling with self-gating, additional experiments were performed (which was not yet implemented and used for aortic 4D flow MRI in **chapter 4**). In these experiments 10 readouts on each pseudo-spiral arm were performed before

returning to the center. Although defining a fixed number of readouts constraints the sampling trajectory, it assures sufficient sampling of k-space center.

For each experiment a 4D flow MRI scan of the aorta was conducted, with TR = 3.9 ms, TE = 2.1 ms, spatial resolution =  $2.5 \times 2.5 \times 2.5 \text{ mm}^3$  resolution and 30 cardiac frames. The readout was chosen to be in feet-head direction. Four flow encoding segments were acquired consecutively, as done in a regular 4D flow MRI scan (VENC of 150 cm/s). For processing of the self-gating signal a fast Fourier transformation was done in readout direction of the raw signal of the k-space center. The self-gating signal was then derived by singular value decomposition and by selecting and averaging only relevant coils, capturing the breathing motion (**Figure 7.3a**). As the self-gating signal was derived from every 10<sup>th</sup> k-line it had a sampling frequency of 6.4 Hz.

Within the same scan, a liver navigator signal was acquired (a pencil beam acquisition capturing motion of the liver-air boundary) at a frequency of 6.4 Hz. And, additionally to self-gating and liver navigator, the breathing was derived by a camera observing the patient motion from outside the MRI scanner with a sampling frequency of 20 Hz using the Philips VitalEye technique.

In order to test the robustness of the self-gating signal and to find the minimal sampling frequency, two additional experiments were performed with the same analysis pipeline. Firstly, a sampling trajectory was designed (PROUD patch) that solely sampled the k-space center. All other settings, also flow encodings, remained the same. Although this did not result in a good image after reconstruction, it provided a dataset with which k-lines at different sampling frequencies could be chosen retrospectively. Secondly, the volunteer was asked to breath with different breathing patterns. The instructions were regular breathing, a breath hold, extremely deep breathing and shallow breathing.

**Figure 7.3b** shows results of a self-gating signal acquired with pseudo-spiral sampling. The captured breathing pattern (a sinusoidal motion between inspiration and expiration) of the self-gating signal was similar to the signal captured by the liver navigator and the VitalEye camera. In **Figure 7.3c** the self-gating signal at different sampling frequencies of the k-space center is shown. From **Figure 7.3c**, we conclude that a sampling frequency of around 1-3 Hz is ideal to still capture the breathing signal (above Nyquist frequency) without compromising efficient k-space filling. The signal breaks down at frequencies <0.6 Hz. **Figure 7.3d** shows different breathing patterns of the volunteer, which were similar for self-gating in comparison to the VitalEye signal of the same scan.

Although the VitalEye camera captured the motion of the subjects' chest, whereas the navigator recorded the motion of the diaphragm and similarly did the self-gating signal, differences between methods were small. For this experiment, the self-gating motion signals seemed more similar to the navigator pattern than to the VitalEye recordings. In order to include  $k = 0$  regularly in the pseudo-spiral sampling approach, the spiral has to return to the k-space center in regular time intervals, which may limit the length of the spirals and thus can be in conflict with an optimal k-space filling pattern.

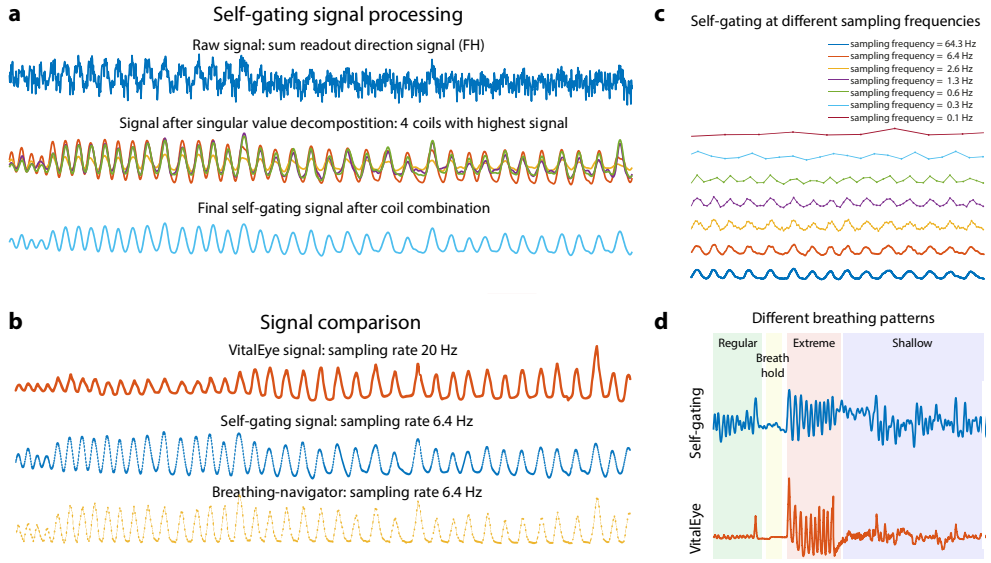


**Figure 7.3** Self-gating to extract the breathing signal from an aortic pseudo spiral 4D flow MRI acquisition. (a) Signal processing: raw signal (sum over the readout direction in image space), signal after singular value decomposition of the time  $\times$  readout matrix (each coil separately) and final breathing signal after coil combination. (b) Breathing signal measured with the Philips VitalEye in comparison to the self-gating signal and liver navigator signal of the same dataset. (c) Self-gating signal derived from center k-space data sampled at different frequencies. (d) Self gating signal and VitalEye signal in comparison under different breathing patterns.

#### 7.1.4 Applicability of the PROUD patch for other time-resolved sequences

The CS sampling strategy as implemented in the PROUD patch can be applied in other Cartesian sequences. Using pseudo-spiral sampling with the PROUD patch (**chapter 3**) has been demonstrated useful in ECG triggered scans, but can also be used for real-time imaging. Additionally, not only flow imaging, but also other MRI sequences can be combined with PROUD pseudo-spiral sampling and CS reconstruction strategies.

##### Real-time imaging of bowel motility

Real-time imaging can be useful for imaging of non-periodic motion. Bowel motility for example changes in Crohn's disease and can be imaged with dynamic MRI sequences. However, typically 2D images are acquired, which do not capture through-plane motion. 3D sequences would be a better solution, but are limited in temporal resolution. To capture bowel motility, a temporal resolution of around 3s is required [8]. In [9] we showed that 3D real-time imaging of the bowel is possible using a CS undersampling and reconstruction method.

We implemented a undersampling strategy for real-time 3D bowel motility imaging using the PROUD patch. **Figure 7.4a** shows the Poisson disk sampling pattern in  $k_y$ - $k_z$  dimension on the left and in  $k_y$ -time dimension next to it. More time frames resulted in a higher temporal resolution, which means the undersampling factors were higher for scans with a higher temporal resolution. Using a CS

reconstruction similar to the ones in **chapter 3** and in **chapter 4**, undersampled data could be recovered.

For real-time sampling no interleaving of k-spaces over time was possible, as done for ECG triggered scans. Although pseudo-spiral sampling can still be applied, for example to keep temporal flexibility during reconstruction, also regular line-by-line sampling can be used. Like this any sampling pattern, *e.g.* a perfect Poisson disk, can be sampled for each k-space and time frame. For time-resolved scans that means that each time frame is sampled with a slightly different Poisson disk to achieve random undersampling over time.

With this strategy we could show that a 4 times CS accelerated real-time scan with a temporal resolution of 4.1s was possible and similar compared to a fully sampled real-time scan of 16.2s temporal resolution (**Figure 7.4b**).

### **ECG-triggered black blood scans using pseudo-spiral sampling**

Time-resolved, ECG triggered 3D Black Blood scans would be an interesting application to derive accurate time-resolved segmentations of the vessel wall for WSS or WT estimation. This has already been demonstrated by Koktzoglou *et al.* [10] for 3D kooshball acquisitions. In a single experiment we tested if this would work for PROUD pseudo-spiral sampling in a similar fashion.

In a first test run, pseudo-spiral sampling for iMSDE sequences with a TFE preparation pulse before each spiral arm was possible and similar to Koktzoglou *et al.* [10]. However, image quality was not satisfactory, which is why we decided for a slightly different strategy. In order to still achieve time resolved Black Blood MRI, a singular gradient in FH direction was added to a 3D carotid artery balanced SSFP scan (**Figure 7.4c**). Consequently, the steady state for spins moving along FH direction was disturbed, leading to signal void.

This method worked surprisingly well, and in combination with ECG triggering, PROUD pseudo-spiral sampling and a CS reconstruction 50 cardiac frames could be acquired. **Figure 7.4d** shows a axial view of the 3D Black Blood scan at two time points. Next to it, all 50 cardiac frames are shown, in which the movement of the carotid artery can be seen. In **Figure 7.4d** a comparison between the time-resolved 3D bSSFP and a static 3D iMSDE scan is shown. A limitation remained the fat suppression, as with fat suppression, the SNR of the scan was low and without fat suppression the visibility of the vessel wall was limited, which means an optimum still has to be found. Overall, the mechanisms behind this method are not yet clear.

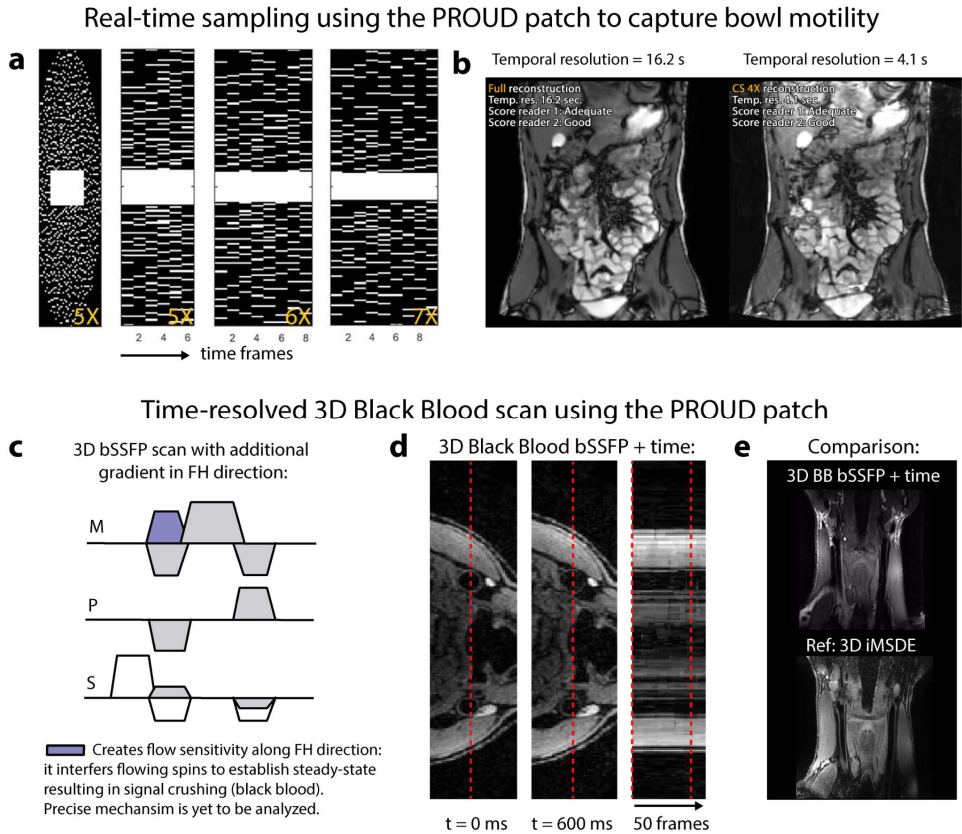


**Figure 7.4** (a) Real-time acquisition of bowel motion using the PROUD patch. For this application a three dimensional k-space is sampled with a Poisson disk undersampling pattern, shown on the left. This pattern is different for consecutive time frames, which results in a random sampled k-space over time. The higher the undersampling factor per 3D k-space, the more time frames can be sampled within the same scan time. (b) A reconstruction of a fully sampled real-time acquisition in comparison to a CS reconstruction with a 4 times higher temporal resolution, which is able to capture bowel motility [9]. (c) A time-resolved 3D Black Blood scan of the carotid arteries acquired using the PROUD patch, pseudo spiral sampling and retrospective cardiac triggering leading to 50 cardiac frames. To avoid the usage of a preparation pulse, as for example used in the 3D iMSDE references scan, a gradient was added to a balanced SSFP sequence to disturb the steady state of spins flowing in FH direction, leading to black blood images. (d) Resulting 3D, time-resolved black blood images of the carotid artery. (e) A comparison between the time-resolved bSSFP black blood scan and a regular, static, 3D iMSDE scan.

### 7.1.5 The future of clinical flow MRI

Despite the accessibility and cost efficiency of ultrasound, we believe that multiparametric MRI protocols including flow, WSS, PWV and WT, will become part of a comprehensive clinical vascular imaging protocol as it can assess various aspects of atherosclerosis. Also, MRI can be easily translated to regions less accessible for ultrasound, *e.g.* the brain and 3D image planning decreases operator dependency. Currently, MRI is available in every hospital and the idea of a ‘one-stop shop’ MRI protocol for WT and flow assessment is promising.

Nevertheless, image recovery, manual processing and segmentation of multidimensional data is labor intensive and time consuming. To include these protocols in clinical routines in future, it will be necessary to process them with automated, machine learning reconstruction and segmentation techniques.

### 7.1.6 Bibliography

1. Dyverfeldt P, Bissell M, Barker AJ, Bolger AF, Carlhäll CJ, Ebbers T, *et al.* 4D flow cardiovascular magnetic resonance consensus statement. *J Cardiovasc Magn Reson.* 2015;17:1–19.
2. Haacke EM, Brown RW, Thompson MR, Venkatesan R. Haacke - Magnetic Resonance Imaging - Physical Principles and Sequence Design. *J. Appl. Phys.* 1999. p. 914.
3. Bernstein MA, King KF, Zhou XJ. *Handbook of MRI Pulse Sequences.* 2004.
4. Giese D, Schaeffter T, Kozerke S. Highly undersampled phase-contrast flow measurements using compartment-based  $k-t$  principal component analysis. *Magn Reson Med.* 2013;69:434–43.
5. Markl M, Wallis W, Strecker C, Gladstone BP, Vach W, Harloff A. Analysis of pulse wave velocity in the thoracic aorta by flow-sensitive four-dimensional MRI: Reproducibility and correlation with characteristics in patients with aortic atherosclerosis. *J. Magn. Reson. Imaging.* 2012. p. 1162–8.
6. Muñoz-Torrero JFS, Tardio-Fernandez M, Valverde-Valverde JM, Duque-Carrillo F, Vega-Fernandez JM, Joya-Vazquez P, *et al.* Pulse Wave Velocity in Four Extremities for Assessing Cardiovascular Risk Using a New Device. *J Clin Hypertens.* 2014;16:378–84.
7. Uribe S, Beerbaum P, Sørensen TS, Rasmusson A, Razavi R, Schaeffter T. Four-dimensional (4D) flow of the whole heart and great vessels using real-time respiratory self-gating. *Magn Reson Med.* 2009;62:984–92.
8. Quigley EMM. Gastric and small intestinal motility in health and disease. *Gastroenterol Clin North Am.* 1996;25:113–45.
9. de Jonge CS, Coolen BF, Peper ES, Motaal AG, Nio CY, Somers I, *et al.* Evaluation of compressed sensing MRI for accelerated bowel motility imaging. *Eur Radiol Exp. European Radiology Experimental;* 2019;3.
10. Koktzoglou I. 4D dark blood arterial wall magnetic resonance imaging: Methodology and demonstration in the carotid arteries. *Magn Reson Med.* 2013;69:956–65.
11. Runderkamp BA, Peper ES, Schoormans J, Zhang Q, Coolen BF, Strijkers GJ, *et al.* Accelerated 4D flow MRI using a Low-Rank Tensor reconstruction. *Proc Intl Soc Mag Reson Med* 27. 2019;1958.

## 7.2 Summary

4D flow MRI can quantify and visualize complex blood flow in the heart and arteries by encoding for flowing blood in cardiac triggered MRI scans. The main disadvantage of 4D flow MRI is a very long acquisition time, which is typically addressed by undersampling data or reducing the temporal resolution. In this thesis a new compressed sensing (CS) acquisition and reconstruction technique is presented that enables high temporal resolution 2D flow MRI scans for regional PWV calculation as well as 4D flow MRI with short scan times. To demonstrate the accuracy of accelerated 4D flow MRI, the effect of acceleration on hemodynamic biomarkers such as flow and wall shear stress (WSS) was investigated. A novel, specialized pig heart model provided detailed images of intra-cardiac and coronary flow.

In **chapter 2**, a smart combination of retrospective cardiac gating, temporal binning and CS reconstruction was presented that enables high temporal resolution 2D flow MRI. With this technique, it was demonstrated that PWV can be measured accurately in small vessel segments of the carotid artery. Accurate PWV estimation in small vessel regions may be a valuable addition to comprehensive MRI examinations of the vasculature, investigating the formation and progress of atherosclerosis.

In **chapter 3**, a pseudo-spiral Cartesian undersampling strategy was developed, which, in combination with an iterative CS reconstruction, enabled highly accelerated 4D flow MRI on phantom and *in vivo* scans of the carotid artery. It was shown that even at acceleration factors of  $R=30$  and 2:30 min scan time, reconstructions of the velocity vectors and pathlines were possible. However, as the measured peak flow decreased with higher acceleration factors in comparison to 2D flow MRI, a maximum acceleration factor of  $R=20$  was finally recommended. At this acceleration factor peak velocity and peak WSS underestimations were acceptable ( $<10\%$ ) in comparison to a  $R=10$  accelerated 4D flow scan.

In **chapter 4**, the developed CS acceleration technique for Cartesian 4D flow MRI in the aorta was compared to another well-established acceleration technique: k-t PCA. Both techniques demonstrated the ability to accelerate aortic 4D flow MRI measurements for acceleration factors up to  $R=8$ . However, it was shown that peak flow values were underestimated less in CS accelerated 4D flow MRI scans in comparison to 2D flow MRI. Additionally, it was found that the CS accelerated sampling strategy led to flexibility in temporal binning, which allowed for changing the temporal resolution retrospectively.

In **chapter 5**, a clinical study investigated PWV, vessel wall thickness (WT) and WSS in 43 patients with familial hypercholesterolemia and 18 unaffected siblings using 4D and 2D flow MRI. No significant difference in PWV, WT and WSS were found between FH patients and unaffected sibling, which was indicative for the effectiveness of the lipid-lowering treatment these patients received.

In **chapter 6**, 4D flow MRI in an MRI-compatible isolated beating pig heart model was demonstrated. The working pig heart model was attached to a heart lung machine, pumping real pig blood, and mimicking physiological conditions. The working pig heart model could be used in an MRI scan, while providing a stable experimental environment for several hours. In the future the working heart model can help in investigating hemodynamic changes after aortic valve replacement.



### 7.3 Nederlandse samenvatting

Met 4D-flow-MRI kan de bloedstroom in het hart en de bloedvaten gekwantificeerd en gevisualiseerd worden door het coderen van het stromende bloed in op de hartslag getriggerde MRI-scans. Het nadeel van 4D-flow-MRI is een lange acquisitietijd, die in de praktijk meestal wordt beperkt door de scans niet volledig te bemonsteren of door het verminderen van de temporele resolutie. In dit proefschrift wordt een nieuwe “compressed sensing” (CS) acquisitie- en beeldreconstructietechniek gepresenteerd die 2D-flow-MRI scans met hoge temporele resolutie voor regionale polsgolfsnelheidsberekening (PWV)- en 4D-flow-MRI met korte scantijden mogelijk maakt. Om de nauwkeurigheid van versnelde 4D-flow-MRI aan te tonen werd het effect van de versnelling op hemodynamische biomarkers zoals flow en de wandschuifspanning (WSS) onderzocht. Een nieuw, gespecialiseerd varkenshartmodel leverde gedetailleerde beelden op van de intra-cardiale en coronaire bloedstroom.

In **hoofdstuk 2** werd een slimme combinatie van retrospectieve cardiale gating, temporele sortering van data en beeldreconstructie gepresenteerd die 2D-flow-MRI met hoge temporele resolutie mogelijk maakt. Met deze techniek werd aangetoond dat PWV nauwkeurig kan worden gemeten in kleine vaatsegmenten van de halsslagader. Nauwkeurige PWV-schatting in kleine vaatregio's kan een waardevolle aanvulling zijn op uitgebreide MRI-onderzoeken van het vaatstelsel naar de vorming en voortgang van aderverkalking.

In **hoofdstuk 3** werd een pseudo-spiraal cartesische versnelde meetstrategie ontwikkeld, die, in combinatie met een iteratieve CS reconstructie, een substantieel versnelde 4D-flow-MRI op fantoom- en *in vivo* scans van de halsslagader mogelijk maakte. Er werd aangetoond dat, zelfs bij versnellingsfactoren van  $R = 30$  en 2:30 min scantijd, reconstructies van de snelheidsvectoren en pathlines mogelijk waren. Omdat de gemeten piekstroom echter afnam met hogere versnellingsfactoren in vergelijking met 2D-flow-MRI, werd uiteindelijk een maximale versnellingsfactor van  $R = 20$  aanbevolen. Bij deze versnellingsfactor was de onderschatting van de piek-WSS acceptabel ( $<10\%$ ) in vergelijking met een  $R = 10$  versnelde 4D-flow-scan.

In **hoofdstuk 4** werd de ontwikkelde CS versnellingstechniek voor cartesische 4D-flow-MRI in de aorta vergeleken met een andere gevestigde versnellingstechniek: k-t PCA. Beide technieken waren in staat om 4D-flow-MRI metingen van de aorta te versnellen voor versnellingsfactoren tot  $R = 8$ . Er werd echter aangetoond dat piekstroomwaarden minder werden onderschat in CS versnelde 4D-flow-MRI scans in vergelijking met 2D-flow-MRI. Bovendien werd vastgesteld dat de CS versnelde bemonsteringsstrategie leidde tot flexibiliteit in temporele binning, waardoor de temporele resolutie achteraf kon worden gewijzigd.

In **hoofdstuk 5** onderzochten we in een klinische studie PWV, vaatwanddikte (WT) en WSS bij 43 patiënten met familiale hypercholesterolemie (FH) en 18 niet-aangedane broers en zussen met behulp van 4D- en 2D-flow-MRI. Er werd geen significant verschil in PWV, WT en WSS gevonden tussen FH patiënten en niet-aangedane broers en zussen. Dit was indicatief voor de effectiviteit van de lipideverlagende behandeling die deze patiënten ontvingen.

In **hoofdstuk 6** werd 4D-flow-MRI toegepast in een MRI-compatibel geïsoleerd kloppend varkenshartmodel. Het werkende varkenshartmodel was bevestigd aan een hart-longmachine

waarmee varkensbloed werd rondgepompt en fysiologische omstandigheden werden nagebootst. Het werkende varkenshartmodel kon worden gebruikt in een MRI-scan, waar het gedurende een aantal uren een stabiele experimentele omgeving bood. Dit model kan in de toekomst helpen bij het onderzoek naar hemodynamische veranderingen na aortaklepperving.



# APPENDIX

PhD portfolio

List of publications

Curriculum vitae

Acknowledgement

## Portfolio

Name PhD student: Eva Sophia Peper

PhD period: 1. July 2015 – 31. January 2020

Name PhD supervisor: prof. dr. ir. A.J. Nederveen and prof. dr. ir. G.J. Strijkers

PhD training	Year	ECTS
<b>Graduate school courses</b>		
Scientific Writing	2017	1.5
Project Management	2016	0.6
Citation Analysis and Impact Factors	2015	0.1
<b>Seminars and workshops</b>		
Institute QuantiVision Winterschool on Machine Learning	2018	0.6
ESMRMB Non-Cartesian MRI: Implementation and application	2016	0.9
<b>Conferences and symposiums attended</b>		
12 <sup>th</sup> Annual Meeting of ISMRM Benelux chapter, Arnhem, NL	2020	0.3
10 <sup>th</sup> Symposium on Ultrahigh Field MR, Berlin, Germany	2019	0.3
4 <sup>th</sup> 4D flow MRI workshop, York, England	2019	0.6
27 <sup>th</sup> Annual Meeting of ISMRM, Montreal, Canada	2019	2.0
11 <sup>th</sup> Annual Meeting of ISMRM Benelux chapter, Leiden, NL	2019	0.3
Amsterdam Cardiovascular Sciences symposium, Amsterdam, NL	2018	0.3
26 <sup>th</sup> Annual Meeting of ISMRM, Paris, France	2018	2.0
10 <sup>th</sup> , Annual Meeting of ISMRM Benelux chapter, Antwerp, BE	2018	0.3
25 <sup>th</sup> Annual Meeting of ISMRM, Honolulu, USA	2017	2.0
11 <sup>th</sup> International symposium on Biomechanics in Vascular Biology and Cardiovascular Disease, Rotterdam, NL	2017	0.6
Institute QuantiVision Conference, Amsterdam, NL	2017	0.3
9 <sup>th</sup> Annual Meeting of ISMRM Benelux chapter, Tilburg, NL	2017	0.3
Amsterdam Cardiovascular Sciences symposium, Amsterdam, NL	2016	0.3
24 <sup>th</sup> Annual Meeting of ISMRM, Singapore	2016	2.0
8 <sup>th</sup> Annual Meeting of ISMRM Benelux chapter, Eindhoven, NL	2016	0.3
23 <sup>rd</sup> Annual Meeting of ISMRM, Toronto, Canada	2015	2.0
<b>Podium presentations</b>		
4 <sup>th</sup> 4D flow MRI workshop, York, England	2019	0.2
10 <sup>th</sup> Symposium on Ultrahigh Field MR, Berlin, Germany	2019	0.2
ISMRM Philips PPE event, Montreal, Canada	2019	0.2
26 <sup>th</sup> Annual Meeting of ISMRM, Paris, France	2018	0.2
10 <sup>th</sup> , Annual Meeting of ISMRM Benelux chapter, Antwerp, BE	2018	0.2
25 <sup>th</sup> Annual Meeting of ISMRM, Honolulu, USA	2017	0.2

	Teaching	
Institute QuantiVision Conference, Amsterdam, NL	2017	0.2
8 <sup>th</sup> Annual Meeting of ISMRM Benelux chapter, Eindhoven, NL	2016	0.2
<b>Poster presentations</b>		
12th Annual Meeting of ISMRM Benelux chapter, Arnhem, NL	2020	0.2
Amsterdam Cardiovascular Sciences symposium, Amsterdam, NL	2018	0.2
25th Annual Meeting of ISMRM, Honolulu, USA	2017	0.2
11th International symposium on Biomechanics in Vascular Biology and Cardiovascular Disease, Rotterdam, NL	2017	0.2
9th Annual Meeting of ISMRM Benelux chapter, Tilburg, NL	2017	0.2
Amsterdam Cardiovascular Sciences symposium, Amsterdam, NL	2016	0.2
24th Annual Meeting of ISMRM, Singapore	2016	0.2
23rd Annual Meeting of ISMRM, Toronto, Canada	2015	0.2

## Teaching

---

### Lecturing

Data analysis in MATLAB	2017-2018	3.0
-------------------------	-----------	-----

### Tutoring

Data analysis in MATLAB	2015,2016, 2019	2.1
-------------------------	--------------------	-----

### Supervising

V. Čaluković, Physics, MSc Internship	2019	2.0
B.A. Runderkamp, Physics, MSc Graduation project	2017-2018	2.5
L. van Dongen, Medical Imaging and Intervention, MSc Internship	2017	2.0
V.Q. Pronk, Physics, BSc Graduation project	2016-2017	2.0
V. Čaluković, Physics, BSc Graduation project	2017	2.0
S.A.P. Nannan Panday, Cardiovascular Research, MSc Internship	2016	2.0

## Parameters of Esteem

---

### Grants

Travel grant Amsterdam University	2019
ISMRM educational stipend	2015-2017

### Awards and Prizes

Power Pitch award, Berlin Ultra High Field Symposium	2019
Magna Cum Laude ISMRM Merit award	2017

**Organizational Activities**

9<sup>th</sup> Annual Meeting of ISMRM Benelux chapter, Tilburg, NL

2017

2.0

**International Journal Reviewing**

Journal of Cardiovascular Magnetic Resonance (4 papers)

Magnetic Resonance in Medicine (2 papers)

NMR in Biomedicine (1 paper)

Journal of Biomechanics (1 paper)

Magnetic Resonance Materials in Physics, Biology and Medicine (2 papers)

Quantitative Imaging in Medicine and Surgery (1 paper)

## List of Publications

Pseudo-spiral sampling and compressed sensing reconstruction provides flexibility of temporal resolution in accelerated aortic 4D flow MRI: A comparison with k-t principal component analysis

Lukas M. Gottwald & **Eva S. Peper**, Qinwei Zhang, Bram F. Coolen, Gustav J. Strijkers, Aart J. Nederveen and Pim van Ooij, NMR in Biomedicine, 2020

Highly accelerated 4D flow cardiovascular magnetic resonance using a pseudo-spiral Cartesian acquisition and compressed sensing reconstruction for carotid flow and wall shear stress

**Eva S. Peper** & Lukas M. Gottwald, Qinwei Zhang, Bram F. Coolen, Pim van Ooij, Aart J. Nederveen and Gustav J. Strijkers, Journal of Cardiovascular Magnetic Resonance, 2020

An isolated beating pig heart platform for a comprehensive evaluation of intracardiac blood flow with 4D flow MRI: a feasibility study

**Eva S. Peper**, Alberto M. Leopaldi, Sjoerd van Tuijl, Bram F. Coolen, Gustav J. Strijkers, Jan Baan, R. Nils Planken, Arend de Weger, Aart J. Nederveen, Henk A. Marquering, Pim van Ooij, European Radiology Experimental, 2019

Insufficient slow flow suppression mimics aneurysm wall enhancement in magnetic resonance vessel wall imaging: a phantom study

Bart M.W. Cornelissen, Eva L. Leemans, Bram F. Coolen, **Eva S. Peper**, Henk A. Marquering, C. H. Slump, C.B.L.M. Majoie, Neurosurgical Focus, 2019

Regional assessment of carotid artery pulse wave velocity using compressed sensing accelerated high temporal resolution 2D CINE PC MRI

**Eva S. Peper**, Gustav J. Strijkers, Katja Gazzola, Wouter V. Potters, Abdallah G. Motaal, Ilse K. Luirink, Barbara A. Hutten, Albert Wiegman, Pim van Ooij, Bert-Jan H. van den Born, Aart J. Nederveen, Bram F. Coolen, J Cardiovasc Magn Reson, 2018

Evaluation of compressed sensing MRI for accelerated bowel motility imaging

C. Sofieke de Jonge, Bram F. Coolen, **Eva S. Peper**, Abdallah G. Motaal, C. Yung Nio, I. Somers, Gustav J. Strijkers, Jaap Stoker, Aart J. Nederveen, European Radiology Experimental, 2019

Accelerated 4D phase contrast MRI in skeletal muscles contraction

Valentina Mazzoli, Lukas M. Gottwald, **Eva S. Peper**, Martijn Froeling, Bram F. Coolen, Nico Verdonshot, Andre M. Sprengers, Pim van Ooij, Gustav J. Strijkers, Aart J. Nederveen, Magn Reson Med, 2018



## Appendix

Advancing Cardiovascular, Neurovascular, and Renal Magnetic Resonance Imaging in Small Rodents using Cryogenic radiofrequency coil technology

Thoralf Niendorf, Andreas Pohlmann, Henning M. Reimann, Helmar Waiczies, **Eva S. Peper**, Till Huelnhagen, Erdmann Seeliger, Adrian Schreiber, Ralph Kettritz, Klaus Strobel, Min-Chi Ku, Sonia Waiczies, *Frontiers in Pharmacology*, 2015

### Other

Article on beating pig heart, Klopt dat? NWO Relatiemagazine Impact nummer 4, 2016, p.28-30

Article on beating pig heart, Kloppend hart in de MRI, AMC Magazine, issue 9, 2016, p.4-5

## Curriculum Vitae

Eva Sophia Peper was born in Heidelberg, Germany on 16<sup>th</sup> of November 1987. She went to primary school in Freiburg i. Br., Germany and received her high school diploma at Rotteck-Gymnasium Freiburg in 2007. She then started her Bachelor studies in Physics at the University of Heidelberg. After finishing her Bachelor graduation project on satellite remote sensing, she continued with a Physics Master. At the same time she worked as student research assistant at the Max Planck Institute for Nuclear Physics and at the Kirchhoff Institute for Physics. Following lectures on medical imaging, she became interested in the field of magnetic resonance imaging and in 2013 she started her one year graduation project at the Berlin Ultra High Field Facility in Berlin under supervision of professor dr. Thoralf Niendorf. The project focused on performing magnetic resonance imaging for quantitative susceptibility mapping of the rodent heart. After graduating in 2014 at the University of Heidelberg, she moved for her PhD to Amsterdam, the Netherlands. At the Amsterdam Medical Centre she worked on compressed sensing accelerated imaging for fast 4D flow MRI under supervision of professor dr. ir. Aart Nederveen, professor dr. ir. Gustav Strijkers, dr. ir. Pim van Ooij and dr. ir. Bram Coolen. The project focussed on the implementation of acquisition and reconstruction techniques for fast imaging and image recovery. Experiments on the dynamic imaging of the blood flow in arteries were carried out in phantoms, volunteers and patients with cardiovascular disease. Next to her own research she supervised several students, and was part of the ISMRM Benelux organizing committee. In February 2020 Eva started at the ETH Zurich under supervision of professor dr. Sebastian Kozerke.

## Acknowledgement

Four and a half years in the Netherlands have gone by so quickly! I am very thankful to everyone supporting me during my PhD and on the way there. That includes the help and patience of my supervisors and colleagues, but also the warm welcome in Amsterdam I received by so many. And although the final PhD defense was shadowed by the Coronavirus, I felt like I was connected to everyone more than ever before.

First of all I would like to thank my **committee members** for taking the time reading my thesis and attending my defense – even during these uncertain times.

Dear **Aart**, thanks a lot for your never-ending support, trust and encouragements! I remember from the moment we met that I thought it was going to be a lot of fun and laughing, which turned out to be true. Writing ISMRM abstracts in the middle of the night, making movies – you always took good care of us! I really appreciate that one of your goals is to foster a social and supportive research group. You taught me that we should accept everyone just the way they are and see their strengths. I think this is also how you supported me, which gave me a lot of freedom and confidence.

Dear **Gustav**, I think this also applies to you, I do not remember when we were not making jokes at our meetings, although you probably could not stand these pulse wave velocity discussions anymore. I really appreciate your support and knowledge in moments when I really needed it, like very late-night corrections and endless rebuttals. You always encouraged critical thinking and scientific proof – that helped me a lot. And yet you never took our research work too hard, you encouraged the spirit of just enjoying the science we are doing.

Dear **Pim**, after my first day at the AMC you offered going for a drink. I thought I shouldn't do that on my first day and I ordered a coke. I am glad we had many beers afterwards! I experienced you as a very loyal person and as that, from day one on, you gave me the feeling of being part of your 4D flow team. I am very thankful for all the advice you gave me about the research world, for your 4D flow expertise and for your paper writing skills. Thanks for being part of the rage against the MR machine!

Dear **Bram**, I remember a lot of very interesting conversations with you, luckily not all were on pulse wave velocity! You always had very inspiring and positive ideas. I think I really agree with you on your concept of research, which should not just be fast, but should appreciate critical thinking. Thank you for your support and patience – for coaching me before presentations and asking the right question. I also enjoyed when we all went bouldering, your music quizzes, dancing and eating coriander sauce!

Lieber **Lukas**! I remember you were asking for the bill for your 1.20 € croissant at AH Togo the first day and I thought – oh man, this is going to be so German. And I think I was right, but in a very positive way. I actually realized how happy I was to have someone around with the same sense of German humor (ja, ik weet het, wij Duiters hebben geen humor...), and I also liked your interest in politics, your green heart, your reliability and your planning skills. It was like we already knew each other for long. Thank you for all these years as my partner in crime, the scan sessions, the discussions, the waffle baking, the Feuerzangenbowle, and the road trips to Würzburg and on Hawaii. You are a great worker, presenter, programmer and organizer from who I could learn a lot. So PROUD!

Dear **Jasper**! I am a really big fan of your working attitude! If you feel like you are getting too stressed, you just let it be, take a break, go for a camping trip, and you come back refreshed with the greatest ideas. I remember you were staying next to my table at a moment when I was very stressed, saying “Why are you doing this? Why is this all so messy?” and you cleaned up the table. I really appreciate you being there in these crazy moments. I learned from you that what we do should only be driven by our interest, as otherwise we just lose energy. You also said, grass mowing is the best human activity. Thank you for the scientific discussions, the Carrgo patch, the Grand Opening and all Aloha Fridays. I am very happy for your future steps with Abigail and Zora!

Dear **Z0-Team**, what would have this been without you. My PhD time at Z0 feels like one big journey with the Pineapple Express! Dear **Joena**, you immediately took good care of me from the day I arrived. With our energy levels matching, we had so much fun in creating Halloween dinners and Paasontbijts. Swimming, horse riding, a weekend in Germany, mountain biking in the Ardennen – so many great moments happened because of you! Dear **Kerry**, thanks a lot for all your support and pulse programming help these years. It was great to be your paranymp and making your movie – so smart, every single day! I hope we will all have another hot pot together, also if that means we have to fly to China. Dear **Lena**, I enjoyed sitting next to you most of my PhD years, you helped me out in so many situations – I hope I could give something back to you. I think you guided me a lot on my PhD track and I am so happy for you doing a great job as a pulse programmer now! **Jithsa**, my sports-buddy! I really enjoyed going to the gym with you and Marthe – not to forget our regular kwarktiertjes. Keep eating your proteins! Dear **Sofieke**, Ms Business, we had great times as ISMRM roomies and compressed sensing buddies! Dear **Valentina**, I love your sarcasm, always with this very subtle smile on your face. ISMRM and LA, I am curious where we meet next. Dear **Paul de Heer**, PdH, you were always there when we had a lot of fun. I hope you forgive me all my jokes at some point. **Melissatje**, I was so happy when you joined Z0, you are a great worker and a sweet colleague. And you always protected me when cycling home at night! Dear **Esther**, thank you so much for being so open, you helped me a lot in getting started and you always organized great events. And, of course, thank you for the perfect match with Joany. **Paul Groot** thank you for all your patience and help! I am logged out of the flux now and I finally cleared my parrec folder. Dear **Sandra** and **Raschel**, so many moments of happiness – not only as poldersport teammates, but also behind the scanner! Dear **Wouter**, thank you for your help in the beginning of my PhD. When I started I had so many questions and you patiently helped me through. I also have your wedding and the BBQ at your house in very good memory! **Anouk, Bada, Bobby, Carmen, Claudia, Dorien, Geor, Henk-Jan, Jordi, Jos, Jules, Koen, Laura, Liza, Luuk, Mariah, Marieke, Matthan, Michelle, Oliver, Ot, Sophie, Toni**, my room and next-room mates! I remember great ISMRM and 4D flow meetings, Kerstborrels, Café Vrijdag evenings, Airbnb stays, hikes (with Boen and Kobby), tiny houses and football games (and no Jasper you don't have 11 Mexican friends). For those who are still about to finish, I wish you good luck and you all know the spirit of Z0 – het komt goed!

Dear **AMC students**, Krolos, Vera K, Vera P, Bobby, Lotte, Sanjay – thank you for all your work and contributions to this thesis. I experienced you as smart and hard-working, and I wish you all the best with finding your way through your studies and with what follows afterwards.

Dear **collaborators** from the AMC, Lund, Leiden and LifeTec, thank you for all your support and contributions. I always enjoyed our collaborations. In particular, I would like to thank **Sjoerd, Alberto** and **Luca** from LifeTec for their intensive support, also during late-night scan sessions. I also would like to thank **Martin** and **Gerard** from Gyrotools, I was glad that I could ask you many questions and got a fast reply. Who doesn't have a "Martin Bühner" folder on their PC? I also would like to thank **Maarten** Versluis from Philips – your continuous pulse programming support was so much appreciated!

Liebe **Berliner MRT** Gruppe, lieber Herr **Niendorf**, ich freue mich immer Euch auf der ISMRM oder auf anderen Konferenzen zu sehen. **Henning**, danke für unsere schönen Gespräche! And of course not to forget: my dear **Ji Yiyi** and **Ku MinChi**! On the stairways to heaven, in the jungle or with noodles in Toronto. So glad to have you!

Liebe **ETH Gruppe**, lieber **Sebastian**, vielen Dank, dass ihr mich so freundlich aufgenommen habt, ich fühle mich sehr wohl und bin (virtuell) umgeben von so vielen netten Kollegen. Aus dem Home Office haben wir sicher das Beste gemacht. Vor allem nochmals Danke an **Jonas** und **Hannes**, dass ihr Euch gerade am Anfang so viel Zeit für mich genommen habt!

To all **wintersport** fans! Although always in different groups, I am so happy that we went to Mayerhofen, La Plagne and Ischgl. I really feel like wintersport brings you closer together. Dear **Gijs**, thanks for being a great roommate and for helping me so much with the transition from Amsterdam to Zürich.

Meine liebe **Joany**, I was so happy the moment I moved into our amazing flat, it was like coming home. We were a great match from day one, being happy with cooking and caring for our plants. I think we even dared to do some big investments. I was glad to have someone at home who was in a similar situation and understood the PhD life. You are such a caring person and I wish you to be always surrounded by people who appreciate that!

Dear **Thomas, Daniel and Cecile, Nicola**, thank you all for taking such good care of me! You welcomed me in your family and you introduced me to so many new things. With you I saw Georgies, the closure, Alex, Hunee, Bobby, LSV, Wildeburg, Koningsdag, ADE, the Krampus, the Efteling, Scotland – and it changed me a lot. Cecile, thank you for our deep conversations and our spontaneous Georgies wedding! I am sure my magic card collection and my sinterklaas staf will be needed at some point. Amsterdam, Amsterdam!

Liebe **Heidelberger Physiker**, so schön, dass wir uns nach all den Jahren noch regelmässig sehen. Immer wenn wir zusammen sind, fühlt es sich an als wäre man gar nicht weg gewesen. Meine liebe **Ying Ying**, leider haben wir uns lange nicht getroffen, aber ich weiss, dass Du immer für mich da bist. Liebe **Caro**, auch Du bist eine Heidelberger Physikerin und ich bin froh, dass wir uns noch immer sehen! Liebe **Anna Ka, Maria**, und **Chrissi**, danke für die schönen WG Erinnerungen und unsere Treffen in Freiburg. Meine liebe **Johanna**, wenn wir zusammen sind erleben wir immer etwas! Ich bin froh, dass wir uns haben und uns so oft sehen. Meine liebe **Anna**, ich bin froh eine Freundin wie Dich zu haben, Du bist eine Konstante auf die ich mich immer verlassen kann. Ohne deine Unterstützung wäre vieles nicht möglich gewesen.

Liebe **Katharina**, lieber **Dieter**, danke für Eure fortwährende Unterstützung und Euer Interesse an meiner Arbeit! Lieber **Carl**, so viel haben wir schon zusammen erlebt und ich bin froh, dass wir fast täglich telefonieren, lachen und uns unterstützen, egal wo wir uns gerade befinden! #Ichkanndasverstehen. Liebe **Helen**, ich freue mich, dass Du Teil unserer Familie bist und bin stolz auf alles was Du erreicht hast. Liebe **Eltern**, ihr habt mich immer gefördert und unterstützt, danke! Ich denke vor allem das positive Denken habe ich von Euch – es gibt nie eine Situation in der man nicht auch die positiven Seiten sehen kann. Das hat mir bisher und besonders in der PhD-Zeit sehr geholfen.